THE UNIVERSITY *of* EDINBURGH

Sustainable photocatalytic oxidation processes for the treatment of emerging microcontaminants

Konstantina Davididou

Submitted for the degree of Doctor of Philosophy at

The University of Edinburgh

THE UNIVERSITY *of* EDINBURGH

2018

Sustainable photocatalytic oxidation processes for the treatment of emerging microcontaminants

by

Konstantina Davididou

Supervised by

Dr Efthalia Chatzisymeon

Declaration

I hereby declare that this thesis has been completed solely by Konstantina Davididou, under the supervision of Dr Efthalia Chatzisymeon. Full reference is given where other sources are used. This work has not been submitted for any other degree or professional qualification.

Konstantina Davididou

26/02/2018

Abstract

This work investigates the elimination of new and emerging microcontaminants (EMs) from water by means of photochemical oxidation processes, namely heterogeneous and homogeneous photocatalysis. Representative compounds of artificial sweeteners (saccharin, SAC), endocrine disruptors (bisphenol-A, BPA), and pharmaceuticals (antipyrine, AP) of high environmental persistence and widespread occurrence in the water cycle are used as case studies. Novel concepts that can make photochemical oxidation a more cost-effective and environmentally benign technology are tested.

In Chapter 4, the photocatalytic treatment of SAC and BPA is investigated. Novel submicronic anatase–rutile nanocomposite particles with tuned phase ratio are used as catalysts to increase the photocatalytic performance under UVA irradiation. At the best-assayed conditions (C_0 = 3 mg/L, catalyst = 400 mg/L), SAC and BPA are completely degraded within 90 and 150 min of photocatalytic treatment, respectively. [variables: anatase-rutile ratio; initial substrate concentration; catalyst concentration; catalyst reuse; sonication during catalyst recovery]

In Chapter 5, a UVA light-emitting diode (UVA-LED) and sunlight are used as irradiation sources to reduce energy requirements and environmental impacts of photocatalytic processes. The photocatalytic degradation of SAC and BPA is studied under UVA irradiation provided by either a UVA-LED or a conventional fluorescent blacklight UVA lamp (UVA-BL) and solar irradiation. At the best-assayed conditions (C_0 = 2.5 mg/L, TiO_2 = 250 mg/L), BPA is completely degraded within 20, 30, and 120 min under UVA-LED, solar, and UVA-BL irradiation, respectively. The treatment time required for the complete elimination of SAC is 20 min under UVA-LED and 90

min under UVA-BL irradiation. [variables: initial substrate concentration; catalyst concentration; water matrix; light source; reactor configuration]

In Chapter 6, a comparative study is carried out among the photocatalytic systems of Chapters 4 and 5 in terms of EMs removal, photonic and energy efficiencies. Technical and economic aspects of all the processes are assessed. LED-driven photocatalysis achieves the highest efficiency in terms of organic removal with the minimum energy consumption, rendering it the most sustainable technology for the treatment of EMs.

In Chapter 7, olive mill wastewater (OMW) is used as an iron-chelating agent in the photo-Fenton reaction to obviate the need for water acidification at pH 2.8. Conventional, OMW- and EDDS-assisted photo-Fenton treatment is applied for SAC degradation in a solar compound parabolic collector (CPC). It was found that OMW forms iron complexes able to catalyse H_2O_2 decomposition and generate hydroxyl radicals. At the optimal OMW dilution (1:800), 90% of SAC is degraded within 75 min. [variables: pH; iron-chelating agent; initial SAC concentration; OMW dilution]

In Chapter 8, other complexing and oxidising agents, namely oxalate and persulfate, are used for the intensification of AP degradation during UVA-LED photo-Fenton treatment. Neural networks are applied for process modelling and optimisation. At the optimal conditions (hydrogen peroxide = 100 mg/L, ferrous iron = 20 mg/L, oxalic acid = 100 mg/L), complete degradation of AP and 93% mineralisation is achieved within 2.5 and 60 min, respectively. [variables: initial concentration of hydrogen peroxide, ferrous iron, oxalic acid, persulfate]

It is concluded that LED-driven photocatalysis is a sustainable technology for the elimination of EMs from water. Results from this work highlight the need for

development and optimisation of engineering proper LED reactors. Furthermore, this work introduces a new concept towards the sustainable operation of photo-Fenton that is based on the use of wastewaters rich in polyphenols instead of pricey and hazardous chemicals for iron chelation. The addition of ferrioxalate complexes is proposed for the intensification of EMs mineralisation during UVA-LED photo-Fenton treatment. Finally, the findings of this work encourage the use of chemometric tools as predictive and optimisation tools.

Lay Summary

New and emerging microcontaminants (EMs) are a growing, widespread threat to surface water and groundwater. Chemicals used in everyday life enter the water cycle via the effluent discharges of conventional wastewater treatment plants (WWTPs), which fail to provide a barrier to resistant, hazardous, and bio-recalcitrant EMs. As a result, EMs, such as antibiotics, personal care products, and industrial chemicals, are released into water bodies, raising major environmental and health concerns. Adverse effects associated with the presence of EMs in the aquatic environment include ecotoxicity, endocrine disruption, and development of antibiotic-resistant bacteria and resistance genes. Therefore, there is considerable interest in the development of sustainable treatment technologies that are highly efficient in removing EMs. The present thesis investigates the photocatalytic degradation of EMs and evaluates novel concepts aimed towards the delivery of sustainable photochemical oxidation technologies.

Acknowledgements

All the good things come to an end and, at this point, I would like to thank all the people that contributed to the work presented in this thesis.

First and foremost, I would like to express my gratitude to my super supervisor Dr Efthalia Chatzisymeon. My PhD has been an amazing experience and this would not have been possible without Thalia's exemplary guidance, motivation, support and all the wonderful opportunities offered. I thank Thalia for being a true mentor in every aspect, for making me better and setting an excellent example for me to follow.

I am also very grateful to Dr Andrea Semião, Miss Louise Hogg, Miss Isabel Fernández, Miss Elisa Ramos, Mr Agustín Carrión, Dr John Fakidi, and Miss Ana Belén Martínez for their support during my lab work.

During this journey, I had the privilege to learn from the best; special thanks to Prof Sixto Malato, Prof José María Monteagudo, and Dr Leonida Perez-Estrada for the exceptional collaborations.

Many thanks to the MEng students, Miss Emily Hale, Miss Nicky Lane, Mr Robin Nelson, and Mr Calum McRitchie for being so motivated and enthusiastic lab-partners.

Special thanks to my co-authors, Prof Antonio Durán, Dr Antonio José Expósito, Dr Alexandre Pichavant, Dr Jean-François Hochepied, Dr Isabel Oller, Dr Maria Antonopoulou, and Prof Ioannis Konstantinou for their constructive feedback and contribution to publishing this work.

Special mention to Prof Alistair Borthwick, my co-supervisor, for his valuable feedback on this thesis.

I would also like to thank my thesis examiners, Dr Andrea Semião and Dr Patrick Dunlop, for their comments, thoughts, and the very fruitful experience during my Viva.

A big thank you to the good friends that I made during my PhD for making my life more beautiful, inside and outside the university.

Finally, but by no means least, I would like to thank mum, dad, and Mikey, who mean the world to me, for their unbelievable support and endless love.

Table of Contents

List of Tables

List of Figures

Abbreviation list

ACE	Acesulfame
AOP	Advanced Oxidation Process
AP	Antipyrine
AS	Artificial Sweetener
BL	Blacklight
BPA	Bisphenol-A
CCED	Central Composite Experimental Design
CPC	Compound Parabolic Collector
CYC	Cyclamate
DI	Deionised water
EDC	Endocrine Disrupting Compound
EDDS	Ethylenediamine-N, N-disuccinic acid
EM	Emerging Microcontaminant
HA	Humic Acids
HPLC	High Performance Liquid Chromatography
HRT	Hydraulic Retention Time
LED	Light-Emitting Diode
L-H	Langmuir-Hinshelwood
LMCT	Ligand-to-Metal Charge Transfer
NN	Neural Network
OMW	Olive Mill Wastewater
ROS	Reactive Oxygen Species
RPR	Raceway Pond Reactor
SAC	Saccharin
SRT	Sludge Retention Time
SUC	Sucralose
TEM	Transmission Electron Microscopy
TOC	Total Organic Carbon
TP	Transformation Product
US	Ultrasound Cleaning
WWTP	Wastewater Treatment Plant
XRD	Xray-Diffractogram

1 Introduction

The widespread occurrence in water of new and emerging microcontaminants (EMs), such as pharmaceuticals, personal care products, artificial sweeteners, endocrine disrupting compounds, ionic liquids, industrial additives and numerous other chemicals used in everyday life, constitutes a water quality challenge worldwide [1-3]. The presence of EMs in the aquatic environment has been linked to several negative effects, including ecotoxicity, endocrine disruption and development of antibiotic-resistant genes and bacteria, raising serious concerns about human health and ecosystems [4-7]. Conventional wastewater treatment plants (WWTPs) are not typically designed for the treatment of such persistent compounds [8-10]. Trace level concentrations and diversity of EMs complicate even more their elimination by conventional treatment processes. Hence, a large fraction of EMs escapes into the aquatic environment by means of the effluent discharges of WWTPs. New, efficient treatment methods are required as barriers to the release of EMs into the environment. Treatment technologies should be developed that are not only highly efficient in the complete elimination of EMs, but also inexpensive and environmentally benign in order to obtain, ultimately, net environmental benefits.

In this direction, the efficiency of advanced oxidation processes (AOPs) for the elimination of recalcitrant, non-biodegradable and hazardous EMs has been widely demonstrated [4, 9, 11-13]. Yet the high energy requirements of AOPs lead to increased operational costs and high environmental impacts, which in turn restrain their wide application at full-scale [14-16]. Among several AOPs, photocatalysis,

homogeneous and heterogeneous, is emerging as a promising technique for water and wastewater treatment mainly due to the potential use of solar light as an energy source [17-19].

This thesis investigates the photocatalytic degradation of EMs. For this purpose, novel concepts that can make photochemical oxidation a more cost-effective and environmentally friendly technology are tested. The specific objectives of this thesis are summarised as follows:

- Study the use of novel TiO_2 nanocomposites as catalysts to increase photocatalytic efficiency under UVA irradiation. Understand the effect of key operating parameters, namely initial substrate concentration, catalyst type and concentration on photocatalytic performance. Evaluate catalyst activity on repeated use.
- Study the use of light-emitting diodes (LEDs) and sunlight as irradiation sources to reduce the energy requirements and environmental impacts of the photocatalytic process. Understand the effect of key operating parameters, namely initial substrate and catalyst concentration, water matrix and light source on photocatalytic performance.
- Study the use of agro-industrial wastewater as an iron-chelating agent in order to minimise the amount of chemical reagents added in the treatment process and the related shortcomings (e.g. cost of chemicals, effluent with increased salinity). Understand the effect of key operating parameters, namely initial substrate concentration, agro-industrial wastewater dilution and accumulated UV energy on photocatalytic performance.

- Study the addition of other complexing agents and oxidants to improve photocatalytic efficiency under UVA-LED irradiation. Use of chemometric optimisation tools, such as central composite experimental design and neural networks, to model the process and optimise selected operational parameters. Understand the simultaneous effects of various operating parameters, such as initial concentration of hydrogen peroxide, ferrous ion, oxalic acid, and persulfate on photocatalytic performance.
- Carry out a comparative study among several photocatalytic oxidation processes in terms of EMs removal, photonic, and energy efficiencies in order to evaluate their technical and economic benefits.

The findings of this work could contribute to the delivery of photocatalytic technologies of high removal efficiency and increased sustainability. Results can be used to overcome technical barriers of photocatalytic oxidation and become a powerful tool for stakeholders to further proceed with process scaling-up.

2 Theoretical background

2.1 Emerging microcontaminants

Contaminants of emerging concern or emerging microcontaminants (EMs) are '*chemical substances that have no regulatory standard, have been recently "discovered" in natural streams and potentially cause deleterious effects in aquatic life at environmentally relevant concentration*' [20].

EMs are not necessarily new chemicals; they may be compounds newly introduced in the environment (e.g. industrial additives), compounds possibly present in the environment for a long time but recently detected (e.g. pharmaceuticals) due to the advances in analytical chemistry and instrumentation during the last two decades, or compounds present in the environment for a long time but whose negative potential impacts on human health, aquatic life, wildlife and ecosystems have been only recently identified (e.g. hormones) [1, 21].

A large variety of natural and synthetic chemical compounds used in everyday life and industrial applications have been characterised as EMs, including pharmaceuticals, personal care products, engineered nanomaterials, hormones, steroids, surfactants and surfactant metabolites, pesticides, herbicides, fungicides, industrial additives, antiseptics, and, recently, artificial sweeteners and ionic liquids [7, 21-23]. A list of the major groups of EMs is given in Table 2-1.

The classification of EMs is not definite and several groupings have evolved, depending on the perspective [1]. Hence, EMs can be also categorised into:

- EDCs (endocrine disrupting compounds) and CMR (carcinogenic, mutagenic, toxic to reproduction) depending on their toxicological effects,
- PBT (persistent, bioaccumulative, toxic), vPvB (very persistent, very bioaccumulative), POP (persistent organic pollutant) depending on their environmental properties,
- priority pollutants, etc. depending on their legislative status, and
- HPV (high production chemicals).

Table 2-1 List of major groups of EMs, adapted in part from Stefanakis and Becker (2016) [21]. (Bold letters: representative EMs used in this study).

Emerging contaminant groups	Examples
Pharmaceuticals	
• Human antibiotics & veterinary	Trimethoprim, erythromycin, amoxicillin
• Analgesics, anti-inflammatory drugs	Ibuprofen, diclofenac, **antipyrine**
• Psychiatric drugs	Diazepam, carbamazepine, primidone
• β-blockers	Metoprolol, propanolol, timolol
• Lipid regulators	Bezafibrate, clofibric acid, fenofibric acid
• X-ray contrasts	Iopromide, iopamidol, diatrizoate
Personal care products	
• Fragrances	Nitro, polycyclic and macrocyclic musks
• Sun-screen agents	Benzophenone
• Insect repellents	N,N-diethyltoluamide
Endocrine disrupting compounds	**Bisphenol-A**, octylphenols, nonylphenols
Hormones & steroids	Estradiol, estrone, estriol
Perfluorinated compounds	Perfluorotoctane sulfonates
Surfactants & surfactant metabolites	Alkylphenol ethoxylates, 4-nonylphenol
Industrial additives & agents	Chelating agents, aromatic sulfonates
Gasoline additives	Dialkyl ethers, methyl-t-butyl ether
Antiseptics	Triclosan, chlorophene
Artificial sweeteners	Acesulfame, **saccharin**, sucralose

In this study, representative EMs will be used as case studies. Specifically, the photocatalytic oxidation of saccharin (artificial sweetener), bisphenol-A (endocrine

disrupting compound), and antipyrine (anti-inflammatory analgesic and antipyretic drug) will be investigated.

2.1.1 Artificial sweeteners

Artificial sweeteners (ASs) are used worldwide as low-calorie or calorie-free sugar substitutes in food, beverages, pharmaceuticals, and personal care products, such as mouth washes and tooth pastes [24]. Fast growing health threats, such as diabetes and obesity, as well as the move of many people towards a healthier lifestyle, have increased considerably the demand for ASs [25, 26]. The use of ASs is also preferred by food industry because they are cheaper than sugar and result in products of longer shelf-life [27].

ASs have been recently recognised as EMs due to their environmental persistence and widespread detection in the aqueous environment [28, 29]. They are metabolically inert in the human body and after consumption are excreted with urine and pass virtually unchanged to WWTPs [30]. It has been shown that the conventional processes applied in WWTPs are ineffective for the complete elimination of ASs [31, 32]. As a result, ASs are introduced continuously into receiving water bodies, untreated or partially treated, with the effluent discharges. Among ASs, acesulfame (ACE), sucralose (SUC), saccharin (SAC), and cyclamate (CYC) are widely detected in wastewater effluents, surface water, and groundwater at trace level concentrations, μg/L, much higher than other anthropogenic chemicals [28, 33]. The widespread occurrence of ASs coupled with their recalcitrance render them, ironically, ideal markers of domestic wastewaters in natural waters [34].

While these sugar substitutes, at the detected concentrations, are safe for human consumption, concerns are mostly related to their ecotoxicological impact, which is largely unknown [29]. During the past three years, there has been a rise in the number of studies revealing toxicity of ASs and their transformation products (TPs) on aquatic organisms. For instance, Saucedo-Vence et al. (2017) reported that exposure to environmentally relevant concentrations, 0.05 and 155 µg/L, of SUC, although not bio-accumulated in the organs and tissues, induces damage to proteins and lipids in the liver, brain, muscle and gills of the common carp (*Cyprinus carpio*) [35]. Ren et al. (2016) showed that although ACE itself had no adverse effects, TPs formed during ACE UV photolysis caused oxidative stress to increase in the liver of *Carassius auratus* [36]. Li et al. (2016) also reported that ACE photogenerated TPs, at low g/L concentrations, induced adverse effects on the development of zebra fish embryo [37].

2.1.1.1 Saccharin

SAC is a sulfimide, whose main physicochemical characteristics are presented in Table 2-2. It is the forerunner of ASs, firstly synthesised in 1879, and it is used in blends with aspartame or CYC covering each other's off taste. SAC is the E954 food additive in the European Union with an acceptable daily intake of 0-5 mg/kg of body weight [38]. Except for human consumption, SAC is also registered as an additive in piglet feed and as a brightening agent in electroplating solutions [39, 40].

SAC has been widely detected in influent (3.9 – 43 µg/L) and effluent of WWTPs (< 0.1 – 3.5 µg/L), surface water (0.01 – 3.8 µg/L), and groundwater (< 0.21 – 10.3 µg/L) in Switzerland, Germany, Serbia, Canada and China [28, 31, 33, 34, 41, 42].

Ecotoxicity assessments of SAC have indicated a low hazard and risk potential towards aquatic organisms and no evidence for human toxicity [43]. However, the long-term ecotoxicological effects of SAC and SAC TPs formed during natural attenuation are still largely unknown.

Table 2-2 Physicochemical properties of SAC [44].

Structure	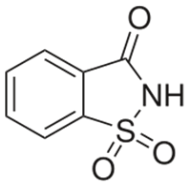
IUPAC name	1,1-dioxo-1,2-benzothiazol-3-one
Molecular formula	$C_7H_5NO_3S$
Molecular weight, g/mol	183.18
Solubility in H_2O, g/L	4 (25 ^{0}C)
logKow[a]	0.91
pKa[b]	2.2

[a] logKow is the logarithm of the octanol-water partition coefficient
[b] pKa is the negative logarithm of the dissociation number

2.1.2 Endocrine disrupting compounds

Endocrine disrupting compounds (EDCs) are exogenous substances that can interfere with the '*synthesis, secretion, transport, binding, action or elimination of natural hormones in the body that are responsible for the maintenance of homeostasis, reproduction, development and/or behaviour*' [45]. Phthalates, pesticides, bisphenols, parabens, synthetic steroids, brominated flame-retardants, phytoestrogens, and heavy metals are some of the chemicals classified as EDCs. The full list can be found in the report of the Commission of the European Communities (Annex 1) [46].

The main sources of EDCs are domestic and industrial wastewaters and the main pathway into the environment are effluent discharges from WWTPs [47, 48]. The

occurrence of natural and synthetic EDCs, at ng/L to μg/L concentrations, in WWTP effluents, surface water, groundwater, and even drinking water has been widely reported [49-52]. Among them, bisphenol-A (BPA), estrogens, nonylphenols, and octylphenols are the most abundant endocrine disruptors in the aquatic environment [10, 53].

EDCs are pseudo-persistent compounds detected at trace level concentrations in the environment, which can be sufficient to induce adverse effects on human health, wildlife and aquatic organisms [4, 53, 54]. EDCs have been linked with various health problems in humans, including reproductive damage, developmental impairment, and increased cancer incidents in both females and males [55]. Further evidence links EDCs to metabolic disorders, such as diabetes, obesity and endometriosis [55, 56]. Also, it has been reported that exposure to EDCs induces: (i) feminisation of male fishes, (ii) reproductive problems in fishes, reptiles, birds, and mammals, and (iii) alterations to the immune system of marine mammals [13, 57].

2.1.2.1 Bisphenol-A

BPA is an alkylphenol used extensively in the synthesis of polycarbonate polymers and epoxy resins [58, 59]. BPA, whose main physicochemical characteristics are presented in Table 2-3, is one of the highest production volume chemicals with a growing global consumption projected to reach 10.6 million metric tons by 2022 [60, 61]. Due to its heat resistance and elasticity, BPA is found in numerous products such as food containers, metal cans, baby bottles, soaps, lotions, shampoos, nail polishes, sunscreens, and toys [55, 59, 61]. Changes in temperature and pH result in hydrolysis of the ester bonds of BPA, which subsequently lead to BPA leaching into foods and

beverages. Ingested BPA is thought to be absorbed by the gastrointestinal tract and then excreted with urine [55]. Dermal exposure and inhalation of household dust are other exposure ways to BPA [62].

BPA has been detected in influent (< 0.013 – 2.14 μg/L) and effluent of WWTPs (< 0.03 – 1.10 μg/L), surface water (2.1 – 881 ng/L), groundwater (79 ng/L), and drinking water (0.14 – 420 ng/L) in Europe, the US, Canada, China, and Korea [63-76].

Table 2-3 Physicochemical properties of BPA [44].

Structure	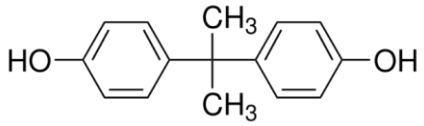
IUPAC name	4,4'-(propane-2,2-diyl)diphenol
Molecular formula	$C_{15}H_{16}O_2$
Molecular weight, g/mol	228.29
Solubility in H_2O, g/L	0.3 (25 ^{0}C)
logKow	3.32
pKa	9.6

In humans, BPA is detectable in the urine of most of the population tested (adults and children), in the serum of pregnant women, amniotic fluid, placental tissue, breast milk etc. proving that exposure to BPA is ubiquitous [62]. Many studies have shown that BPA at environmentally relevant concentrations can have significant health effects [77]. For instance, serum and urinary BPA at concentrations 0.3-2.6 μg/L, which are in the same range with BPA concentrations measured in surface and drinking water, have been associated with reduced fertility in both men and women undergoing in vitro fertilization (IVF) treatment [78-81]. Other health issues related to BPA include endometriosis [82] and polycystic ovary syndrome [83], obesity [84], type-2 diabetes

[85], miscarriage [86], premature delivery [87], and cardiovascular disease [88]. The presence of BPA in the environment has been also linked to growth, developmental, and reproductive effects on aquatic invertebrates, fishes, amphibians, reptiles, birds, and mammalian wildlife [53, 89].

2.1.3 Pharmaceuticals

Pharmaceuticals (or pharmaceutically active compounds) are either synthetic or natural chemicals used in prescription medicines, over-the-counter therapeutic drugs, and veterinary drugs [90]. They can be classified into six main medicinal classes depending on their applications and biological activity, as seen in Table 2-1. Nowadays, more than 3,000 pharmaceutical substances are produced worldwide featuring a great variety of biological and physicochemical properties [21, 91]. Many of these compounds undergo structural changes within the human or animal body [91]. In many cases, pharmaceuticals are not fully absorbed and metabolised, therefore, parent compounds and/or metabolites are excreted with the urine and pass to the WWTPs [92].

The presence of pharmaceuticals in the environment has been a concern for a long time [93]. Pharmaceuticals are detected at concentrations ranging from ng/L to µg/L levels in the effluent of medical centres, influent and effluent of WWTPs, surface water, groundwater, and drinking water [21, 91]. Among pharmaceuticals, anti-inflammatory and antibiotic drugs are the most widely detected in the aquatic environment [10].

The risks related to the presence of pharmaceuticals in water, even at low concentrations, include bioaccumulation, chronic toxicity, development of bacteria resistant to antibiotics, and endocrine disrupting effects [67, 94, 95].

2.1.3.1 Antipyrine

Antipyrine (AP; also known as phenazone) is a widely used anti-inflammatory, analgesic, and antipyretic drug that belongs to the class of the organic compounds called phenylpyrazoles [96]. The main physicochemical characteristics of AP are presented in Table 2-4. Its absorption in the human body is relatively low; therefore, AP passes to the WWTPs mainly unchanged from which escapes untreated or partially treated [97, 98].

Table 2-4 Physicochemical properties of AP [44].

Structure	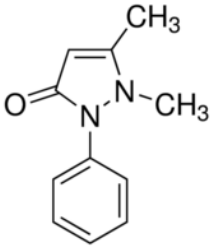
IUPAC name	1,5-dimethyl-2-phenylpyrazol-3-one
Molecular formula	$C_{11}H_{12}N_2O$
Molecular weight, g/mol	188.23
Solubility in H_2O, g/L	51.9 (25 ^{0}C)
logKow	0.38
pKa	1.4

AP and AP metabolites have been detected in effluent of WWTPs (0.16 µg/L), surface waters (0.024 – 0.75 µg/L), in influent of drinking water treatment plants (1.34 – 400 ng/L), finished water (0.05 – 0.25 µg/L), and groundwater (< 3 µg/L) [97-101].

In humans, long-term exposure to AP has been linked with toxicity towards lungs and mucosas, resulting in target organ damage [102]. Meanwhile, Gong et al. (2017) have reported acute toxicity of AP on *Artemia salina* (brine shrimps) [96].

2.1.4 Sources of EMs into the environment

The main sources of EMs into the environment are presented in Fig. 2-1 and can be summarised into: (i) domestic wastewater (i.e. from excretion, bathing, shaving, spraying, laundry, dishwashing, leaching out of the material, flushing unused drugs, etc.), (ii) hospital effluents, (iii) industrial wastewater (from cleaning and product manufacturing discharges), (iv) run-off from concentrated animal feeding operations and aquaculture, and (v) agricultural run-off [4, 8, 91]. Domestic, hospital and industrial wastewaters end up in WWTPs, which fail to provide a complete barrier to the release of EMs into the environment, rendering them the main hotspots of contamination [4, 8-10, 53, 103]. Infiltration of treated effluent via surface water (e.g. river water) can transfer the pollution to the groundwater [34]. Contamination of drinking water resources (e.g. groundwater, seawater) combined with inefficient drinking water treatment processes in EMs elimination, lead to the occurrence of EMs in drinking water. EMs are further 'recycled' in the water cycle via the reuse of treated wastewater (non-potable water), as can be seen in Fig 2-1.

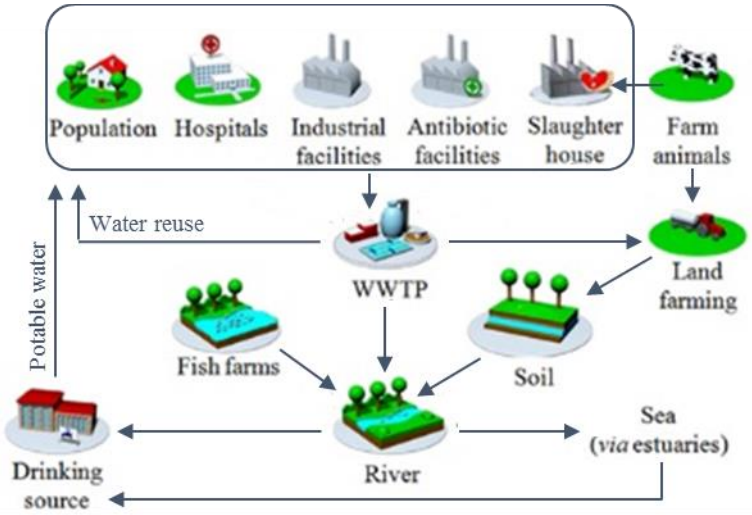

Fig. 2-1 Main sources and pathways of EMs into the environment, adapted in part from PILLS project [92].

2.1.5 Elimination of EMs in conventional WWTPs

In raw wastewater, the concentration of EMs presents temporal and spatial variations, which are functions of several factors, including local production rate, specific sales and practices, metabolism (i.e. excretion rate), usage/ consumption rate, and climatic conditions (e.g. rainfall which affects the dilution of EMs in combined sewer systems) [4, 8, 91]. Furthermore, the concentration of EMs in influent to WWTPs depends on factors, such as the serving population, which will define the volume of wastewater and, hence, the dilution of EMs, and the origin of the wastewater (i.e. domestic, hospital, industrial) [59].

Conventional WWTPs are typically designed for the control of organic substances, nutrients, and pathogens by means of physical, chemical, and biological processes [8]. While these substances can be treated efficiently by the applied treatment processes, WWTPs turn out to be insufficient in terms of the complete elimination of EMs [4, 8-10, 53]. Thus, EMs escape into the environment, untreated or partially treated, via effluent discharges by virtue of their recalcitrance and/or continuous input [8, 10]. Studies have shown that the removal of EMs varies greatly not only between different WWTPs for individual compounds, but also between compounds of the same usage class (e.g. plasticizers, antibiotics, etc.), as can be seen in Table 2-5 [4, 8]. The fate of EMs in WWTPs is governed by several factors, closely related to the properties of EMs (i.e. hydrophobicity and biodegradability) and the operational conditions applied in WWTPs (e.g. sludge retention time, hydraulic retention time, etc.) [8].

A typical treatment train applied in the WWTPs consists of preliminary treatment (i.e. coarse screens for the removal of large objects and heavy solids), primary treatment (i.e. sedimentation tank for the removal of suspended solids), secondary treatment (i.e.

aeration tank for the biodegradation of pollutants followed by a sedimentation tank for the removal of sludge) and optionally tertiary treatment for the removal of nutrients [104]. In this treatment train, the removal of pollutants is based mainly on sorption and biodegradation and, to a lesser extent, to volatilisation [59, 105].

Broadly, it can be said that the hydrophobicity of a compound will define whether it will be sorbed to the solid phase or not [4, 8]. ASs are readily water-soluble compounds, characterised by low $\log K_{ow}$ and low value of Henry's constant. Hence, the removal of ASs by volatilisation or sorption in WWTPs has been found to be negligible [28, 106]. Poor adsorption onto sludge has been also reported for EDCs, explained by their low $\log K_{ow}$ values [53, 107-109]. On the other hand, pharmaceuticals are usually polar and hydrophilic compounds (i.e. low $\log K_{ow}$) featuring moderate solubility in water [4]. Therefore, sorption is an important removal mechanism for this class of contaminants, influenced by their chemical structure, nature and amount of the sorbents, distribution coefficients (Kd), and the presence of neutral and ionic species [4, 91]. The higher the hydrophilicity of a pollutant is, the lower its bioaccumulation in the solid phase will be. Rogers et al. (1996) suggested a generic rule for the estimation of the sorption of compounds based on the $\log K_{ow}$. According to Rogers et al. rule, compounds with $\log K_{ow} < 2.5$ have a low sorption potential, $2.5 < \log K_{ow} < 4$ medium sorption potential, and $\log K_{ow} > 4$ a high sorption potential [110]. However, given the variety of biological and physicochemical properties of pharmaceuticals, no single rule can describe their sorption properties. For instance, the sorption and distribution of antibiotics are strongly dependent on chemical structure and cannot be predicted by the $\log K_{ow}$. On the other hand, the solubility, hydrophobicity, distribution and sorption behaviour of pharmaceutical

compounds, such as ciprofloxacin, depend on pH. However, the sorption of compounds containing planar aromatic structures is a function of $\log K_{ow}$, pH, redox potential, and the chemical structure of both sorbed compound and sorbent [91].

The biodegradability of EMs is strongly dependent on their structure (i.e. complexity and functional groups); recalcitrant EMs are usually either (i) compounds with long, branched sides, (ii) polycyclic or saturated compounds, or (iii) compounds with electron withdrawing, sulfate or halogen functional groups [8]. SAC and CYC have been found to be more easily degraded during biological treatment, contrary to the persistent ACE and SUC, Table 2-5 [33, 34, 106]. Among pharmaceuticals, anti-inflammatories and analgesics are the most recalcitrant to biodegradation, with removal percentages for AP ranging from 15 to 33% [59]. On the other hand, several studies have pointed out the biodegradability of BPA with removal percentages between 62.6 and 99% in different WWTPs [8].

The main WWTP-specific factors that influence EMs removal are the sludge retention time (SRT) and hydraulic retention time (HRT) [8]. SRT controls sludge characteristics, such as size and biodiversity. Studies have shown that long SRTs promote the growth of nitrifying bacteria, which have been found to have a positive effect on the degradation of EMs, such as ibuprofen, naproxen, ethinylestradiol and BPA [111, 112]. HRT expresses the available time for biodegradation and sorption, hence, at short HRTs, pollutants with slow kinetics (e.g. antibiotics) are less likely to be eliminated [8, 111]. Biodegradation in WWTPs can be complete or partial. Partial degradation of pharmaceuticals and EDCs can result in the formation of by-products of higher recalcitrance, and bioaccumulation potential than the parent compound, while their toxicity can vary [4, 91].

In some cases, the concentration of EMs in effluent has been found to be higher than influent concentration [59]. Influent may contain human metabolites and/or TPs that are transformed back to their parent compounds (e.g. diclofenac, erythromycin, and carbamazepine) during biological treatment, thus explaining the negative removal [63, 113]. Another possible explanation may be the desorption of EMs from sludge and suspended particles [114, 115].

In conclusion, EMs are partially mineralised in conventional WWTPs with a fraction of them (parent compounds and/or metabolites/TPs) escaping along with effluent discharges into receiving water bodies. However, the presence of EMs in the aquatic environment, even at trace level concentrations, is sufficient to cause adverse effects to human health and ecosystems [2, 10]; a fact that raises serious concerns and calls for immediate treatment solutions.

Table 2-5 Influent, effluent concentrations and removal efficiencies of selected EMs in conventional WWTPs.

Category	Selected compounds	Sampling site	Influent, µg/L	Effluent, µg/L	Removal, %
Pharmaceuticals[a]					
• Analgesic and anti-inflammatory drugs	Acetaminophen	Korea, Spain, WB[g]	1.57 – 56.9	nd[h] – 0.03	98.7 – 100
	Diclofenac	EU-wide, Greece, Korea, Sweden, Switzerland, UK, WB	< 0.001 – 94.2	< 0.001 – 0.69	0 – 81.4
	Ibuprofen	China, EU-wide, Greece, Korea, Sweden, UK, US, WB	< 0.004 – 603	nd – 55	72 – 100
	Ketoprofen	China, EU-wide, Korea, Spain, UK, WB	< 0.004 – 8.56	< 0.003 – 3.92	10.8 – 100
	Naproxen	Greece, Korea, Spain, Sweden, UK, WB	< 0.002 – 52.9	< 0.002 – 5.09	43.3 – 98.6
	Salicylic acid	Greece, Spain, UK	0.58 – 63.7	nd – 0.50	89.6 – 100
	Antipyrine[b,c,d]	Germany	0.04	0.16	15 – 33
Industrial chemicals[a]					
• Plasticizers	**Bisphenol-A**	China, France, Greece, US,WB	< 0.013 – 2.14	< 0.03 – 1.10	62.5 – 99.6
	DBP[i]	Austria, China	nd – 11.8	nd – 4.13	73.6 – 75.5
	DEHP[j]	Austria, China, US	0.003 – 70.0	0.0001 – 54.0	25 – 97
Artificial sweeteners[e,f]	Acesulfame	Switzerland, Germany, Singapore	8 – 47	11 – 46	0 – 23
	Saccharin	Switzerland, Germany, Singapore	3.9 – 43	< 0.1 – 3.2	> 90
	Sucralose	Sweden, Switzerland, Germany	0.82 – 7.9	0.6 – 10.8	0.8 – 24.6

References: [a][8], [b][97], [c][100], [d][59], [e][28], [f][106]; [g]WB: Western Balkan Region (including Bosnia and Herzegovina, Croatia, and Serbia); [h]nd: not detected, [i]dibutyl phthalate, [j]bis(2-ethylhexyl) phthalate

2.1.6 Current legislation in EU

The most relevant European legislation for the control of micropollutants in water and wastewater is summarised below [116]:

- The Urban Waste Water Directive (91/217/EEC) defines effluent standards for WWTPs based on conventional parameters, such as BOD, COD, pH, suspended solids, nitrogen, phosphorus, and the total number of *E. coli*.
- The Water Framework Directive (2000/60/EC) and its amendment (Environmental Quality Standards Directive (EQSD) 2008/105/EC) established a list of 45 priority substances and 8 other pollutants and set their environmental quality standards (EQS) in surface waters based on their toxicity, environmental persistence, and increased risk for human health and environment. This list includes selected chemicals, plant protection products, biocides, metals, and other groups like polyaromatic hydrocarbons (PAHs) and polybrominated biphenyl ethers (PBDEs).
- The proposal (COM(2011)876) introduces 15 additional priority substances (6 of them designated as priority hazardous substances), revises EQS of existing priority substances, and provides for improved monitoring and watch-list mechanisms of substances of possible concern.
- The first watch-list was adopted in Decision 2015/495, and included: the natural hormones, oestrone (E1) and oestradiol (E2); the synthetic hormone ethinyl oestradiol (EE2); the anti-inflammatory diclofenac; three antibiotics; several pesticides; a UV filter; and an antioxidant used as food additive.

- The REACH regulation (EC 1907/2006) aims to protect human health and the environment through the early identification of hazardous chemicals manufactured or imported into the EU (in quantities of ≥ 1 tonne per year) and their replacement by suitable alternatives.

According to current legislation, EQS have been set at μg/L levels for 48 priority substances. However, considering that more than 700 EMs and their TPs are detected in the European aquatic environment [2], we can safely deduce that the regulated substances represent a minuscule fraction of the hazardous chemicals present in the environment. The discharge of EMs in surface water even at extremely low concentrations is sufficient to cause a long-term and transferable contamination [2, 10]. Furthermore, knowledge about the ecotoxicological effects of mixtures of EMs remains limited, because evaluation has focused, so far, mostly on the effects of individual compounds [91, 117]. Pharmaceuticals, for instance, are usually present in the environment as multi-component mixtures and, when they have the same mode of action and common receptor, accumulative effects can be expected [91].

On this basis, the legislation should become more inclusive and set as a requirement the complete elimination of EMs, including their metabolites and TPs, in WWTPs. The latter necessitates the upgrade of existing WWTPs with treatment methods not only efficient in EMs removal, but also low-cost and environmentally benign in order to obtain, ultimately, net environmental benefits.

Currently, activated carbon adsorption, ozonation, and membrane technology are most commonly applied as tertiary treatment processes in WWTPs for the elimination of EMs [110-113]. Although highly efficient in removing EMs from water [110, 114], ozonation and membrane filtration are technologies of high investment and

maintenance cost (high energy demand) significantly reducing the environmental and economic sustainability of treatment [115, 116]. Furthermore, the formation of potentially human carcinogenic by-products (e.g. bromate) during ozonation raises concerns regarding the safety of the effluent [117, 118]. While, the transfer of pollutants from one phase to another during membrane filtration and adsorption onto activated carbon creates disposal issues afterwards [8, 115]. In addition to that, membrane fouling and the need for regeneration and replacement of the activated carbon are technical limitations that complicate even more the treatment [8, 115]. To this end, sustainable alternatives to existing processes are sought being able of mineralising completely the EMs.

2.2 Advanced oxidation processes

Advanced oxidation processes (AOPs) are a class of oxidation techniques tackling water, air and soil pollution, that are characterised by a common chemical feature: the production of hydroxyl radicals ($HO^{\bullet}$) [19, 118, 119]. Hydroxyl radicals, are among the most powerful oxidants (E^{o} = 2.73 V) and can attack unselectively organic compounds, oxidising them via a progressive break-up of molecules into CO_2 and inorganic ions [17]. Depending on the specific treatment requirements, several reacting systems can be used to produce hydroxyl radicals including heterogeneous photocatalysis (TiO_2/UV), Fenton-related systems (e.g. H_2O_2/Fe^{2+}, H_2O_2/Fe^{3+}, H_2O_2/Fe^{2+} (Fe^{3+})/UV), ozone-based systems (e.g. O_3/H_2O_2, O_3/UV, O_3/UV/H_2O_2), electrolysis, ultrasound, wet air oxidation, ionising radiation, pulsed plasma, and ferrate reagent [118, 119]. Among them, photocatalysis, heterogeneous and

homogeneous, is of special interest because sunlight, a free and plentiful energy source, can be used to power the reacting system [17-19].

2.2.1 Heterogeneous photocatalysis

Heterogeneous photocatalysis makes use of oxygen as an oxidising agent and a semiconductor metal oxide (e.g. TiO_2, ZnO, CdS, ZnS, Fe_2O_3) as the catalyst. Many catalysts have been tested so far with titanium dioxide (TiO_2) demonstrating the highest quantum yield [120, 121]. The electronic band structure of TiO_2, presented in Fig. 2-2, consists of an electron-filled valence band (VB) and vacant conduction band (CB). When TiO_2 is illuminated with photons of energy equal or greater than its band gap energy (E_g = 3.0 eV; band gap wavelength < 380 nm), an electron from the VB is excited to the CB, leaving a positive hole behind in the VB [122]. In the absence of a suitable scavenger (e.g. oxygen), the electron-hole (e^- - h^+) pair recombines dissipating the stored energy within a few nanoseconds. Recombination is prevented in the presence of scavengers that trap the hole or the electron triggering reduction-oxidation (redox) reactions.

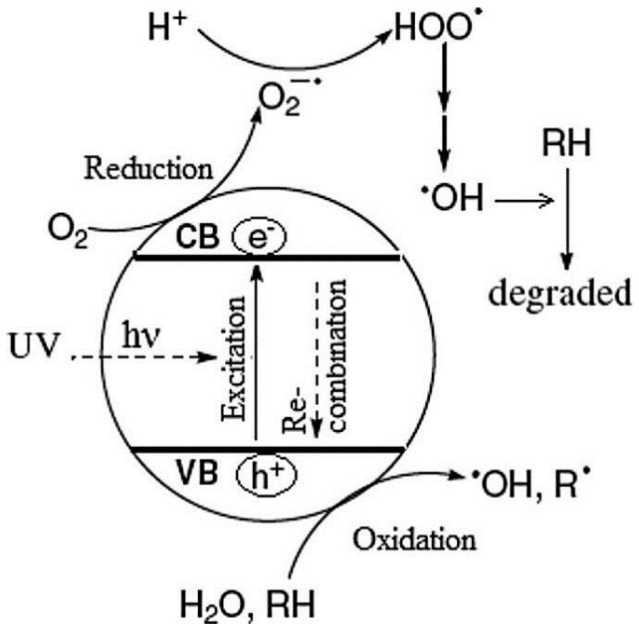

Fig. 2-2 Schematic illustrating the principle of TiO_2 photocatalysis in the presence of water pollutant (RH), adopted from Dong et al. (2015) [123].

The photoexcited electrons are able of reducing some metals and dissolved oxygen to form superoxide radical ions, $O_2^{\bullet-}$, while the positive holes react with the adsorbed H_2O and OH^- groups on TiO_2 surface producing surface adsorbed hydroxyl radicals, $HO^{\bullet}_{(ads)}$ [123]:

$$TiO_2 + hv \rightarrow h^+ + e^- \qquad (2-1)$$

$$TiO_2(e^-) + O_{2(ads)} \rightarrow TiO_2 + O_2^{\bullet-} \qquad (2-2)$$

$$TiO_2(h^+) + H_2O_{(ads)} \rightarrow TiO_2 + HO^{\bullet}_{(ads)} + H^+ \qquad (2-3)$$

$$TiO_2(h^+) + HO^-_{(ads)} \rightarrow TiO_2 + HO^{\bullet}_{(ads)} \qquad (2-4)$$

The generated hydroxyl radicals attack the organic compounds (RH) present in the reactant mixture mainly via three pathways [(i) electrophilic addition, reaction (2-6); (ii) hydrogen atom abstraction, reaction (2-7); and (iii) electron transfer, reaction (2-

8)], degrading them to their corresponding TPs and, finally, mineralising them to CO_2, water, and inorganic ions [123, 124].

$$RH \xrightarrow{TiO_2/hv} intermediate\,(s) \rightarrow CO_2 + H_2O + inorganic\ anions \qquad (2-5)$$

$$RHC = CR_2 + HO^{\bullet} \rightarrow RHC(OH) - C(^{\bullet})R_2 \qquad (2-6)$$

$$R_3C - H + HO^{\bullet} \rightarrow R_3C(^{\bullet}) + H_2O \qquad (2-7)$$

$$RH + HO^{\bullet} \rightarrow R^{\bullet} + H_2O \qquad (2-8)$$

The overall photocatalytic reaction (2-5) can be divided into five independent steps [120]: (i) transfer of the reactants in the liquid phase to TiO_2 surface, (ii) adsorption of the reactants onto the photoactivated TiO_2 surface (photonic activation of TiO_2 occurs simultaneously at this step), (iii) photocatalytic reaction in the adsorbed phase onto TiO_2 surface, (iv) desorption of TPs from TiO_2 surface, and (iv) TPs transfer from the interface region to the bulk liquid. Rate limiting steps of the process are considered the mass transfer of the reactants onto TiO_2 surface [step (i)] and the photocatalytic reaction [step (iii)] [123]. The reaction of TiO_2 electrons with oxygen is also thought to be a rate-determining step, although this has not been verified yet [125].

The key features of heterogeneous photocatalysis that make it a promising technological solution for water decontamination are summarised as follows [17]:

(i) operation at ambient temperature and pressure,

(ii) no production of secondary waste streams,

(iii) atmospheric oxygen is used directly as an oxidising agent,

(iv) the catalyst itself is cheap, stable against chemical breakdown and photocorrosion, non-toxic, and recyclable,

(v) the catalyst can be immobilised on inert matrices obviating the need for post-separation treatment.

2.2.1.1 Process parameters and their influence

Several parameters govern photocatalytic kinetics. These include the initial concentration of substrate, mass and type of catalyst, light wavelength and intensity, water matrix, pH, and temperature.

Initial concentration of the substrate

In TiO_2-mediated photocatalysis, the initial rate of organic degradation has been widely reported to fit well with the Langmuir–Hinshelwood (L–H) kinetic model (Eq. 2-9) [17, 120, 126]. According to this model, the reaction rate (r) is proportional to the fraction of the surface of the catalyst covered by the substrate (θ_x), the reaction rate constant (k_r), the concentration of the substrate X (C), and the reactant adsorption constant (K).

$$r = -\frac{dC}{dt} = k_r\theta_x = \frac{k_r KC}{1 + KC} \qquad (2-9)$$

During photocatalytic degradation the substrate is mineralised; therefore, less and less of the surface of the catalyst is covered. Ultimately, at total mineralisation, the kinetic order changes from first to zero and the reaction rate decreases as the irradiation time increases. The L-H model, with minor modifications, can be used to express the organic photomineralisation rate for any of the following scenarios [17]: (i) a reaction occurring between two adsorbed substances, (ii) a reaction that takes place between an adsorbed substance and a radical in the bulk liquid, (iii) a reaction that occurs between

a substrate in the bulk liquid and a radical linked to the surface, and (iv) a reaction taking place with both substance and radical in the bulk liquid.

Under fixed photocatalytic conditions (i.e. catalyst concentration, light intensity), increase of the initial substrate concentration lowers the ratio of oxidant species to substrate molecules, leading to decreased degradation yields [127]. When the substrate concentration is too high, the organic compounds and their intermediate by-products formed during treatment, lead to saturation of the catalyst surface, affecting the photonic efficiency and, ultimately, the reaction rate [126, 128].

It has been widely shown that photocatalytic degradation of organic micropollutants fits well to a pseudo-first-order kinetic model, with respect to substrate concentration [11, 129-135].

TiO_2 concentration, modification and mode of utilisation

a- TiO_2 concentration

Increase of TiO_2 concentration up to the point where all the catalyst particles are fully illuminated enhances oxidation rates by offering more photoactive surface area and, hence, increased generation of oxidising species [120, 136]. At catalyst concentration above this point, which depends on the nature of the organic compound, reactor geometry and the applied working conditions, removal efficiency becomes independent of catalyst mass, and levels off. This stems from the agglomeration of TiO_2 particles and the subsequent reduction in available surface area, as well as the increased opacity and light scattering that further reduce the light passage through the solution [120]. In photocatalytic applications, the selection of the optimal catalyst

concentration is crucial in order to prevent catalyst overloading and to ensure the highest photon absorption [120].

b- TiO_2 modification

TiO_2 can be found in nature in three distinct crystallographic phases, anatase, rutile, and brookite. TiO_2 in the anatase form is a widely used photocatalyst in environmental applications due to its low cost and high performance [120, 125, 137]. For practical applications, TiO_2 use encounters some limitations related to the fast recombination of the photogenerated electron-hole pairs and its low absorption in the visible light, which accounts for the 44% of the solar irradiation reaching Earth's surface [17]. Therefore, a substantial research effort focuses on TiO_2 surface modification as a means to improve photocatalytic efficiency by either enhancing charge transport and trapping or extending TiO_2 absorption spectrum to the visible region for higher exploitation of the solar irradiation [138-141].

In this direction, TiO_2 doping with metal and non-metal elements, dye sensitisation, and semiconductor coupling are some of the methods applied [139, 142, 143]. Table 2-6 gives an overview of these modification approaches. Briefly, in doping, a foreign atom is included or substituted in the TiO_2 lattice for the creation of new electronic states and optical transitions [138]. The photocatalytic properties of the final product depend on the nature, chemical state, and the mass of the dopant [124]. Semiconductor coupling has been suggested as an effective method to obtain visible-active TiO_2 [142, 144, 145]. In this method, TiO_2 is coupled with semiconductors of narrower band gap (e.g. CdS, Fe_2O_3, CdSe, V_2O_5, ZnO, SnO_2, or Bi_2S_3). In principle, when a sensitizer semiconductor is irradiated with visible light, an electron is promoted to its conduction band. If the conduction band is more negative than that of TiO_2, then the electron can

be injected into the conduction band of TiO_2 [142]. The driving force in this method is the interfacial charge transfer, which depends strongly on the degree of matching of the conduction band and valence band of the two semiconductors. Dye sensitisation has been reported as an alternative approach to obtain TiO_2 with an extended absorption spectrum to the visible region [17, 143, 146, 147]. This approach is based on the excitation of adsorbed dye molecules onto TiO_2 upon visible irradiation and the injection of electrons to the conduction band of TiO_2, in a similar way as in the semiconductor coupling.

In addition to material modification, the control of nano-architecture and morphology provides another way to enhance catalyst activity [148, 149]. It is thought that the enhanced performance of TiO_2 Aeroxide P25 and other anatase-rutile mixtures is due to the interfacial properties between the two phases (i.e. anatase and rutile) [150-152]. Commonly studied preparation methods for anatase-rutile interfaces are controlled sol-gel growth [153] and thermal processing [154, 155].

Table 2-6 Summary of modification approaches for the enhancement of charge separation and development of visible-active TiO_2 catalysts, adopted from Dionysiou et al. (2016) [124].

	TiO_2 doping	Semiconductor coupling	Dye sensitisation
Main elements and compounds used	• Non-metal dopants and co-dopants: N, C, S, F • Metal dopants: transition metals (Cu, Fe, Mn, Ni, V, Zn, Zr, etc.); noble metals (Ag, Au, Os, Pd, Pt, etc.)	• CdS • Fe_2O_3 • CdSe • ZnO • SnO_2 • WO_3 • Bi_2S_3	• 8-hydroxyquinone • methylene blue • acid red 44 • reactive red dye 198 • rhodamine B, etc.
Drawbacks	• Metal ions may also serve as recombination centres for electrons and holes, thus reducing the overall photocatalytic activity.	• Possible disaggregation and/or dissolution during the photocatalytic reaction.	• Possible oxidative degradation of the dye itself in the absence of other organic molecules. • Desorption of dye molecules greatly reduces practical applications.

c- Mode of utilisation

TiO_2 can be applied as (i) a powder suspended in the reactant solution, (ii) immobilised on a suitable support, or (iii) used as a continuous thin film [156, 157]. Studies have shown that, in general, slurry systems perform better than those based on immobilised catalysts [158-160]. This stems from the uniform catalyst distribution, the lack of mass-transfer limitations, and the high ratio of illuminated catalyst surface to the effective reactor volume provided by the slurry photoreactors. However, this approach suffers several drawbacks, such as the need for a catalyst-recovery step at the end of treatment, aggregation of TiO_2 particles, and the difficulty in operating in a continuous flow mode [159]. TiO_2 immobilisation on inert matrices (e.g. glass, stainless steel, activated carbon, silica, ceramics [161-165]) is a way to overcome the requirement for

catalyst separation from the effluent and to enable operation in continuous mode. Yet, the main challenges of the immobilised systems to be addressed are the provision of uniform light distribution and the mass transfer limitations of pollutants onto catalyst surface that in turn result in the loss of photocatalytic efficiency [159, 160].

Light wavelength, intensity, and light sources

a- Light wavelength

Light wavelength, λ, should fall within catalyst's absorption spectrum providing photons of energy equal or greater than its band gap energy in order to excite the catalyst and trigger redox reactions [120]. In the case of TiO_2 Aeroxide P25, $\lambda \leq 380$ nm is required that is near-UV wavelength (i.e. UVA) [120]. When artificial lighting is employed, the energy consumption for photon generation governs process economics. Therefore, the use of light sources with narrowband UVA emission spectrum is highly encouraged in order to ensure efficient photonic use and decrease energy requirements.

b- Light intensity

The effect of light intensity on photocatalytic efficiency can be divided into three domains; (i) at low light intensities, the rate of photocatalytic reaction increases linearly with the light intensity due to the prevention of the electron-hole pairs recombination, (ii) at intermediate light intensities, reaction rate increases with the square foot of the light intensity because separation of electron-hole pairs competes with recombination, and (iii) at too high light intensities, reaction rates becomes independent of the light intensity and mass transfer is the main limitation [120, 166-168].

The optimal photonic efficiency (i.e. ratio of reaction rate to rate of photon absorption), corresponds to the optimal light power usage, which is obtained in the domain, where the reaction rate is linearly dependent on the light intensity [120].

c- Light sources

In photocatalytic applications, artificial UV irradiation has been traditionally provided by conventional incandescence and gas discharge (i.e. blacklight, fluorescent, germicidal) lamps [169-171]. There are several issues related to these lamps however, including their content of toxic heavy metals (i.e. mercury and lead), low energy efficiency, waste of energy in the form of heat, power instability, broadband emission spectrum, and short lifespan [170, 172, 173]. USEPA reported that replacement costs in UV systems can be as high as the 45% of the annual electric consumption costs [174]. As a result, the use of conventional UV lamps in photocatalytic systems impedes process scale-up due to high operational and maintenance costs, and environmental impacts [16, 175]. Life cycle analyses have listed UV heterogeneous photocatalysis among the least environmentally benign AOPs due to increased CO_2 emissions and fossil depletion caused by UV lamps, as well as the environmental hazards related to their content in toxic chemicals [15, 16, 176]. To date, 128 countries have signed the Minamata Convention on Mercury, which aims at the gradual phase-out of mercury-containing products (e.g. compact fluorescent lamps, batteries, thermometers) by 2020. Therefore, one of the current challenges is the identification of mercury-free UV sources to power photochemical oxidation technologies.

In this regard, natural sunlight, a free and plentiful energy source, can be used instead of UV lamps as an irradiation source. Solar heterogeneous photocatalysis makes use of the near-UV band of the solar spectrum to excite TiO_2 catalyst [17]. Process

efficiency in degrading persistent EMs, such as EDCs, herbicides, insecticides, fungicides, and pharmaceuticals, has been widely demonstrated [17, 136, 177-181]. Solar photocatalysis can serve as an affordable, sustainable, and simple treatment option in areas with high solar energy potential, e.g. Mediterranean Region and developing countries [178, 182-185]. The process features significant environmental and economic benefits, however, its dependence on solar availability limits the possible areas of application. Other issues to be taken into consideration are the requirement of large area and high capital costs, as well as limited operation restricted to daylight hours [17, 170].

When sunlight is inadequate, artificial irradiation is required. On this basis, UV-LEDs have attracted considerable attention as eco-friendly alternatives to conventional UV lamps. LEDs are semiconductor p-n junction diodes that emit light when activated due to recombination of electrons and holes (i.e. electroluminescence) [170]. The emission wavelength of LEDs, which is nearly monochromatic, depends on the band gap of the semiconductor material (e.g. gallium arsenide, indium gallium nitride), with the light output directly proportional to the voltage applied [170]. Key features of LEDs include energy efficiency, extended lifetime, and their toxic-free nature (i.e. free of mercury and lead, and absence of gas fill), which can lower cost and improve process sustainability. Moreover, the small footprint of LEDs, directional light output, and narrowband emission spectra allow for flexible design and development of compact water treatment units [169, 172, 186]. Furthermore, LEDs are programmable for high-frequency periodic illumination, which has been found to have a beneficial effect on photocatalytic kinetics [187, 188]. The emission wavelength of LEDs is tunable and can be tailored for each system, which in turn can result in enhanced catalyst photon

absorption and reduced inner filter effects. Recent studies have also explored the use of photovoltaic-powered UV and visible LEDs for water disinfection and decontamination, opening the way to an even more sustainable operation [189, 190].

UVA-LEDs were firstly employed by Chen et al. (2005) for the photocatalytic treatment of perchloroethylene [191] and since then LED-photocatalysis has been efficiently applied to the treatment of a wide range of EMs, including BPA [192, 193], dimethyl phthalate [187], cyanide [194], diazinon [195], sodium dodecylbenzenesulfonate [196], 17β-estradiol [197], ibuprofen [198], acetaminophen [199], sulfamethoxazole, and trimethoprim [199].

LED-driven photocatalysis can be used as a polishing step in existing WWTPs to remove EMs in areas where solar photocatalysis might not be feasible due to inadequate sunlight (e.g. in Scotland). LEDs can be also used as back-up irradiation sources in solar photocatalytic systems during less sunny days or periods with increased influent loads (e.g. touristic periods). Also, given their small footprint and directional light output, LEDs are a valuable tool in the developing field of compact, miniaturised, or portable water photochemical systems (e.g. microstructured reactors, point-of-use systems for water disinfection) [171, 200, 201].

Water matrix

The chemical composition of water affects the photocatalytic efficiency to a great extent [202]. Inorganic ions (e.g. Cl^-, SO_4^{2-}, NO_3^-, NO_2^-, PO_4^{3-}, and HCO_3^-) present in water have been found to affect negatively the reaction kinetics [118, 202, 203]. For instance, hydroxyl radicals in the presence of chlorides are converted into chlorine

radicals, which have a lower oxidation potential than hydroxyl radicals, hence lowering the degradation rates [202, 203].

$$HO^{\bullet} + Cl^{-} \rightarrow [ClOH]^{\bullet -} \quad (2-10)$$

$$[ClOH]^{\bullet -} + H^{+} \rightarrow [HClOH]^{\bullet} \quad (2-11)$$

$$[HClOH]^{\bullet} + Cl^{-} \rightarrow {Cl_2}^{\bullet -} + H_2O \quad (2-12)$$

Inorganic ions, such as phosphate, carbonate and bicarbonates, act as hydroxyl radical scavengers, reducing the reaction rate [118, 202, 203].

$$HO^{\bullet} + {HPO_4}^{2-} \rightarrow {HPO_4}^{\bullet -} + HO^{-} \quad (2-13)$$

$$HO^{\bullet} + {CO_3}^{2-} \rightarrow {CO_3}^{\bullet -} + HO^{-} \quad (2-14)$$

$$HO^{\bullet} + {HCO_3}^{-} \rightarrow {CO_3}^{\bullet -} + H_2O \quad (2-15)$$

The presence of ions can further suppress the photocatalytic reaction rates via turbidity generation, photon absorption and adsorption onto catalyst surface [202].

Likewise, organics (e.g. humic compounds) present in surface waters, groundwater and wastewater diminish the rate of photocatalytic process via [204-206]: (i) ROS scavenging, (ii) adsorption on TiO_2 surface, and (iii) absorption of UV light.

pH

The pH of the aqueous solution influences TiO_2 charge and the size of clusters formed. However, variations of pH between 4 and 10 do not affect noticeably the efficiency of photocatalytic oxidation [17]. Above and below the zero-point charge (pHzpc), which for TiO_2 lies between 4.5 and 7 depending on the preparation method, the catalyst is negatively or positively charged according to the following equilibria [202]:

$$pH < pH_{zpc}: TiOH + H^+ \leftrightarrow TiOH_2{}^+ \quad (2-16)$$

$$pH > pH_{zpc}: TiOH + OH^- \leftrightarrow TiO^- + H_2O \quad (2-17)$$

Mean-size particle clusters (~ 300 nm) are formed at pH far from pHzpc, which can increase up to 2 - 4 μm at pH close to pHzpc. When pH reaches pHzpc, large TiO_2 aggregates form due to the zero-electrostatic surface potential that fails to draw apart the catalyst particles. Therefore, attention should be paid to these conditions given that photon absorption may be reduced and more vigorous mixing may be needed to prevent TiO_2 sedimentation.

Temperature

Photocatalytic systems are based on photonic activation; therefore, operation at ambient temperatures is feasible because heating is not required [120]. The optimal operating temperature (θ) occurs between 20 and 80 ^{0}C; at very low temperatures (−40 °C ≤ θ °C ≤ 0 °C) the desorption of the final product is the step that limits the reaction rate, while at temperatures higher than 80 ^{0}C, which is close to the boiling point of water, the exothermic adsorption of reactants is disfavoured and the solubility of oxygen decreases, lowering reaction rates [17, 120].

Oxygen concentration

In semiconductor photocatalysis, molecular oxygen (O_2) is necessary for the complete mineralisation of pollutants. O_2 serves as an electron acceptor preventing the recombination of the electron-hole pairs, takes part in the formation of reactive oxygen species (ROS) (i.e. hydroxyl radicals, hydrogen peroxide, and superoxide radical anions), and in the mineralisation of the organics [125]. O_2 concentration affects the

reaction rate, however, there is not much difference in the reaction kinetics when using pure oxygen (pO_2 = 1 bar) instead of air (pO_2 = 0.21 bar) [17]. In a full scale application, the selection of O_2 source would be based solely on the economy of design. Oxygen concentrations at values above air saturation ($\geq pO_2$ = 0.21 atm) are regarded as the optimal for photocatalytic treatment. At values below air saturation (0 < pO_2 < 0.21 atm), the reaction rate decreases considerably and its the dependence on O_2 concentration becomes less profound, suggesting the mass transfer of O_2 to TiO_2 surface as the rate-determining step of the process [17, 207].

2.2.1.2 State of the art

The efficiency of heterogeneous photocatalysis in degrading a wide range of recalcitrant, non-biodegradable and hazardous organic micropollutants into CO_2, H_2O and inorganic ions has been widely reported [9, 11-13, 129, 208-213]. Sin et al. (2012) in their review article focus on the efficiency of TiO_2-mediated photocatalysis for EDCs abatement [209]. Sin et al. report the complete mineralisation of phthalates, BPA and chlorophenols during photocatalytic treatment under UV, visible light, and solar irradiation. The effect of key operating parameters, such as initial substrate concentration, catalyst loading, light wavelength, and intensity on the photocatalytic removal of EDCs is also discussed by Sin et al., who point out the need for their optimisation to achieve sustainable and highly competent water treatment technologies. Other EDCs successfully degraded by photocatalysis are PAHs, pesticides and pesticide derivatives, natural and synthetic steroids, and parabens [9, 12, 129, 208, 210-212]. Likewise, TiO_2-mediated photocatalysis has been efficiently applied to the treatment of pharmaceutical compounds of several classes including

antibiotics, anticonvulsants and anti-anxiety agents, antipyretics and non-steroidal anti-inflammatory drugs, histamine H_2-receptor antagonists, and lipid regulators [11, 12, 213, 214].

Studies on the photocatalytic treatment of ASs are still scarce due to their recent identification as EMs. An overview is given in Table 2-7. As can be seen, most of studies focus on the decontamination and detoxification of ACE and SUC aqueous solutions. Calza et al. (2013) examined the photocatalytic treatment of SUC in TiO_2 Aeroxide P25 suspensions under simulated solar irradiation [215]. With the use of chemometric optimisation tools, Calza et al. found that light intensity and TiO_2 concentration were the main factors influencing the degradation of SUC. At the early stages of treatment, the formation of intermediates with increased toxicity relative to the parent compound was reported, however, these were efficiently degraded during treatment, reducing the toxicity to 1%. These findings are in agreement with Sang et al. (2014) [42], who observed enhancement of toxicity during SUC and ACE photocatalytic treatment, due to the formation of toxic intermediates. Likewise, Sang et al. demonstrated the efficiency of TiO_2-mediated photocatalysis in degrading SUC and ACE, as well as eliminating the toxicity of the irradiated solutions. Recent studies further explore the use of newly synthesized catalysts for the photocatalytic treatment of ACE as a means to improve process efficiency. Visible-active bare and Ce-doped zinc oxides have been employed by Calza et al. (2017), demonstrating higher performance than TiO_2 Aeroxide P25, especially for the decontamination of river water [216]. Munoz et al. (2018) synthesized titanium oxides using a modified sol-gel process for the photocatalytic treatment of ACE [217]. Munoz et al. observed increased efficiency in the presence of the new catalysts compared to TiO_2 Aeroxide P25 in terms

of ACE degradation and mineralisation. So far, the photocatalytic degradation of SAC has been studied only by Chen et al. (2013) who obtained 93% mineralisation within 3 h of treatment in TiO_2 Aeroxide P25 suspensions under UVA irradiation [218].

On the other hand, the photocatalytic degradation of BPA has been investigated extensively because its endocrine disrupting nature has been long known. Table 2-8 summarizes representative studies and their main findings. The process efficiency in degrading and mineralizing BPA, as well as reducing the compound's estrogenic activity in the presence of TiO_2 Aeroxide P25 suspensions under UVA and UV-vis irradiation has been demonstrated in several studies [177, 219-222]. The use of natural sunlight as an irradiation source has been also investigated for the photocatalytic treatment of BPA [136, 177, 223]. Kaneco et al. (2004) reported complete mineralisation of BPA in a lab-scale reactor under solar light, while Rodriguez et al. (2010) and Saggioro et al. (2014) carried out photocatalytic studies on solar compound parabolic collector (CPC) reactors at pilot-scale. High removal efficiencies were achieved in both CPCs. In particular, Saggioro et al. (2014) observed enhanced reaction rates in the solar CPC relatively to a batch reactor under artificial UVA irradiation, ascribing this to the improved optical characteristics of the CPC.

The use of immobilized TiO_2 instead of TiO_2 powders has been also studied as a means to overcome the requirement for post-separation of catalyst particles from effluent [128, 177, 197, 224-228]. For this purpose, methods such as heat-attachment [224], sol-gel [128, 177], microwave-assisted liquid phase deposition [227], and dip-coating procedures [226] have been employed to immobilize TiO_2 onto glass plates, spheres, fibers [177, 224, 226], polyurethane foam cubes [227], and titania sheets and films [128, 197]. Wang et al. (2009) studied the degradation of BPA in a horizontal

circulating bed photocatalytic reactor using TiO_2 immobilized on the surface of polyurethane foam cubes under vis-LED irradiation. Wang et al. reported 95% mineralisation and 97% degradation of BPA after 6 h of treatment at optimal conditions.

Much existing literature focuses on the use of modified catalysts for the treatment of BPA [193, 222, 225, 229-234]. Subagio et al. (2010) studied the photocatalytic degradation of BPA using nitrogen-doped TiO_2 hollow sphere (NhT) in a vis-LED reactor, obtaining 66% mineralisation within 6 h [193]. NhT led to higher oxidation rates under blue, green, and yellow lights than the undoped TiO_2 hollow sphere, powder TiO_2, and Hombikat UV100. Subagio et al. ascribed this behaviour to the increased surface area and porosity of NhT, which in turn led to higher photonic efficiency. Using a carbon-nitrogen co-doped TiO_2 (CN-TiO_2), Wang and Lim (2010) obtained 70% mineralisation after 5 h under visible irradiation [192]. This high catalytic activity was attributed to the synergistic effects of C and N co-doping and the mesoporous system, which enhanced the diffusion and adsorption of BPA molecules. TiO_2 catalysts modified by non-metal dopants, such as C, N, P [192, 193, 225], metal dopants, such as Cu and Ni [233, 235], and noble metals, such as Pt, Ru, Pd, and Rh [222, 229], have been also used for the photocatalytic treatment of BPA.

There is no a single rule to describe EMs degradation by means of photocatalytic treatment due to the complex chemistry of such processes [17]. Degradation pathways differ not only between different compounds of the same usage class, but also for individual EMs in the presence of different catalysts or different experimental conditions [209]. Therefore, preliminary research is necessary to assess process

efficiency in eliminating individual EMs and to optimise treatment on a case-by-case basis [17].

Table 2-7 Removal of ASs by heterogeneous photocatalysis.

Compound	Operating conditions	Results and comments	References
ACE	C_0 = 10 mg/L; catalysts (1 g/L): TiO_2 P25, newly synthesized TiO_2-SG1 and TiO_2-SG2; UVA irradiation (40 W, λ = 360 nm); lab-scale, batch-operated slurry reactor	Mineralisation efficiency: P25 (90% in 6 h) < TiO_2-SG1 (90% in 2.5 h) < TiO_2-SG2 (90% in 2 h); identification of TPs	[217]
ACE	C_0 = 20 mg/L; catalysts (100 mg/L): TiO_2 P25, newly synthesized bare and Ce-doped zinc oxides; water matrix: distilled (DI) and river water (RW); simulated solar and visible irradiation (1500 W, 750 W/m^2, xenon arc lamp, Suntest CPS+); lab-scale, batch-operated slurry reactor	In most cases, the best performance was obtained in the presence of Ce1Cl (ZnO doped with 1% $CeCl_3$); removal in DI in 90 min with Ce1Cl: 70% under solar, 65% under visible light; removal in RW in 90 min with Ce1Cl: 50% under solar, 40% under visible light	[216]
ACE	C_0 = 400 mg/L; titanium (IV) oxide (8 g/L); UVC irradiation (1630 μW/cm^2, λ = 254 nm); lab-scale, batch-operated reactor	99.9% removal in 19 h; TPs, at g/L levels, induce adverse effects on the development of zebrafish embryos; identification of TPs	[37]
ACE, SUC	ACE: C_0 = 5 mg/L, TiO_2 P25 (100 mg/L); SUC: C_0 = 1 mg/L, TiO_2 P25 (20 mg/L); UVC irradiation (128 W total power, λ = 254 nm, 16 germicidal lamps); lab-scale, batch-operated slurry reactor	ACE: 100% removal in 60 min; SUC: 100% removal in 120 min	[42]
SUC	C_0 = 15 mg/L; TiO_2 P25 (58.6 - 341.4 mg/L); simulated solar irradiation (1500 W, 486.9 - 713.12 W/m^2, xenon arc lamp, Suntest CPS+); lab-scale, batch-operated slurry reactor	89% removal within 15 min (TiO_2 = 294 mg/L, light intensity = 698 W/m^2); complete mineralisation within 4 h (TiO_2 = 200 mg/L); removal of toxicity after 120 min of treatment; identification of TPs	[215]
SAC	C_0 = 35 mg/L; TiO_2 P25 (0.2 - 4 g/L); UVA irradiation (500 W, Hg lamp); lab-scale, batch-operated slurry reactor	93% mineralisation after 3 h of treatment (TiO_2 = 0.8 g/L, 500 W mercury lamp, pH = 7)	[236]

Table 2-8 Removal of BPA by heterogeneous photocatalysis.

Operating conditions	Results and comments	References
a- C_0 = 20 mg/L; TiO_2 P25 (0.01 - 0.2 g/L); (i) UVA irradiation; lab-scale, batch-operated slurry reactor (125 W, Hg-lamp), (ii) natural sunlight; pilot-scale CPC, b- C_0 = 100 µg/L; TiO_2 supported on glass spheres; natural sunlight; pilot-scale CPC	a- degradation (TiO_2 = 0.1 g/L): 100% in CPC (39 kJ/L), 85% in batch (68.95 kJ/L), b- 100% degradation (3.3 kJ/L), 100% mineralisation (13.39 kJ/L)	[177]
C_0 = 0.05 - 0.2 mg/L; TiO_2 P25 immobilized onto glass plates (36.1 - 150.7 mg/cm^2); simulated solar irradiation (150 W, $16.5 \cdot 10^{-5}$ Einstein/m^2, xenon lamp); lab-scale, batch-operated reactor	80% degradation within 90 min (C_0 = 0.1 mg/L, TiO_2 = 150.7 mg/cm^2)	[224]
C_0 = 5 mg/L; C-N co-doped TiO_2 (0.5 g/L); pH = 3 - 11; vis-LED strips emitting blue (λ = 465 nm), green (λ = 523 nm), yellow (λ = 589 nm), and white light (λ = 450 - 600 nm); lab-scale, batch-operated slurry reactor	> 99, > 99, and 84% degradation under white, blue, and green light irradiation within 5 h (pH = 7); corresponding mineralisation: 70, 60, and 45%; silica and bicarbonate suppressed BPA removal	[192]
C_0 = 5 mg/L, N-doped TiO_2 hollow sphere (0.5 g/L); vis-LED strips emitting blue light (λ = 465 nm), green light (λ = 523 nm), and yellow light (λ = 589 nm); lab-scale, batch-operated reactor	90% degradation in 2 h under blue light irradiation; 66% mineralisation after 6 h of treatment	[193]
C_0 = 40 mg/L; TiO_2 (1 g/L); UVA irradiation (200 W, 10 mW/cm^2, Hg-Xe lamp); lab-scale, batch-operated slurry reactor	100% mineralisation after 20 h of treatment; estrogenic activity reduced to 10% within 6 h	[220]
C_0 = 10 mg/L; TiO_2 anatase (0 - 20 g/L); θ = 10 - 70 °C; pH = 2 - 10; natural sunlight (0 - 1.7 mW/cm^2); lab-scale, batch-operated slurry reactor	100% mineralisation after 11 h of treatment (TiO_2 = 10 g/L, θ = 30 °C, pH = 6)	[136]
C_0 = 22.83 mg/L; TiO_2 P25 (2 g/L), UVA irradiation (75 W, 2.5 mW/cm^2 at 360 nm, Hg lamp); lab-scale, batch-operated slurry reactor	100% degradation and ~ 90% mineralisation in 2 h	[221]
C_0 = 1 - 50 mg/L; TiO_2 (5 - 600 mg/200 cm^3); pH = 3 - 11; θ = 10 - 70 °C; UVA irradiation (0.9 W, λ = 365 nm); lab-scale, batch-operated slurry reactor	97% removal within 60 min (C_0 = 20 mg/L, TiO_2 = 100 mg/200 cm^3, pH = 7, θ = 25 °C)	[219]

2.2.2 Homogeneous photocatalysis

In homogeneous photocatalytic processes, the catalysts used are mostly transition metal complexes, such as iron and chromium [237]. The best-known system of this type is the Fenton reagent (H_2O_2/ Fe^{2+}). In Fenton processes, hydroxyl radicals ($HO^{\bullet}$) are formed during the catalytic decomposition of hydrogen peroxide (H_2O_2) by iron species. Ferrous iron (Fe^{2+}) reacts with hydrogen peroxide yielding hydroxyl radicals, while oxidised in ferric iron (Fe^{3+}) [17, 18]:

$$Fe^{2+} + H_2O_2 \rightarrow Fe^{3+} + OH^- + HO^{\bullet} \quad (2-18)$$

$$Fe^{2+} + HO^{\bullet} \rightarrow Fe^{3+} + OH^- \quad (2-19)$$

$$Fe^{2+} + HO_2^{\bullet} \rightarrow Fe^{3+} + HO_2^- \quad (2-20)$$

$$Fe^{3+} + H_2O_2 \rightarrow Fe^{2+} + HO_2^{\bullet} + H^+ \quad (2-21)$$

$$Fe^{3+} + HO_2^{\bullet} \rightarrow Fe^{2+} + O_2 + H^+ \quad (2-22)$$

$$Fe^{3+} + O_2^{\bullet -} \rightarrow Fe^{2+} + O_2 \quad (2-23)$$

The rate-limiting step of the process is the regeneration of Fe^{2+} from Fe^{3+}, reactions (2-19) - (2-21). In water, Fe^{3+} is hydrolysed extensively forming different Fe^{3+}-aqua complexes, depending on the pH, as shown in Fig. 2-3. At pH between 2.5 and 3, the prevailing iron species is $[Fe(H_2O)_5(OH)]^{2+}$, which is highly photoactive in the UV and visible regions of the solar spectrum [238]. Upon irradiation, Fe^{3+} is reduced to Fe^{2+} and a hydroxyl radical is produced via a photo-assisted Fenton reaction (photo-Fenton):

$$[Fe(H_2O)(OH)]^{2+} + h\nu \rightarrow Fe^{2+} + HO^{\bullet} + H^+ \quad (2-24)$$

The produced hydroxyl radicals attack and degrade the organic compounds present in the photo-Fenton system mainly via three pathways: (i) electrophilic addition, reaction (2-6); (ii) hydrogen atom abstraction, reaction (2-7); and (iii) electron transfer, reaction (2-8) [124].

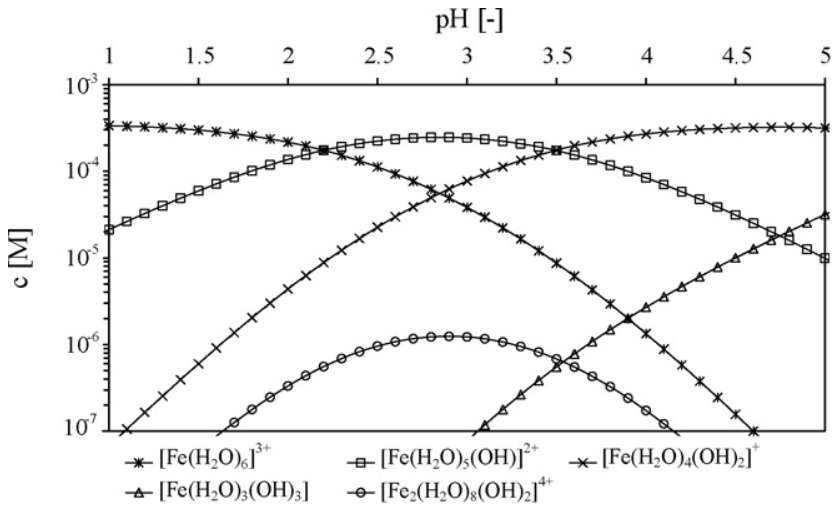

Fig. 2-3 Fe^{3+} species present in aqueous solution at different pH (C = 20 mg/L, θ = 20 ^{0}C), adopted from Malato et al. (2009) [17].

Fenton-related systems are practical, economical ways to produce ROS because iron is a non-toxic element and the fourth most abundant in nature [17], while hydrogen peroxide is inexpensive, easy to handle, and readily decomposes into water and oxygen making it environmentally safe [18, 118].

2.2.2.1 Process parameters and their influence

pH

The formation of Fe^{3+}-aqua complexes is strongly influenced by the pH of the solution, as can be seen in Fig. 2-3. pH 2.8, is widely accepted as optimal because at this pH there is no iron precipitation and the prevailing species is $[Fe(H_2O)_5(OH)]^{2+}$, which is the most photoactive Fe^{3+}-aqua complex in the UV and visible regions of the solar

spectrum. Therefore, strict pH control is required (acidification of the influent and later neutralisation of the effluent), which is regarded as the major drawback of the process [17]. In this direction, iron-chelating agents, such as oxalate, citrate, EDDS (ethylenediamine-N, N-disuccinic acid) [239] or wastewaters rich in polyphenolics [238], can be used to extend the operational pH of the photo-Fenton treatment, as discussed in Chapter 7.

Iron concentration and iron sources

Reaction rate increases with iron concentration up to a point (e.g. 1mM) [11, 240, 241] due to increased H_2O_2 decomposition rate, which subsequently leads to higher production of hydroxyl radicals. At iron concentrations beyond this point, which depends on the nature of the wastewater and the optical pathlength of the reactor, oxidation rates level off. In the photoreactor, the light attenuates along the optical pathlength (i.e. the tube diameter in a tubular reactor such as CPCs) depending on the extinction coefficient of the solution. High iron concentrations generate dark zones in the photoreactor, as a result of the high attenuation of light along the optical pathlength, hence reducing the number of available photons for the photo-Fenton reaction and, consequently, lowering the reaction rate [17].

Inner filter effects (i.e. competitive absorption of photons by the contaminants) in the reactant mixture also occur. These effects may lead to some direct photolysis; however, the expenditure of photons by the contaminants is not desirable because photolysis has typically a lower quantum yield than photo-Fenton reaction [17]. Therefore, when coloured wastewaters are to be treated, high catalyst concentration is required to compete effectively for the photons.

Iron can be also applied as a heterogeneous catalyst (e.g. in the form of suspended oxides, fixed on a support, or as a combination of these two) [242-244]. The advantages of this approach are the easy iron separation and the potential for operation without pH control; however, as in the case of immobilised TiO_2, mass transfer limitations and problematic light penetration due to the presence of solids should be overcome to obtain comparable reaction rates with the homogeneous photo-Fenton process.

Hydrogen peroxide concentration

When the concentration of hydrogen peroxide is too low, process reaction kinetics are suppressed due to the insufficient generation of hydroxyl radicals for the degradation of pollutants and intermediate by-products. On the other hand, presence of excess hydrogen peroxide, induces a scavenging effect on hydroxyl radicals according to the following reactions:

$$H_2O_2 + HO^{\bullet} \rightarrow HO_2^{\bullet} + H_2O \qquad (2-25)$$

$$HO_2^{\bullet} + HO^{\bullet} \rightarrow H_2O + O_2 \qquad (2-26)$$

The hydroperoxyl radical, $HO_2^{\bullet}$, formed has a lower oxidation potential than hydroxyl radicals, hence limiting the reaction rate. In between the two extremes, the reaction rate increases with hydrogen peroxide concentration. The stoichiometric amount of hydrogen peroxide required can be calculated theoretically and depends on the chemical structure and concentration of the substrate. However, in many cases, the optimal experimental value for hydrogen peroxide concentration has been found to be much higher than the theoretical stoichiometric need, implying inefficient use of oxidant [17, 245].

Initial substrate concentration

Increase in the initial substrate concentration triggers two antagonistic events: event (i) increases the probability of collision between substrate with hydroxyl radicals; and event (ii) increases the concentration of radical scavengers (i.e. substrate) [241]. Intensification of the inner filter effects, at higher substrate concentrations, is also possible [17]. In general, higher substrate concentrations have been found to slow down reaction kinetics, therefore longer treatment time is required [17].

Light wavelength, intensity, and light sources

a- Light wavelength

In photo-Fenton reactions, the most important light wavelengths are found in the range between λ = 300 - 400 nm (i.e. UVA), where Fe^{3+}-aqua complexes are photoactive [241]. This region is extended to the visible in the presence of Fe^{3+}-complexes formed via ligand-to-metal charge transfer (LMCT) reactions between chelating agents and iron because these absorb light at longer wavelengths than Fe^{3+}-aqua complexes [17]. Light wavelength is strongly related to the inner filter effects, as well. Oliveros et al. (1999) studied the effect of the light source (i.e. polychromatic medium-pressure mercury lamp, λ = 300 - 500 nm; low-pressure arc, λ = 254 nm; excimer lamp, λ = 222 nm) on the photo-Fenton treatment of highly contaminated industrial wastewater [246]. Oliveros et al. found that the highest reaction rates were obtained under irradiation provided by the polychromatic light source, ascribing them to inner filter effects induced at lower wavelengths (i.e. λ = 222 and 254 nm). Likewise, Gernjak et al. (2003) reported improved reaction kinetics for the degradation of UV-absorbing compounds (i.e. vanillin) under sunlight in comparison to a medium-pressure lamp during photo-Fenton process [247]. In this sense, the combined use of iron-chelating

agents and sunlight (i.e. a polychromatic light source), appears to be a good strategy to reduce the inner filter effects caused by compounds absorbing in the UV region.

b- Light intensity

Perez et al. (2002) investigated the effect of light intensity on the degradation of the organic fraction of a bleaching Kraft mill effluent by photo-Fenton treatment. The irradiation source employed was a Xenon lamp. Perez et al. reported that reaction rates increased with light intensity up to $7.55 \cdot 10^{-8}$ Einstein/s [248]. Similar results were reported by Sabaikai et al. (2014) in their study on the photo-Fenton degradation of polyphenols in tea manufacturing wastewater [249]. Sabaikai et al. found that mineralisation rates were enhanced when the number of the UVA lamps (15 W blacklight fluorescent lamps, λ = 352 nm) increased from 0 to 3. In both studies, the improved performance, at increased light intensities, was attributed to the acceleration of the iron redox cycle, which in turn led to higher photogeneration of hydroxyl radicals.

c- Light sources

Artificial photon generation by conventional light sources in photocatalytic systems incurs large operating costs [250]. When mercury lamps are to be employed, except for the high CO_2 emissions, additional environmental risks related to the presence of toxic mercury impede process scale-up. To improve the sustainability of the photo-Fenton process, natural sunlight, a renewable energy source, can be used as an irradiation source [18]. Among AOPs, the photo-Fenton process seems to be the most suitable to be powered by sunlight because iron-hydroxy and iron-organic acid complexes absorb both in the UV and visible spectrum [17]. Solar photo-Fenton has been proved to be an effective treatment method for EMs including pharmaceuticals,

artificial sweeteners, herbicides, insecticides, pesticides, and EDCs [223, 251-255]. Table 2-9 presents some of the most frequently employed solar reactors in photo-Fenton applications.

In sun-rich areas, solar photo-Fenton can be applied as a tertiary treatment step in WWTPs for the removal of bio-recalcitrant EMs. When sunlight is inadequate however, artificial generation of photons is required. In this case, LEDs, thoroughly discussed in paragraph 2.2.1.1 'Light sources', can be used as eco-friendly alternatives to conventional mercury lamps. So far, LEDs have been employed as irradiation sources in the photo-Fenton treatment of the insecticide acetamiprid [256, 257], phenol [258], and the dye Rhodamine B [259], resulting in high removal yields. Therefore, LED-driven photo-Fenton could serve as a polishing step for the removal of EMs in areas with reduced sunshine or as a back-up plan to solar photocatalytic systems (e.g. during periods with increased influent loads).

Table 2-9 Examples of solar photocatalytic reactors.

Parabolic trough concentrator (PTC)  (type 'Helioman', PSA)	PTC is a tubular plug-flow reactor with turbulent flow. The parabolic reflector redirects radiation to the absorber tube, through which flows the wastewater. • Advantages: good mass transfer, weatherproof (no contamination, no vaporization of volatile compounds). • Disadvantages: use of direct irradiation only (useless when the sky is cloudy), a sun tracking system is necessary increasing the investment cost considerably [17].
Compound parabolic collector (CPC)  (▲PSA) 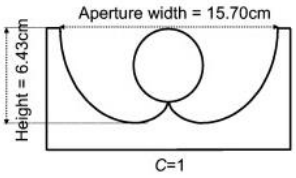 (◄concentration factor of 1, adopted from Polo-López et al. (2011) **[260]**)	CPC is a static tubular reactor placed above two truncated reflecting parables with concentration factor (i.e. ratio of tube perimeter to aperture) of 1. • Advantages: higher optical efficiency and quantum yields than Helioman, use of direct and diffuse radiation, weatherproof, lower investment cost than Helioman. • Disadvantages: short light pathlength (tube diameter 5 cm, inefficient photon use) [261].
Raceway pond reactor (RPR)  (CIESOL, University of Almería)	RPR is a reactor with channels in which wastewater is recirculated by a paddlewheel [262]. • Advantages: variable light pathlength (better use of photons reaching the reactor surface, higher treatment capacity per surface area), construction from low cost materials, i.e. plastic liners (reduction of capital investment, construction cost 10 €/m^2 compared to 100 €/m^2 for CPC), reduced energy requirement for mixing (4 W/m^3 compared to 80 W/m^3 in the CPCs) [261]. • Disadvantages: open to air (short treatment times should be applied to avoid water evaporation).

Water matrix

Inorganic ions (e.g. Cl^-, SO_4^{2-}, NO_3^-, PO_4^{3-}, and HCO_3^-) typically found in groundwater, surface water, and wastewater affect the reaction kinetics of photo-Fenton process. Complexation with iron, scavenging of hydroxyl radicals, and formation of less reactive species (e.g. $Cl^{\bullet}$, $Cl_2^{\bullet-}$, $SO_4^{\bullet-}$) than hydroxyl radicals are some of the possible reactions that lower degradation rates [18, 263-266]. The salinity of wastewater has also been found to induce retardation effects on reaction kinetics, nevertheless, photo-Fenton can still work at salt concentrations of the same level as seawater, although with slower reaction rates [265, 266].

Temperature

Reactions (2-21) – (2-23) (thermal Fenton reactions) are driven by thermal energy [18]. Therefore, increase of temperature from 20 to 50 °C has been found to have a beneficial effect on the reaction kinetics [240, 248, 267].

2.2.2.2 Ferrioxalate-assisted photo-Fenton

Photo-Fenton reaction can be intensified with the use of ferrioxalate complexes [118, 268]. Process enhancement is mainly achieved via the higher quantum yields of ferrioxalate than Fe^{3+}-aqua complexes and the faster Fe^{2+} regeneration. The addition of oxalic acid yields extra ROS, such as superoxide radical ions and hydroxyl radicals. Ferrioxalate, $[Fe^{3+}\ (C_2O_4)_3]^{3-}$, is formed *in situ* by the reaction between oxalic acid ($H_2C_2O_4$), and Fe^{3+} [269]:

$$Fe^{3+} + H_2C_2O_4 \rightarrow [Fe^{3+}\ (C_2O_4)_3]^{3-} + 6H^+ \qquad (2-27)$$

Upon UV-Vis irradiation (200 - 400 nm), oxalyl radical anions ($C_2O_4^{\bullet -}$) are formed and Fe^{2+} is regenerated:

$$[Fe^{3+}\ (C_2O_4)_3]^{3-} + hv \rightarrow Fe^{2+} + 2{C_2O_4}^{2-} + {C_2O_4}^{-\bullet} \qquad (2-28)$$

Oxalyl radical anions are oxidised by the dissolved oxygen, yielding superoxide radical anions ($O_2^{\bullet -}$):

$$C_2O_4^{\bullet -} + O_2 \rightarrow O_2^{\bullet -} + 2CO_2 \qquad (2-29)$$

Oxalyl radical anions quickly decompose into carbon dioxide radical anions ($CO_2^{\bullet -}$) reaction (2-30), which in turn react with oxygen generating extra superoxide radical anions, reaction (2-31):

$$C_2O_4^{\bullet -} \rightarrow CO_2^{\bullet -} + CO_2 \qquad (2-30)$$

$$CO_2^{\bullet -} + O_2 \rightarrow O_2^{\bullet -} + CO_2 \qquad (2-31)$$

Finally, extra hydrogen peroxide and hydroxyl radicals are formed by the following reactions:

$$O_2^{\bullet -} + H^+ \rightarrow HO_2^{\bullet} \qquad (2-32)$$

$$HO_2^{\bullet} + HO_2^{\bullet} \rightarrow H_2O_2 + O_2 \qquad (2-33)$$

$$CO_2^{\bullet -} + Fe^{3+}[(C_2O_4)_3]^{3-} \rightarrow Fe^{2+} + CO_2 + 2C_2O_4^{2-} \qquad (2-34)$$

$$Fe^{2+} + H_2O_2 + 3C_2O_4^{2-} \rightarrow Fe^{3+}(C_2O_4)_3^{3-} + OH^- + HO^{\bullet} \qquad (2-35)$$

2.2.2.3 Persulfate

The addition of extra oxidants, such as persulfate, is another method to improve the efficiency of photo-Fenton process [270, 271]. Persulfate ion ($S_2O_8^{2-}$) is a strong oxidising agent, which can decompose into highly reactive sulfate radicals ($SO_4^{\bullet -}$, E^o

= 2.6 V), upon activation by heat, UVC irradiation ($\lambda \leq 270$ nm) or transition metals (Me^{n+}), such as Fe^{2+} [272, 273]:

$$S_2O_8^{2-} + heat/UV \rightarrow 2SO_4^{\bullet-} \qquad (2-36)$$

$$S_2O_8^{2-} + Me^{n+} \rightarrow SO_4^{\bullet-} + Me^{(n+1)+} + SO_4^{2-} \qquad (2-37)$$

2.2.2.4 State of the art

Photo-Fenton process has been reported extensively as an efficient method for the treatment of wastewaters containing pesticides, phenols, natural phenolic pollutants, PAHs, and pharmaceuticals [11, 17, 103, 129, 210, 211, 214, 251, 274-277]. De la Cruz et al. (2013) investigated the removal of 22 EMs (i.e. pharmaceuticals, X-ray contrast media, corrosion inhibitors, and biocides/pesticides) applying photo-Fenton at neutral pH under UVC irradiation [276]. For this purpose, a continuous flow pilot reactor was placed at the end of the treatment train of a WWTP, receiving the secondary effluent as influent. The global degradation of the selected EMs was reported by De la Cruz et al. to be 88%, even with the lowest residence time tested of 10 s. In this study, Fenton reactions took place with the iron already present in the wastewater (1.6 mg/L), which remained undissolved at the natural pH of the wastewater, suggesting a heterogeneous photo-Fenton regime. Klamerth et al. (2013) employed natural sunlight as irradiation source, with iron chelators added to the system in order to obviate the need for water acidification [251]. Klamerth et al. compared conventional (pH = 3) with modified photo-Fenton (with either humic acids or ethylenediamine-N, N-disuccinic acid (EDDS) at neutral pH) for the treatment of 62 EMs (e.g. psychoactive drugs, nonsteroidal anti-inflammatory drugs, lipid regulators, antibiotics, beta blockers, histamine-2 blockers, antipyretic, analgesics, and

herbicides) found in real WWTP effluents. The experiments were carried out in a solar CPC reactor applying low concentrations of iron and hydrogen peroxide. In all cases, removal percentages over 95% were reported for all the contaminants. Klamerth et al. observed that during photo-Fenton with humic acids pH decreased during treatment. Hence, among the three processes considered, EDDS-assisted photo-Fenton was found to be the most promising process due to maintenance of pH at the neutral range.

Photo-Fenton has been efficiently applied to the treatment of ASs, as well. An overview is given in Table 2-10. In a lab-scale photoreactor, Calza et al. (2013) studied the degradation of SUC by photo-Fenton treatment under simulated solar irradiation, reporting 96% removal within 15 min at optimal conditions [278]. ACE removal during photo-Fenton process under UVA irradiation was investigated by Kattel et al. (2017) [279]. At the best-assayed conditions, complete removal was obtained after 10 min of treatment and 81.7% mineralisation after 2 h. When photocatalytic experiments were carried out in groundwater or wastewater, the oxidation rates were significantly suppressed due to radical scavenging induced by the inorganic ions and alkalinity present in these matrices. Arzate et al. (2017) studied EMs treatment in WWTP secondary effluents by continuous solar photo-Fenton process in a raceway pond reactor (RPR) [252]. RPRs were used as low-cost alternatives to solar CPCs and the target pollutants were 58 EMs, pharmaceuticals and artificial sweeteners, detected in actual WWTP effluent. Arzate et al. reported 89% removal of EMs on average (HRT = 80 min), with removal rates of AP, ACE, SAC, and SUC, in particular, being 99, 86, 62 and 51% respectively, rendering the studied system as a promising tertiary treatment option.

The addition of ferrioxalate has been suggested as an efficient method to intensify photo-Fenton process for the treatment of EMs, such as pesticides, herbicides, and pharmaceuticals [268, 280-288]. Table 2-11 gives an overview of the studies applying ferrioxalate-assisted photo-Fenton for the treatment of antibiotics, antiepileptics, and non-steroidal anti-inflammatory drugs. Duran et al. (2013) investigated the degradation of AP by solar photo-Fenton treatment intensified by ferrioxalate in a CPC at pilot-scale [283]. Duran et al. employed chemometric optimisation tools, such as factorial design and neural networks, to study the simultaneous effects of key operating parameters on AP mineralisation. At optimal conditions, 60% mineralisation within 5 min was reported with a total cost of 4.5 cent €/g TOC removed, highlighting the economic feasibility of the process. In a following study, Duran et al. (2014) studied the industrial applicability of ferrioxalate-assisted photo-Fenton process for the degradation of AP in synthetic municipal wastewater effluent [284]. For this purpose, a semi-industrial UVC/solar CPC plant with continuous flow was used. At the optimal conditions with a mean retention time of 15.3 min, the mineralisation of AP was reported to be 77%. This could further increase up to 88% with extra irradiation provided by photovoltaic-powered UVC lamps, delivering a cost-efficient treatment method with an estimated total cost of 2.78 cent €/g TOC removed.

Addition of extra oxidants, such as persulfate, is another way to enhance the efficiency of photo-Fenton process. Monteagudo et al. (2015) studied the oxidation of carbamazepine using persulfate simultaneously activated by heat energy (thermal, ultrasound), UVC light, Fe^{2+} ions and hydrogen peroxide [270]. Under acidic conditions, Fe^{2+} could decompose H_2O_2 and persulfate into hydroxyl and sulfate radicals, respectively, leading to complete mineralisation of carbamazepine within 90

min. Furthermore, Monteagudo et al. found that the presence of chloride ions had a negligible effect on process efficiency due to selective reactivity of sulfate radicals.

Table 2-10 Removal of ASs by photo-Fenton.

Compound	Operating conditions	Results and comments	References
ACE, SAC, SUC	$[ACE]_0$ = 741 ± 96 ng/L, $[SAC]_0$ = 420 ± 55 ng/L, $[SUC]_0$ = 421 ± 55 ng/L; Fe^{2+} = 5.5 mg/L; H_2O_2 = 30 mmol/L; pH = 2.8; natural sunlight; secondary effluent; RPR (liquid depth = 5 cm, HRT = 20 - 80 min, continuous operation)	Increase of removal with HRT up to 80 min; removal at HRT = 80 min: ACE 86%, SAC 62%, SUC 51%	[252]
ACE	C_0 = 75 µM; ACE:H_2O_2:Fe^{2+} - 1:10:1; pH = 3, UVA irradiation (11W, 2.2 mW/cm^2, Hg lamp); lab-scale, batch-operated reactor	100% removal in 10 min; 81.7% mineralisation in 2 h	[279]
SUC	C_0 = 15 mg/L; Fe^{2+} = 0.36 - 6.36 mg/L; H_2O_2 = 0.43 - 4.99 mmol/L; pH = 2 - 4; simulated solar irradiation (1500 W, Xenon arc lamp, Suntest CPC+); lab-scale, batch-operated reactor	At optimal conditions (Fe^{2+} = 6 mg/L, H_2O_2 = 2.9 mmol/L, pH = 3): 96% removal within 15 min	[215]

Table 2-11 Removal of pharmaceuticals by ferrioxalate-assisted photo-Fenton.

Compound	Operating conditions	Results and comments	References
Carbamazepine	C_0 = 15 mg/L; Fe^{2+} = 2.5 - 30 mg/L; H_2O_2 = 0 - 300 mg/L; oxalic acid = 12.1 - 145.2 mg/L; pH = 2.5 - 5; natural sunlight; pilot-scale CPC plant	80% mineralisation in 5 min (H_2O_2 = 150 mg/L, Fe^{2+} = 2.5 mg/L, oxalic acid = 12.1 mg/L, pH = 5); extension of the operational pH	[285]
Levofloxacin	C_0 = 20 mg/L; iron: oxalate - 1:3, 1:6, 1:9 (Fe^{3+} = 1, 2 mg/L); H_2O_2 = 20 mg/L; pH = 3 - 6; θ = 25 ^{0}C; pure water, secondary effluent; simulated sunlight (41.6 W_{UV}/m^2); lab-scale CPC	iron: oxalate - 1:3 (Fe^{3+} = 1 mg/L) led to reaction rates 1.8, 3.2 and 8.9 times higher for pH 4, 5 and 6, respectively, compared to conventional photo-Fenton (pH = 2.8); in the same order, mineralisation increased by 25, 7.7 and 13.2%	[286]
Oxytetracycline	C_0 = 20 mg/L; iron: oxalate - 1:3 (Fe^{3+} = 1, 2, 5 mg/L); internal additions of H_2O_2; pH = 3, 4, 5; simulated sunlight (44 W_{UV}/m^2); lab-scale CPC	75% mineralisation in 45 min (Fe^{3+} = 2 mg/L, H_2O_2 consumed = 1.5 mM, pH = 4); loss of antibacterial activity against *E. coli*	[287]
Diclofenac	C_0 = 20 mg/L; iron: oxalate - 1:3, 1:6, 1:9 (Fe^{3+} = 2 mg/L); diclofenac: H_2O_2 = 1:33; pH = 5, 6; θ = 25 ^{0}C; simulated sunlight (41.6 W_{UV}/m^2); lab-scale, batch-operated reactor	63% mineralisation in 90 min (iron: oxalate - 1:9, H_2O_2 consumed = 1.9 mM, pH = 6); 55% mineralisation in 90 min (iron: oxalate - 1:3, H_2O_2 consumed = 2 mM, pH = 5)	[288]
Trimethoprim, sulfamethoxazole	C_0 = 20 mg/L; iron: oxalate - 1:3 (Fe^{3+} = 5 mg/L); H_2O_2 = 5 mg/L; pH = 4 - 6.5; simulated sunlight (44 W_{UV}/m^2); lab-scale, batch-operated reactor	70 and 53% mineralisation of sulfamethoxazole and trimethoprim (pH = 4, Q_{UV} = 2 kJ/L, H_2O_2 consumed = 2 mM)	[282]
Antipyrine	C_0 = 50 mg/L; oxalic acid = 30 - 150 mg/L; Fe^{2+} = 1 - 20 mg/L; H_2O_2 = 100 - 1000 mg/L; pH = 2.7; synthetic secondary effluent; natural sunlight (22.3 - 30.4 W/m^2); pilot-scale CPC, continuous flow (680 - 1200 L/h)	77% mineralisation (H_2O_2 = 750 mg/L, Fe^{2+} = 12 mg/L, oxalic acid = 66.2 mg/L, flow rate = 1200 L/h)	[284]
Antipyrine	C_0 = 50 mg/L; oxalic acid = 0 - 150 mg/L; Fe^{2+} = 4.4 - 14 mg/L; H_2O_2 = 50 - 1500 mg/L; pH = 2.7; natural sunlight (22.3 - 36.46 W/m^2); pilot-scale CPC	60% mineralisation in 5 min (H_2O_2 = 250 mg/L, Fe^{2+} = 14 mg/L, oxalic acid = 80 mg/L)	[283]

2.2.3 Photocatalytic oxidation technologies: integration, scale-up and current challenges

The key features of photocatalytic processes, which promote their use as tertiary treatment steps in WWTPs for the removal of EMs, are summarised as follows:

(i) high removal efficiency,

(ii) complete oxidation of organics rather than transfer to another phase via conventional sorption or stripping,

(iii) inexpensive reagents,

(iv) mild operating conditions (i.e. temperature and pressure),

(v) easy and safe operation, and

(vi) potential use of sunlight as an energy source.

2.2.3.1 Process integration

The coupling of photocatalytic systems with biological treatment in WWTPs can offer a technically sound and environmentally friendly solution for integrated wastewater management [119]. Photocatalytic processes can be implemented as a final polishing step for the degradation of recalcitrant compounds that have not been eliminated by conventional treatment processes [117, 119, 135]. In this approach, biodegradable compounds are removed by the biological step, which is regarded to be the most inexpensive and environmentally benign treatment option [289]. Therefore, the treatment requirement by photocatalysis is reduced merely to the degradation of bio-recalcitrant compounds and, hence, significant cost reduction is expected [117]. Several studies have reported the efficiency of photochemical oxidation processes as

a post-treatment step after biological processes at lab and pilot-scale [251, 252, 276, 290-293]; however, the implementation of these technologies at full-scale is still pending. This can be attributed, firstly, to the absence of discharge limits for EMs in effluent from WWTPs and, secondly, to the relatively high treatment costs (e.g. electricity for the artificial light sources, etc.) of photochemical oxidation technologies.

2.2.3.2 Scale-up and current challenges

The wide application of photochemical oxidation technologies sets a requirement the reduction of their treatment cost. To accomplish this, strategies should be adopted aiming at the minimisation of energy demand, the use of reagents, and the need for effluent pre/post-treatment. Energy efficiency can be achieved using natural sunlight as irradiation source where applicable, or, alternatively, energy-efficient artificial light sources; in both cases, the design of photocatalytic reactors with high illumination efficiency is of utmost importance [294]. Additives which improve process efficiency either in terms of kinetics or operational pH range [17], as well as operation at optimised conditions can significantly reduce the requirement for reagents. Meanwhile, immobilised catalysts or complexing agents can obviate the need for post-separation or pH control making photocatalytic processes more sustainable [17].

In this view, the major challenges arising to date regarding process implementation at full-scale can be summarised into:

- the identification of eco-friendly, energy-efficient light sources in areas where sunlight is inadequate [171],

- the development of catalysts with improved photocatalytic efficiency via enhanced charge transport and trapping and/or extended absorption spectrum to the visible region of the solar spectrum [124, 237],
- the identification of cost-effective solid-liquid separation processes for slurry photoreactors [126]; or alternatively, the development of immobilised catalysts with high durability of the coating, improved light penetration, augmented fluid-to-catalyst mass transfer, and increased lifetime [295],
- the identification of inexpensive and eco-friendly additives, such as oxidants and complexing agents, to improve oxidation rates, and overcome the requirement for pH control [296], and
- the design and fabrication of engineering proper photoreactors providing increased and uniform light distribution and optimised mass transfer of reactants and products [126, 297].

2.3 Factorial design and Neural networks

In photochemical oxidation technologies, the influence of operational parameters and their joint effects on process efficiency cannot be easily determined due to the complexity of the reactions involved [18]. Therefore, the design and scale-up of photocatalytic reactors become challenging tasks. Toward this direction, chemometric optimisation tools, such as factorial design and response surface methodology, can be used. These methods offer the advantage of process optimisation with minimal experimentation, particularly, in cases where the mechanism may not be well defined [298]. Chemometric optimisation tools have also been applied in photocatalytic studies [215, 283, 299-301].

2.3.1 Factorial design

The solution of a problem requires the determination of '*which* factors do *what* to *which* response' [298]. With this in mind, the one-factor-at-a-time design can be applied, whereby one factor changes at a time while the remaining factors remain constant. This is an approach that is statistically easy to handle, however, it can only provide information about the effect of a single factor at fixed conditions [298]. Alternatively, factorial design can be implemented that allows the evaluation of two or more independent variables (factors) and their joint effects on one or more dependent variables (response functions) [302]. In a two-level factorial design, each factor is studied at two levels, a low (-1) and a high (+1), and the full arrangement is denoted as 2^k, with k being the number of factors. In a 2^3 full factorial design, for instance, all possible combinations of the codified values (+1) and (-1) of the A, B and C factors are coded as shown in Fig. 2-4a and can be geometrically represented by the vertices of a cube, Fig. 2-4b [298].

(a)

Experiment	A	B	C
1	-	-	-
2	+	-	-
3	-	+	-
4	+	+	-
5	-	-	+
6	+	-	+
7	-	+	+
8	+	+	+

(b)

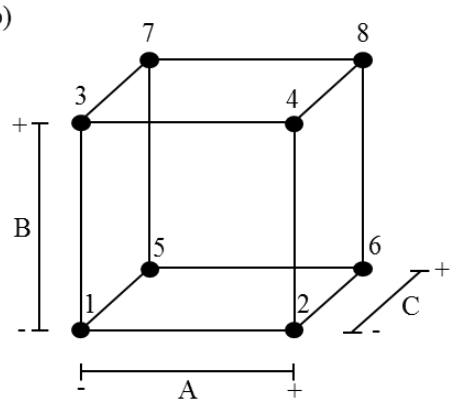

Fig. 2-4 A 2^3 factorial design (a) coded in standard order, and (b) represented by the vertices of a cube.

Two-level factorial designs can be used efficiently for the fitting of first-order polynomial models. However, when a better approximation is required, response surface methodology (RSM) is employed. RSM is useful for building second-order (quadratic) models and can optimise the process by finding the best set of factor levels that lead to the optimal responses. Central composite experimental design (CCED) is one of the basic tools of RSM. CCED contains a factorial design with centre points, which is further augmented with the star design shown in Fig. 2-5. In a CCED, if the distance from the centre point (0,0,0) is coded as ± 1 unit for each factor, then the respective distance of the star points is denoted as ± a, where $|a| > 1$. The value of a for a full factorial design, as in the present study, is calculated from:

$$a = [2^k]^{1/4} \qquad (2-38)$$

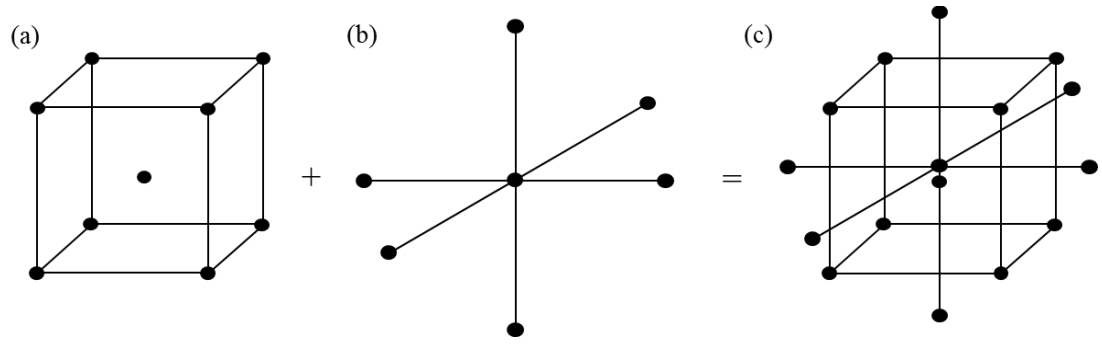

Fig. 2-5 (a) A 2^3 factorial design with centre point, (b) star, and (c) combined.

2.3.2 Neural networks

Artificial neural networks (NNs) are an information processing technique inspired by the learning process of the human brain [303]. NNs have been applied increasingly the last years in many areas of science and engineering for process modelling [304]. Their

aptitude to 'learn' from experimental databases without actual knowledge of the laws (i.e. physical, chemical, mathematical, etc.) that govern a process make NNs ideal for data analysis of complicated systems [304].

A NN consists of neurons organised into layers, related with each other by parallel connections. The topology of a NN is defined by the number of layers, the number of nodes in each layer and the type of the transfer functions [304]. In every NN the first layer is the input layer (independent variables) and the last one is the output layer (dependent variables). In a feed-forward network, the signal flows in one direction, from the input to the output layer. The input layer of neurons is the input distributor of the hidden layer, as can be seen in Fig. 3-8. In the hidden layer two processes take place: (i) the total input is calculated via a weighted summation of all the inputs received from the preceding layer (denoted as Σ in Fig. 3-8) by means of a base function and (ii) the output is calculated with the use of a transfer function (denoted as T in Fig. 3-8), with the sigmoid transfer function being the most widely used [303, 304]:

$$f(U_i) = \frac{1}{1 + e^{-U_i}} \qquad (2-39)$$

where $f(U_i)$ is the output of the hidden layer. The outputs of the hidden layers are the inputs of the output layers, in which a weighted summation of all inputs takes place for the calculation of the final outputs.

The strength of neural connections is determined by the weight associated with the neurons, which explains the influence of the input units on the output units [304, 305]. The connection weights are determined via the training process of the network based on experimental datasets and the use of a back-propagation algorithm. The objective

of the training is to optimise the network by minimising the mean squared error of the system that measures the difference between measured and predicted values.

2.4 Aims and Objectives

The aim of this work is to study the photocatalytic degradation of representative EMs, namely saccharin (SAC), bisphenol-A (BPA) and antipyrine (AP). Novel approaches are adopted to increase the overall sustainability of the process by improving photocatalytic performance, while minimising treatment cost and environmental impact. To achieve this the following objectives will be accomplished:

- Study the use of novel TiO_2 nanocomposites as catalysts to increase photocatalytic efficiency under UVA irradiation. For this purpose, the photocatalytic degradation of SAC and BPA in the presence of novel interfaced anatase-rutile catalysts produced by thermohydrolysis and tuned by Sn(IV) is investigated. The effect of key operating parameters, such as initial substrate concentration, catalyst type and concentration, and treatment time, on photocatalytic performance is evaluated. Furthermore, catalyst reuse – an important but little-studied aspect – is studied and the effect of ultrasound cleaning on catalyst regeneration is evaluated (Chapter 4).
- Study the use of LEDs and natural sunlight as irradiation sources to reduce the energy requirement of photocatalytic processes. For this purpose, the photocatalytic degradation of SAC and BPA is investigated under UVA irradiation provided by either a LED (UVA-LED) or a conventional blacklight lamp (UVA-BL), and solar irradiation in parallel experimental series. The

influence of key operating parameters, including initial substrate and catalyst concentration, water matrix, treatment time, irradiation source, and system on process performance is assessed. Furthermore, the main transformation products (TPs) of SAC formed during photocatalytic treatment are identified and possible degradation pathways are elucidated (Chapter 5).

- To compare the photocatalytic processes applied in terms of technical and economic benefits. For this purpose, a comparative study is carried out based on the removal, photonic, and energy efficiencies of the systems, obtained at the best-assayed operating conditions (Chapter 6).
- Study the potential of polyphenols, present in olive mill wastewater (OMW), as iron-chelating agents in the photo-Fenton process, as a means to obviate the need for water acidification at pH 2.8 and the related shortcomings (i.e. cost of chemicals and effluent with high salinity). For this purpose, the treatment of SAC by photo-Fenton process is investigated in a pilot-scale solar compound parabolic collector (CPC). The effect of key operating parameters, namely initial SAC concentration, accumulated UV energy, and OMW dilution on photocatalytic performance is assessed. For comparison, ethylenediamine-N,N'-disuccinic acid (EDDS), known for its ability to form photoactive iron complexes, is also used at circumneutral pH. Furthermore, the TPs formed during conventional photo-Fenton (pH = 2.8) are identified and linked to toxicity evolution (Chapter 7).
- Study the addition of complexing and oxidising agents, such as ferrioxalate and persulfate, to improve photo-Fenton efficiency under UVA-LED irradiation. For this purpose, the degradation and mineralisation of AP by UVA-LED

photo-Fenton treatment intensified by ferrioxalate complexes and persulfate anions is examined. Chemometric optimisation tools, namely a CCED and a NN, are used to model the process and optimise selected operational parameters, such as initial concentration of hydrogen peroxide, ferrous ion, oxalic acid, and persulfate. Furthermore, the contribution of hydroxyl radicals to the degradation mechanism is evaluated with the use of radical scavengers (Chapter 8).

The ground-breaking aspects of this work lie in:

- Use of novel TiO_2 nanocomposites for the degradation of EMs under UVA irradiation. Reuse of the catalysts, as a means to reduce treatment costs.
- The thorough investigation of the photocatalytic degradation of SAC, which has been recently recognised as an EM and therefore studies on its treatment are still scarce. The study includes treatment under several types of irradiation (i.e. UVA-LED, UVA-BL, and natural sunlight) at lab and pilot-scale, as well as, TPs identification, elucidation of degradation pathways, and toxicity assessment. It should be highlighted that studies employing natural sunlight, as irradiation source, for the photocatalytic treatment of ASs are missing from the literature. Furthermore, to the author's knowledge, the degradation of ASs by means of photocatalysis at pilot-scale has not been reported to date.
- Use of eco-friendly irradiation sources, such as natural sunlight and energy-efficient UVA-LEDs, for the photocatalytic degradation of EMs. The effect of light source on process efficiency is evaluated and an exhaustive comparison

with a conventional UVA lamp is carried out in terms of removal, photonic, and energy efficiencies.

- Use of OMW as a 'green' iron-chelating agent in the photo-Fenton treatment instead of expensive, hazardous chemicals as a means to extend the operational pH of the process. This study opens up the way for the use of wastewaters originating from natural products processing as iron complexing agents to improve the overall sustainability of the process.
- Optimisation of EMs degradation and mineralisation using ferrioxalate-assisted photo-Fenton process with the addition of persulfate. To the author's knowledge, ferrioxalate-assisted photo-Fenton under UVA-LED irradiation has not been reported to date, as well as the synergy with persulfate anions.

3 Materials and Methods

3.1 TiO_2-mediated treatment under UVA irradiation in the presence of nanocomposites tuned by Sn(IV)

3.1.1 Materials

Saccharin (SAC; 98+% purity, CAS No. 81-07-2) and bisphenol-A (BPA; ≥ 99% purity, CAS No. 80-05-7) were purchased from Acros Organics and Sigma-Aldrich, respectively. Stock solutions of SAC and BPA (~ 40 mg/L) were prepared in ultra-pure water (UPW; 18.2 MΩ.cm), obtained from an ELGA LabWater purification system, and were further diluted to the desired concentrations (2.5 - 10 mg/L) prior to experiments. For catalyst synthesis, $TiOSO_4 \cdot xH_2O$, $SnCl_4 \cdot 5H_2O$, and H_2SO_4 were supplied by Sigma-Aldrich. Three commercial catalysts were used for comparative purposes, whose characteristics are shown in Table 3-1.

Table 3-1 Commercial TiO_2 catalysts used: abbreviations and characteristics.

Catalyst	Crystal phase	Particle size, nm	Surface area, m^2/g	Supplier
Aeroxide P25 (P25)[a]	Anatase: rutile-80:20	21	50 ± 15	Evonik Industries
KRONOClean 7050 (Kr7050)[b]	Anatase	15	> 225	KRONOS Worldwide,Inc.
CristalACTiV PC105 (PC105)[c]	Anatase	20 ± 5	90	CRISTAL

Data source: [a] [306], [b] [307], [c] [308]

3.1.2 Catalyst preparation

Syntheses of anatase-rutile composites were performed according to a previously published protocol by Pichavant et al. (2014) [149], where low quantities of Sn(IV)

were used as a rutile phase promoter. In detail, $TiOSO_4 \cdot xH_2O$ and $SnCl_4 \cdot 5H_2O$ were dissolved in distilled water acidified with H_2SO_4 so that the total concentration of [Ti(IV)] + [Sn(IV)] was 1.5 mol/L and the total sulfate concentration was 2 mol/L. The quantity of Sn introduced, X_{Sn} = [Sn(IV)] / ([Ti(IV)] + [Sn(IV)]), was 0, $1.7 \cdot 10^{-3}$, and $6.8 \cdot 10^{-3}$ mol/L for pure anatase (ANA), 15% rutile (R15), and 30% rutile (R30) catalyst samples, respectively (for the catalyst characterisation techniques applied, see paragraph 3.5.10). Pichavant et al. (2014) found that rutile phase ranging between 15 - 30% led to the highest photocatalytic removal of phenol [149]. Given this, catalysts with rutile content higher than 30% (w/w) were not used in this study. The obtained transparent solutions were transferred into Teflon vials and heated in a microwave oven (Synthos 3000, Anton Paar) without stirring, following a ramp from room temperature to 120 °C at 5 °C/min, reaching a plateau at 120 °C for 1 h, and, finally, returning to room temperature at approx. -5 °C/min. The white precipitates were washed by successive centrifugation/ redispersion in water and powders were, finally, obtained by freeze-drying.

3.1.3 Photocatalytic experiments

Experiments were conducted in a borosilicate immersion well, batch-operated, slurry photoreactor at lab-scale (Fig. 3-1), purchased from Ace Glass (Vineland, NJ, USA). UVA irradiation was provided by an 11 W low-pressure blacklight fluorescent lamp (UVA-BL; PLS G23, Casell Lighting) emitting predominantly at λ = 365 nm. The lamp was placed inside a quartz tube and immersed in the centre of the reactor. The reactor was covered externally with aluminium foil to reflect back to the reactant mixture the exerting irradiation and to prevent penetration of ambient light. This

optimised reactor geometry takes full advantage of the lamp irradiation and provides a symmetric irradiation field [309]. Potassium ferrioxalate actinometry, as described by Murov [310], was applied for the estimation of the incident photon flux received by the reactant solution (see paragraph 3.5.8), which was found to be $4.98 \cdot 10^{-6}$ Einstein/s.

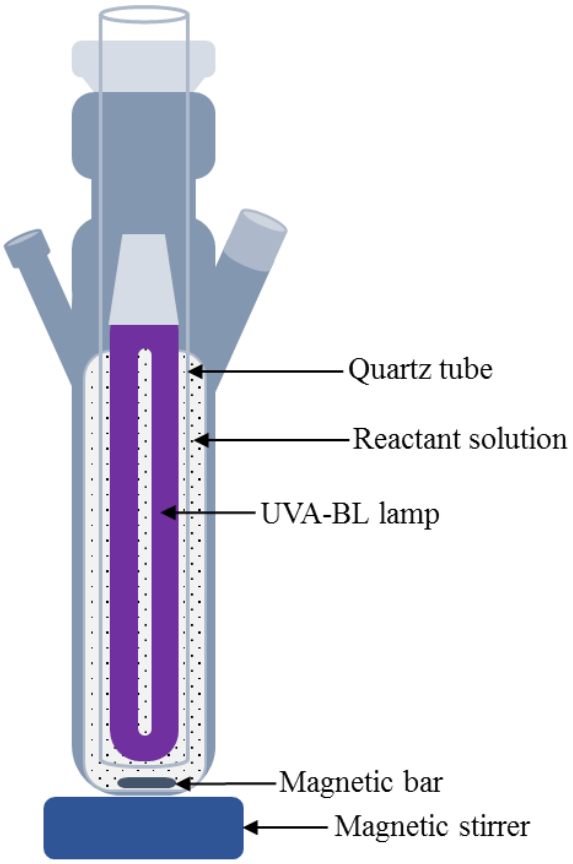

Fig. 3-1 Schematic of the immersion well, batch-operated photoreactor.

In a typical run, 500 mL of SAC or BPA solution were introduced in the photoreactor and a prescribed amount of catalyst was added. The obtained slurry solution was continuously stirred magnetically at 500 rpm to promote uniform dispersion of catalyst powder and dissolved oxygen. At the beginning of each experiment, the solution was

stirred in the dark for 30 min to ensure complete adsorption-desorption equilibrium of the organic compounds on catalyst surface. It is anticipated that a well-adsorbed substrate is more likely to be oxidised by the short-life photogenerated holes on catalyst surface [222]. After adsorption, the UVA-BL lamp was switched on (taken as t = 0) initiating the photocatalytic redox reactions. Samples were withdrawn at regular time intervals and filtered through 0.45 μm polyvinylidene fluoride (PVDF) syringe filters (CM Scientific Ltd) to remove catalyst particles and further analysed in terms of their organic content (see paragraphs 3.5.1 & 3.5.3). All experiments were conducted at room temperature (22^{o} C), at the inherent pH of SAC and BPA solutions (~ 4.6 and 6.4 for SAC and BPA, respectively), which remained constant during photocatalytic treatment.

3.1.4 Catalyst recovery and reuse

Experiments were performed to assess the activity of the prepared catalysts on repeated use after three successive photocatalytic runs. Catalyst recovery was performed at the end of each cycle, by centrifuging the reactant mixture at 4800 rpm for 8 min to separate catalyst particles from the supernatant effluent. The obtained TiO_2 precipitate was then reused as catalyst for the successive photocatalytic run. The effect of ultrasound cleaning (US) on catalytic performance was also investigated by placing, at the beginning of each cycle, the reactant mixture (i.e. SAC or BPA solution mixed with the recovered catalyst) into an ultrasound bath for 10 min.

3.2 TiO_2-mediated treatment under solar, LED, and conventional blacklight irradiation

3.2.1 Materials

SAC and BPA solutions were prepared as described in paragraph 3.1.1. Leonardite humic acid (HA) IHSS standard was used. HA stock solution was prepared by dissolving a prescribed amount of HA in 0.1M NaOH and further diluting it in UPW. TiO_2 Aeroxide P25 was the catalyst used in this study, whose characteristics are presented in Table 3-1.

3.2.2 Photocatalytic experiments

Experiments under artificial irradiation were performed in batch-operated, slurry photoreactors at lab-scale. For LED-driven photocatalysis, an indium gallium nitride (InGaN) UVA emitter (UVA-LED; λ = 365 nm; LZ4-00U600, LED Engin, data sheet in Appendix A) was employed providing continuous irradiation. The UVA emitter was mounted onto a heat sink (588-SV-LED-176E, Ohmite S Series, data sheet in Appendix A) to prevent radiant flux decrease due to temperature rise. The LED assembly was placed directly above the reactor and a quartz protective plate was placed between them (Fig. 3-2a). The second irradiation source was a UVA low-pressure blacklight fluorescent lamp (UVA-BL; PLS G23, Casell Lighting), emitting predominantly at λ = 365 nm. UVA-BL was housed in a quartz tube and, for the sake of comparison, positioned on top of the reactor, at the same height as the LED assembly (i.e. 8 cm distance between irradiation source and surface of reactant mixture at the beginning of each experiment) (Fig. 3-2b).

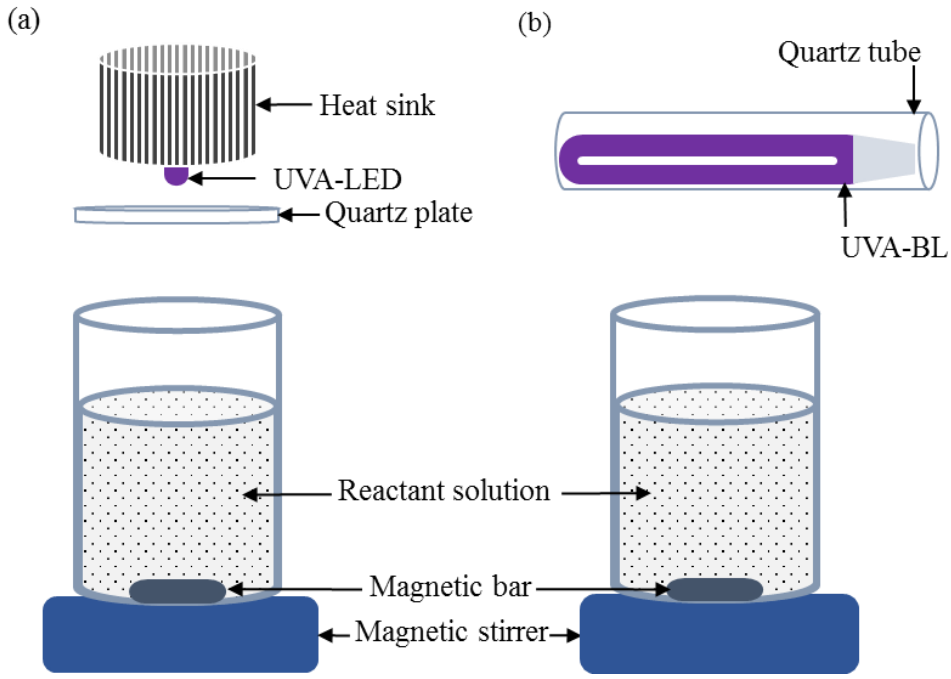

Fig. 3-2 Schematics of the (a) UVA-LED and (b) UVA-BL reactors.

Both set-ups were covered with an aluminium shield to prevent light diffusion out of the reactors and minimise penetration of ambient light. The reactors (250 mL Schott Duran beakers, diameter 7 cm, height 9 cm) provided an illuminated area of 38.5 cm^2. The quartz glasses were UV transparent and used to protect the lamps from water spills. UVA-LED and UVA-BL irradiation sources were driven by electrical power of 11 W and were connected in series to a DC power supply. The incident photon flux received by the reactant solution was determined by potassium ferrioxalate actinometry (see paragraph 3.5.8), as described by Murov [310], and was estimated at $3.32 \cdot 10^{-6}$ and $3.15 \cdot 10^{-7}$ Einstein/s under UVA-LED and UVA-BL irradiation, respectively. The irradiance of UVA-LED and UVA-BL irradiation sources was measured with a Labsphere spectral irradiance receiver head (E1000) and it was found to be 1005 and 22.49 W/m^2, respectively (see paragraph 3.5.9).

In a typical run, 150 mL of SAC or BPA solution were introduced in the photoreactor and the experimental procedure as described in paragraph 3.1.3 was followed.

The photocatalytic experiments under solar irradiation were carried out at the Department of Chemical Engineering, University of Castilla-La Mancha (Spain). For this purpose, a compound parabolic collector (CPC) of 0.25 m^2 total illuminated surface area (Fig. 3-3), manufactured by Ecosystem S.A, was used. The CPC reactor consisted of 2 borosilicate tubes providing an irradiated volume of 2 L, solar reflectors (anodised aluminium with a concentration factor of 1, Table 2-9), a continuously stirred tank (1.5 L), a centrifugal recirculation pump (flow rate = 30 L/min), connecting tubes, and valves. The CPC reactor was mounted on a south-facing platform tilted 39º in Ciudad Real (Spain) and a radiometer (Ecosystem, ACADUS 85), tilted 45º, was used to provide the global (direct + diffuse) UV (200 - 400 nm) radiation data. The light intensity of solar irradiation during the photocatalytic experiments ranged between 25 – 30 W/m^2.

At the beginning of each experiment, BPA solution and TiO_2 were added to the continuously stirred tank and pumped through the covered reactor for 30 min. This step was applied to ensure adequate mixing and complete equilibration of adsorption-desorption of BPA onto catalyst surface. The reactor was then uncovered initiating the photocatalytic redox reactions and the experimental procedure as described in paragraph 3.1.3 was followed.

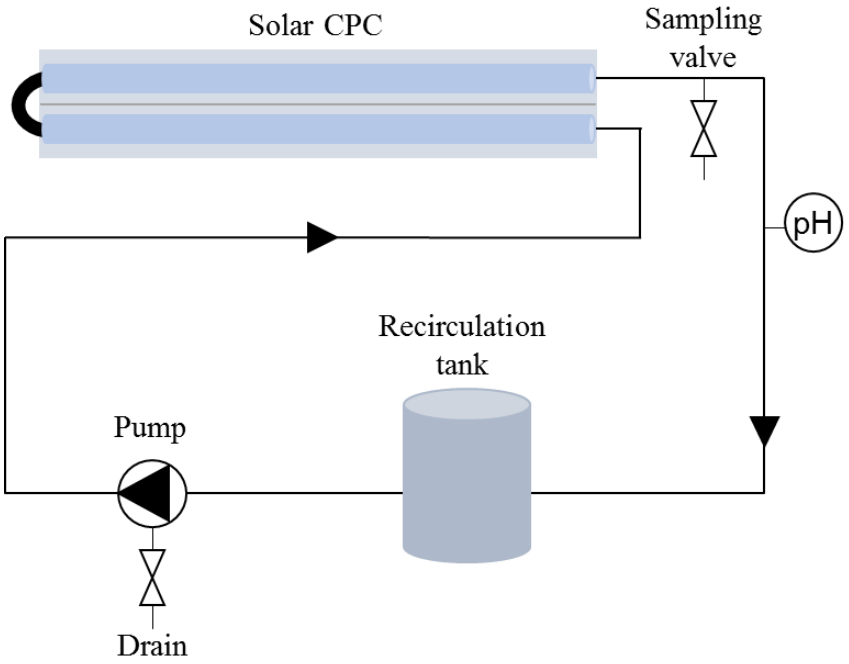

Fig. 3-3 Schematic of the solar CPC reactor (Department of Chemical Engineering, University of Castilla-La Mancha, Spain).

3.3 Solar photo-Fenton treatment with the use of olive mill wastewater as iron-chelating agent

3.3.1 Materials

SAC (98% purity, CAS No. 81-07-2) was obtained from Sigma-Aldrich. For photo-Fenton at pH 2.8, $FeSO_4 \cdot 7H_2O$ and H_2O_2 (30% w/w) were obtained from Panreac. For photo-Fenton at circumneutral pH, $Fe_2(SO_4)_3 \cdot H_2O$ (75% purity) was purchased from Panreac and (S,S)-ethylenediamine-N,N'-dissucinic acid trisodium salt solution (EDDS; 35% w/v) from Sigma-Aldrich. The experiments were performed using deionised water (DI; conductivity < 10 μS/cm, organic carbon < 0.5 mg/L) or natural water supplied by Plataforma Solar de Almería (300 - 450 mg/L Na^+, 5 - 10 mg/L K^+,

30 - 50 mg/L Mg^{2+}, 80 - 120 mg/L Ca^{2+}, 250 - 300 mg/L SO_4^{2-}, 250 - 350 mg/L Cl^-, organic carbon < 1.0 mg/L).

3.3.2 Olive mill wastewater

Olive mill wastewater (OMW) was provided by an olive mill in Andalucía (Spain) and was stored in 4 ºC. OMW had an initial pH of 4.2, total organic carbon (TOC) concentration of 12 g/L and its polyphenolic content was 6.2 g/L.

3.3.3 Photocatalytic experiments

Preliminary experiments were performed in the solar simulator (SunTest XLS+, Atlas) of Fig. 3-4. Irradiation was provided by a Xe lamp with an average UV irradiance of 35 W/m^2. Irradiance was monitored during the experiment with a SOLARLIGHT PMA2100 radiometer, placed inside the simulator.

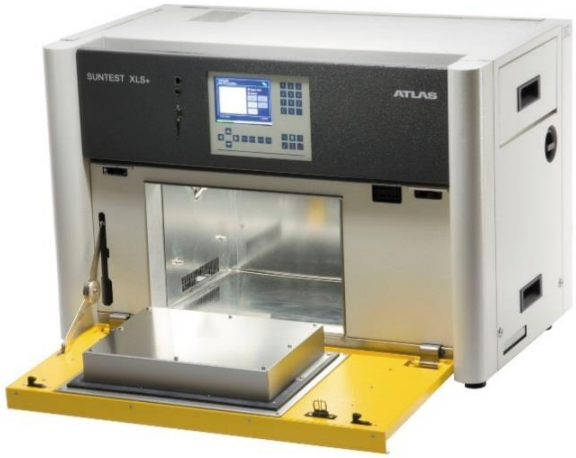

Fig. 3-4 Solar simulator (Plataforma Solar de Almería, Spain).

In a typical run, 1 L of SAC solution, adjusted to pH 2.8 with H_2SO_4, was loaded in an open cylindrical Pyrex glass reactor (height 8.5 cm, diameter 19 cm, wall thickness 3.2 mm). The reactor was then placed inside the simulator and prescribed amounts of Fe and H_2O_2 were added. Photo-Fenton reactions were initiated by switching on the lamp. The reactant mixture was continuously stirred magnetically and samples were taken at regular time intervals. The samples were analysed in terms of Fe and H_2O_2 concentrations (see paragraphs 3.5.4 & 3.5.5), then filtered through 0.2 μm nylon syringe filters (Fisherbrand) and analysed in terms of their organic content (see paragraph 3.5.1).

Experiments at pilot-scale were carried out in a 39 L CPC plant of 3 m^2 total illuminated area, installed at Plataforma Solar de Almería (Spain). The CPC plant consisted of 12 borosilicate tubes (30.0 mm inner diameter, 31.8 mm outer diameter, and 1.41 m length), solar reflectors (anodized aluminium with a concentration factor of 1, Table 2-9), a recirculation tank, a centrifugal pump, connecting tubes, and valves, as can be seen in Fig. 3-5. The illuminated area of CPC varied from 3 to 0.75 m^2, between experiments, by covering part of it. This enabled the reduction of the experimental reaction rates, allowing for proper evaluation of intermediates formation and toxicity assessment. Experiments with different illuminated area are comparable to each other by using Eq. (3-9), described in paragraph 3.5.13. The plant was tilted 37°, equally to the local latitude, and a radiometer (CUV3 Model, Kipp & Zonen), equally tilted, provided the global (direct + diffuse) UV radiation data. For experiments at pH 2.8, the pH of DI or natural water was initially fixed with H_2SO_4 addition. SAC solution, Fe, and H_2O_2 were then added to the recirculation tank and pumped into the tubes while the reactor was covered. Similarly, for the experiments without water

acidification, SAC solution, Fe:EDDS (or OMW followed by Fe) and then H_2O_2 were added and the system was left to recirculate. Fe:EDDS complexes were prepared prior to each experiment by dissolving $Fe_2(SO_4)_3 \cdot H_2O$ in 30 – 40 mL of DI acidified at pH 3 and then adding EDDS solution. In the experimental series for TPs identification and toxicity assessment, H_2O_2 was added in doses of 1 mg/L during treatment. This method was applied to ensure that there is no residual H_2O_2 in the collected samples that could oxidise SAC and/or TPs or affect the *Vibrio fischeri* bacteria, which were used for ecotoxicity evaluation (see paragraph 3.5.7). Solar photo-Fenton reactions were initiated by uncovering the reactor and samples were collected at predetermined times. The samples were analysed in terms of Fe and H_2O_2 concentrations (see paragraphs 3.5.4 & 3.5.5), then filtered through 0.2 μm nylon syringe filters (Fisherbrand) and analysed in terms of their organic content (see paragraphs 3.5.1 & 3.5.3).

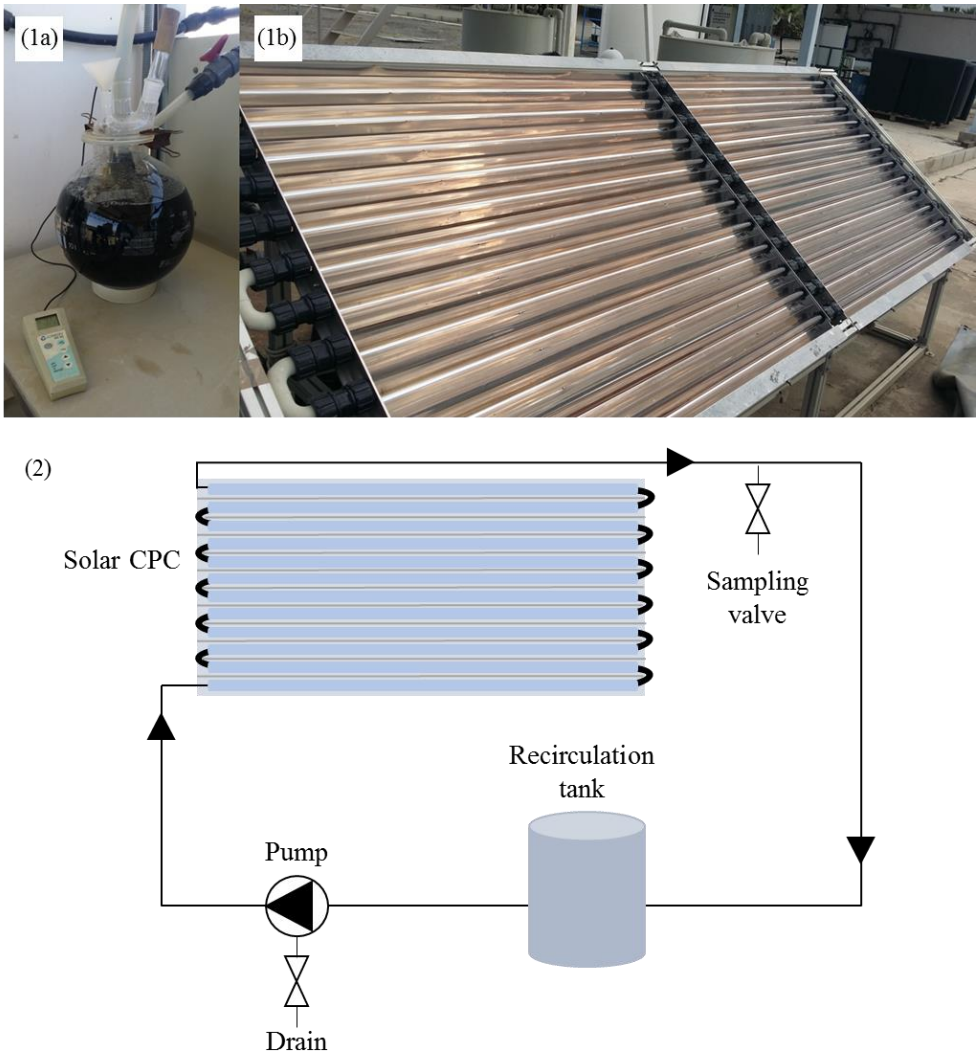

Fig. 3-5 Solar CPC pilot plant; photograph of the (1a) recirculation tank and (1b) solar collectors, (2) schematic of the plant (Plataforma Solar de Almería, Spain).

3.4 Photo-Fenton process intensified by ferrioxalate complexes and persulfate oxidising agents under LED irradiation

3.4.1 Materials

Antipyrine (AP; 99% purity, CAS No. 60-80-0) was obtained from Acros Organics. $FeSO_4 \cdot 7H_2O$, $Na_2S_2O_8$, $H_2C_2O_4 \cdot 2H_2O$ and *tert*-butyl alcohol were purchased from Panreac. H_2O_2 (30% w/v) was obtained from Merck and methanol from Sigma-Aldrich.

3.4.2 Photocatalytic experiments

Experiments were performed in the batch-operated, UVA-LED reactor, described in paragraph 3.2.2 (Fig. 3-2a). In a typical run, 150 mL of tap water (TOC = 1 ± 0.1 mg/L), adjusted at pH 2.8 with H_2SO_4, were introduced into the photoreactor. Prescribed amounts of Fe, $S_2O_8^{2-}$, $H_2C_2O_4$, H_2O_2, and AP were then added and photo-Fenton process was initiated by turning on the UVA-LED. In all experiments, the initial concentration of AP was 50 mg/L (TOC = 35 mg/L). At regular time intervals, samples were withdrawn and immediately treated with excess Na_2SO_3 to quench the residual H_2O_2 and prevent further oxidation. Quantofix peroxide test sticks (1-100 mg/L, Sigma-Aldrich) were used to ensure complete neutralisation of H_2O_2. Samples were then filtered through 0.2 μm nylon syringe filters (Fisherbrand) to remove catalyst particles and analysed in terms of their AP and TOC concentrations, as described in paragraphs 3.5.1 and 3.5.3. Dissolved oxygen concentration was

monitored throughout the experiment. All experiments were conducted at room temperature (22 ^{0}C).

Additional experiments were carried out in the presence of radical scavengers, namely *tert*-butyl alcohol and methanol, to evaluate the contribution of hydroxyl radicals to AP mineralisation. For this purpose, solution of 1M *tert*-butyl alcohol or methanol was used.

3.5 Analytical techniques and Protocols

3.5.1 Saccharin, bisphenol-A, and antipyrine concentrations

SAC, BPA, and AP concentrations in filtrate samples were measured by a high performance liquid chromatography (HPLC) system (S200 Pump, S225 Autosampler, Perkin Elmer) coupled with a diode array detector (S200 EP, Perkin Elmer). The methods for SAC and BPA measurement were obtained from Trandafir et al. (2009) [311] and Frontistis et al. (2011) [312], respectively, and appropriately modified. In Chapter 7, the concentration of SAC was measured using SAC(ii) method, adopted from Trovo et al. (2009) [313]. The method for AP measurement was obtained from Expósito et al. (2017) [314]. Separation was performed on a reverse phase C18 analytical column (Luna Phenomenex 5u, 250 x 4.6 mm) in isocratic elution mode. The applied chromatographic conditions for each organic compound are described in Table 3-2 and the established calibration curves are presented in Fig. 3-6.

Table 3-2 HPLC parameters for the measurement of SAC, BPA, and AP concentrations.

Parameter	SAC	BPA	AP
Eluent composition, v/v	(i) A - 0.02M KH_2PO_4 B - CH_3CN A:B – 85:15 *or* (ii) A - 0.1% CH_2O_2 B - CH_3CN A:B – 90:10	A - UPW B - CH_3CN A:B – 35:65	A - 0.1% CH_3COOH B - CH_3OH A:B – 40:60
Flow rate, mL/min	1	1	0.6
Injection volume, µL	40	40	20
Detection wavelength, nm	216	225	286
Retention time, min	7.3 *or* 4.3	4.4	6.2
LOQ[a], µg/L	10 *or* 160	50	1000

[a]LOQ: limit of quantification

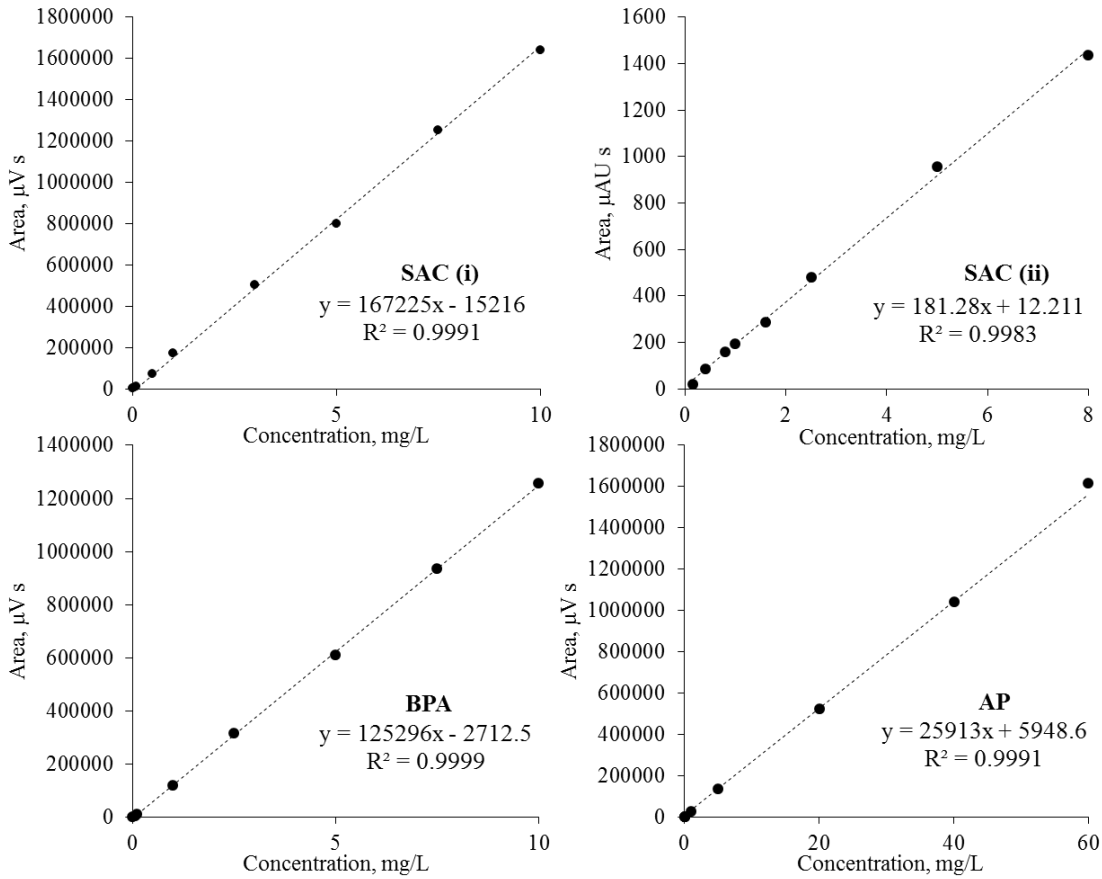

Fig. 3-6 Calibration curves of SAC, BPA, and AP established for HPLC analysis.

3.5.2 Identification of transformation products

A Bruker micrOTOF Focus II interfaced to a Dionex (Thermo Scientific) Ultimate 3000 Ultra-HPLC (UHPLC) system was used for the identification of SAC TPs in Chapter 5. Chromatographic separation was performed using a Thermo Scientific Acclaim™ RSLC 120 C18 column thermostated at 30 °C. The mobile phase consisted of liquid chromatography mass spectrometry (LC-MS) grade water – 0.01% formic acid (A) and LC-MS grade acetonitrile (B) with a flow rate of 0.25 mL/min. The following elution was adopted: A:B – 99:1 (0 min), A:B – 1:99 (15 min), A:B – 99:1 (17 min), A:B – 99:1 (18 min). The micrOTOF Focus II was operated in negative ionization mode. Dry gas at 8 L/min, nebulizer press at 2.4 bar, dry heater at 200 °C, hexapole RF at 100 Vpp and capillary were adjusted at 4200 V. The analysis was carried out by Dr Maria Antonopoulou at the Department of Environmental & Natural Resources Management, University of Patras (Greece).

For the identification of SAC TPs in Chapter 7, LC-MS analysis was performed using an UHPLC Agilent 1260 Infinity system (Agilent Technologies, USA) coupled with a high resolution quadrupole time-of-flight mass spectrometer (HR-QTOF-MS), Triple TOF 5600+ System (AB SCIEX, Concord, ON, Canada). The chromatographic separation was performed using an Agilent Zorbax Eclipse Plus C18 (3 x 150 mm, 5µm) analytical column. The mobile phases Milli-Q water with 0.1% formic acid (A) and acetonitrile (B) were eluted with a linear gradient starting with 10% B (2 min), increasing to 100% B in 15 min, where it was held for 3 min before the post-column re-equilibration of 2 min. The flow rate was fixed at 0.5 mL/min and the injection volume was 50 µL.

The LC system was connected to the HRMS by a DuoSpray™ ion source, used in negative electrospray ionisation (ESI) mode. The equipment worked via TOF-MS survey scan followed by IDA (Information Dependent Acquisition). Scanned mass range was from m/z = 50 to 600 Da. IDA criteria considered dynamic background subtraction and, for MS/MS fragmentation for the four most intense ions, a collision energy of 30 ± 15 V spread was used. Accurate mass measurements of each peak were obtained with an automated calibrant delivery system (CDS) using 0.3 mL/min of negative calibrating solution (AB Sciex). The calibration of the HRMS system was done daily and automatically after five injections. Three AB Sciex software packages (Analyst® TF 1.7.1, PeakView® 2.2, MasterView® 1.1) were used to process the HRMS data files and for TPs identification. The analysis was carried out by Miss Ana Belén Martínez at the Department of Analytical Chemistry, University of Almería (Spain).

3.5.3 Total organic carbon concentration

TOC was measured with a Shimadzu TOC-V_{CPH} analyser in the non-purgeable organic carbon (NPOC) mode. Prior to analysis, the sample was acidified with 2M HCl and sparged with N_2 to remove inorganic carbon. The sample then underwent combustion through heating to 680 °C inside a combustion tube filled with platinum catalyst in an oxygen-rich environment. The generated CO_2 was detected by an infrared gas analyser (NDIR).

3.5.4 Iron concentration

The concentration of total dissolved iron in Chapter 7 was estimated spectrophotometrically after complexation with 1,10-phenanthroline according to ISO 6332. According to this method, Fe^{2+} forms a stable orange-red coloured complex with 1,10-phenanthroline, the absorbance of which at 510 nm is proportional to Fe^{2+} concentration. Total iron concentration can be determined spectrophotometrically at 510 nm after Fe^{3+} reduction to Fe^{2+} with ascorbic acid. Finally, Fe^{3+} concentration can be calculated as the difference between total iron and Fe^{2+} concentrations.

3.5.5 Hydrogen peroxide concentration

The concentration of H_2O_2 in Chapter 7 was determined spectrophotometrically using titanium(IV) oxysulfate following DIN 38402H15 Standard. In this method, H_2O_2 forms a stable yellow coloured complex with titanium(IV) oxysulfate according to reactions (3-1) and (3-2) whose absorbance at 410 nm is proportional to H_2O_2 concentration.

$$TiOSO_4 + 5H_2O \rightarrow [Ti(OH)_3(H_2O)_3]^+ + HSO_4^- \qquad (3-1)$$

$$[Ti(OH)_3(H_2O)_3]^+ + H_2O_2 \rightarrow [Ti(O_2)(OH)(H_2O)_3]^+ + 2H_2O \qquad (3-2)$$

In Chapter 8, Quantofix peroxide test sticks (1-100 mg/L, Sigma-Aldrich) were used to ensure complete neutralisation of the residual H_2O_2 after Na_2SO_3 addition.

3.5.6 pH and dissolved oxygen concentration

pH was measured with a HANNA HI 9025 pH meter and dissolved oxygen (DO_2) concentration was monitored with a Jenway 9200 DO meter.

3.5.7 Ecotoxicity assessment

Acute and chronic toxicities were evaluated by monitoring changes in the bioluminescence of the marine bacteria *Vibrio fischeri* in accordance with DIN EN ISO 11348-3. For this purpose, a commercial BioFix Lumi Luminescent kit was used. Prior to toxicity analysis, the pH of the samples was adjusted to 6 - 8 and the salinity to 2% NaCl. The toxicity was determined with a BioFix Lumi-10 (Macherey-Nagel) luminometer and the data, as presented in this study, are based on the bioluminescence inhibition observed at 30 min and 24 h.

3.5.8 Photon flux measurement

The photon flux of UVA-LED and UVA-BL light sources, received by the reactant solution, was determined by potassium ferrioxalate actinometry, as described by Murov [310]. The method is based on Fe^{3+} reduction to Fe^{2+} upon UV-vis illumination (250 - 577 nm) of sulfuric acid solutions of $K_3Fe(C_2O_4)_3$, according to the following reaction:

$$2Fe^{3+} + C_2O_4^{2-} + h\nu \rightarrow 2Fe^{2+} + 2CO_2 \qquad (3-3)$$

The concentration of Fe^{2+} is determined spectrophotometrically by measuring the absorbance of the red-coloured complex that Fe^{2+} forms with 1,10-phenanthroline at 510 nm [315]. It should be noted that chemical actinometry gives an approximation of the radiation received by the solution and does not account for the loss of photons due to scattering phenomena [316].

3.5.9 Light intensity and spectral irradiance distribution

The light intensity and spectral distribution of UVA-LED and UVA-BL light sources were acquired by a Labsphere spectral irradiance receiver head (E1000) with a concentrator area of 1 cm^2. The distance between the receiver head and the irradiation source was set at 8 cm (i.e. the distance between UVA-LED or UVA-BL and the surface of the reactant mixture). More information about the analysis can be found at Tsonev et al. (2015) [317]. The spectral irradiance of UVA-LED relatively to UVA-BL can be seen in Fig. 3-7. The irradiance of UVA-LED and UVA-BL was estimated to be 1005 and 22.49 W/m^2, respectively. The analysis was carried out by Dr John Fakidis at the Li-Fi R&D Centre, University of Edinburgh (UK).

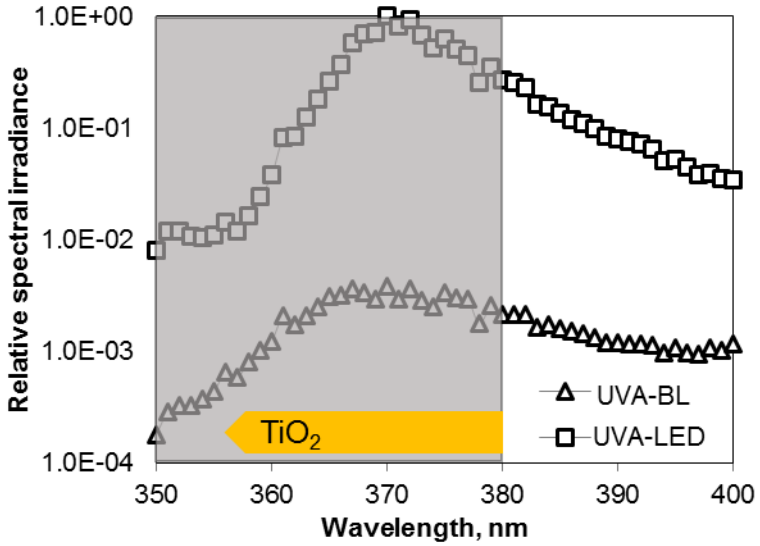

Fig. 3-7 Relative spectral irradiance of UVA-LED and UVA-BL irradiation sources and the action spectra of TiO_2 P25 catalyst (in grey).

3.5.10 Catalyst characterisation

To characterise the novel catalysts used in Chapter 4, X-ray diffractograms (XRD) were obtained by a Bruker D8 using Co $K\alpha_1$ radiation, λ = 1789 Å and a scintillation

counter. The rutile ratio was calculated according to the law $X_R = I_R(110) / (0.884 * I_A(101) + I_R(110))$ [318], with $I_R(110)$ and $I_A(101)$ being the integrated intensity of rutile (110) peak and anatase (101) peak, respectively, after signal deconvolution. The specific surface area was measured by nitrogen gas adsorption at 77K with an ASAP2000 instrument from Micromeritics. Transmission Electron Microscopy (TEM) was performed on a TECNAI 20F. The characterisation of the catalysts was carried out at the Materials Centre, MINES ParisTech (France).

3.5.11 Central composite experimental design

In Chapter 8, a CCED was applied to investigate the joint effects of the initial concentrations of H_2O_2, Fe^{2+}, $H_2C_2O_4$, and $S_2O_8^{2-}$ on the degradation and mineralisation of AP. The applied CCED consists of three experimental series [298]:

(i) a factorial design with 2^k trials (all the possible combinations of the codified values (+1) and (-1)), which in the case of $k = 4$ factors consists of 16 experiments (experiments 1 – 16, Table 8-1),

(ii) selection of the axial distance of the star points (codified values $a = [2^k]^{1/4} = 2$) consisting of $2k = 8$ experiments (experiments 17 – 24), and

(iii) replicates of the central point (experiments 25 – 27).

The design also involves an experiment at the optimal conditions (experiment 28). Furthermore, two experiments (29, 30) were performed at the optimal conditions in the presence of radical scavengers to evaluate the contribution of hydroxyl radicals to AP degradation. Table 8-1 presents the complete CCED and additional experiments performed to obtain the optimal conditions, as well as the levels of the variables and the obtained response functions values. The CCED matrix was designed by Prof José

María Monteagudo at the Department of Chemical Engineering, University of Castilla-La Mancha (Spain).

3.5.12 Neural network strategy

The experimental results obtained by the CCED were fitted by using a NN. In detail, the NN, graphically displayed in Fig. 3-8, was employed to simulate AP degradation and mineralisation during UVA-LED photo-Fenton process. A linear basis function (linear combination of inputs, Xj, and weight factors, Wji) was used to determine the effect of the input variable i on the neuron j:

$$U_i = \sum_{j=1}^{n} W_{ji} X_j \qquad (3-4)$$

The NN was solved with two neurons, using a sigmoid transfer function. A solution strategy based on a back-propagation algorithm was used for training purposes [305, 319]. Parameters were fitted using the Solver tool in a custom spreadsheet in Microsoft Excel using a non-linear fitting method. The input variables and the chosen response functions were the same as in the CCED described in paragraph 3.5.11 and are presented in Fig. 3-8. The equation and parameters obtained by the NN fitting were plotted with the use of ORIGIN software. Furthermore, the relative importance of each input variable was determined by a saliency analysis, based on the connection weights of the neural networks. The saliency analysis was performed according to Garson's model [320] using:

$$I_j = \frac{\sum_{m=1}^{m=N_h} \left(\left(\left| W_{jm}^{ih} \right| / \sum_{k=1}^{N_i} \left| W_{km}^{ih} \right| \right) \times \left| W_{mn}^{ho} \right| \right)}{\sum_{k=1}^{k=N_i} \left\{ \sum_{m=1}^{m=N_h} \left(\left| W_{km}^{ih} \right| / \sum_{k=1}^{N_i} \left| W_{km}^{ih} \right| \right) \times \left| W_{mn}^{ho} \right| \right\}} \qquad (3-5)$$

where I_j is the relative importance of the j^{th} input variable on the output variable; N_i and N_h are the numbers of input and hidden neurons, respectively; W is the connection weight, superscripts i, h, and o refer to input, hidden, and output layers, respectively; and subscripts k, m, and n refer to input, hidden, and output neurons, respectively. It should be noted that the NN in this study is used only as an interpolation function. Further details about the NN applied can be found in Durán et al. (2006) [321]. NN simulations were carried out by Dr Antonio José Expósito at the Department of Chemical Engineering, University of Castilla-La Mancha (Spain).

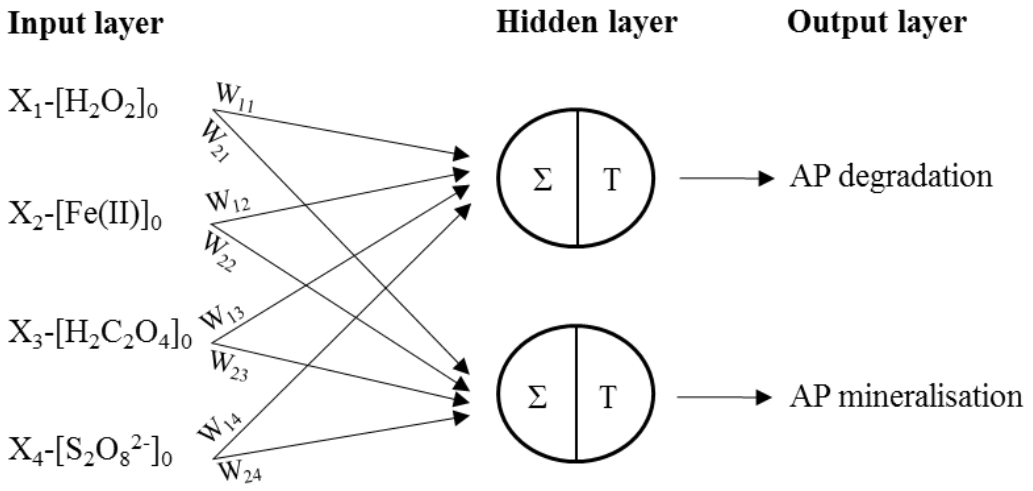

Fig. 3-8 Structure of the feed-forward NN with a single hidden layer containing two neurons.

3.5.13 Photocatalytic performance

In this work, the photocatalytic performance was evaluated in terms of removal efficiency, reaction kinetics, photonic and energy efficiencies as follows.

a- Removal efficiency

The removal efficiency was calculated using:

$$SAC, BPA\ or\ AP\ removal\ (\%) = \frac{C_i - C_f}{C_i} 100 \qquad (3-6)$$

where C_i and C_f are the initial and final concentrations (mg/L) of the selected EM.

$$TOC\ removal\ (\%) = \frac{TOC_i - TOC_f}{TOC_i} 100 \qquad (3-7)$$

where TOC_i and TOC_f are the initial and final concentrations (mg/L) of TOC.

$$Toxicity\ removal\ (\%) = \frac{BioL_i - BioL_f}{BioL_i} 100 \qquad (3-8)$$

where $BioL_i$ and $BioL_f$ are the initial and final values of bioluminescence (BioL) of the marine bacteria *Vibrio fischeri*.

b- Kinetic evaluation

In Chapters 4, 5 and 8, the removal rate is expressed as a function of treatment time. In Chapter 7, the photocatalytic removal of SAC is presented as a function of accumulated UV energy, Q_{UV}, which is calculated using Eq. (3-9). Q_{UV} is used instead of time in order to compare the efficiency of the solar simulator and solar CPC pilot plant (i.e. reactors of different geometry and size) and to include the daily variation of solar irradiation in the CPC pilot plant.

$$Q_{UV,n+1} = Q_{UV} + \Delta t_n \cdot \overline{UV}_{G,n+1} \cdot \frac{A_i}{V_T};\ \Delta t_n = t_{n+1} - t_n \qquad (3-9)$$

where Q_{UV} (kJ/L) is the accumulated UV energy per unit of volume, $\overline{UV}_{G,n+1}$ (W/m^2) is the average solar UV radiation ($\lambda < 400$ nm) measured between t_{n+1} and t_n, A_i (m^2) is the illuminated area and V_T (L) is the total volume of the reactor. In the solar simulator, UV irradiance was constant at 35 W/m^2.

In Chapters 4 and 5 the Langmuir-Hinshelwood (L-H) kinetic model was found to describe well the photocatalytic removal of SAC and BPA assuming pseudo-first-order kinetics with respect to substrate concentration:

$$r = -\frac{dC}{dt} = \frac{k_r KC}{1 + KC} \qquad (3-10)$$

When the substrate concentration and its adsorption onto catalyst are relatively low (as in this study), Eq. (3-10) can be reduced to:

$$-\frac{dC}{dt} = kKC = k_{app}C \leftrightarrow ln\frac{C_0}{C} = k_{app}t \qquad (3-11)$$

where k_{app} (min^{-1}) is a pseudo-first-order kinetic constant.

In Chapter 7, the degradation of SAC was found to fit well with first-order degradation kinetics:

$$C = C_0 e^{-kQ_{UV,n}} \qquad (3-12)$$

or formulated as:

$$\ln\frac{C}{C_0} = -kQ_{UV,n} \qquad (3-13)$$

where k (L/kJ) is an apparent reaction rate constant.

In Chapter 8, the degradation of AP followed pseudo-first-order kinetics with respect to substrate concentration:

$$r = -\frac{dC}{dt} = k_{AP}C \leftrightarrow ln\frac{C_0}{C} = k_{AP}t \qquad (3-14)$$

where k_{AP} (min^{-1}) is a pseudo-first-order kinetic constant.

In all cases, the plot of normalised substrate concentration against treatment time or accumulated UV energy resulted in straight lines with the coefficient of linear fitting, r^2, always being ≥ 0.834. From the slopes of the resulting lines, k_{app}, k or k_{AP} values were computed. For consistency purposes, a reference point was selected for the computation of k_{app}, k or k_{AP} in each chapter. This was the common treatment time of all the experimental runs with substrate degradation < 99.9% (i.e. t = 20 min in Chapters 4 and 5, except for the runs with C_0 = 2.5 mg/L in which the selected t was reduced to 10 min; t = 10 min in Chapter 8). In Chapter 7, the computation of k was based on Q_{UV} = 1.5 - 2.3 kJ/L for conventional photo-Fenton, Q_{UV} = 0.28 - 0.54 kJ/L for EDDS-assisted photo-Fenton, and Q_{UV} = 1.72 - 3.22 kJ/L for OMW-assisted photo-Fenton due to the wide variability of process kinetics.

c- Photonic efficiency

Photonic efficiency, ζ, is another way to evaluate photocatalytic performance. It is determined as the ratio of the initial rate of substrate degradation to the rate of the incident photons reaching the reactor (obtained by actinometry) [322].

$$\zeta(\%) = \frac{rate\ of\ reaction\ \left(\frac{M}{s}\right)}{incident\ photon\ flux\ \left(\frac{Einstein}{L \cdot s}\right)} 100 \qquad (3-15)$$

In Chapter 6, the calculation of ζ is based on the reaction rates, k_{app}, obtained for t = 20 min for ANA/UVA and R30/UVA systems and t = 10 min for TiO_2/UVA-LED and TiO_2/UVA-BL systems.

d- Energy efficiency

The energy consumption of UV-LED and UVA-BL light sources was estimated by figures-of-merit, developed to evaluate the energy efficiency of electric-energy-driven

AOPs. Bolton et al. (2001) introduced the electric energy per order, E_{EO}, defined as the energy required for 90% degradation of a pollutant per cubic meter of contaminated water [323]. The E_{EO} (kWh/m^3/order) for a batch-operated photoreactor is calculated using:

$$E_{EO} = \frac{P \times t \times 1000}{V \times 60 \times \log\left(C_i / C_f\right)} \qquad (3-16)$$

where P is the power of the irradiation source (kW), t is the irradiation time (min), V is the volume of the treated effluent (L), and C_i and C_f are the initial and the final pollutant concentrations (mg/L). In Chapter 6, C_f is the concentration of SAC or BPA at: t = 90 min for ANA/UVA, R30/UVA, and SAC/TiO_2/UVA-BL systems; t = 20 min for TiO_2/UVA-LED system: and t = 120 min for BPA/TiO_2/UVA-BL system.

3.5.14 Standard error

The presented results are subject to approximately 5% standard error, as estimated by experimental duplicates using [298]:

$$SE_{\bar{y}}(\%) = \frac{s}{\sqrt{n}} 100 \qquad (3-17)$$

where $SE_{\bar{y}}$ is the standard error of the mean, s is the standard deviation of the mean, and n is the number of replicate experiments.

4 TiO_2-mediated treatment under UVA irradiation in the presence of nanocomposites tuned by Sn(IV)

4.1 Introduction

A way to enhance the photocatalytic activity of TiO_2 anatase is to improve the charge separation and migration to the catalyst surface by means of interfaces with semiconductor or metallic particles [138, 140]. In addition to material modification, the control of nano-architecture and morphology is another method to enhance catalyst performance [148]. Therefore, a combination of these two levers (i.e. creating interfaces between anatase and rutile polymorphs) could be a key asset to improve photocatalytic performance. In general, homogeneous precipitation by thermohydrolysis of acidic Ti(IV) precursors offers an easy approach by which to produce titania nanoparticles, yet the control of anatase: rutile ratio is rather difficult to master and it is very sensitive to physicochemical conditions [149, 324, 325]. To obtain anatase–rutile interfaces, co-precipitating anatase and rutile in a single pot by thermohydrolysis can, therefore, be a challenging task, especially if one wants to tune anatase: rutile ratio with small and controlled amounts of metals that act as rutile phase promoters. In this work a direct approach, just by hydrolysing as-received commercial products without additives nor surfactants, is proposed to produce interfaced anatase-rutile photocatalysts tuned by Sn(IV).

The obtained anatase-rutile nanocomposites were then used as catalysts to improve the photocatalytic degradation of SAC and BPA under UVA irradiation. The effect of key operating parameters, such as initial substrate concentration, anatase: rutile ratio,

catalyst concentration, and treatment time on photocatalytic performance was assessed. Furthermore, the catalytic activity of the newly synthesized nanocomposites on repeated use was studied and the effect of ultrasound cleaning on catalyst performance was evaluated.

This study proposes a novel method for the synthesis of interfaced anatase-rutile photocatalysts and further investigates the photocatalytic potential of the synthesized materials for the treatment of EMs, such as SAC and BPA. The photocatalytic degradation of ASs is a new topic and to the author's knowledge, only Chen et al. (2013) have dealt with the photocatalytic degradation of SAC to date [236]. However, the investigation of the optimal operating parameters of a UVA/TiO_2 system, as described in this study, still remains a missing element in the open literature.

4.2 Results and Discussion

4.2.1 Catalyst characterisation

The specific surface areas of pure anatase (ANA), 15% rutile (R15), and 30% rutile (R30) catalyst samples were 197, 201, and 172 m^2/g, respectively, with the corresponding equivalent spherical diameters being 7.8, 7.6, and 8.9 nm (see paragraph 3.5.10 for catalyst characterisation). These relatively small particle sizes suggest a low particle growth step after nucleation during thermohydrolysis with well-crystallised particles, contrary to other methods requiring calcination. XRD characterizations for the produced TiO_2 nanocomposites are shown in Fig. 4-1, where it is clear that Ti(IV) thermohydrolysis in sulfuric medium yields pure anatase particles. Furthermore, XRD analysis of R15 and R30 samples, described in 3.5.10, shows that the incorporation of

a small amount of Sn^{4+} in the crystal lattice is sufficient to induce considerable rutile crystallisation, revealed by the emergence of (110), (101), and (111) peaks. The incorporation of Sn^{4+} ions into TiO_2 lattice inducing rutile crystallisation is further evidenced by the lack of a peak indicating SnO_2 crystallisation.

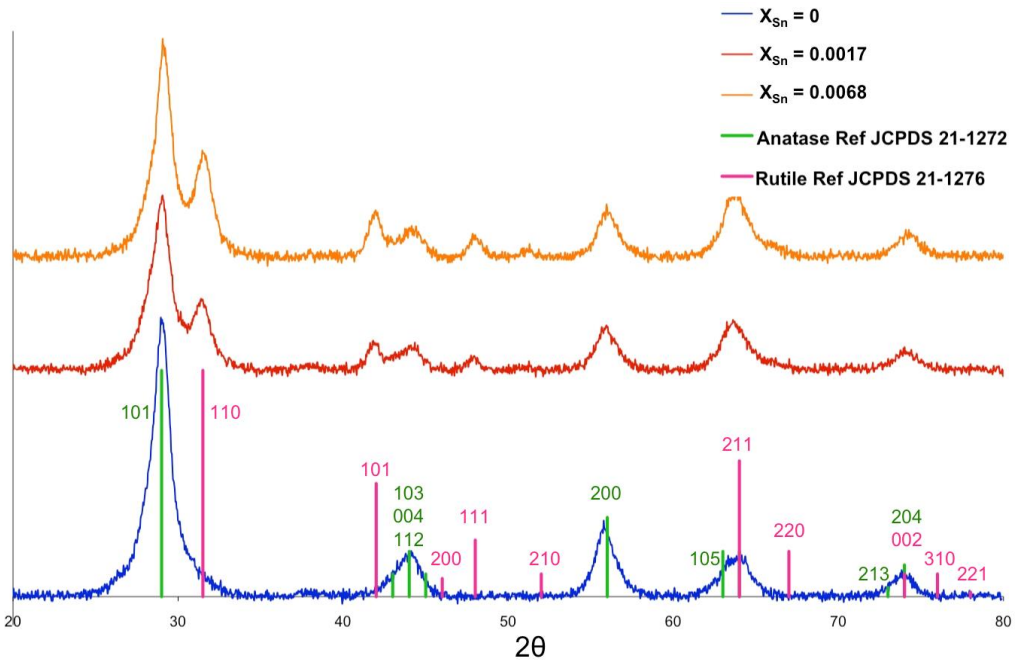

Fig. 4-1 XRD measurements obtained for synthesized particles ANA (X_{Sn} = 0 mol/L), R15 (X_{Sn} = 0.0017 mol/L), and R30 (X_{Sn} = 0.0068 mol/L). X_{Sn} is the amount of Sn^{4+} measured in the solid phase.

Finally, TEM observations (Fig. 4-2) indicate that nanocrystals are largely agglomerated and form spherical substructures of around 100 nm size. In addition to the specific surface area values, these observations suggest that the synthesised structures are porous agglomerates. At higher magnification, it can be also seen that reticular plans are highly oriented between neighbour nanocrystals. The main characteristics of the synthesized catalysts are summarised in Table 4-1.

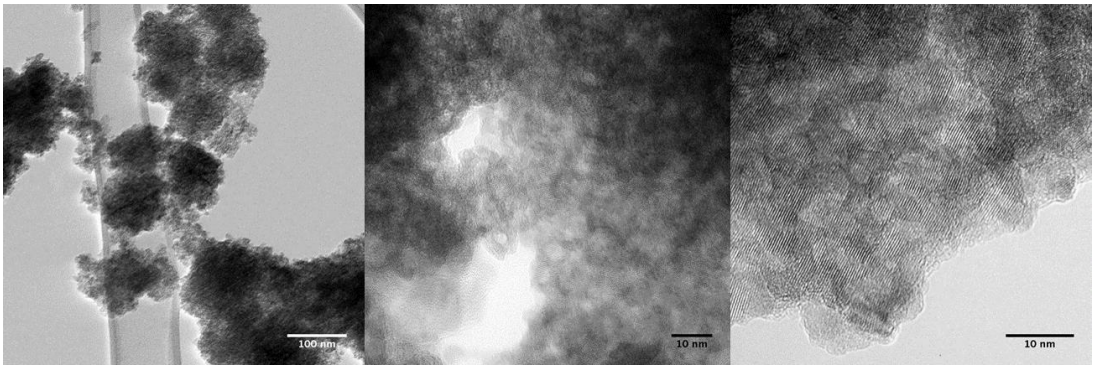

Fig. 4-2 TEM observations of the synthesized anatase-rutile nanocomposites.

Table 4-1 Characteristics of the synthesized catalysts.

Catalyst	Crystal phase	Particle size, nm	Surface area, m^2/g
ANA	Anatase	7.8	197
R15	Anatase: rutile-85:15	7.6	201
R30	Anatase: rutile-70:30	8.9	172

4.2.2 Evaluation of photocatalytic activity

Control experiments were performed under UVA irradiation (photolysis) to assess the effect of catalyst presence on process efficiency. Photolysis was found to be an important removal mechanism for both compounds, as can be seen in Fig. 4-3.

To evaluate the relative activity of the prepared catalysts ANA, R15, and R30, preliminary experiments were carried out at 5 mg/L SAC or BPA initial concentration in the presence of 50 mg/L catalyst concentration. Commercially available photocatalysts, P25, KR7050, and PC105, were also employed, at the same operating conditions, for comparative purposes. As can be seen in Fig. 4-3, the highest SAC and BPA photocatalytic removal (i.e. 98 and 99%, respectively) was obtained when P25 was used as the catalyst. 67% of SAC and 38% of BPA were removed in the presence

of PC105, whereas KR7050 resulted in 43% degradation of both organics within 90 min of photocatalytic treatment (data not shown). ANA, R15, and R30, yielded similar efficiencies with each other (Fig. 4-3). In detail, their performance ranged from 21 to 27% and from 22 to 25% in terms of SAC and BPA removal, respectively, indicating that, under the experimental conditions applied, anatase-rutile interfaces do not affect SAC or BPA degradation.

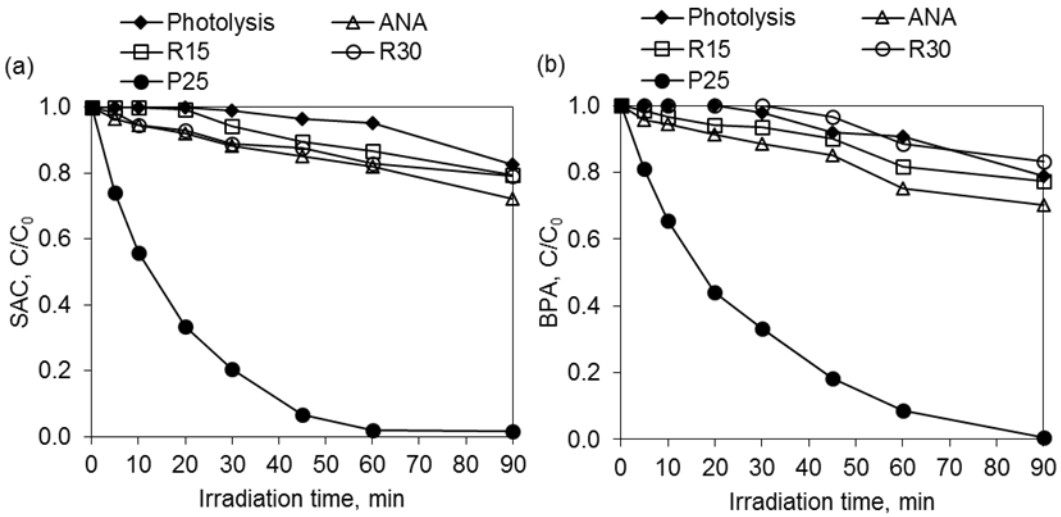

Fig. 4-3 (a) SAC and (b) BPA removal during photolysis and UVA photocatalytic treatment in the presence of different catalysts (C_0 = 5 mg/L, [catalyst] = 50 mg/L).

This is in contrast to Pichavant et al. (2014), who examined the photocatalytic treatment of phenol in the presence of such catalysts, and found that anatase–rutile interfaces could affect process efficiency [149]. Pichavant et al. achieved complete degradation of phenol (C_0 = 7.5 mg/L) within 90 min of treatment in the presence of 400 mg/L of 15% rutile, while the corresponding removal with the use of pure anatase and 30% rutile was reduced to 75 and 80%, respectively. Also, Fresno et al. (2009) investigated the gas-phase photocatalytic degradation of trichloroethylene in the presence of $Ti_{1-x}Sn_xO_2$ catalysts [326]. Sn^{4+} addition was found beneficial to TiO_2

activity, owing to the formation of anatase–rutile mixtures. Fresno et al. obtained the highest photocatalytic activity in the presence of the catalyst with composition $Ti_{0.93}Sn_{0.07}O_2$, characterised by an anatase: rutile ratio close to 3.

Additional experiments were carried out in the dark to assess the adsorption behaviour of ANA, R15, R30, and P25 catalysts. The results, presented in Fig. 4-4, suggest that there is no any correlation between the adsorption capacity of the catalysts and their photocatalytic activity under the experimental conditions applied. For instance, P25, which led to the highest photocatalytic removal of both organics, has low adsorption capacity (i.e. 3% for BPA and 0.8% for SAC) that is very close to those of ANA, R15, and R30 catalysts. Moreover, BPA was found to be adsorbed slightly more than SAC onto catalyst surface explained by its higher LogKow (3.32 for BPA, 0.91 for SAC) [110] and higher molecular weight (228.29 g/mol for BPA, 183.18 g/mol for SAC) [311] compared to SAC, given that the remaining experimental parameters were unchanged. From Fig. 4-4 it also becomes evident that the increased adsorption of BPA onto catalyst surface does not translate into higher photocatalytic degradation, thus explaining the need to assess process efficiency on a case-by-case basis for individual compounds due to the complex chemical reactions involved [17].

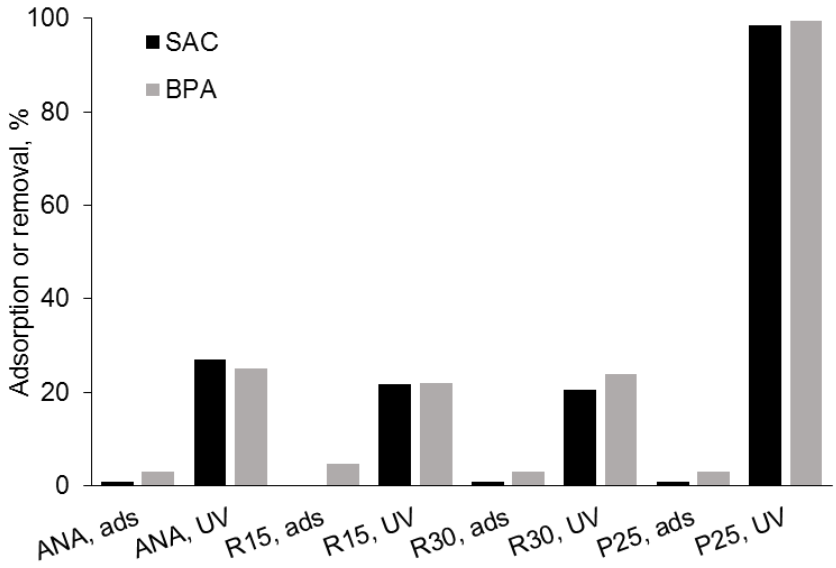

Fig. 4-4 SAC and BPA removal, in the presence of different catalysts, during adsorption (ads) in the dark and UVA photocatalytic treatment (UV) (C_0 = 5 mg/L, [catalyst] = 50 mg/L, treatment time = 90 min).

Considering the above findings and previously published works, which encourage the use of such type of materials as photocatalysts, it was decided to proceed with further experiments, to optimise the process and explore the capacity of these catalysts to eliminate SAC or BPA.

4.2.3 Effect of operating parameters

4.2.3.1 Effect of initial substrate concentration

Initial SAC or BPA concentration, in the range of 3 – 10 mg/L, was applied in the presence of 400 mg/L ANA or R30, respectively, to evaluate the effect of initial substrate concentration on photocatalytic performance. Fig. 4-5 indicates that an increase in the initial organic concentration, at a given catalyst loading, leads to decreased removal efficiency. In particular, the increase of SAC concentration from 3

to 10 mg/L resulted in the gradual removal decrease from 88 to 52% (Fig. 4-5a). Likewise, BPA conversion rate decreased from 48 to 17% when the initial BPA concentration increased from 3 to 10 mg/L (Fig. 4-5b).

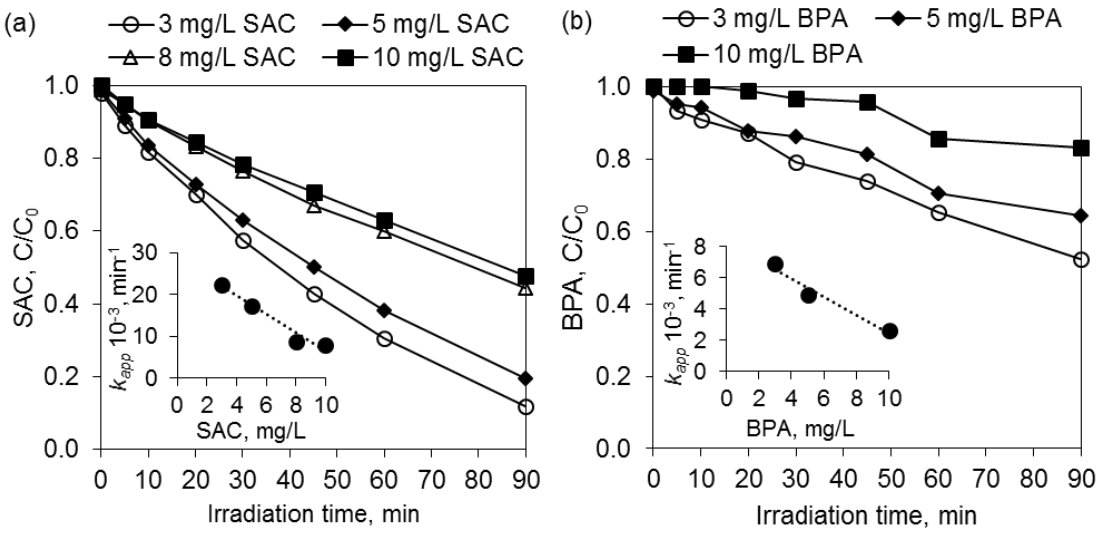

Fig. 4-5 Effect of initial (a) SAC and (b) BPA concentration on photocatalytic degradation. Inset graphs: relationship between k_{app} and initial (a) SAC and (b) BPA concentration ((a) [ANA] = 400 mg/L, (b) [R30] = 400 mg/L).

The L-H kinetic model was found to describe well the photocatalytic removal of SAC and BPA, following pseudo-first-order kinetics with respect to substrate concentration. The plot of normalised SAC and BPA concentration against irradiation time resulted in straight lines with the coefficient of linear fitting, r^2, ranging from 0.981 to 0.999 and 0.941 to 0.994, for SAC and BPA, respectively. From the slopes of the resulting lines, k_{app} values were computed. As can be seen in the inset graphs of Figs 4-5a and 4-5b, there is an almost linear relationship between k_{app} and the initial substrate concentration. For example, when the initial concentration of BPA is doubled (e.g. from 5 to 10 mg/L) k_{app} decreases almost two times from 0.0049 to 0.0026 min^{-1}. At a fixed catalyst concentration, efficiency is dictated by the ratio of catalyst active sites to organic molecules. At relatively low substrate concentrations, the active sites

provided by the semiconductor are in excess and can take up most of the organic molecules, thus resulting in higher removal rates. The gradual increase of the initial SAC or BPA concentration results in saturation of the limited catalyst surface by the organic molecules and their reaction by-products [128]. Therefore, the photonic efficiency of the system is negatively affected and lower degradation rates are obtained, explaining the above findings.

Several studies have demonstrated the evolution of toxic TPs during the photocatalytic treatment of ASs and BPA [215, 327]. Calza et al. (2013) evaluated the ecotoxicity of SUC solutions treated by heterogeneous photocatalysis. The authors observed that toxicity increased during treatment due to the formation of TPs more toxic than the parent compound [215]. Similarly, Kondrakov et al. (2014) studied the TiO_2-mediated photocatalytic degradation of BPA during which they identified potentially genotoxic by-products [327]. SAC and BPA mineralisation was therefore monitored, at the best-assayed conditions (C_0 = 3 mg/L; catalyst = 400 mg/L), to obtain an indication of the formation of potentially hazardous by-products. Results showed that TOC decreased 54 and 43% after 90 min of SAC and BPA photocatalytic treatment, respectively. Discrepancies between the concentration of TOC and parent compounds (i.e. SAC, BPA) were observed, indicating the formation of organic TPs during treatment. In specific, SAC degradation was 88% while TOC removal was only 54% after 90 min of treatment. Similarly, when BPA degradation was 48%, TOC was removed by 43%. It should be noted that although BPA degradation is almost the half of SAC (48% for BPA, 88% for SAC), the mineralisation of BPA (43%) is comparable to that of SAC (54%), implying possibly the formation of more easily degraded by-products during the photocatalytic treatment of BPA relatively to that of SAC.

4.2.3.2 Effect of catalyst concentration

To investigate the effect of catalyst concentration on process efficiency, several TiO_2 concentrations (i.e. 50, 200, 400, and 600 mg/L) were examined for the photocatalytic degradation of 5 mg/L SAC or BPA. As can be seen in Fig. 4-6, although SAC degradation increased considerably with catalyst concentration, this was not the case for BPA.

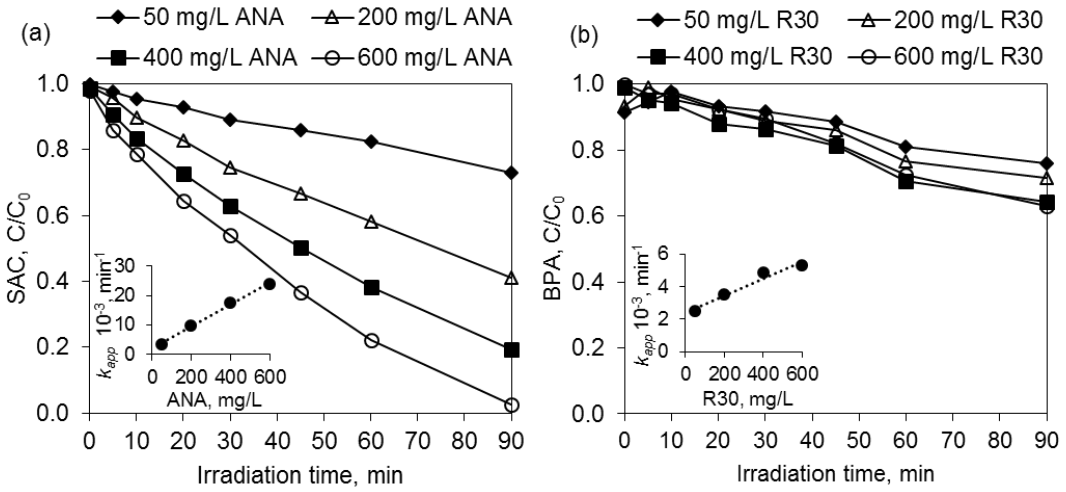

Fig. 4-6 Effect of catalyst concentration on the photocatalytic degradation of (a) SAC and (b) BPA. Inset graphs: relationship between k_{app} and catalyst concentration (C_0 = 5 mg/L, catalyst: (a) ANA, (b) R30).

In detail, SAC removal was 27, 59, 81, and 97% in the presence of 50, 200, 400 and 600 mg/L of ANA catalyst, respectively, and thus process efficiency was increased by 70% when catalyst concentration was increased from 50 to 600 mg/L (Fig. 4-6a). The relationship between k_{app} and catalyst concentration is almost linear; increase of ANA concentration in the range of 50 – 600 mg/L results in k_{app} increase from 0.0034 to 0.0238 min^{-1} (inset graph of Fig. 4-6a). These results are explained by the fact that at higher amounts of TiO_2 (i.e. surface area), the increased number of active sites result

in a higher photogeneration rate of oxidising species responsible for the photocatalytic oxidation [120]. BPA is affected to a smaller degree by the changes in catalyst concentration than SAC perhaps due to the reduced catalytic activity of R30 compared to ANA. During BPA degradation, increase of R30 concentration from 50 to 400 mg/L led to a 12% increase of process efficiency (Fig. 4-6b). Further increase of R30 from 400 to 600 mg/L did not improve the photocatalytic performance, as can be seen in Fig. 4-6b. A possible explanation for this arises from the screening effects associated with catalyst concentration above a certain point, which seems to be around 400 mg/L for BPA; the excessive TiO_2 particles mask the photosensitive active sites and the removal efficiency becomes independent of catalyst mass [120]. The effect of catalyst overloading on BPA photocatalytic degradation can also be seen in the inset graph of Fig. 4-6b; k_{app} increases linearly from 0.0025 to 0.0049 min^{-1} up to 400 mg/L catalyst concentration. However, with a further increase of TiO_2 concentration to 600 mg/L, k_{app} remains almost unchanged (0.0053 min^{-1}).

4.2.3.3 Effect of catalyst reuse

Catalyst recovery and reuse may be a good practice to reduce the operational cost of photocatalysis and hence to promote its competitiveness among other processes for water and wastewater treatment [328]. In this sense, ANA catalyst was subjected to three successive reuse cycles to determine its efficiency for SAC treatment (for catalyst recovery and reuse methodology, see paragraph 3.1.4). As can be seen in Fig. 4-6, the photocatalytic performance was kept stable during the 1st and 2nd cycle with SAC removal being 81 and 84%, respectively. At the 3rd cycle, catalyst effectiveness dropped to 70%, explained by catalyst loss during the centrifugation recovery process

between reuse cycles. It should be noted that, at the end of the 3rd cycle, the residual catalyst was collected by membrane filtration and its concentration was found to be about 300 mg/L, instead of 400 mg/L which was the initial catalyst loading at cycle 1. Lower catalyst concentration implies fewer active sites for ROS photogeneration and therefore lower degradation rates, thus explaining the above result. Another possible explanation may be the depletion of TiO_2 active sites by residual unreacted SAC molecules and TPs formed during treatment, leaving less active sites available for photocatalytic oxidation [137, 329, 330]. However, this does not apply in this case because the obtained 70%, at cycle 3, is the expected SAC removal percentage in the presence of 300 mg/L ANA, based on the results shown in paragraph 'Effect of catalyst concentration', which are also presented in the inset graph of Fig. 4-7. The formation of free radicals and other ROS on catalyst surface is not affected at low organic concentrations or when TiO_2 reuse follows separation from the reactant solution [331, 332].

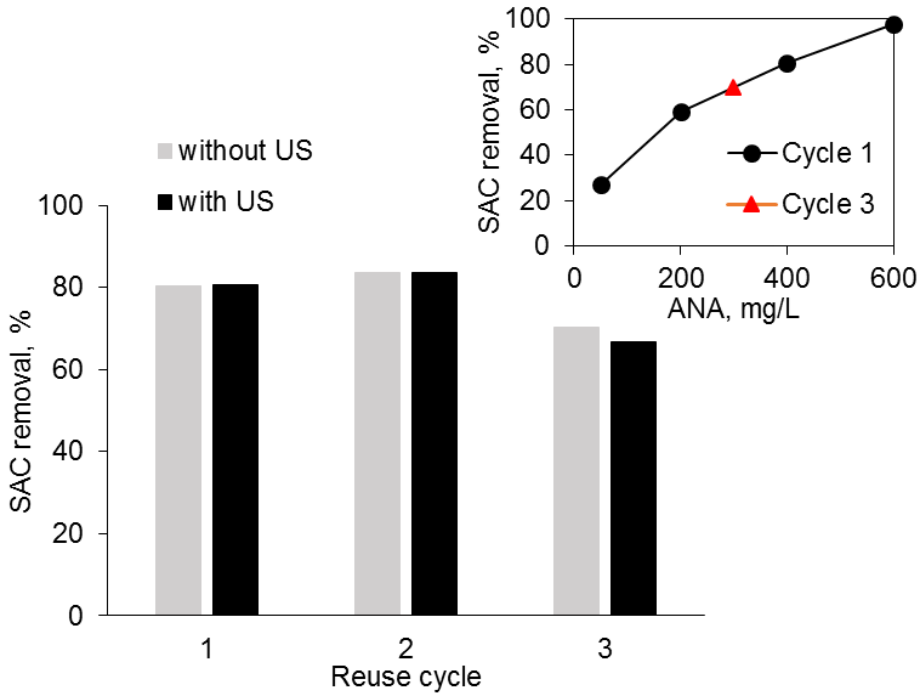

Fig. 4-7 Effect of catalyst reuse on the photocatalytic degradation of SAC (US: ultrasound cleaning) ($[SAC]_0$ = 5 mg/L, [ANA] = 400 mg/L at 1st cycle, treatment time = 90 min). Inset graph: photocatalytic removal of SAC as a function of ANA concentration after three consecutive catalyst reuse cycles ($[SAC]_0$ = 5 mg/L).

Additional catalyst reuse experiments were performed with the catalyst being subjected to ultrasound cleaning (US) before its further use (see paragraph 3.1.4) in order to determine the impact of US on catalyst activity (Fig. 4-7). It is well-known that US can remove impurities from the surface of heterogeneous metal catalysts, such as TiO_2, and bring the reactant materials into more intimate contact with the catalyst surface, improving the reaction rates. Also, US assists catalyst dispersion and emulsification and can, therefore, increase the available contact surface area, which enhances chemical reactions between the components of the emulsion [333]. In this case, however, it becomes clear from Fig. 4-7 that US did not improve process efficiency. SAC removal remained unchanged at 81 and 84% during the 1st and 2nd reuse cycles, respectively, while the removal at the 3rd cycle decreased by about 4%

compared to the respective experiments in the absence of US. This indicates that photocatalytic degradation takes place mainly through free radical and other ROS reactions and that catalyst agglomeration and presence of unreacted SAC molecules and TPs on catalyst surface are not limiting factors in the system under study. The negligible effect of US on process efficiency can be also attributed to catalyst loss, which was greater than in the absence of US, between reuse cycles. In particular, the residual catalyst concentration was estimated at about 200 mg/L at the end of the 3rd reuse cycle (i.e. 100 mg/L less than the residual catalyst in the corresponding experiment without US; the degree of agglomeration may be reduced by fracture in an ultrasonic field [333] and thus higher amounts of catalyst are lost through centrifugation and membrane filtration).

4.3 Conclusions

The photocatalytic treatment of saccharin (SAC) and bisphenol-A (BPA) was studied in the presence of interfaced anatase–rutile photocatalysts produced by thermohydrolysis using small amounts (< 1%) of Sn(IV) as a rutile phase promoter. The effect of key operating parameters, such as initial substrate concentration, catalyst type, concentration, and reuse, on photocatalytic performance was assessed and the conclusions drawn are summarised as follows:

- The photocatalytic efficiency of the novel TiO_2 nanocomposites was very similar with each other in terms of SAC or BPA degradation. Factors that most affected process performance were the initial substrate and catalyst concentration. Reaction rate constants increased when the initial substrate concentration was decreased and when the catalyst concentration was

increased up to 400 mg/L. Further increase of catalyst concentration to 600 mg/L did not improve BPA degradation due to masking effects ascribed to excessive catalyst particles. In all cases, SAC and BPA degradation was found to fit well with the pseudo-first-order L-H kinetic model. At the best-assayed conditions (C_0 = 3 mg/L, TiO_2 = 400 mg/L), the removal percentages for SAC and BPA were 88 and 48%, respectively, after 90 min of treatment.

- TOC measurement revealed the presence of transformation products after the end of treatment, thus indicating the need for eco-toxicity estimation before any further scaling-up of the process.
- Recycled catalyst was used in three successive cycles without losing much of its efficiency and thus yielding 70% SAC removal at the end of the 3rd cycle. Finally, ultrasound cleaning of the reactant mixture, at the beginning of each reuse cycle, did not improve removal efficiency.

All in all, the new catalysts showed good photocatalytic activity, which was maintained on repeated use.

5 TiO_2-mediated treatment under solar, LED, and conventional blacklight irradiation

5.1 Introduction

TiO_2-mediated photocatalysis is of special interest among other AOPs because sunlight, a free and plentiful renewable energy source, can be used as a photon source for catalyst activation [334]. Solar photocatalysis makes use of the near-UV band of the solar spectrum to excite TiO_2 catalyst [17]. When the available sunlight is inadequate, artificial irradiation is required. However, the energy-intensive blacklight fluorescent UVA lamps (UVA-BL) that are commonly used result in high operational cost and increased environmental impact, restraining the large-scale application of photocatalytic process [14]. To overcome this, UVA-LEDs can be used as eco-friendly alternatives to UVA-BL lamps.

UVA-LEDs were firstly employed by Chen et al. (2005) for the photocatalytic treatment of perchloroethylene [191] and since then LED-photocatalysis has been applied for the treatment of a wide range of contaminants. Lately, the development of LED photocatalytic reactors has attracted increasing attention; UV and visible LEDs of various irradiation wavelengths have been tested, in several configurations (i.e. flexible LED strips, LED arrays, single LEDs, etc.) and reactor set-ups (i.e. LEDs placed above, wrapped around, mounted on, immersed in the reactor, etc.) [172, 173, 192, 335, 336]. Some studies have also compared the efficiency of LEDs with germicidal and blacklight lamps in photocatalytic applications [194, 336-338]. However, the comparison has been usually made between irradiation sources of different electrical power or at reactor geometries optimised for U shaped lamps (i.e.

germicidal and blacklight lamps), without considering the optical characteristics of LEDs. The directional light output of LEDs affects dramatically the irradiation uniformity [335] and when LEDs are integrated within the reactor at a close distance from catalyst the non-uniform irradiation of the latter results in lower oxidation rates compared to blacklight lamps [338]. Therefore, a study evaluating a UVA-LED relative to a UVA-BL at a set-up providing uniform irradiation, at the same spectral irradiance, electrical power, and reactor geometry, in terms of organic removal, and under a variety of photocatalytic conditions is still missing from the literature.

The aim of this study is the investigation of the photocatalytic degradation of SAC and BPA under UVA irradiation emitted from either a UVA-LED or a UVA-BL lamp. For this purpose, a UVA-LED and a UVA-BL lamp (see paragraph 3.2.2) of the same electrical power and peak emission wavelength were tested in parallel experimental series, under identical photocatalytic conditions (i.e. initial substrate concentration, TiO_2 concentration and water matrix). The influence of key operational parameters, such as initial substrate concentration, TiO_2 concentration, water matrix, treatment time, and irradiation source on photocatalytic performance was assessed. The main TPs of SAC formed during photocatalytic treatment under UVA-LED and UVA-BL irradiation were identified and possible degradation pathways were elucidated.

In additional experimental series, the photocatalytic degradation of BPA was investigated in a CPC pilot plant under natural sunlight. The applied experimental conditions were identical in the three systems (i.e. TiO_2/UVA-LED, TiO_2/UVA-BL, and TiO_2/solar, see paragraph 3.2.2 for the description of the systems) with the variables being the reactor geometry and the irradiation source.

Results of this work will create important scientific knowledge on the kinetic rates of SAC and BPA degradation under several irradiation sources and how these can be affected by altering basic operating parameters. The existence of an environmentally friendly, low-cost irradiation source with constant availability is the main technical barrier that impedes the large-scale application of TiO_2-mediated photocatalytic water treatment. Therefore findings of this work can be used as a tool for researchers and water industry to further scale-up the process by using the most suitable irradiation source (or a combination of them) that will enable an effective and sustainable treatment of water and/or wastewater. Moreover, to the author's knowledge, the degradation of BPA under UVA-LED irradiation in the presence of TiO_2 P25 suspensions, as well as the photocatalytic treatment of ASs under LED irradiation have not been reported in the literature yet.

5.2 Results and Discussion

5.2.1 Effect of operating parameters

5.2.1.1 Effect of initial substrate concentration

Initial SAC or BPA concentration in the range of 2.5 – 10 mg/L was applied to assess the effect of initial substrate concentration on photocatalytic performance in the presence of 125 mg/L TiO_2. The photocatalytic removal of SAC and BPA was found to fit well with the pseudo-first-order L-H kinetic model. The plot of the normalised SAC and BPA concentrations against irradiation time resulted in straight lines with r^2 ranging from 0.900 to 0.998 (Table 5-1). From the slopes of the resulting lines, k_{app}

values were computed, which are presented in Table 5-1 and the inset graphs of Figs 5-1 and 5-2.

As can be seen in Figs 5-1 and 5-2, increase in the initial substrate concentration resulted in decreased removal efficiencies for both SAC and BPA. In particular, increase of SAC concentration from 2.5 to 10 mg/L led to removal decrease from 99.9 to 86.1% (k_{app} = 0.198 – 0.043 min^{-1}) during UVA-LED photocatalysis (Fig. 5-1a) and from 71.2 to 35.1% (k_{app} = 0.030 – 0.010 min^{-1}) under UVA-BL irradiation (Fig. 5-1b). BPA photocatalytic removal decreased from 99.9 to 79.7% (k_{app} = 0.179 – 0.036 min^{-1}) and 66.8 to 29.5% (k_{app} = 0.021 – 0.007 min^{-1}) under UVA-LED and UVA-BL irradiation, respectively, when the initial BPA concentration increased from 2.5 to 10 mg/L (Figs 5-2a, 5-2b). Similarly, gradual increase of initial BPA concentration decreased the removal efficiency from 99.9 to 72.9% at 10 mg/L BPA in the CPC reactor (Fig. 5-2c). Increase in the initial organic substrate concentration, at a fixed catalyst concentration, lowers the ratio of oxidant species to substrate molecules and further results in decreased degradation yields [127, 128], thus explaining the findings as presented above.

According to the results, TiO_2/UVA-LED system could degrade up to 5 mg/L of SAC within 30 min of photocatalytic treatment, whereas, under UVA-BL irradiation SAC removal, even at the lowest SAC concentration applied (i.e. 2.5 mg/L), was not higher than 71% after 45 min of treatment. TiO_2/UVA-LED and TiO_2/solar systems were found to be able of degrading up to 8 and 7.2 mg/L of BPA, respectively, within 45 min of treatment, while the corresponding removal for TiO_2/UVA-BL system was limited to 2.9 mg/L.

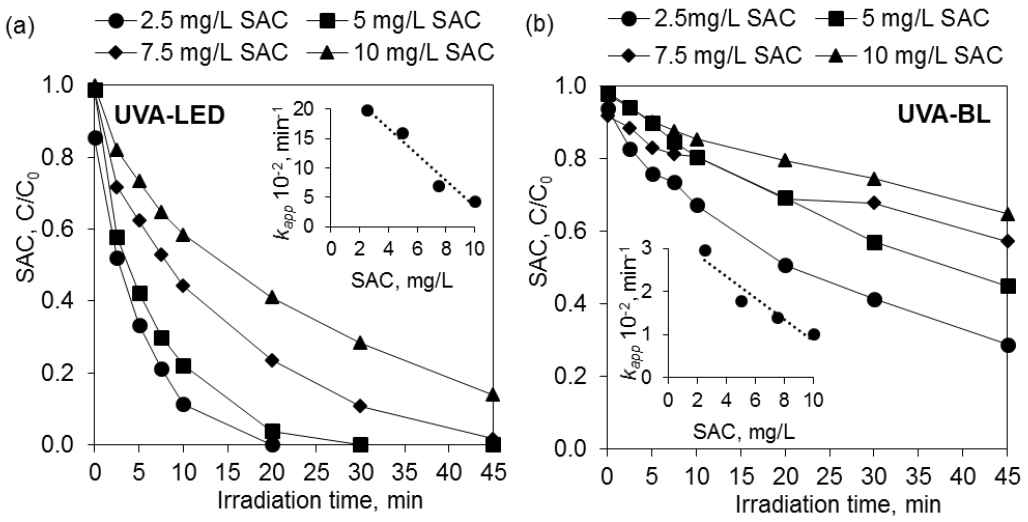

Fig. 5-1 Effect of initial SAC concentration on photocatalytic degradation under (a) UVA-LED and (b) UVA-BL irradiation. Inset graphs: relationship between k_{app} and initial SAC concentration ($[TiO_2]$ = 125 mg/L).

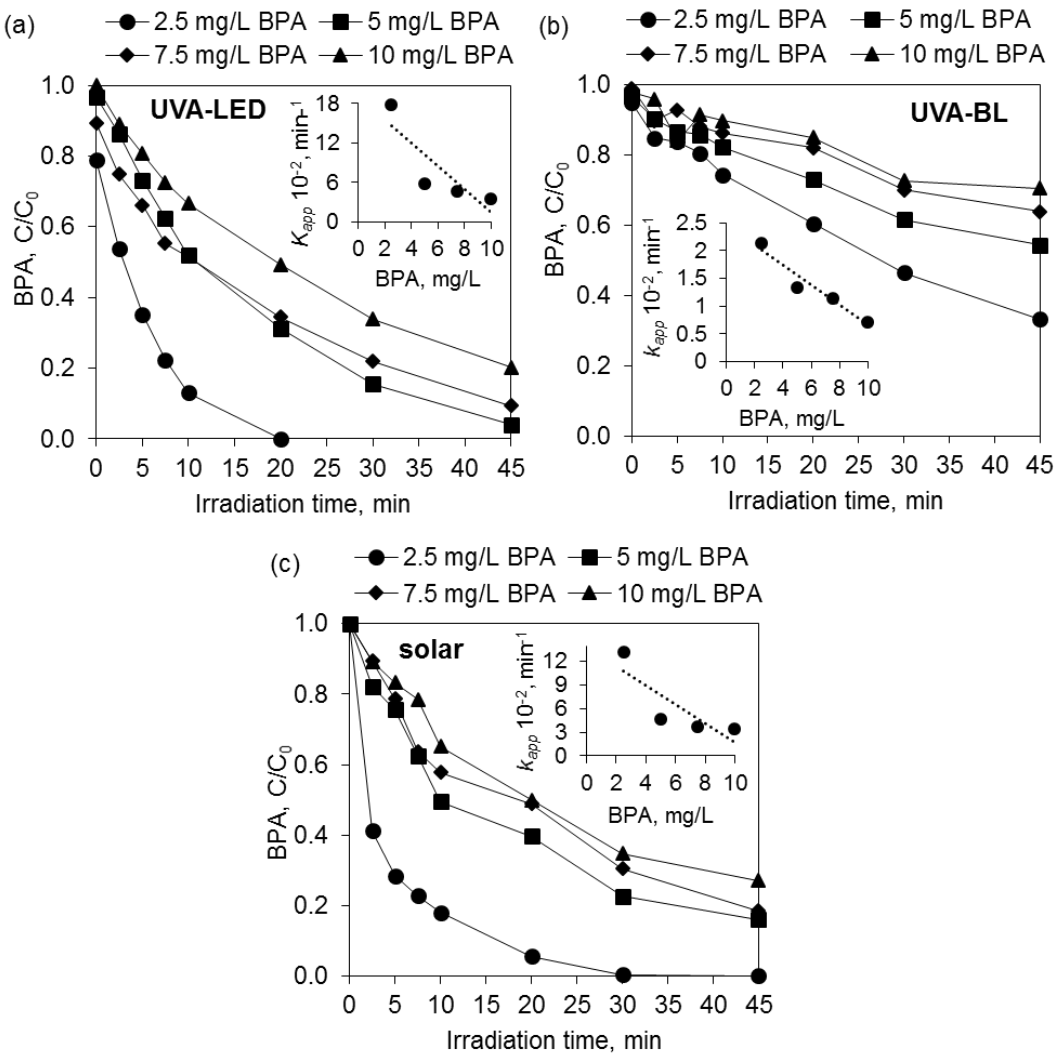

Fig. 5-2 Effect of initial BPA concentration on photocatalytic degradation under (a) UVA-LED, (b) UVA-BL, and (c) solar irradiation. Inset graphs: relationship between k_{app} and initial BPA concentration ([TiO_2] = 125 mg/L).

5.2.1.2 Effect of catalyst concentration

Control experiments (i.e. photolysis and catalysis in the dark) were performed to assess the effect of the presence of catalyst on process efficiency. Figs 5-3 and 5-4 confirm that SAC and BPA degradation is mainly due to the photonic activation of catalyst, proving photocatalysis to be the main removal mechanism.

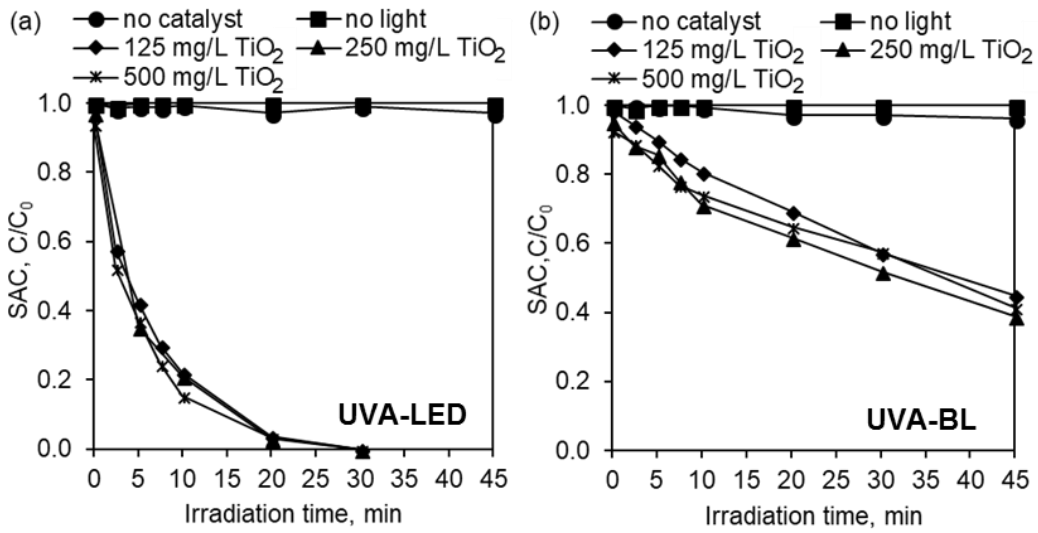

Fig. 5-3 Control experiments and effect of catalyst concentration on the photocatalytic degradation of SAC under (a) UVA-LED and (b) UVA-BL irradiation ($[SAC]_0$ = 5 mg/L; no catalyst (only UVA light); no light (only 125 mg/L TiO_2)).

The effect of catalyst concentration on process efficiency was then investigated by applying various catalyst concentrations (i.e. 100 – 500 mg/L), at 5 mg/L initial substrate concentration. Fig. 5-3a shows that 99.9% of SAC was degraded within 30 min under UVA-LED irradiation, across all the applied catalyst concentrations, making it clear that increase of catalyst concentration beyond 125 mg/L does not improve further process efficiency. In a similar way, catalyst concentration does not affect notably SAC removal under UVA-BL irradiation either, as can be seen in Fig. 5-3b. On the other hand, increase of catalyst concentration from 100 to 250 mg/L enhances significantly BPA removal in the TiO_2/UVA-LED and TiO_2/solar systems. For instance, increase of TiO_2 from 100 to 250 mg/L enhances BPA removal by 21% and nearly doubles the reaction rate in the CPC reactor (Fig. 5-4c, Table 5-1). In TiO_2/UVA-BL system, the effect of TiO_2 concentration on process efficiency is less profound; 4 times increase of TiO_2 concentration (i.e. from 125 to 500 mg/L) increases the reaction rate only 1.5 times, resulting finally in 64.8% BPA removal after 45 min

of treatment. In principle, increase of TiO_2 concentration up to the point where all catalyst particles are fully illuminated enhances oxidation rates by offering more photoactive surface area for adsorption and generation of oxidising species [136], thus explaining the obtained results. In TiO_2/UVA-BL systems, this dependence is less profound possibly due to the lower light intensity offered by the UVA-BL lamp.

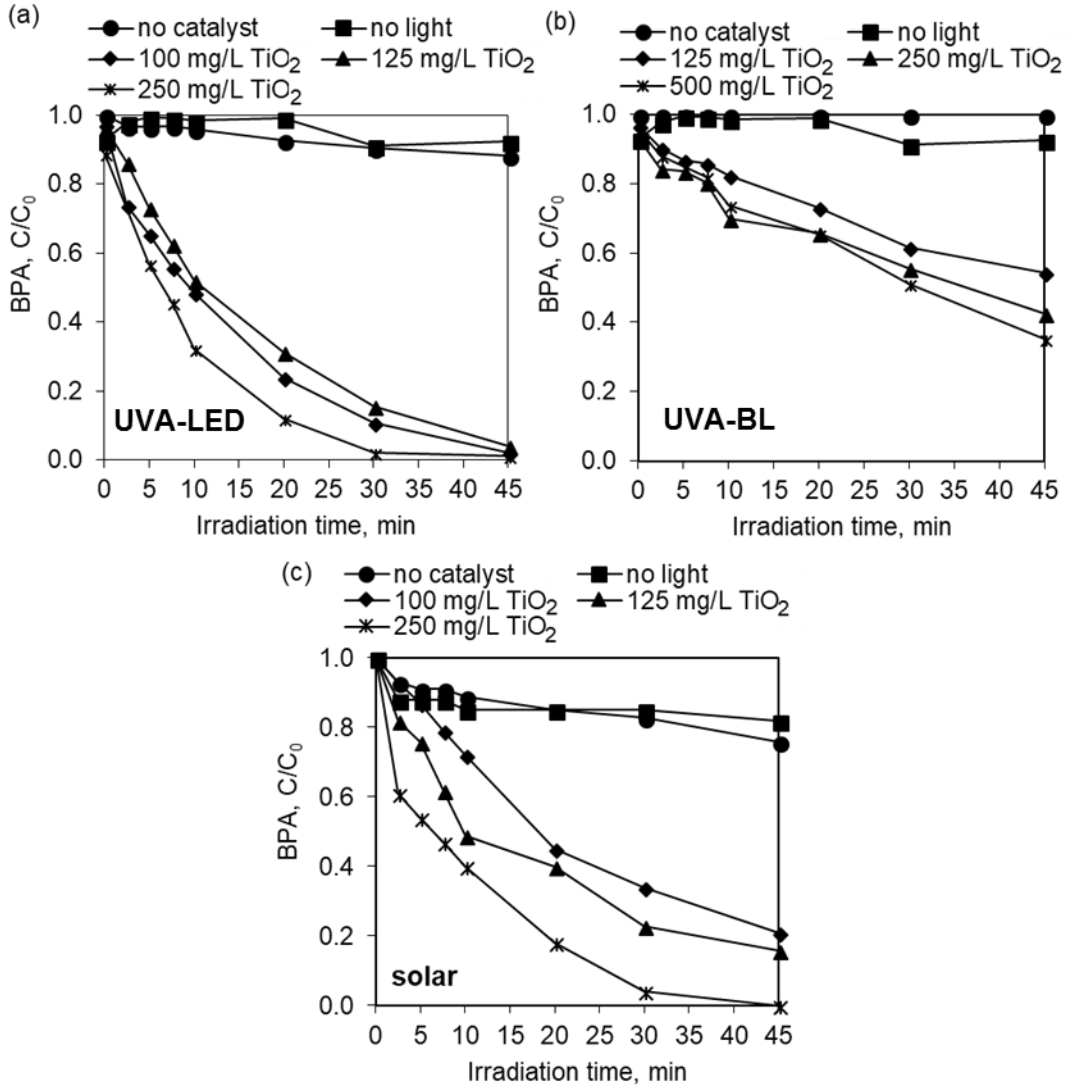

Fig. 5-4 Control experiments and effect of catalyst concentration on the photocatalytic degradation of BPA under (a) UVA-LED, (b) UVA-BL, and (c) solar irradiation ($[BPA]_0$ = 5 mg/L; no catalyst (only UVA light); no light (only 125 mg/L TiO_2)).

Irradiation source had a critical effect on process efficiency. SAC removal was 99.9% across all the applied TiO_2 concentrations after 30 min of LED-driven photocatalysis. Whereas, at the optimal catalyst loading (i.e. 250 mg/L), only about 61% of SAC was degraded after 45 min of treatment under UVA-BL irradiation, indicating that UVA-LED was more efficient in terms of organic removal. Similarly, BPA removal was higher than 96 and 79%, under UVA-LED and solar irradiation, respectively, across the tested catalyst concentrations, whereas, at double catalyst concentration, removal percentage under UVA-BL irradiation was only 65%.

Table 5-1 Removals (R), pseudo-first-order kinetic constants (k_{app}), and coefficients of linear regression of data fitting (r^2) for SAC and BPA photocatalytic degradation under UVA-LED, UVA-BL and solar irradiation.

Operating parameter	Irradiation source	mg/L	R, %	Pseudo-first-order reaction model	
				k_{app}, min^{-1}	r^2
SAC					
Effect of initial concentration[a]	UVA-LED	2.5	99.9	0.198	0.996
		5	99.9	0.159	0.995
		7.5	98.4	0.069	0.989
		10	86.1	0.043	0.974
	UVA-BL	2.5	71.2	0.030	0.988
		5	55.1	0.018	0.993
		7.5	42.7	0.014	0.981
		10	35.1	0.010	0.960
Effect of TiO_2 concentration[b]	UVA-LED	125	99.9	0.159	0.995
		250	99.9	0.170	0.991
		500	99.9	0.163	0.997
	UVA-BL	125	55.1	0.018	0.993
		250	61.0	0.022	0.990
		500	58.6	0.018	0.964
Process efficiency at the best-assayed conditions[c]	UVA-LED		99.9	0.303	0.998
	UVA-BL		85.5	0.044	0.991
BPA					
Effect of initial concentration[a]	UVA-LED	2.5	99.9	0.179	0.996
		5	95.9	0.057	0.996
		7.5	90.6	0.047	0.981
		10	79.7	0.036	0.987
	UVA-BL	2.5	66.8	0.021	0.980
		5	45.6	0.013	0.974
		7.5	36.0	0.011	0.989
		10	29.5	0.007	0.981
	Solar	2.5	99.9	0.132	0.950
		5	84.0	0.047	0.930
		7.5	81.5	0.037	0.900
		10	72.9	0.035	0.980
Effect of TiO_2 concentration[b]	UVA-LED	100	97.9	0.068	0.994
		125	95.9	0.057	0.996
		250	99.0	0.101	0.997
	UVA-BL	125	45.6	0.013	0.974
		250	57.5	0.016	0.971
		500	64.8	0.018	0.992
	Solar	100	79.0	0.040	0.990
		125	84.0	0.047	0.930
		250	99.9	0.080	0.970

Process efficiency at the best-assayed conditions[c]	UVA-LED	99.9	0.230	0.991
	UVA-BL	75.6	0.025	0.983
	Solar	99.9	0.151	0.982

[a][TiO_2] = 125 mg/L, irradiation time = 45 min; [b]C_0 = 5 mg/L, irradiation time = 45 min; [c] additional experiments performed at the optimal initial substrate and catalyst concentration: C_0 = 2.5 mg/L, [TiO_2] = 250 mg/L, irradiation time = 45 min

5.2.1.3 Effect of water matrix

Humic acids (HA), typically found in surface water, may interfere with the ROS and, thus, affect the rate of substrate elimination. With this in mind, 5 and 8 mg/L HA were added to the reactant mixture to examine the effect of water matrix on SAC and BPA photocatalytic removal. Noticeably, the addition of HA has a detrimental effect on SAC photocatalytic oxidation, under both types of irradiation, resulting in removal rates up to 3.6 times lower than in the absence of HA (Fig. 5-5a). Under UVA-LED and UVA-BL irradiation, addition of 8 mg/L HA diminishes the removal percentage of SAC by 73%. When BPA reactant mixture is spiked with 8 mg/L HA, BPA removal is suppressed by 77 and 67% under UVA-LED and UVA-BL irradiation (Fig. 5-5b), respectively. The retardation effect of HA on process efficiency can be ascribed to: (i) the competitive adsorption of HA onto the active sites of TiO_2 that slows down oxidation either via hydroxyl radical ($HO^{\bullet}$) attack or through direct electron transfer between photogenerated holes (h_{vb}^{+}) and target molecules [339], and (ii) the reduced light penetration in the solution which lowers the photonic efficiency [206].

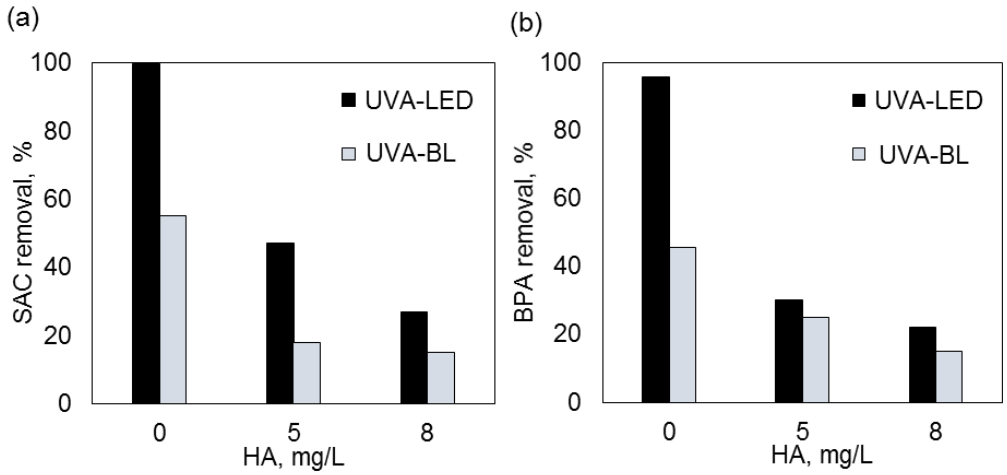

Fig. 5-5 Photocatalytic removal of (a) SAC and (b) BPA in the presence of different concentrations of HA under UVA-LED and UVA-BL irradiation (C_0 = 5 mg/L, [TiO_2] = 125 mg/L, treatment time = 45 min).

Additional experiments were performed at 2.5 mg/L BPA in the presence of 250 mg/L TiO_2 in the CPC reactor. Likewise, the addition of HA progressively lowered the degradation rate of BPA as shown in Fig. 5-6.

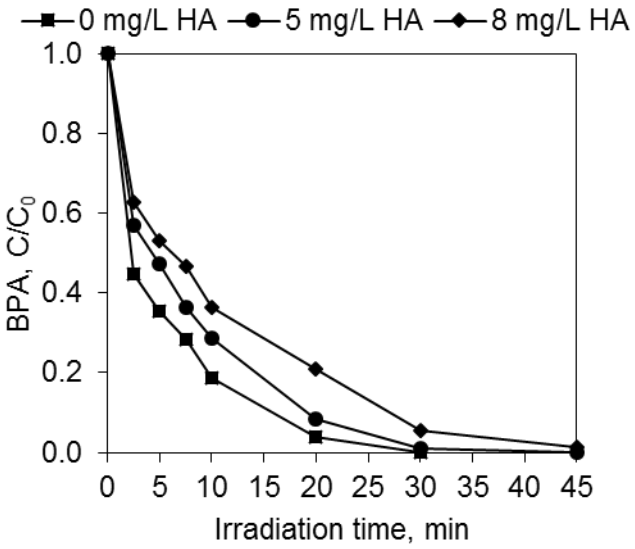

Fig. 5-6 Photocatalytic removal of BPA in the presence of different concentrations of HA under solar irradiation ([BPA]$_0$ = 2.5 mg/L, [TiO_2] = 250 mg/L).

5.2.2 Photocatalytic mineralisation of BPA

Photocatalytic treatment should be efficient in destroying both parent compounds, and intermediate TPs formed during treatment [17]. For this reason, additional experiments were performed at the best-assayed conditions ($[BPA]_0$ = 2.5 mg/L, $[TiO_2]$ = 250 mg/L) to assess the mineralisation efficiency in the three systems. The total mineralisation reaction of BPA by means of photocatalytic degradation in the presence of TiO_2 semiconductors can be expressed by [136]:

$$C_{15}H_{16}O_2 + 18O_2 \rightarrow 15CO_2 + 8H_2O \qquad (5-1)$$

As can be seen in Fig. 5-7, the mineralisation of BPA proceeds slower than BPA degradation. This happens because mineralisation includes a sequence of reactions for the oxidation of BPA and BPA TPs to CO_2 and water, which takes longer than the partial oxidation of BPA. In detail, 99.9% of BPA is degraded within 20, 30, and 120 min under UVA-LED, solar, and UVA-BL irradiation, while the respective TOC removals after 90 min of treatment are 88, 67, and 33%.

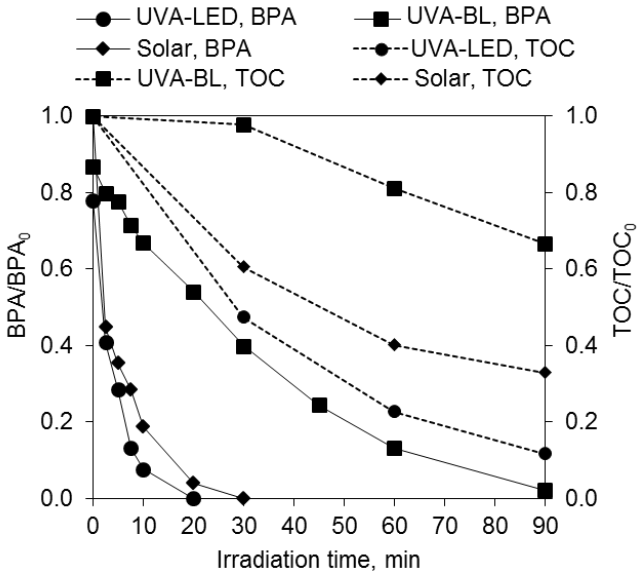

Fig. 5-7 BPA and TOC removal under UVA-LED, UVA-BL, and solar irradiation ($[BPA]_0$ = 2.5 mg/L, $[TiO_2]$ = 250 mg/L).

Kondrakov et al. (2014) reported that the TiO_2 photocatalytic oxidation of BPA is driven by photogenerated holes and hydroxyl radicals leading to the formation of seven TPs according to the mechanism illustrated in Fig. 5-8 [327]. Briefly, BPA oxidation proceeds via hydroxylation yielding hydroxylated and oxidized TPs that are transformed into aliphatic alcohols, carboxylic acids and aldehydes via ring opening and further oxidation reactions, before their complete mineralisation [229, 327].

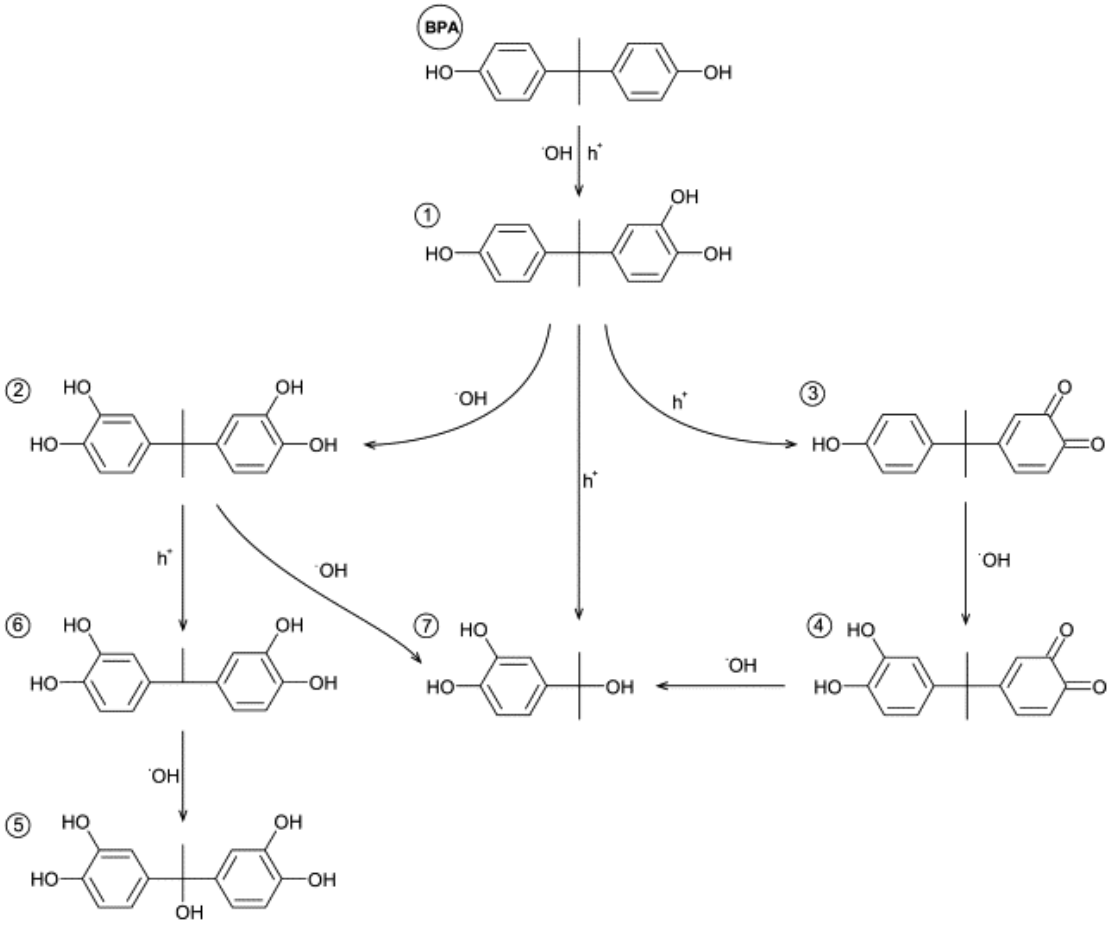

Fig. 5-8 Mechanism of BPA degradation by TiO_2 photocatalysis, adopted from Kondrakov et al. (2014) [327].

5.2.3 Photocatalytic degradation of SAC: transformation products and reaction pathways

For the detection and identification of TPs formed during the photocatalytic treatment of SAC, additional experiments were conducted at increased SAC concentration (i.e. 15 mg/L) in the presence of 250 mg/L TiO_2, under UVA-LED and UVA-BL irradiation. Accurate mass measurements in negative ionization mode revealed the formation of seven and five TPs during SAC degradation under UVA-LED and UVA-BL irradiation, respectively (Table 5-2).

Table 5-2 High resolution mass spectra data of SAC and the identified TPs derived from mass spectrometric analysis ($[SAC]_0$ = 15 mg/L, $[TiO_2]$ = 250 mg/L).

t_R (min)	Code name	Elemental composition of deprotonated molecule	Theoretical m/z $[m-H]^-$	Experimental m/z $[m-H]^-$	Δ (ppm)	RDBE
UVA-LED						
1.6	TP1	$C_7H_4NO_6S^-$	229.9765	229.9756	3.7	6.5
2.3	TP2	$C_7H_6NO_6S^-$	231.9921	231.9917	1.8	5.5
3.3	TP3	$C_6H_6NO_4S^-$	188.0023	188.0025	-0.9	4.5
3.7	TP4	$C_7H_4NO_4S^-$	197.9867	197.9867	0	6.5
4.0	TP5	$C_7H_4NO_4S^-$	197.9867	197.9870	-1.9	6.5
4.1	TP6	$C_7H_4NO_4S^-$	197.9867	197.9867	0	6.5
4.3	TP7	$C_7H_4NO_5S^-$	213.9816	213.9815	0.3	6.5
4.7	SAC	$C_7H_4NO_3S^-$	181.9917	181.9920	-1.4	6.5
UVA-BL						
2.3	TP2	$C_7H_6NO_6S^-$	231.9921	231.9925	-1.8	5.5
3.7	TP4	$C_7H_4NO_4S^-$	197.9867	197.9871	-2.3	6.5
4.0	TP5	$C_7H_4NO_4S^-$	197.9867	197.9858	4.1	6.5
4.1	TP6	$C_7H_4NO_4S^-$	197.9867	197.9858	4.1	6.5
4.3	TP7	$C_7H_4NO_5S^-$	213.9816	213.9810	2.6	6.5
4.7	SAC	$C_7H_4NO_3S^-$	181.9917	181.9915	1.1	6.5

Possible structures of the generated TPs and degradation pathways of SAC are proposed and shown in Fig. 5-9. These were based on the mass spectra data (m/z $[M-H]^-$ ions) and the elemental composition of the deprotonated ions, obtained by the mass

instrument software and the kinetic profiles of the TPs, Fig. 5-10. According to the results, the photocatalytic transformation of SAC, under both irradiation sources, commences with hydroxylation of the molecule giving rise to the formation of three isomers (TP4, TP5, TP6). The hydroxylation mechanism proposed herein is consistent with Toth et al. (2012) who reported relatively high reactivity of hydroxyl radicals towards SAC and proposed that the oxidation mechanism involves the addition of hydroxyl radicals in the aromatic ring, resulting in hydroxylated products [340].

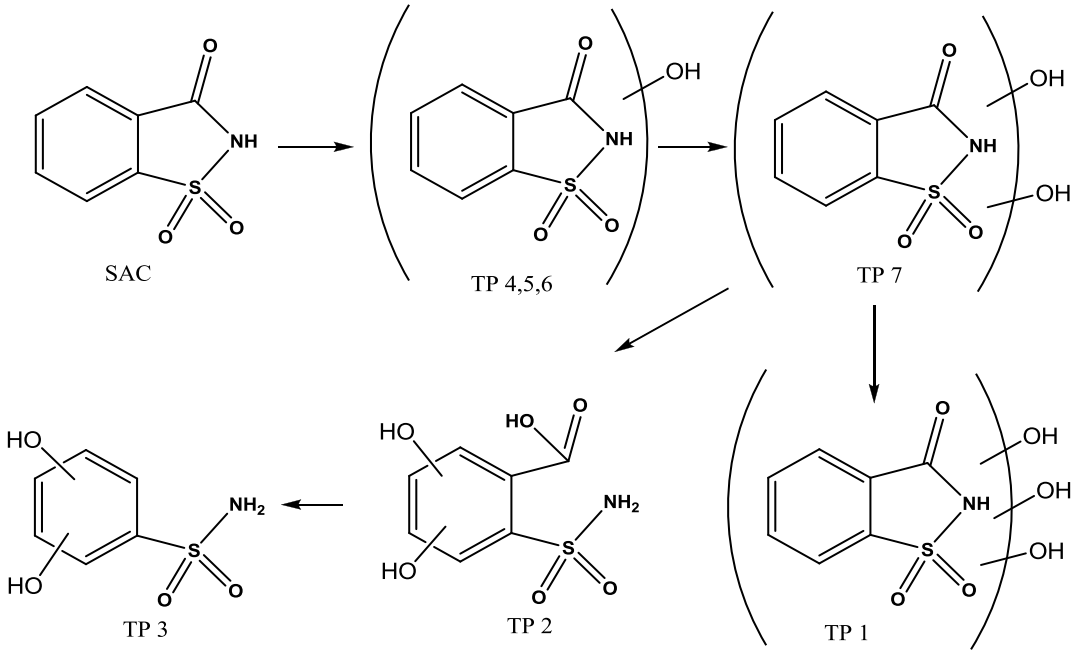

Fig. 5-9 Photocatalytic degradation pathways of SAC under UVA-LED and UVA-BL irradiation.

Hydroxylation of the phenyl ring and N atom are now considered. Sequential hydroxylation of the above-mentioned TPs results in di- and tri-hydroxy derivatives (TP7 and TP1). The sequential steps of hydroxylation are also confirmed by the evolution profiles of TPs (Fig. 5-10) that reveal that TP7 and TP1 peak concentrations are recorded at longer irradiation times than that of mono-hydroxylated TPs.

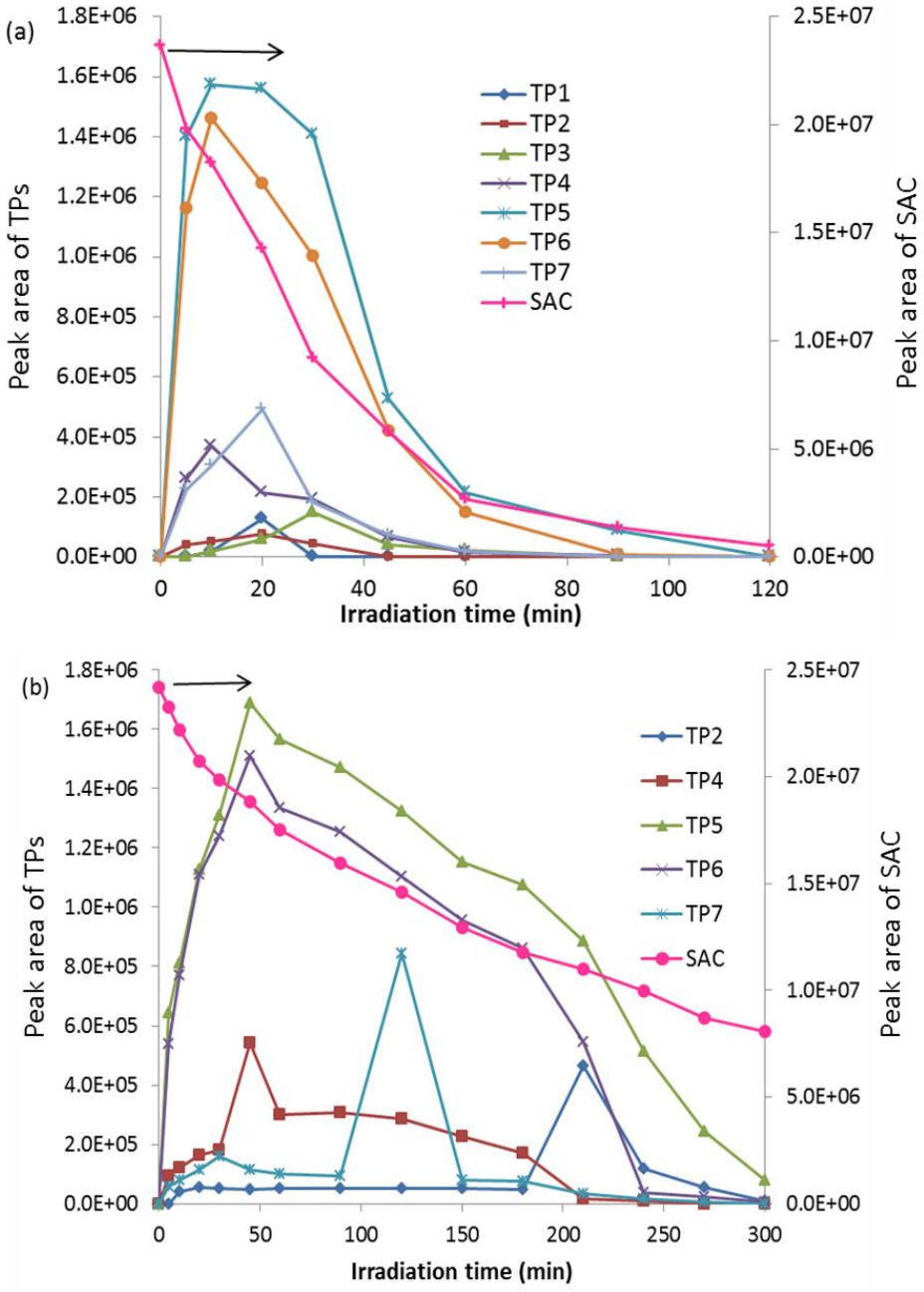

Fig. 5-10 Kinetic profiles of SAC TPs under (a) UVA-LED and (b) UVA-BL irradiation ($[SAC]_0$ = 15 mg/L, $[TiO_2]$ = 250 mg/L).

Based on the fact that mono-hydroxylated TPs attained their maximum concentration within the first stages of the process, they can be characterized as primary TPs. TP7 and TP1, di-hydroxylated and tri-hydroxylated products, are recorded at longer

irradiation times simultaneously with the slower degradation of mono-hydroxylated derivatives, proving the sequential steps of hydroxylation. Their rapid disappearance can be associated with the formation of ring-opening products and the favoured cleavage of the molecule after successful hydroxylation. TP5 is the most abundant mono-hydroxylated product identified during the photocatalytic degradation of SAC. TP5 exhibits a slower degradation rate compared to the other TPs and thus a prolonged irradiation time is required for its complete removal.

Cleavage of the C–N bond of sulfonamide group and further oxidation lead also to the formation of TP2 and TP3, bearing amine and/or carboxylic acid functional groups. As depicted in Fig. 5-10, under UVA-LED irradiation all the TPs are completely removed between 30 and 120 min of photocatalytic treatment. On the other hand, some TPs remain at trace levels after 300 min of treatment when UVA-BL is used as irradiation source. Short-chain carboxylic acids, such as oxalic, formic, and maleic acid are expected as end-products from the oxidative transformation of SAC primary TPs using AOPs [341].

5.2.4 Effect of the photocatalytic system

From the results presented so far, the artificial irradiation sources [although driven by the same electrical power of 11 W and have the same peak emission wavelength at λ = 365 nm] resulted in different SAC and BPA degradation yields, with UVA-LED leading constantly to higher oxidation rates than UVA-BL.

Catalyst activity depends strongly on photon energy (i.e. wavelength) and P25 is sufficiently photo-activated at λ < 380 nm [120]. Fig. 3-7 presents the spectral irradiance distribution of the two light sources. As can be seen, UVA-LED has a

narrowband emission spectrum centred at about 370 nm, making possible the absorbance of all the incident irradiation for catalyst activation. On the other hand, the broadband emission spectrum of UVA-BL lamp consists of a higher fraction of photons with $\lambda > 380$nm that are beyond the action spectrum of P25, thus resulting in decreased oxidation rates when compared to UVA-LED.

Photon flux is another critical, and possibly the most important, parameter to be considered. Increased photon flux can lead to the formation of more hydroxyl radicals and therefore higher oxidation rates of organic substances [166]. As revealed by potassium ferrioxalate actinometry, the incident photon flux on reactant solution under UVA-LED irradiation (i.e. $3.32 \cdot 10^{-6}$ Einstein/s) was an order of magnitude higher than that of UVA-BL lamp (i.e. $3.15 \cdot 10^{-7}$ Einstein/s), explaining the higher removal efficiency under UVA-LED irradiation. This ten-fold gap is ascribed to the different directionality of the light sources. UVA-BL lamp emits light in all directions and although aluminium foil is used to reflect the irradiation back into the reactor a fraction of the photons is lost. Meanwhile, UVA-LED produces a directional beam of light so there is no leak of UVA light outside the reactor.

Under a closer look, although the light intensity provided by UVA-LED is 10 times higher, k_{app} values during LED-photocatalysis were only $4-9$ times higher than those obtained under UVA-BL irradiation; suggesting the lower photonic efficiency (i.e. ratio of reaction rate to the rate of incident photons) of UVA-LED compared to UVA-BL system. In general, at low light intensities, the reaction rate increases linearly with light intensity and then, at higher light intensities, increases with the square root of the light intensity [166, 342] due to the higher recombination of the photogenerated electron-hole pairs [209]. That means that increase in light intensity beyond a point

enhances process efficiency to a lesser extent, thus lowering the photonic efficiency. This tendency has been also reported by Chen et al. (2007) [343] and Coutts et al. (2011) [342] and highlights the need for the correct balance between removal efficiency and energy consumption when it comes to the determination of light intensity.

In terms of UV energy requirement, calculated from Eq. (3-9), at the best-assayed conditions ($[BPA]_0$ = 2.5 mg/L, $[TiO_2]$ = 250 mg/L), the accumulated UV energy required to remove 99% of BPA in the three systems is 30.9 kJ/L for TiO_2/UVA-LED (20 min), 4.2 kJ/L for TiO_2/ UVA-BL (120 min) and 3.54 kJ/L for TiO_2/solar (30 min). LED requires the highest UV energy, indicating that the current reactor configuration does not take full advantage of LED irradiation. In the system under study, the energy transferred by the LED is higher than required, the reactor is irradiated with an excess of photons that do not facilitate any redox reactions, thus explaining the findings above. Considering this, LED-photocatalysis in a reactor of higher pathlength (i.e. bigger volume of wastewater) could lead to increased photonic efficiency. On the other hand, CPC reactor has the lowest UV energy requirement under the studied conditions. Similar results have been reported by Saggioro et al. (2014) [177] and Haranaka-Funai et al. (2017) [344] who compared the photocatalytic performance in the presence of TiO_2 suspensions in CPC and batch-operated reactors. At this point, the effect of reactor geometry should be also taken into account. Solar CPC reactors have been already optimised and provide a high optical efficiency that allows the use of direct and diffuse radiation [177]. However, LED reactors are an emergent technology and still under investigation.

Conceptual reactor designs with encased and covered LED arrays have been developed so far. In the first type of reactor, LEDs arrays are placed in a quartz sleeve and immersed in the direction of flow, mimicking conventional reactors. Alternatively, panel or ring-shaped LED arrays can be used to cover the reactor's walls, top or bottom. In this configuration, UV reflective surfaces and long or tortuous flow path are some of the ways to enhance the UV dose delivery. Covered reactors are better than encased designs in providing uniform irradiation, space for heat-dissipation system, and ability to handle flow fluctuations, suggesting their high suitability in photocatalytic processes [345].

It is evident that the intrinsic differences between LEDs and conventional lamps necessitate the development and optimisation of new reactors tailored for LEDs [345]. In this direction, research on LED reactors in flow-through configurations is encouraged [171, 345]. Future work should address current challenges, such as the optimisation of LED array configuration, identification of the relationship between the radiation pattern of a UV-LED unit, radiation distribution from a UV-LED array, and distribution of UV dose to target pollutants, design of heat-dissipation system, etc. [345].

5.3 Conclusions

The photocatalytic treatment of saccharin (SAC) and bisphenol-A (BPA) was investigated in three different photocatalytic systems under artificial (i.e. UVA-LED and UVA-BL) and natural sunlight. Parallel experimental series were carried out and the systems were assessed in terms of SAC and BPA removal efficiency. The effect of

key operating parameters, namely initial substrate concentration, TiO_2 concentration, treatment time, water matrix, and system on process efficiency was assessed. Furthermore, the transformation products (TPs) formed during the photocatalytic treatment of SAC, under UVA-LED and UVA-BL irradiation, were identified and potential degradation pathways were proposed. The conclusions drawn can be summarised as follows:

- Reaction rates increased with catalyst concentration and decrease of initial substrate concentration. In all cases, SAC and BPA degradation was found to fit well with the pseudo-first-order L-H kinetic model. At the best-assayed conditions (C_0 = 2.5 mg/L, [TiO_2] = 250 mg/L), SAC was degraded within 20 and 90 min under UVA-LED and UVA-BL irradiation, respectively. 99.9% removal of BPA was achieved after 20, 30, and 120 min under UVA-LED, solar, and UVA-LED irradiation, respectively.
- The presence of humic acids (HA) in the reactant solution decreased considerably the removal efficiency in all photocatalytic systems, indicating the significance of the effect of water matrix on process efficiency.
- SAC TPs were identified and the proposed degradation mechanism of SAC includes (i) hydroxylation of the phenyl ring; (ii) cleavage of the C–N bond; and (iii) oxidation reactions.
- Irradiation source had a critical effect on process efficiency. In all cases, UVA-LED yielded higher removal rates than conventional UVA-BL and solar irradiation due to the higher photon flux provided by the LED. Solar photocatalysis resulted in the lowest UV energy requirement, whereas UVA-

LED led to the highest energy requirement, highlighting the need for optimised LED-reactors.

All in all, LED-driven photocatalytic oxidation was proved to be a promising treatment option in cases where sunlight is inadequate. Nevertheless, future efforts should focus on assessing the energy requirements and operating costs of LED-based photocatalysis at real-scale and how this technology can be incorporated into existing WWTPs. Results from this work highlight the need for the development and optimisation of reactors tailored for LEDs. Also, the ecotoxicity of the final effluent should be quantified and comprehensively investigated before any further process scale-up.

6 Comparison of photocatalytic systems

6.1 Introduction

In this chapter, the TiO_2-mediated photocatalytic systems applied for the degradation of SAC and BPA are compared in terms of their technical and economic benefits. For this purpose, the best-assayed conditions obtained in Chapters 4 and 5 were selected, with details listed in Tables 6-1 and 6-2. Tables 6-1 and 6-2 present the removal, photonic, and energy efficiencies obtained in the different photocatalytic systems for the treatment of SAC and BPA, respectively. Removal efficiency is expressed in terms of substrate and TOC removal percentages, and pseudo-first-order kinetic constant, k_{app}, which have been calculated using Eq. (3-6), (3-7), and (3-11), respectively. Photonic efficiency, ζ, calculated from Eq. (3-15), is also used as an index of photocatalytic efficiency to express the efficiency of photon use. Furthermore, the electric energy per order, *EEo*, is calculated using Eq. (3-16) to evaluate the energy efficiency of systems under study.

Table 6-1 Removal of SAC in different photocatalytic systems.

Photocatalytic system	Best-assayed operating conditions	Removal efficiency				Photonic & energy efficiency
		Treatment time, min	SAC removal, %	TOC removal, %	k_{app}, min^{-1}	
ANA/UVA ANA catalyst; working volume = 500 mL; UVA-BL irradiation (11 W, λ = 365 nm, $4.98 \cdot 10^{-6}$ Einstein/s); lab-scale, batch-operated slurry reactor	$[SAC]_0$ = 3 mg/L; [ANA] = 400 mg/L	30	42.5	22.5	0.0225	ζ = 0.086% E_{EO} = 36.155 kWh/m^3/order
		45	57.3	-		
		60	69.4	43.9		
		90	88	54.2		
		120		56.1		
		150		56.4		
TiO_2/UVA-LED TiO_2 Aeroxide P25 catalyst; working volume = 150 mL; UVA-LED irradiation (11 W, λ = 365 nm, $3.32 \cdot 10^{-6}$ Einstein/s); lab-scale, batch-operated slurry reactor	$[SAC]_0$ = 2.5 mg/L; $[TiO_2]$ = 250 mg/L	10	96	-	0.303	ζ = 0.57% E_{EO} = 7.134 kWh/m^3/order
		15	-	60.9		
		20	99.9	-		
		30		78.8		
		60		83.4		
		90		85.8		
TiO_2/UVA-BL TiO_2 Aeroxide P25 catalyst; working volume = 150 mL; UVA-BL irradiation (11 W, λ =365 nm, $3.15 \cdot 10^{-7}$ Einstein/s); lab-scale, batch-operated slurry reactor	$[SAC]_0$ = 2.5 mg/L; $[TiO_2]$ = 250 mg/L	30	68.6	33.6	0.0438	ζ = 2.74% E_{EO} = 32.076 kWh/m^3/order
		45	85.5	-		
		60	94.5	57.7		
		90	99.9	69.9		
		120		74		

Table 6-2 Removal of BPA in different photocatalytic systems.

Photocatalytic system	Best-assayed operating conditions	Removal efficiency				Photonic & energy efficiency
		Treatment time, min	BPA removal, %	TOC removal, %	k_{app}, min^{-1}	
R30/UVA R30 catalyst; working volume = 500 mL; UVA-BL irradiation (11 W, λ = 365 nm, $4.98 \cdot 10^{-6}$ Einstein/s); lab-scale, batch-operated slurry reactor	$[BPA]_0$ = 3 mg/L; [ANA] = 400 mg/L	30	20.7	11.7	0.007	ζ = 0.03% E_{EO} = 116.63 kWh/m^3/order
		45	26.1	-		
		60	34.8	27.9		
		90	47.6	42.6		
		120	-	61.3		
		150	-	67.6		
TiO_2/UVA-LED TiO_2 Aeroxide P25 catalyst; working volume = 150 mL; UVA-LED irradiation (11 W, λ = 365 nm, $3.32 \cdot 10^{-6}$ Einstein/s); lab-scale, batch-operated slurry reactor	$[BPA]_0$ = 2.5 mg/L; $[TiO_2]$ = 250 mg/L	10	92.3	-	0.230	ζ = 0.4% E_{EO} = 7.171 kWh/m^3/order
		15	-	43.5		
		20	99.9	-		
		30		52.6		
		60		77.3		
		90		88.3		
TiO_2/UVA-BL TiO_2 Aeroxide P25 catalyst; working volume = 150 mL; UVA-BL irradiation (11 W, λ = 365 nm, $3.15 \cdot 10^{-7}$ Einstein/s); lab-scale, batch-operated slurry reactor	$[BPA]_0$ = 2.5 mg/L; $[TiO_2]$ = 250 mg/L	30	60.1	-	0.025	ζ = 1.174% E_{EO} = 43.07 kWh/m^3/order
		45	75.6	-		
		60	86.8	18.9		
		90	97.9	33.4		
		120	99.9	40.5		

6.2 Results and Discussion

Notably, LED-photocatalysis led to the highest removal efficiencies for both SAC and BPA, across all the indexes as shown in Tables 6-1 and 6-2. Under UVA-LED irradiation, SAC is totally removed within 20 min, while the corresponding treatment time required by the other systems is at least 90 min (Table 6-1). BPA degradation follows the same trend; 99.9% removal is achieved after 20 and 120 min in TiO_2/UVA-LED and TiO_2/UVA-BL systems, respectively (Table 6-2). Whereas, in the R30/UVA system, removal is limited to 48% after 90 min of treatment.

Although degradation rates are lower in the presence of ANA and R30 catalysts, interestingly, mineralisation efficiency turns out to be close to or even higher than that obtained in the presence of TiO_2 P25, which is widely regarded as the benchmark photocatalyst. For instance, LED-driven photocatalytic treatment of SAC results in 86% mineralisation within 90 min, while the corresponding efficiency in the presence of ANA is 54% (Table 6-1). In ANA/UVA system, catalyst concentration and radiant flux are slightly higher than in TiO_2/UVA-LED system, enhancing mineralisation rates. However, the obtained results still show the high potential of the new catalysts. The mineralisation degree in the presence of R30 is higher than that obtained in the UVA-BL photoreactor for BPA removal. In this case however, safe conclusions cannot be drawn due to the different order of photon fluxes received by the two systems (i.e. $4.98 \cdot 10^{-6}$ and $3.15 \cdot 10^{-7}$ Einstein/s for R30/UVA and TiO_2/UVA-BL, respectively).

Photonic efficiency can be used to express photocatalytic efficiency as a function of the incident photon flux [322]. From this perspective, the most efficient photon use is achieved in TiO_2/UVA-BL system (ζ = 2.74 and 1.17% for SAC and BPA,

respectively), followed by TiO_2/UVA-LED (ζ = 0.57 and 0.4% for SAC and BPA, respectively) and, finally, ANA and R30/UVA systems (ζ = 0.086 and 0.03% for SAC and BPA, respectively) (Tables 6-1 and 6-2). As previously discussed, the optimal photonic efficiency is obtained at low light intensities where efficiency increases proportionally with the light intensity. At higher light intensities, further increase in the light intensity enhances to a lesser extent the reaction rates, thus explaining the lower photonic efficiencies obtained in TiO_2/UVA-LED and (ANA or R30)/UVA systems. It is anticipated that scale-up of LED-driven photocatalysis would increase the photonic efficiency of the process because the high rate of energy transfer provided by UVA-LEDs makes the system ideal for the treatment of large volumes of wastewater. In ANA or R30/UVA system, the low photonic efficiency can be ascribed to the high light intensity combined with the lower catalytic activity of ANA and R30 catalysts than P25.

It is useful to note the different reactor geometries and their effect on photonic efficiency. The limitation of the present comparison lies in the different light geometries. In TiO_2/UVA-BL system, BL lamp emits light in all directions, and although aluminium foil is used to reflect irradiation back into the photoreactor, a fraction of the emitted photons is lost. Whereas, in ANA or R30/UVA and TiO_2/UVA-LED systems, there is no leak of UVA light outside the reactor due to the immersion of BL lamp and the directional light output of UVA-LED, respectively. Therefore, *EEo* values for the TiO_2/UVA-BL system are overestimated because part of the electric power is wasted illuminating around the reactor. This difference in light geometries, however, highlights the flexibility offered by the integration of ultra-small LEDs in photocatalytic reactors, contrary to the mandatory immersion of the bulky UV lamps.

A detailed discussion on the differences between LED and BL is given in Chapter 5, paragraph 5.2.4 '*Effect of the photocatalytic system*'.

The energy consumption of the three systems, expressed as E_{EO}, is presented in Tables 6-1 and 6-2. As can be seen, for both SAC and BPA degradation, UVA-LED requires significantly lower energy compared to the other systems. In detail, the E_{EO} values calculated for the photocatalytic treatment of SAC and BPA in ANA and R30/UVA systems, respectively, are about five and sixteen times higher than LED-photocatalysis, suggesting the increased energy efficiency of the latter. This stems from the lower catalytic activity of ANA and R30 catalysts than P25, therefore longer treatment time is required, thus explaining the obtained results. Photocatalysis in the TiO_2/UVA-BL system is at least four times more energy intensive than under UVA-LED irradiation. In this case, UVA-BL irradiation in all directions results in photon loss, as previously discussed, and makes the system less energy-efficient compared to UVA-LED photocatalytic reactor.

Energy-intensive processes, except for high operational costs, also result in high environmental impacts via their CO_2 emissions and fossil fuels depletion [15, 16, 176]. In our case, the environmental impact of the UVA-BL-driven systems is further increased due to the ecological hazards related to the presence of toxic heavy metals (i.e. mercury and lead) in UVA-BL lamps. In this sense, implementation of energy-efficient and eco-friendly (free of mercury and lead) LEDs is anticipated to improve process sustainability. Furthermore, the long lifespan and robustness of LEDs will cut down operational and maintenance costs.

6.3 Conclusions

The photocatalytic performance of ANA and R30/UVA, TiO_2/UVA-LED, and TiO_2/UVA-BL systems was assessed in terms of their removal, photonic, and energy efficiencies for saccharin (SAC) and bisphenol-A (BPA) degradation. The conclusions drawn can be summarised as follows:

- The removal efficiency of the three systems was found to descend in the order: TiO_2/UVA-LED > TiO_2/UVA-BL > ANA or R30/UVA. SAC and BPA removal under LED irradiation was higher than under irradiation provided by the UVA-BL lamp, due to the higher radiant flux provided by the UVA-LED. On the other hand, ANA and R30/UVA systems, although had a slightly higher radiant flux than TiO_2/UVA-LED system, resulted in the lowest reaction rates due to the decreased catalytic activity of ANA and R30 catalysts compared to P25. Interestingly, the mineralisation efficiencies obtained with the use of ANA and R30 catalysts were comparable to those obtained in the presence of TiO_2 P25, thus encouraging their use.
- The photonic efficiency of the three systems was found to descend in the order: TiO_2/UVA-BL > TiO_2/UVA-LED > ANA or R30/UVA; indicating that high light intensity does not result in an analogous improvement in efficiency. Therefore, a balance should be set between removal efficiency and energy requirements in order to obtain cost-efficient photocatalytic systems.
- The energy efficiency of the three systems was found to descend in the order: TiO_2/UVA-LED > TiO_2/UVA-BL > ANA or R30/UVA. Given that the

systems were driven by the same power (11 W), the determining factor for energy efficiency were the photon flux and catalyst activity.

All in all, TiO_2/UVA-LED system achieved higher photocatalytic efficiency in terms of organic degradation, and was found to be significantly more energy-efficient than ANA or R30/UVA and TiO_2/UVA-BL systems, thus rendering LED-photocatalysis a sustainable technology for the treatment of EMs.

7 Solar photo-Fenton treatment with the use of olive mill wastewater as iron-chelating agent

7.1 Introduction

Photo-Fenton process is pH dependent (optimal pH = 2.8) due to the speciation of Fe^{3+} and therefore strict pH control is required (acidification of influent and later neutralisation of effluent). The additional cost of chemicals and the increased salinity of effluent because of the pH adjustments, constrain the wide application of the process [346]. In this respect, iron-chelating agents can be used to solubilize iron at an extended pH range [347]. At the same time, chelating agents result in increased quantum yields by allowing the exploitation of a wider range of the solar spectrum compared to the Fe^{3+}-aqua complexes. Chelating agents complex with iron and upon illumination via a ligand-to-metal charge transfer (LMCT) reaction form photoactive species, thus keeping iron in solution according to [348]:

$$[Fe^{3+}L] + hv \rightarrow [Fe^{3+}L]^{\bullet} \rightarrow Fe^{2+} + L^{\bullet} \qquad (7-1)$$

Several iron-chelating agents, such as oxalate, citrate, EDDS (ethylenediamine-N, N-disuccinic acid), and EDTA (ethylenediaminetetraacetic acid), have been studied to date [239]. The addition of these chemical reagents to the wastewater can increase considerably the operational cost of the process. Also, the high recalcitrance and increased toxicity of such chemicals pose an environmental threat when it comes to the reuse or safe discharge of effluent [239].

From this perspective, attempts have been made to evaluate the potential of components already present in natural waters for stabilizing photo-Fenton at near-neutral pH [349]. Papoutsakis et al. (2016) explored the use of cork boiling wastewater (CBW), a stream high in polyphenolics, for the photo-Fenton treatment of insecticide imidacloprid at circumneutral pH [238]. Papoutsakis et al. observed that in the presence of CBW the availability of iron increased at near-neutral pH leading to enhanced degradation of imidacloprid and a mixture of contaminants (including phenol and methomyl). In the same study, the mineralisation efficiency of CBM-assisted photo-Fenton treatment at circumneutral pH was found to be as high as that of the conventional photo-Fenton (pH = 3). Phenolic compounds are secondary plant metabolites with strong antioxidant activity based on chain-breaking and metal-chelation [350]. Such phenolic/polyphenolic components can be sourced from industrial wastewater originating from natural products processing (i.e. cork production industry, olive mills, wineries, tea manufacturing industry etc.), making their use in photo-Fenton treatment an economically attractive strategy. Although polyphenols, such as gallic acid and tannins, have been studied as model pollutants [351], their capacity to form stable complexes with iron has not been evaluated yet.

It is known that among these waste streams olive mill wastewater (OMW) features one of the highest phenolic contents (in the range of grams per litre) [352], suggesting its high potential as an iron-chelating agent for the photo-Fenton process. OMW, in particular, contains high amounts of hydroxytyrosol and gallic acid, which are compounds with proven iron-chelating properties at neutral pH [347, 353, 354].

This work investigates the treatment of SAC by photo-Fenton process in a pilot-scale CPC under natural sunlight. The potential of polyphenols, present in OMW, as iron-

chelating agents in photo-Fenton reaction without water acidification at pH 2.8 is evaluated. For comparative purposes, EDDS, known for its ability to form photoactive iron complexes, is also used at circumneutral pH. Furthermore, the transformation products (TPs) formed during conventional photo-Fenton (pH = 2.8) are identified and linked to toxicity evolution.

To the author's knowledge, this is the first study assessing OMW as an iron-chelating agent for the photo-Fenton treatment technology. This work introduces a new concept aimed towards the sustainable operation of photo-Fenton process that is based on the use of wastewaters rich in polyphenols instead of expensive, hazardous chemicals for iron-chelation. Moreover, to the author's knowledge, toxicity evolution during the photocatalytic treatment of SAC has not been monitored to date.

7.2 Results and Discussion

Control experiments revealed the stability of SAC against hydrolysis and photolysis in both DI and natural water.

7.2.1 Conventional photo-Fenton (pH = 2.8)

Preliminary experiments were carried out in the solar simulator to investigate the efficiency of the conventional photo-Fenton process for SAC treatment and tune the experimental protocol at low-scale. The pH of natural water was adjusted to 2.8 and left uncontrolled during treatment, no variations were observed and at the end of the experiment the measured pH was around 2.9. As can be seen in Fig. 7-1, SAC was totally degraded by photo-Fenton, attaining 90% degradation when about 0.5 kJ/L of UV energy were received, approx. within 10 min. The process was then up-scaled to

the solar CPC pilot plant, at the same photocatalytic conditions, where a slightly lower oxidation rate was observed (Fig. 7-1). The respective UV energy for 90% SAC degradation in the CPC was 0.76 kJ/L that corresponds to less than 15 min of irradiation time. The observed variation of the removal efficiencies is small and can be attributed to the different size and geometry of the two systems. From the preliminary experiments, the main conclusions drawn are that: (i) the two systems could be easily compared when using Q_{UV} instead of time; and (ii) Fe concentration of 5 mg/L was able of degrading SAC rapidly. All subsequent experiments were performed at pilot-scale because the obtained results would be more useful for the future scale-up of the process.

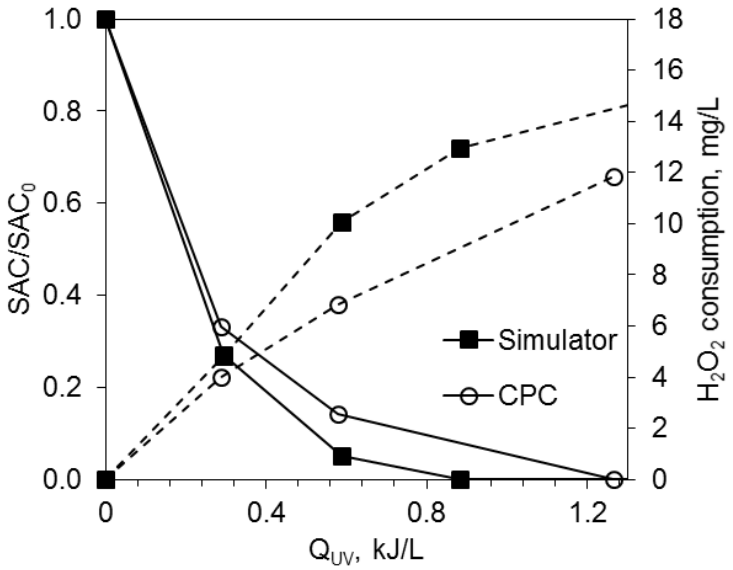

Fig. 7-1 The photocatalytic degradation of SAC (solid line) and the respective consumption of H_2O_2 (dashed line) in the solar simulator and CPC pilot plant ($[SAC]_0$ = 5 mg/L, H_2O_2 = 20 mg/L, Fe = 5 mg/L, pH = 2.8, natural water).

7.2.1.1 Effect of initial SAC concentration

The effect of initial SAC concentration (i.e. 2.5, 5, and 10 mg/L) on photocatalytic degradation was assessed. The concentration of Fe was reduced from 5 to 2 mg/L to

slow down the reaction rate and thus to allow proper evaluation of TPs formation and toxicity evolution. As presented in Fig. 7-1, SAC degradation in the presence of 5 mg/L Fe is rapid and therefore it is difficult to obtain information about intermediates and toxicity evolution during the first steps of treatment. Results in Fig. 7-2 show that the reaction rate decreases with the initial concentration of SAC, implying first-order kinetics according to:

$$\ln\left(\frac{[\mathrm{SAC}]}{[\mathrm{SAC}]_0}\right) = -k\ \mathrm{Q_{UV,n}} \qquad (7-2)$$

where k (L/kJ) is an apparent reaction rate constant. From the plot of the normalized SAC concentration against Q_{UV}, k values in the range of 0.64 - 0.82 L/kJ were obtained with r^2 between 0.987 and 0.992.

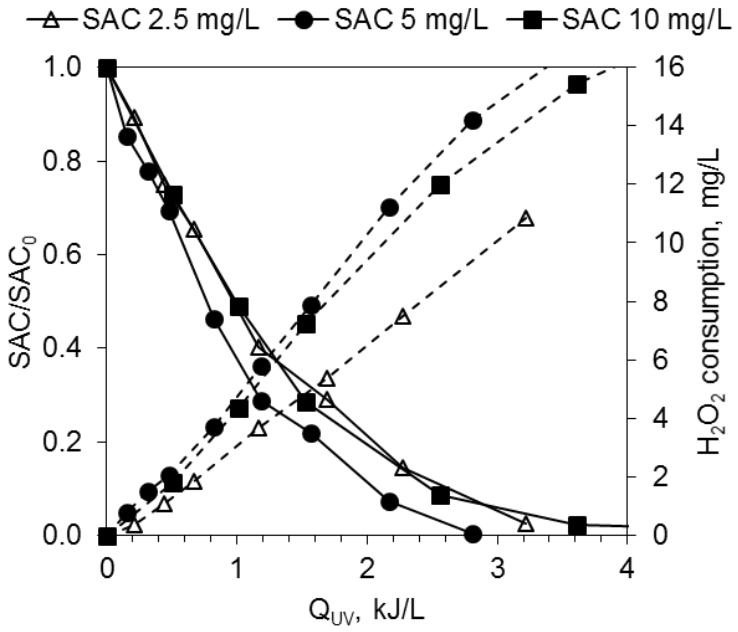

Fig. 7-2 The photocatalytic degradation of SAC (solid line) and the respective consumption of H_2O_2 (dashed line) at various initial SAC concentrations in the solar CPC pilot plant (H_2O_2 = 20 mg/L, Fe = 2 mg/L, pH = 2.8, natural water).

In Fig. 7-2, it can be also seen that H_2O_2 consumption increases with the initial concentration of SAC; in detail, 8.8, 10.5, and 12 mg/L H_2O_2 are consumed to degrade 90% of 2.5, 5, and 10 mg/L of SAC, respectively. H_2O_2 is consumed mainly during the oxidation of Fe^{2+}, reaction (2-18), which is generated by the photoreduction of Fe^{3+}, reaction (2-24). Therefore, at a higher initial concentration of SAC, the increased Q_{UV} requirement results in higher photogeneration of Fe^{2+} that, in turn, corresponds to higher H_2O_2 consumption, explaining the obtained results.

7.2.1.2 Transformation products

LC-QTOF-MS analysis revealed the formation of nine TPs during the photocatalytic treatment of SAC with a high degree of certainty (< 4 ppm error). The high resolution mass spectra data of the detected TPs are summarised in Table 7-1. The evolution profiles of TPs confirm the efficiency of the photo-Fenton process to degrade them in both DI and natural water (Figs 7-3 and 7-4, respectively). Interestingly, the concentration of TP3 increases slightly with treatment time in both water matrices and, likewise, TP3 is the last TP to evolve in Chapter 5 during the TiO_2-mediated photocatalytic treatment of SAC before its complete oxidation. In natural water, the degradation of TPs proceeds slower than in DI water due to the presence of various inorganic and organic species, which act as $HO^{\bullet}$ scavengers [346].

Table 7-1 High resolution mass spectra data of the identified TPs derived from mass spectrometric analysis ($[SAC]_0$ = 10 mg/L, Fe = 2 mg/L, pH = 2.8).

t_R (min)	Code name	Elemental composition of deprotonated molecule	Calculated exact mass $[M-H]^-$	Detected exact mass $[M-H]^-$	Error (ppm)	DBE	logP[#]
DI water							
5,54	TP1-a	$C_7H_4NO_4S^-$	197,9866	197,9851	-7,5	6,5	0,046
6,72	TP1-b	$C_7H_4NO_4S^-$	197,9866	197,986	-3	6,5	0,468
7,08	TP1-c	$C_7H_4NO_4S^-$	197,9866	197,9856	-5	6,5	0,475
11,4	TP1-d	$C_7H_4NO_4S^-$	197,9866	197,9855	-5,5	6,5	0,904
4,91	TP2-a	$C_7H_4NO_5S^-$	213,9815	213,9804	-5	6,5	-0,199/-0,201[$]
5,52	TP2-b	$C_7H_4NO_5S^-$	213,9815	213,9802	-6	6,5	0,081
5,93	TP2-c	$C_7H_4NO_5S^-$	213,9815	213,9802	-6	6,5	0,491
6,42	TP2-d	$C_7H_4NO_5S^-$	213,9815	213,98023	-5,9	6,5	0,652
18,0	TP3	$C_7H_6NO_6S^-$	231,9920	231,99218	-0,7	5,5	
Natural water							
5,54	TP1-a	$C_7H_4NO_4S^-$	197,9866	197,9869	1,24	6,5	0,046
6,72	TP1-b	$C_7H_4NO_4S^-$	197,9866	197,9872	2,76	6,5	0,468
7,08	TP1-c	$C_7H_4NO_4S^-$	197,9866	197,9874	3,77	6,5	0,475
11,4	TP1-d	$C_7H_4NO_4S^-$	197,9866	197,9869	1,24	6,5	0,904
4,91	TP2-a	$C_7H_4NO_5S^-$	213,9815	213,9808	-3,27	6,5	-0,199/-0,201[$]
5,52	TP2-b	$C_7H_4NO_5S^-$	213,9815	213,9808	-3,27	6,5	0,081
5,93	TP2-c	$C_7H_4NO_5S^-$	213,9815	213,981	-2,33	6,5	0,491
6,42	TP2-d	$C_7H_4NO_5S^-$	213,9815	213,9804	-5,14	6,5	0,652
18	TP3	$C_7H_6NO_6S^-$	231,9920	231,9921	-0,43	5,5	

[#] Lipophilicity index (i.e. in a C18 column compounds with logP > 0 will have high retention times, and those with logP < -1 low retention times) calculated using ACD/ChemSketch molecular properties calculator.

[$] Two different isomers might be co-eluting in the same peak due to the similar logP.

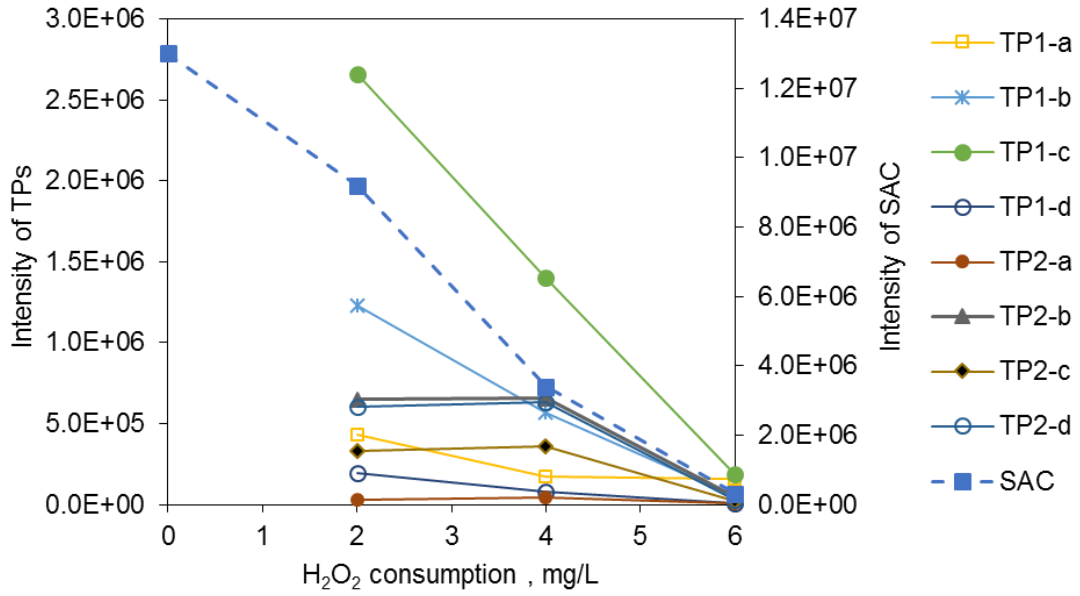

Fig. 7-3 Kinetic profiles of SAC TPs in DI water as a function of H_2O_2 consumption ($[SAC]_0$ = 10 mg/L, Fe = 2 mg/L, pH = 2.8).

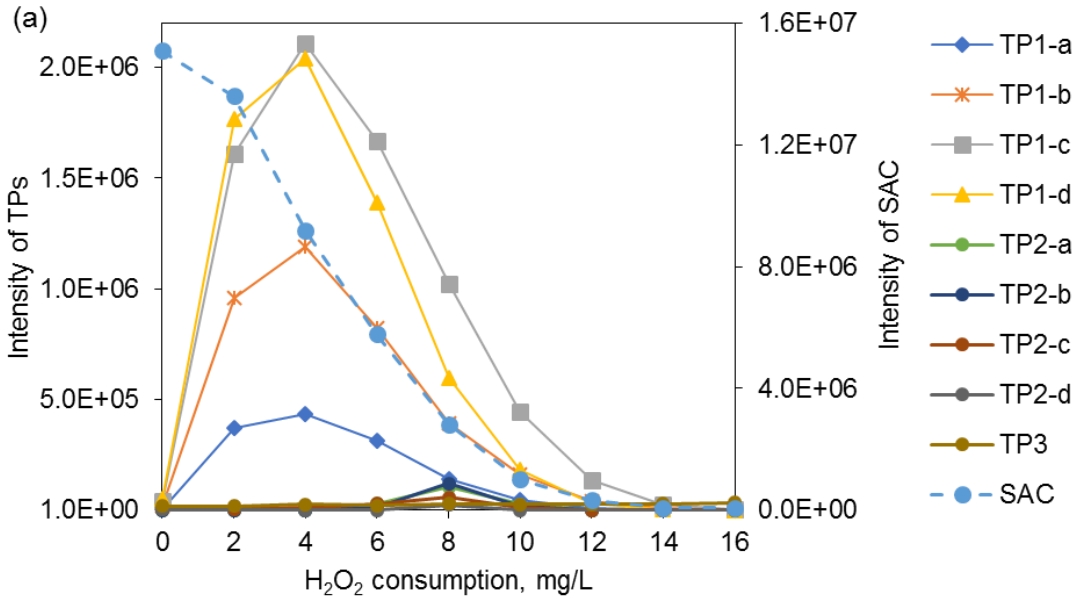

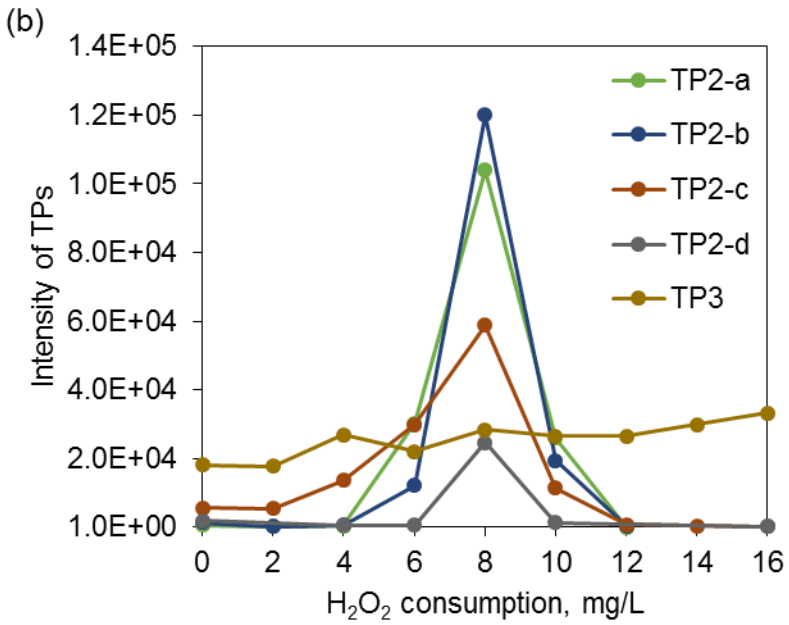

Fig. 7-4 Kinetic profiles of (a) SAC and all the detected TPs and (b) low-intensity TPs alone in natural water as a function of H_2O_2 consumption ($[SAC]_0$ = 10 mg/L, Fe = 2 mg/L, pH = 2.8).

The generated TPs are formed by different types of isomers, following the degradation pathway reported previously in Chapter 5. The proposed molecular structures of TPs are shown in Table 7-2.

Table 7-2 Proposed molecular structures of the identified TPs.

Code name	Structure	Code name	Structure
SAC	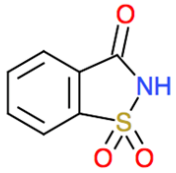	TP2-a	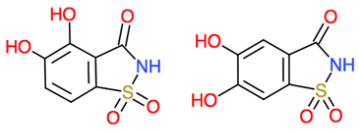 logP -0.199 logP -0.201
TP1-a	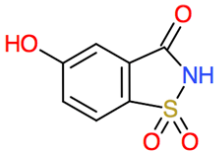	TP2-b	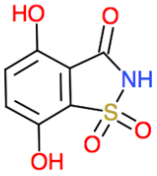
TP1-b	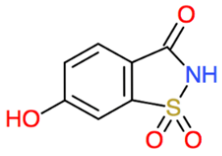	TP2-c	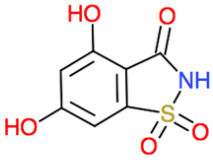
TP1-c	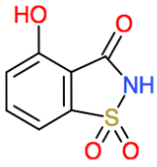	TP2-d	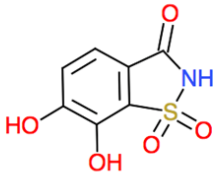
TP1-d		TP3	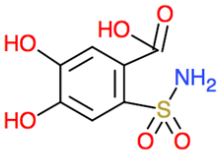

7.2.1.3 Toxicity assessment

The ecotoxicity evaluation of various ASs including SAC, in their original form as food additives, indicates that ASs present a low risk towards aquatic organisms (e.g. activated sewage sludge communities, green algae *Scenedesmus vacuolatus*, and water fleas *Daphnia magna* and duckweed *Lemna minor*) [43]. However, when ASs are released into the environment they undergo transformations after exposure to solar radiation and TPs more toxic than the parent compounds can be formed with adverse effects on aquatic life. Calza et al. (2013), Sang et al. (2014), and Ren et al. (2016)

have confirmed toxicity photo-enhancement for SUC and ACE [36, 42, 278]. However, the toxicity of photocatalytically treated SAC solutions has yet to be studied.

To this end, the acute and chronic toxicities of the treated samples were evaluated by monitoring the inhibition of *Vibrio fischeri* bioluminescence. According to the acute toxicity profile (Fig. 7-5), the bacteria are slightly stimulated in the initial stages of photo-Fenton treatment (H_2O_2 consumption < 8 mg/L); indicating possibly the ability of *Vibrio fischeri* to metabolise the primary SAC intermediates, shown in Fig. 7-4 and Table 7-2, more easily than SAC parent compound. After that, inhibition remains lower than 10%, suggesting that acute toxicity is very low and the solution is innocuous to *Vibrio fischeri* before, during, and after treatment.

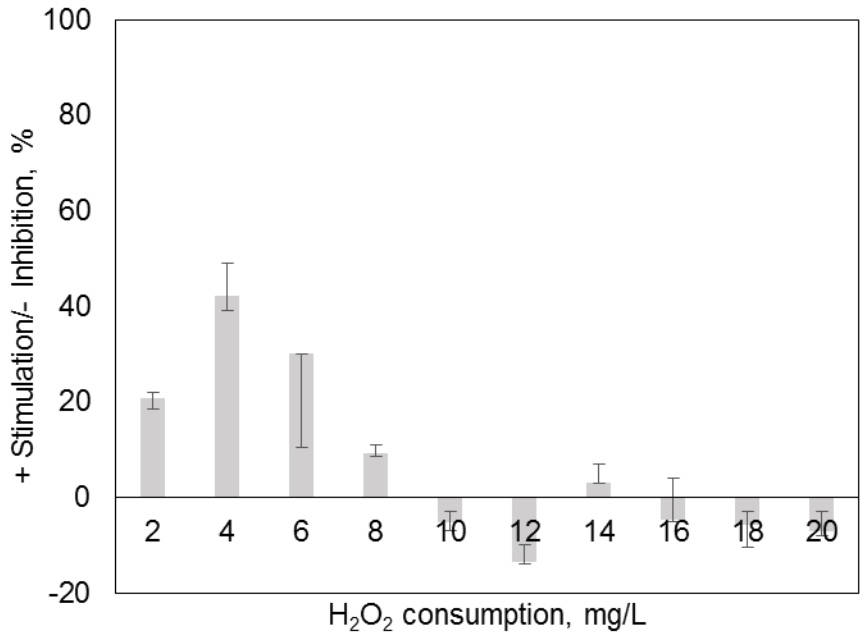

Fig. 7-5 Inhibition of the bioluminescence of *Vibrio fischeri* bacteria as a function of H_2O_2 consumption after 30 min exposure to the treated samples ($[SAC]_0$ = 10 mg/L, Fe = 2 mg/L, pH = 2.8, natural water).

Interestingly, the results of chronic toxicity vary significantly. Exposure of *Vibrio fischeri* to the treated samples for 24 h results in a rapid increase of bioluminescence

inhibition that is gradually reduced during treatment, as can be seen in Fig. 7-6. The results indicate strongly that toxicity is linked with the presence of TPs. The highest inhibition percentages (i.e. 84 - 93%) are measured at the maximum concentration of TPs and then decrease with TPs concentration when H_2O_2 consumption is over 8 mg/L. The connection between chronic toxicity and TPs indicates the toxic nature of the TPs formed during treatment and, furthermore, shows the efficiency of the photo-Fenton process in reducing chronic toxicity from the treated effluent. It is important to remark on the difference between acute and chronic toxicity. As previously discussed, TPs could stimulate *Vibrio fischeri* bacteria after a short contact time but develop toxicity after longer exposure periods, highlighting the necessity of continuing treatment until complete degradation of the main TPs.

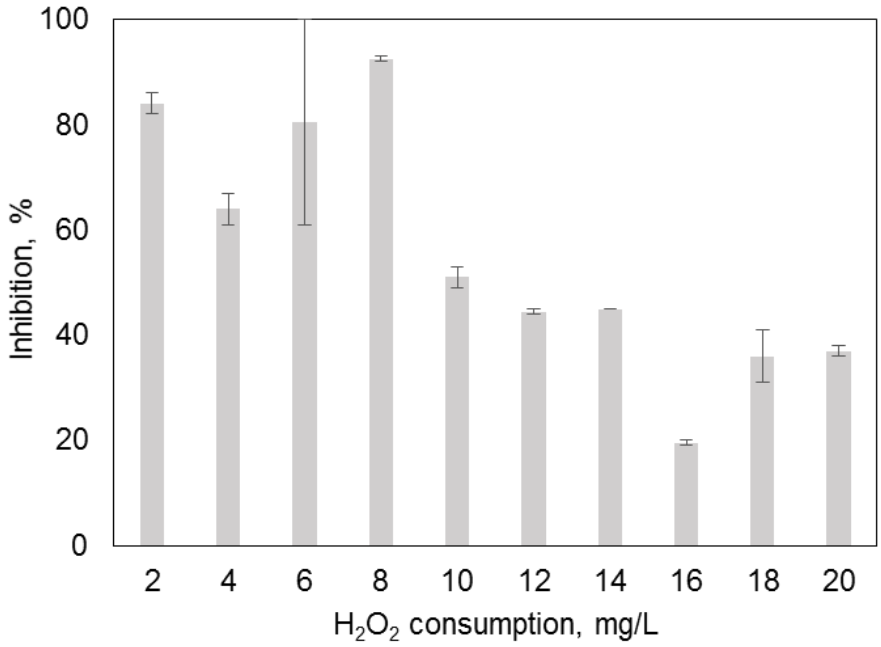

Fig. 7-6 Inhibition of the bioluminescence of *Vibrio fischeri* bacteria as a function of H_2O_2 consumption after 24 h exposure to the treated samples ($[SAC]_0$ = 10 mg/L, Fe = 2 mg/L, pH = 2.8, natural water).

7.2.2 EDDS-assisted photo-Fenton (circumneutral pH)

The photo-Fenton treatment of SAC catalysed by Fe:EDDS complexes at circumneutral pH 5.6-5.9 was then investigated. EDDS is a well-studied iron-chelating agent, non-toxic, and readily biodegradable, which has demonstrated the highest activity among other chelators, such as EDTA, oxalate, and citrate [355]. Based on previous findings of Klamerth et al. (2012) [346], Fe:EDDS was added to the reactant mixture at a molar ratio 1:2. The pH was found to be stable during the treatment.

The effect of initial SAC concentration on its degradation during the EDDS-assisted photo-Fenton process was evaluated by applying various initial concentrations of SAC (i.e. 2.5 - 10 mg/L). As can be seen in Fig. 7-7, removal efficiency decreased with the increase of initial SAC concentration, suggesting first-order kinetics. In detail, increase of SAC concentration from 2.5 to 10 mg/L led to the reduction of k values from 7.88 to 2.21 L/kJ (with r^2 between 0.962 - 0.999). In general, increase in the initial organic substrate concentration, at a fixed set of photocatalytic conditions, lowers the ratio of $HO^{\bullet}$ to substrate decreasing the degradation yields, and thus explaining the results presented above. In Fig. 7-7, it can be also observed that H_2O_2 consumption increases with SAC concentration; this increase is attributed to the increased UV energy requirement as discussed in paragraph 7.2.1.1. Specifically, 5.1, 16.3, and 19.3 mg/L H_2O_2 are consumed for the 90% degradation of 2.5, 5, and 10 mg/L of SAC. It is known that EDDS-assisted photo-Fenton is mostly suitable for short treatment times because Fe:EDDS is photolysed leading to the depletion of EDDS and accumulation of Fe^{3+} in solution that contribute to the faster formation of insoluble iron species [356]. By-products of EDDS could also compete for radical oxidising species. This can also

justify the low reaction rates observed at longer treatment times when 5 and 10 mg/L initial SAC concentration are applied.

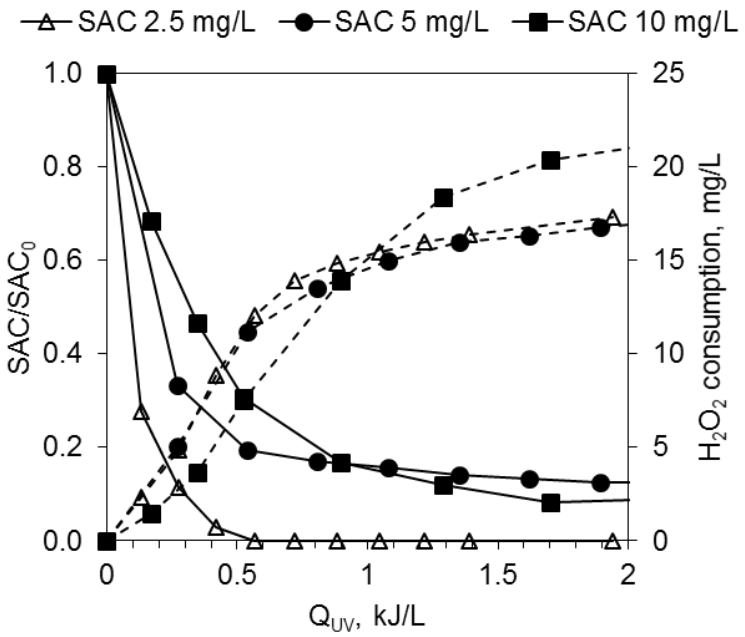

Fig. 7-7 Effect of initial SAC concentration on photocatalytic degradation (solid line) and the respective H_2O_2 consumption (dashed line) using 1:2 mM of Fe:EDDS in the solar CPC pilot plant (H_2O_2 = 20 mg/L, Fe = 2 mg/L, circumneutral pH, DI water).

7.2.3 OMW-assisted photo-Fenton (pH > 4.5)

7.2.3.1 Effect of initial SAC concentration

The potential of OMW to form photoactive Fe^{3+} complexes was assessed, as a means to avoid acidification of water at pH 2.8. For this purpose, OMW was diluted 400 times in the reactant mixture (WW). Considering the organic load of OMW, the concentration of H_2O_2 was monitored throughout the experiment and was always kept > 10 mg/L, starting with an initial H_2O_2 dose of 20 mg/L and proceeding with interim additions. The pH tended to fall during treatment due to the acidic nature of SAC and

OMW, therefore NaOH was added to maintain pH > 4.5 and prevent SAC oxidation due to conventional photo-Fenton process.

As can be seen in Fig. 7-8, SAC degradation is irrespective of the initial SAC concentration, suggesting first-order kinetics. Fe:OMW complex catalyses the decomposition of H_2O_2, leading to the generation of $HO^{\bullet}$ that oxidise SAC yielding k values in the range of 0.05 - 0.1 L/kJ (r^2 between 0.93 and 0.99). The low reaction yields obtained can be attributed to the competition between SAC and organics of OMW (TOC = 30 mg/L) for the available $HO^{\bullet}$. Measurement of iron concentration reveals complete chelation of the 2 mg/L Fe^{3+} and provides evidence of the formation of stable complexes that keep iron in solution during treatment. Considering the observed low oxidation rates, OMW diluted > 400 times is tested in the following experiments in order to reduce the organic content in the reactant mixture, while keeping SAC at 10 mg/L.

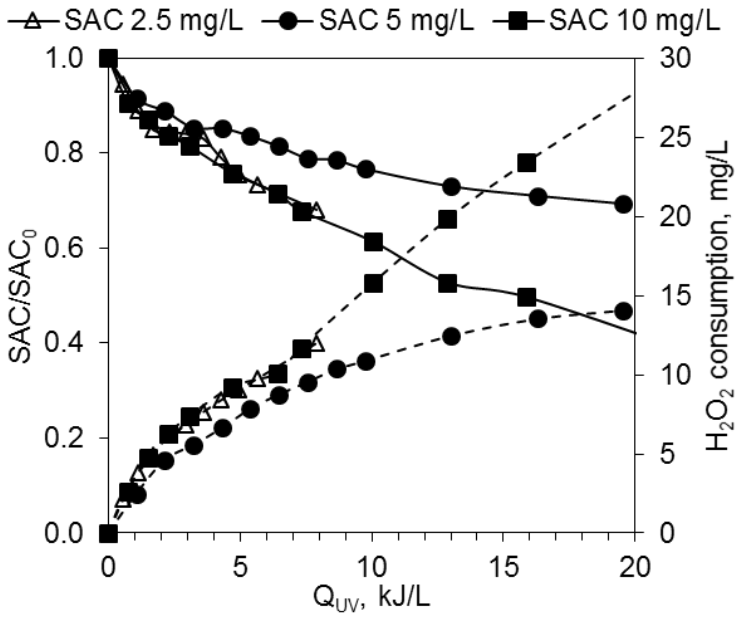

Fig. 7-8 Effect of initial SAC concentration on photocatalytic degradation (solid line) and the respective H_2O_2 consumption (dashed line) using OMW:WW - 1:400 in the solar CPC pilot plant (Fe = 2 mg/L, DI water).

7.2.3.2 Effect of OMW dilution

Higher OMW:WW dilutions (i.e. 1:800, 1:1000, and 1:1200) were applied for the photocatalytic degradation of SAC, as an attempt to increase removal efficiency by reducing the TOC contribution of OMW. TOC was 15, 12 and 10 mg/L, respectively. H_2O_2 concentration was maintained > 10 mg/L throughout the experiment with interim H_2O_2 additions, as previously. As can be seen in Fig. 7-9, OMW:WW - 1:800 is the dilution yielding the highest oxidation rate (k = 0.13 L/kJ) and, in this case, the UV energy required for 90% SAC degradation is 13.5 kJ/L. This ratio OMW:WW was able to keep iron in solution at lower TOC than 1:400. Higher dilutions, however, were not able to keep enough iron in solution.

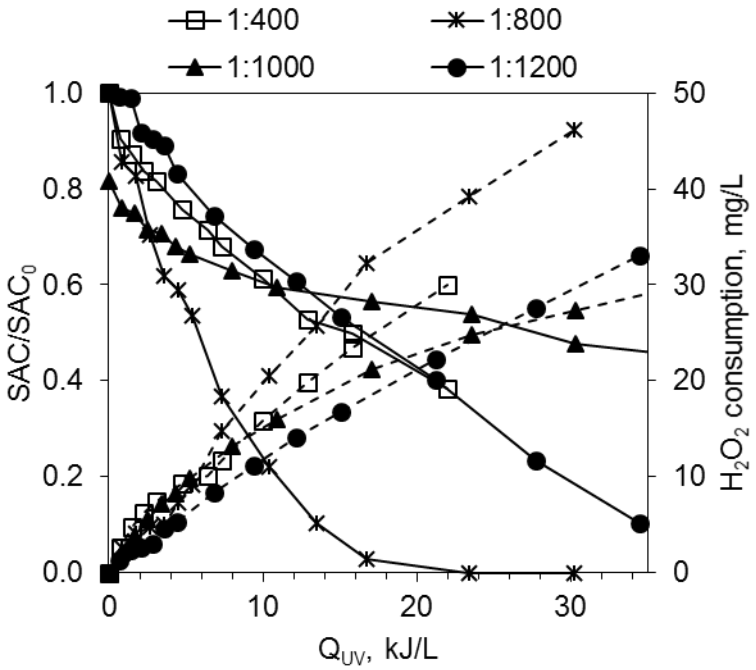

Fig. 7-9 Effect of OMW dilution on the photocatalytic degradation of SAC (solid line) and the respective H_2O_2 consumption (dashed line) in the solar CPC pilot plant ($[SAC]_0$ = 10 mg/L, Fe = 2 mg/L, DI water).

7.2.4 Comparison of conventional, EDDS- and OMW-assisted photo-Fenton

The efficiency of the different photo-Fenton processes in terms of SAC removal was found to descend in the following order: Fe:EDDS at circumneutral pH > photo-Fenton at pH 2.8 > Fe:OMW at pH > 4.5. Similar findings have been reported by Papoutsakis et al. (2015), when they compared conventional with EDDS-assisted photo-Fenton for the degradation of imidacloprid [356]. Papoutsakis et al. suggested that Fe:EDDS is more photoactive than the Fe^{3+}-aqua complexes formed during conventional photo-Fenton. This results in Fe^{2+} becoming available faster for reaction with H_2O_2, which in turn leads to faster generation of $HO^{\bullet}$, thus explaining the high yields obtained when Fe:EDDS complexes were used in this study. The lowest reaction rates were observed when OMW was used as iron-chelating agent, possibly due to its high organic content that consumes the available $HO^{\bullet}$, which otherwise would be intended for SAC degradation.

The initial concentration of iron is maintained throughout the experiment during conventional photo-Fenton, regardless of the received UV energy. Nonetheless, when EDDS or OMW is used, the photogenerated $HO^{\bullet}$ attack both SAC and chelators. As a result, the iron complexes are breaking, iron is released and subsequently precipitates, thus lowering the photocatalytic activity [356, 357]. It should be noted that in the case of EDDS, iron leaching is higher (26 - 33% decrease of soluble iron at a total UV energy of 1.9 - 3.2 kJ/L) than in the OMW-assisted photo-Fenton (4 - 11% decrease of soluble iron at a total UV energy of 8 - 13 kJ/L); a fact that indicates the higher stability of the chelates and their increased resistance against $HO^{\bullet}$ and UV radiation when Fe:OMW is used.

The increased stability of iron-chelating agents against photo-Fenton treatment is highly desirable, although overall efficiency is always important. OMW is a waste stream rich in organics and polyphenols, in the range of grams per litre, with high ecotoxicity and strong antibacterial properties [358]. However, when diluted hundreds of times, ecotoxicity is not of concern, making it an excellent choice (valorisation of a waste stream) for the photo-Fenton treatment of other wastewaters without pH adjustment. Besides, if properly dosed, most of the organic content including polyphenols would be degraded during the process since photo-Fenton has been found to degrade efficiently OMW and to eliminate its toxicity [359, 360].

7.3 Conclusions

The treatment of saccharin (SAC) was investigated in a solar compound parabolic collector pilot plant by means of the photo-Fenton process. Olive mill wastewater (OMW) was used as an iron-chelating agent to obviate the need for water acidification at pH 2.8. For comparative purposes, ethylenediamine-N,N-disuccinic acid (EDDS), a well-studied iron-chelating agent, was also employed at circumneutral pH. The conclusions drawn can be summarised as follows:

- Conventional photo-Fenton at pH 2.8 was found to be an effective method for the degradation of SAC and SAC transformation products (TPs), as well as for the elimination of effluent toxicity. The main TPs formed during SAC treatment were identified and linked to chronic toxicity since acute toxicity was negligible.
- OMW and EDDS formed iron complexes able to catalyse H_2O_2 decomposition and generate $HO^{\bullet}$. OMW yielded lower SAC oxidation rates than EDDS

possibly due to its higher TOC contribution. The degradation rates were improved by increasing OMW dilution in the reactant mixture.

All in all, this study introduces the concept of reusing small amounts of waste streams rich in polyphenols as an alternative to artificial complexing agents. The results obtained by using OMW as an iron-chelating agent are encouraging, rendering this approach a promising step towards increased process sustainability.

8 Photo-Fenton process intensified by ferrioxalate complexes and persulfate oxidising agents under LED irradiation

8.1 Introduction

Solar photo-Fenton intensified by ferrioxalate complexes has been reported as an efficient treatment method for several EMs, including diclofenac, atrazine, and antipyrine (AP). Ferrioxalate is a photo-sensitive complex at 200 - 400 nm and when sunlight is inadequate, artificial photon generation is required. In this study, irradiation is provided by a UVA-LED (λ = 365 nm) as a means to improve process sustainability. Furthermore, persulfate is added to the system as an extra oxidant to evaluate the synergistic effect with ferrous ion and UVA on its potential activation.

Chemometric optimisation tools, namely a central composite experimental design (CCED) and a neural network (NN), were employed to examine the simultaneous effects of key operating parameters on AP degradation and mineralisation and, optimise the process. Experimental tests based on the CCED were analysed and the results were fitted to the NN, which allowed process simulation as a function of the initial concentrations of hydrogen peroxide (H_2O_2), ferrous iron (Fe^{2+}), oxalic acid ($H_2C_2O_4$), and persulfate ($S_2O_8^{2-}$). Finally, the reaction kinetics were studied and the contribution of hydroxyl radicals on AP degradation evaluated.

This study adopts a novel approach aimed towards the intensification of the photo-Fenton process with the simultaneous addition of ferrioxalate and persulfate. The overall sustainability of the process is further improved with the use of a UVA-LED light source instead of energy-intensive, hazardous conventional UVA lamps, as well

as the optimisation of the operating parameters. To the author's knowledge, photo-Fenton intensified by ferrioxalate under UVA-LED irradiation has not been reported to date.

8.2 Results and Discussion

8.2.1 Preliminary experiments

Preliminary experiments were carried out to investigate the degradation of 50 mg/L AP at pH 3 by UVA-LED photolysis, oxidation by H_2O_2, and oxidation by $S_2O_8^{2-}$, within 60 min. Direct photolysis was found to have a negligible effect on AP removal; a fact that can be explained by the light absorbance of AP mainly at $\lambda < 290$ nm, which constitutes only a small fraction of the UVA-LED emission spectrum (Fig. 3-7). AP demonstrated high stability against oxidation when 550 mg/L H_2O_2 or 500 mg/L $S_2O_8^{2-}$ were added to the reactant mixture, confirming that direct or molecular reactions between these single oxidants and AP do not take place, at the conditions under study, or have slow oxidation kinetics.

8.2.2 Central composite experimental design

To evaluate the effect of various parameters on the ferrioxalate-induced UVA-LED photo-Fenton treatment of AP, a statistical approach was chosen based on a two-level factorial experimental design. Four independent variables were considered: the initial concentration of H_2O_2, Fe^{2+}, and H_2C_2O that have been found to be key operating parameters in the photo-Fenton process [283]; and the initial concentration of $S_2O_8^{2-}$, whose effect on the process is under study.

Table 8-1 CCED matrix for UVA-LED photo-Fenton treatment of AP intensified by ferrioxalate with addition of persulfate ($[AP]_0$ = 50 mg/L, treatment time = 60 min).

Experiment	Design				Response functions	
	$[H_2O_2]_0$, mg/L	$[Fe^{2+}]_0$, mg/L	$[H_2C_2O_4]_0$, mg/L	$[S_2O_8^{2-}]_0$, mg/L	k_{AP}, min^{-1}	TOC removal, %
2^4 full factorial design						
1	775	16.25	75	750	0.50	62.3
2	325	16.25	75	750	0.61	66.9
3	775	8.75	75	750	0.48	57.1
4	325	8.75	75	750	0.59	63.1
5	775	16.25	25	750	0.23	62.5
6	325	16.25	25	750	0.20	67.0
7	775	8.75	25	750	0.08	46.6
8	325	8.75	25	750	0.12	58.9
9	775	16.25	75	250	0.89	82.4
10	325	16.25	75	250	1.06	86.6
11	775	8.75	75	250	0.45	71.0
12	325	8.75	75	250	0.67	82.3
13	775	16.25	25	250	0.29	75.8
14	325	16.25	25	250	0.37	79.9
15	775	8.75	25	250	0.11	63.4
16	325	8.75	25	250	0.15	73.6
Axial points of the star design						
17	1000	12.5	50	500	0.34	64.4
18	100	12.5	50	500	0.34	68.0
19	550	20	50	500	0.55	74.1
20	550	5	50	500	0.12	51.7
21	550	12.5	100	500	1.04	74.9
22	550	12.5	0	500	0.06	57.6
23	550	12.5	50	1000	0.40	60.1
24	550	12.5	50	0	0.61	81.9
Replicates of the central points						
25	550	12.5	50	500	0.43	63.4
26	550	12.5	50	500	0.43	63.8
27	550	12.5	50	500	0.43	63.5
Coded	Natural levels					
(+α)	1000	20	100	1000		
(-α)	100	5	0	0		
(+1)	775	16.25	75	750		
(-1)	325	8.75	25	250		
(0)	550	12.5	50	500		
Additional experiments						
28[a]	100	20	100	0	1.51	93.0
29[b]	100	20	100	0	0.01	-
30[c]	100	20	100	0	0.02	-

[a]optimal conditions; [b]optimal conditions in the presence of methanol; [c]optimal conditions in the presence of *tert*-butyl alcohol

Table 8-1 presents the chosen values for the independent variables and the results obtained in terms of the two response functions, namely AP degradation (expressed as k_{AP}, min^{-1}) and mineralisation (expressed as TOC removal, %). The values of each variable were chosen based on previous findings of Duran et al. (2013) [283]. Furthermore, CCED requires experiments outside the experimental range, which is defined by the (-1) and (+1) values, to predict the response functions outside the cubic domain. These values are the star points denoted as ($-\alpha$) and ($+\alpha$). The value of α for a full factorial design with four factors (k = 4) is 2, calculated from Eq. (2-38). Based on that, ($-\alpha$) and ($+\alpha$) values were calculated for each variable and presented in Table 8-1.

AP degradation was found to fit well with the pseudo-first-order kinetic model, Eq. (3-14, yielding pseudo-first-order kinetic constants, $k_{AP,}$ in the range 0.016 - 1.51 min^{-1} with r^2 being $\geq$ 0.834 (Table 8-1).

8.2.3 Neural network fitting

A NN was employed to simulate the UVA-LED photo-Fenton treatment of AP and evaluate the significance of each operating variable on process efficiency. The experimental data listed in Table 8-1 were used to feed the NN. In all cases, a satisfactory correlation was obtained between experimental and predicted results, with an average error lower than 15%, indicating a good fit by the model. The equation and parameters for the fitting of the response functions using the NN are summarised in Table 8-2. N_1 and N_2 are general factors related to the first and the second neuron. W_{11} - W_{14} are the contribution parameters to the first neuron and represent the influence of each of the four variables on AP degradation (W_{11}: $[H_2O_2]_0$, W_{12}: $[Fe^{2+}]_0$, W_{13}:

$[H_2C_2O_4]_0$, W_{14}: $[S_2O_8^{2-}]_0$); W_{21} - W_{24} are the contribution parameters to the second neuron and represent the influence of each of the four variables on AP mineralisation. The equation in Table 8-2 allows estimation of k_{AP} and TOC removal values as a function of the input variables within the experimental range studied. The plot of this equation results in the three-dimensional Figs 8-1 and 8-2, which are used to obtain the optimal conditions. The saliency analysis of the input variables reveals the relative importance of each variable on the response functions. AP degradation and mineralisation were mainly influenced by the initial concentration of $S_2O_8^{2-}$ (negative effect) and the initial concentration of Fe^{2+} (positive effect), as discussed below.

Table 8-2 Equation and parameters for NN fitting.

Neurons and weight factors	Parameters	Values of neurons and factors to obtain k_{AP}, min^{-1}	Values of neurons and factors to obtain TOC removal, %
Equation[a] Response function $= N_1 \times (1/(1 + 1/\exp([H_2O_2]_0) \times W_{11} + ([Fe^{2+}]_0) \times W_{12} + ([H_2C_2O_4]_0) \times W_{13} + ([S_2O_8^{2-}]_0) \times W_{14}))) + N_2 \times (1/(1 + 1/\exp([H_2O_2]_0) \times W_{21} + ([Fe^{2+}]_0) \times W_{22} + (([H_2C_2O_4]_0) \times W_{23} + (([S_2O_8^{2-}]_0) \times W_{24}+))))$			
N_1	Neuron	-3.6600	-1.3037
W_{11}	$[H_2O_2]_0$	-0.3770	0.7156
W_{12}	$[Fe^{2+}]_0$	-2.4656	-2.066
W_{13}	$[H_2C_2O_4]_0$	0.7370	-1.026
W_{14}	$[S_2O_8^{2-}]_0$	-1.9863	-0.832
N_2	Neuron	2.7738	2.5320
W_{21}	$[H_2O_2]_0$	-0.5871	0.024
W_{22}	$[Fe^{2+}]_0$	-1.1411	-0.3002
W_{23}	$[H_2C_2O_4]_0$	2.2131	-0.0696
W_{24}	$[S_2O_8^{2-}]_0$	-2.0302	-0.8043
Saliency analysis of the input variables for the NN - Importance (%)			

Neural	$[H_2O_2]_0$	$[Fe^{2+}]_0$	$[H_2C_2O_4]_0$	$[S_2O_8^{2-}]_0$
k_{AP}, min^{-1}	8.30	31.70	25.15	34.84
TOC, %	8.74	34.78	13.97	42.52

[a] Parameter values ($[H_2O_2]_0$, $[Fe^{2+}]_0$, $[H_2C_2O_4]_0$, $[S_2O_8^{2-}]_0$ in mg/L) in the equation should be previously normalised to the (0.1) interval so that their magnitudes are relatively similar.

8.2.4 Effect of operating parameters

The equation and parameters, presented in Table 8-2, enabled a simulation analysis of the effects of the variables on the response functions. Figs 8-1 and 8-2 illustrate the simulated effects of $[H_2O_2]_0$, $[Fe^{2+}]_0$, $[H_2C_2O_4]_0$ and $[S_2O_8^{2-}]_0$ on k_{AP} and TOC removal, respectively, at the centre point operating conditions and the selected optimal conditions using the NN. Fig. 8-1a, for instance, shows the effects of $[Fe^{2+}]_0$ and $[S_2O_8^{2-}]_0$ on AP degradation (simulation conditions at central values: $[H_2O_2]_0$ = 550 mg/L, $[H_2C_2O_4]_0$ = 50 mg/L). While Fig. 8-2d presents the effects of $[Fe^{2+}]_0$ and $[H_2C_2O_4]_0$ on AP mineralisation (simulation conditions at optimal conditions: $[H_2O_2]_0$ = 100 mg/L, $[S_2O_8^{2-}]_0$ = 0 mg/L).

8.2.4.1 Effect of the initial concentration of Fe^{2+} and $H_2C_2O_4$

The initial concentrations of Fe^{2+} and $H_2C_2O_4$ have a positive effect on k_{AP} and TOC removal, as can be seen in Figs 8-1d and 8-2d. This can be explained by the ferrioxalate photochemistry that forms extra intermediate ROS (i.e. superoxide radical anions, hydroperoxyls and hydroxyl radicals), thus improving the oxidation rates [361].

Figs 8-1d and 8-2d show that k_{AP} and TOC removal increase with the stoichiometric molar ratio of $[H_2C_2O_4]_0$:$[Fe]_0$ up to 3:1. In detail, the highest k_{AP} = 1.51 min^{-1} and TOC removal = 93% correspond to (100 mg/L $H_2C_2O_4$):(20 mg/L Fe) (i.e. molar ratio 1.11 mM $H_2C_2O_4$: 0.36 mM Fe ≈ 3 : 1). At this molar ratio, ferric ions bind with three oxalate ions (i.e. the maximum) in the form of the saturated complex $Fe(C_2O_4)_3^{3-}$ according to reaction (2-27). At lower molar ratios, the amount of oxalate is insufficient to complexate with all the ferric iron present in solution, resulting in iron precipitation in the form of $Fe(OH)_3$, thus decreasing the yield of ferrous iron

regeneration. On the other hand, excess of oxalate acts as an additional organic carbon source and leads to decreased reaction rates due to competition with AP and AP by-products for the generated hydroxyl radicals.

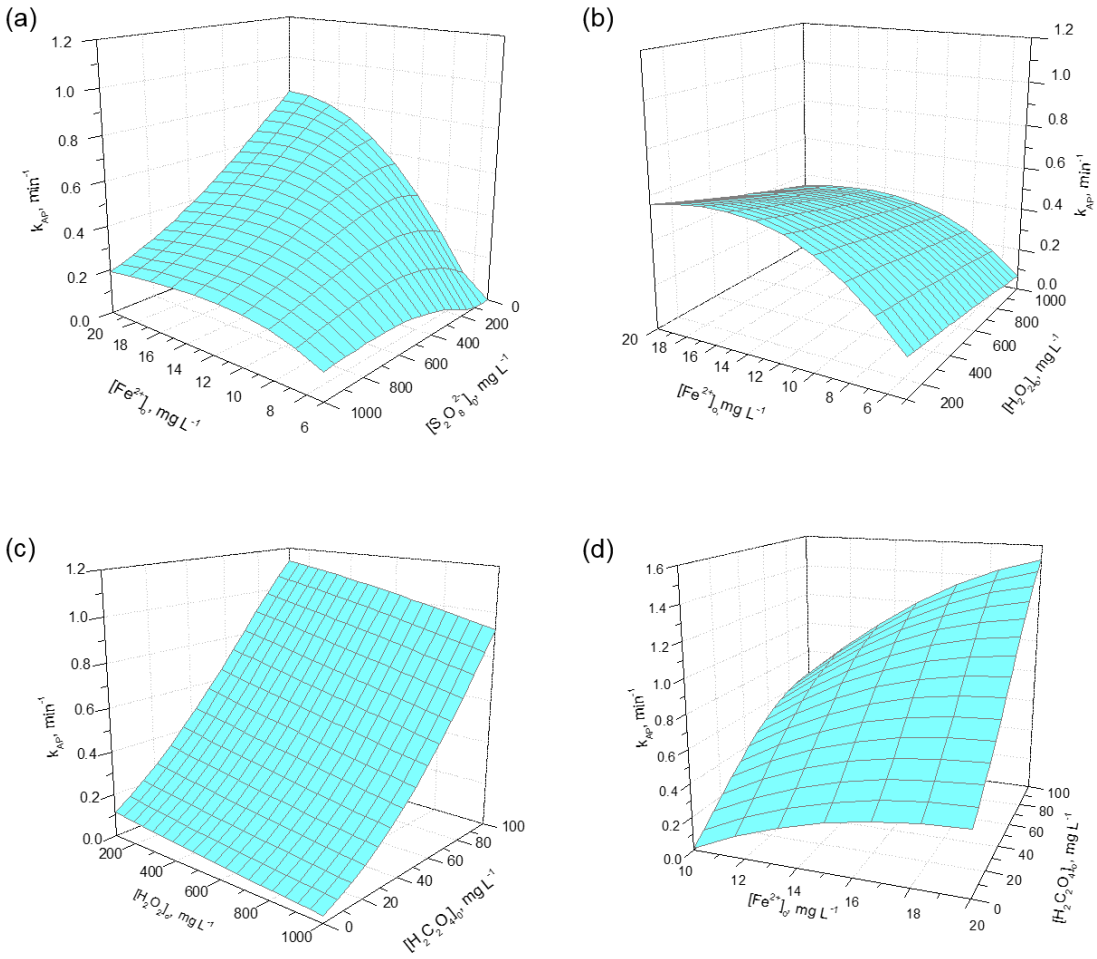

Fig. 8-1 NN simulation of the effects of (a) $[Fe^{2+}]_0$ and $[S_2O_8^{2-}]_0$, (b) $[Fe^{2+}]_0$ and $[H_2O_2]_0$, (c) $[H_2O_2]_0$ and $[H_2C_2O_4]_0$, and (d) $[Fe^{2+}]_0$ and $[H_2C_2O_4]_0$ on AP degradation ((a), (b), (c): centre point operating conditions; (d): optimal operating conditions).

Under a closer look, it can be observed that changes in the initial concentration of oxalic acid affect mainly the degradation of AP (Figs 8-1c and 8-1d) and to a lesser extent the mineralisation of AP (Figs 8-2c and 8-2d). This is in agreement with the saliency analysis that is presented in Table 8-2; the importance of the initial

concentration of oxalic acid for AP degradation is 25.15% and almost the half (i.e. 13.97%) for AP mineralisation. Considering this, we can safely deduce that oxalic acid plays an important role mainly during the first steps of degradation mechanism, when AP oxidation takes place. Later, oxalate reacts with the HO• yielding CO_2, which under acidic conditions is converted to CO_3^{2-} or HCO_3^- that act as HO• scavengers [283].

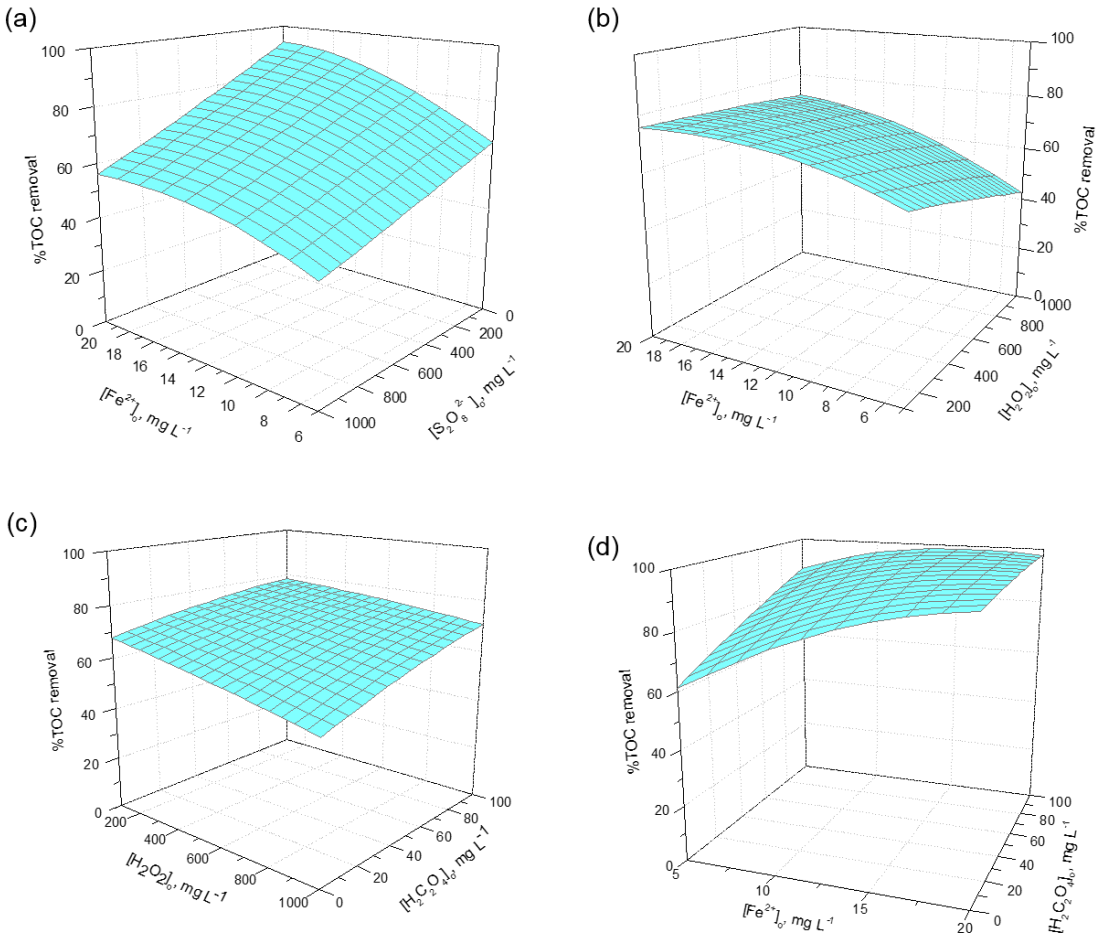

Fig. 8-2 NN simulation of the effects of (a) $[Fe^{2+}]_0$ and $[S_2O_8^{2-}]_0$, (b) $[Fe^{2+}]_0$ and $[H_2O_2]_0$, (c) $[H_2O_2]_0$ and $[H_2C_2O_4]_0$, and (d) $[Fe^{2+}]_0$ and $[H_2C_2O_4]_0$ on AP mineralisation ((a), (b), (c): centre point operating conditions; (d): optimal operating conditions).

8.2.4.2 Effect of the initial concentration of H_2O_2

It becomes clear from Figs 8-1b and 8-1c that the optimal concentration of H_2O_2 is the minimum applied (i.e. 100 mg/L). This concentration seems to be the threshold value because in our preliminary study further decrease of $[H_2O_2]_0$ results in reduced oxidation rates, as can be seen in Table 8-3; a fact possibly explained by the inadequate generation of ROS for the oxidation of AP and AP by-products. Ferrioxalate photochemistry provides extra sources of H_2O_2, according to reactions (2-32) and (2-33), that have a beneficial effect on process efficiency by allowing the generation of a higher amount of $HO^{\bullet}$. However, H_2O_2 in excess has a scavenging effect on the produced $HO^{\bullet}$, according to reaction (8-1), explaining the increase of oxidation rates with the decrease of H_2O_2 concentration.

$$H_2O_2 + HO^{\bullet} \rightarrow HO_2^{\bullet} + H_2O \qquad (8-1)$$

Table 8-3 Effect of initial concentration of H_2O_2 on AP degradation (preliminary study; $[AP]_0$ = 50 mg/L, pH = 2.8, treatment time = 60 min).

$[H_2O_2]_0$, mg/L	$[Fe^{2+}]_0$, mg/L	$[H_2C_2O_4]_0$, mg/L	$[S_2O_8^{2-}]_0$, mg/L	k_{AP}, min^{-1}
100	12.5	50	500	0.346
90	12.5	50	500	0.302
70	12.5	50	500	0.248
50	12.5	50	500	0.113
20	12.5	50	500	0.014

8.2.4.3 Effect of the initial concentration of $S_2O_8^{2-}$

Increase of $[S_2O_8^{2-}]_0$ has a negative effect on both AP degradation and mineralisation (Figs 8-1a and 8-2a), indicating that persulfate is not activated under the applied conditions. Possible explanations are: (i) UVA-LED irradiation at wavelengths (λ =

365 nm) outside the action spectrum of $S_2O_8^{2-}$, which is activated at $\lambda < 288$ nm; and (ii) depletion of Fe^{2+}, which activates $S_2O_8^{2-}$, as a result of Fe^{2+} conversion into Fe^{3+} and the subsequent formation of ferrioxalate complexes. Furthermore, persulfate at increased concentrations has a scavenging effect on $HO^{\bullet}$, reaction (8-2) [362]; a fact that can also explain the reduced degradation efficiency with increase in $S_2O_8^{2-}$ concentration. The presence of persulfate in solution could also affect light penetration and subsequently the activation of ferrioxalate. As a consequence, the addition of persulfate was found not to be necessary for the ferrioxalate-photochemistry-based system under study.

$$S_2O_8^{2-} + HO^{\bullet} \rightarrow S_2O_8^{\bullet -} + OH^- \qquad (8-2)$$

8.2.5 Reaction analysis

Fig. 8-3 shows the evolution of AP, TOC, and dissolved oxygen concentrations during treatment at the optimal operating conditions (i.e. $[H_2O_2]_0 = 100$ mg/L, $[Fe^{2+}]_0 = 20$ mg/L, $[H_2C_2O_4]_0 = 100$ mg/L). AP is degraded within 2.5 min and 93% TOC removal is achieved after 60 min of treatment. Compared to the previous study of Monteagudo et al. (2010), ferrioxalate-assisted photo-Fenton under UVA-LED irradiation leads to higher mineralisation efficiency than under solar irradiation (84% TOC removal in 115 min) [361]. However, a direct comparison of the two systems would be challenging considering the different geometry and size of the reactors. A possible explanation of UVA-LED system's higher efficiency is the monochromatic irradiation of UVA-LED at $\lambda = 365$ nm which overlaps with the maximum absorbance wavelength of ferrioxalate complex, appeared at $\lambda = 358$ nm. Therefore, ferrioxalate is photolysed to

a greater extent under UVA-LED than solar irradiation, leading to a higher generation of ROS due to the ferrioxalate photochemistry and thus enhancing process efficiency.

At optimal conditions, the measured k_{AP} was 1.5 min^{-1} (Table 8-1), a value that was successfully predicted by the model, as can be seen in Fig. 8-1d. However, this was not the case for the predicted mineralisation degree (~ 99%, Fig. 8-2d), which was slightly higher than the measured one (93%, Table 8-1). The mathematical model does not encounter the possible formation of intermediates resistant towards $HO^{\bullet}$, which may pause mineralisation reaction, thus explaining the observed discrepancy between predicted and obtained data. As can be seen in Fig. 8-3, TOC removal is rapid during the first 15 min, then TOC decreases at a slower rate and finally reaches a plateau (TOC = 6 mg/L) at t = 30 min; a fact that indicates the formation of TPs resistant towards oxidation by $HO^{\bullet}$. This is in agreement with previous studies that report the formation of 2-butenedioic acid, butanedioic acid, 4-oxo-pentanoic acid, acetate, and formate, at the final stages of AP mineralisation, which are compounds with high resistance against $HO^{\bullet}$, justifying the residual TOC [363].

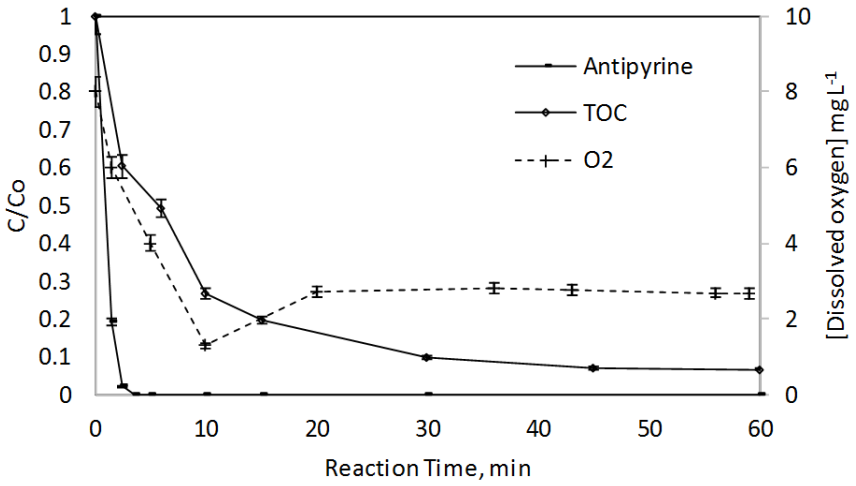

Fig. 8-3 Evolution of AP, TOC, and dissolved oxygen concentrations during treatment at the optimal conditions ($[H_2O_2]_0$ = 100 mg/L, $[Fe^{2+}]_0$ = 20 mg/L, and $[H_2C_2O_4]_0$ = 100 mg/L).

As can be seen in Fig. 8-3, dissolved oxygen concentration falls below 1.5 mg/L within the first 10 min, then increases and reaches a plateau at 2 mg/L. This is due to ferrioxalate being photolysed generating oxalyl radical anions ($C_2O_4^{\bullet-}$), which subsequently undergo a rapid decarboxylation to form a carbon dioxide radical anion ($CO_2^{\bullet-}$) according to reactions (2-28) and (2-30). The production of $CO_2^{\bullet-}$ results in the consumption of oxygen during the first 10 min, reaction (2-31) [364]. Furthermore, $HO^{\bullet}$ radicals generated from ferrioxalate photochemistry react with the organic molecules present in the system to form $R^{\bullet}$ radicals that also consume oxygen generating peroxo-organic radicals, $ROO^{\bullet}$, through the reactions (8-3) and (8-4) [365].

$$HO^{\bullet} + RH \rightarrow R^{\bullet} \qquad (8-3)$$

$$R^{\bullet} + O_2 \rightarrow ROO^{\bullet} \qquad (8-4)$$

The small increase in dissolved oxygen concentration that follows is possibly due to the decomposition of peroxide into water and oxygen.

$$HO^{\bullet} + HO_2^{\bullet} \rightarrow H_2O + O_2 \qquad (8-5)$$

8.2.6 Investigation of the free radical mechanism

Additional experiments were carried out in the presence of $HO^{\bullet}$ quenchers such as *tert*-butyl alcohol and methanol, to evaluate the contribution of $HO^{\bullet}$ on the degradation of AP. $HO^{\bullet}$ radicals react with methanol and *tert*-butyl alcohol according to reactions (8-6) and (8-7), respectively [366, 367]:

$$HO^{\bullet} + CH_3OH \rightarrow H_2O + \cdot CH_2OH \qquad (8-6)$$

$$HO^{\bullet} + (CH_3)_3COH \rightarrow \cdot CH_2(CH_3)_2COH + H_2O \qquad (8-7)$$

As can be seen in Fig. 8-4, AP degradation is negligible in the presence of *tert*-butyl alcohol or methanol indicating that $HO^{\bullet}$ are the main oxidising species. At the beginning of the reaction with *tert*-butyl alcohol, we can see a slightly higher degradation of AP than that in the presence of methanol. This can be explained by the lower reaction rate between $HO^{\bullet}$ and *tert*-butyl alcohol (k' = (3.8-7.6) $\cdot 10^8$ M^{-1} s^{-1}) than methanol (k' = 9.7$\cdot 10^8$ M^{-1} s^{-1}), which translates into slower scavenging of $HO^{\bullet}$ and thus more time for oxidation reactions.

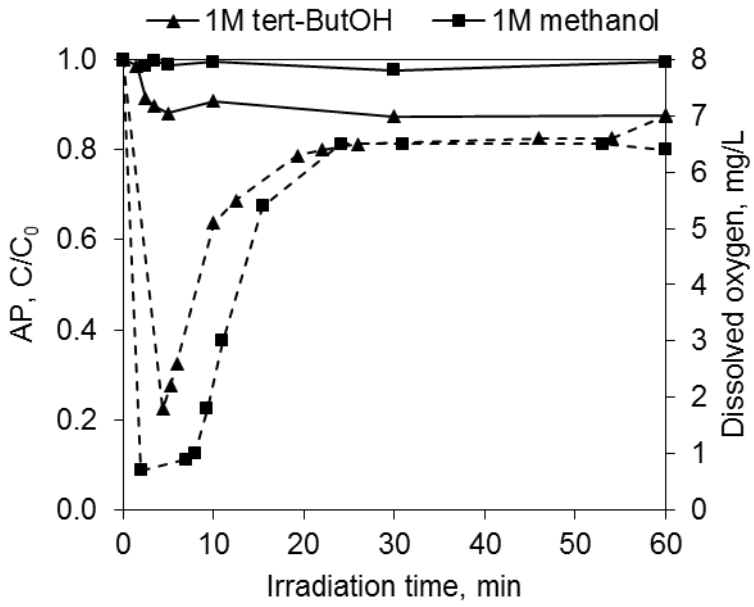

Fig. 8-4 Effect of 1M *tert*-ButOH and methanol on AP degradation (solid line) and dissolved oxygen concentration (dashed line) at the optimal conditions ($[H_2O_2]_0$ = 100 mg/L, $[Fe^{2+}]_0$ = 20 mg/L, and $[H_2C_2O_4]_0$ = 100 mg/L).

A rapid decrease in the concentration of dissolved oxygen is observed when methanol or *tert*-butyl alcohol are added to the reactant mixture (Fig. 8-4). Once HO• radicals are quenched and AP degradation ceases, dissolved oxygen returns to saturation levels due to the decomposition of peroxide into water and oxygen, reaction (8-5).

8.3 Conclusions

The degradation of antipyrine (AP) was studied by UVA-LED-photo-Fenton reaction intensified by ferrioxalate complexes and with the addition of persulfate anions. The efficiency of the reaction was evaluated in terms of AP degradation and mineralisation at different initial concentrations of hydrogen peroxide, ferrous ion, oxalic acid, and persulfate. Experimental data obtained from tests based on a central composite

experimental design were analysed, and the results fitted using neural networks. The conclusions drawn can be summarised as follows:

- Iron: oxalic acid molar ratio plays an important role with regard to process efficiency, with the optimal ratio being 3. Process efficiency was improved with increase of oxalic acid up to 100 mg/L. On the other hand, increase of hydrogen peroxide and persulfate concentrations suppressed reaction rates due to their scavenging effect on hydroxyl radicals. AP degradation kinetics were found to fit well with the pseudo-first-order kinetic model. At optimal operating conditions ($[H_2O_2]_0$ = 100 mg/L, $[Fe^{2+}]_0$ = 20 mg/L, $[H_2C_2O_4]_0$ = 100 mg/L), complete degradation of AP and 93% TOC removal were achieved in 2.5 and 60 min, respectively.
- Hydroxyl radicals were found to be the main ROS responsible for the degradation and mineralisation of AP. In the last step of the reaction, the generated intermediates either could not be degraded by HO• radicals or else their reaction was very slow.
- This ferrioxalate-assisted system reduced the amount of H_2O_2 needed to 100 mg/L for AP degradation, and persulfate was found not to be necessary because it could not be activated either with UVA LED or with Fe^{2+}, which was quickly converted to Fe^{3+} to form ferrioxalate complexes.

Overall, this ferrioxalate-photochemistry-based UVA-LED oxidation system showed high potential in degrading wastewater containing EMs such as AP.

9 General conclusions and Future work

This work investigated the photocatalytic degradation of emerging microcontaminants (EMs). Representative compounds of artificial sweeteners (saccharin, SAC), endocrine disrupting compounds (bisphenol-A, BPA), and pharmaceuticals (antipyrine, AP) were used as case studies. Novel concepts aimed at the minimisation of treatment costs and improvement of the overall sustainability of photochemical oxidation processes were tested. The detailed conclusions are listed as follows:

- Novel submicronic anatase–rutile nanocomposite particles with tuned phase ratio, produced by thermohydrolysis of acidic Ti(IV) solutions in the presence of controlled amounts of Sn(IV), were used as catalysts for the photocatalytic treatment of SAC and BPA under UVA irradiation. Process efficiency was found to be strongly dependent on the initial substrate and catalyst concentration. On the other hand, anatase: rutile ratio did not affect catalyst activity at the photocatalytic conditions applied. The pseudo-first-order L-H kinetic model was found to describe well the degradation of SAC and BPA. At the best-assayed conditions (C_0 = 3 mg/L, catalyst = 400 mg/L), 88 and 45% of SAC and BPA was removed within 90 min of treatment. Recycled catalyst maintained its activity on repeated use, yielding 70% SAC degradation at the end of the 3rd cycle. In additional experimental runs, ultrasound cleaning was applied to the reactant mixture at the beginning of each reuse cycle; however no difference was observed on catalytic activity. Overall, the new catalysts demonstrated good photocatalytic activity, which remained high after three successive reuse cycles without the need for catalyst regeneration.

- Natural sunlight, a UVA light-emitting diode (UVA-LED), and a conventional UVA blacklight fluorescent lamp (UVA-BL) were used as irradiation sources for the photocatalytic degradation of SAC and BPA. In all cases, the main factors that influenced process removal efficiency were found to be the initial substrate and catalyst concentration, water matrix, light source and reactor configuration. The pseudo-first-order L-H kinetic model was found to describe well the degradation of SAC and BPA. At the best-assayed conditions (C_0 = 2.5 mg/L, TiO_2 = 250 mg/L), complete elimination of SAC was achieved within 20 and 90 min under UVA-LED and UVA-BL irradiation, respectively. The corresponding treatment time for BPA was 20, 30 and 120 min under UVA-LED, solar and UVA-BL irradiation, respectively. The presence of humic acids suppressed the photocatalytic performance in all systems. Furthermore, LC-HR/MS analysis revealed that the photocatalytic degradation of SAC occurs via hydroxylation of the phenyl ring, cleavage of C–N bond and further oxidation reactions. Altogether, the highest photocatalytic performance was obtained with the TiO_2/UVA-LED system, followed by TiO_2/solar and, finally, TiO_2/UVA-BL systems, rendering UVA-LED photocatalysis a sound treatment option in areas where sunlight is not adequate.
- The heterogeneous photocatalytic processes applied for the treatment of SAC and BPA were compared in terms of organic removal, photonic, and energy efficiencies. LED-photocatalysis demonstrated the highest removal and energy efficiencies, suggesting its high sustainability as a treatment method for EMs abatement.

- Photo-Fenton treatment was applied for SAC degradation in a pilot compound parabolic collector (CPC) under natural sunlight. Conventional photo-Fenton process (pH = 2.8) demonstrated high efficiency in degrading SAC and SAC transformation products formed during treatment and eliminated the chronic toxicity of the effluent. The use of olive mill wastewater (OMW), a waste stream rich in polyphenols, as an iron-chelating agent led to the formation of iron complexes able to catalyse decomposition of H_2O_2, yielding hydroxyl radicals. SAC removal rates were found to be lower when OMW was used as an iron-chelating complex than ethylenediamine-N,N-disuccinic acid (EDDS), an artificial complexing agent used for comparison. However, degradation rates were improved with the increase of OMW dilution. In all cases, SAC degradation followed a first-order kinetic model. Overall, OMW showed high potential as an iron-chelating agent in photo-Fenton technology, rendering this approach promising towards process operation without the need for pH control.
- Photo-Fenton process intensified by ferrioxalate with addition of persulfate was studied for the treatment of AP under UVA-LED irradiation. Process efficiency was enhanced with the increase of ferrous iron and oxalic acid concentrations, and the optimal molar ratio $[H_2C_2O_4]_0:[Fe^{2+}]_0$ was found to be 3. On the other hand, increase of hydrogen peroxide and persulfate lowered the reaction rates due to their scavenging effect on hydroxyl radicals. The addition of persulfate did not improve process performance because it could not be activated either with UVA-LED irradiation or with ferrous iron, which was quickly reduced to ferric iron to form ferrioxalate complexes. AP degradation followed the pseudo-first-order kinetic model. Experiments with appropriate

quenchers demonstrated that hydroxyl radicals are the main oxidising species of the applied system. Overall, ferrioxalate-assisted UVA-LED photo-Fenton was found to be an efficient treatment process for the complete mineralisation of pharmaceuticals, such as AP.

Results from this work have shown that both TiO_2 photocatalysis and photo-Fenton-based processes are efficient in degrading the selected EMs and the TPs formed during treatment. A direct comparison of the two processes, however, is difficult because of the different reactor configurations and scales applied, and kinetic rate expressions used (i.e. function of treatment time in Chapters 4, 5, and, 8; function of accumulated UV energy in Chapter 7).

Photo Fenton-based processes have been shown to be superior to TiO_2 photocatalysis in terms of treatment efficiency and can be potentially applied at larger scales, e.g. for treatment of industrial wastewaters containing non-biodegradable fractions (e.g. herbicides, pharmaceuticals) [17, 266]. In addition to that, photo-Fenton is possibly the most suitable process among AOPs to be powered by sunlight, as the absorption of iron-hydroxy and iron-organic complexes is extended to the visible part of the solar spectrum [17]. The main limitation of this process is the requirement for strict pH control [11]. Therefore, in a WWTP, where the photocatalytic system would be applied as a polishing step following biological treatment, the application of photo-Fenton process would be hampered due to the requirement for pH control (acidification of the influent and later neutralization of the effluent) and recovery of dissolved iron from the treated effluent [11, 368]. The use of iron-chelating agents could extend the operational pH range and thus obviate the need for pH control, as shown in Chapter 7; however, an extra step would be still required to recover the iron from the effluent.

TiO_2 photocatalysis is considered technically more feasible than photo-Fenton process requiring, apart from UVA irradiation, only the addition of TiO_2, which is a cheap, non-toxic, and recyclable, as shown in Chapter 4, material. From the engineering point of view, the need for catalyst post-separation after treatment is the major constraint of TiO_2 photocatalytic systems [11, 368]. To this end, coupling of photocatalytic process with membrane separation could offer a possible solution for water treatment [369, 370]. In this scenario, the membranes separate the catalyst from the effluent and retain unreacted EMs and TPs, which can be later recycled into the photoreactor for further treatment. Immobilized catalysts on inert surfaces could be alternatively used, obviating the need for a post-separation step. It should be noted, however, that immobilized catalysts provide lower surface area for photocatalytic reactions and higher mass transfer limitations relatively to slurry systems [11]. The uncertainty regarding the durability of the coating and the lifetime of catalyst further delay the up-scale of the process, thus justifying the preference for slurry systems.

The photocatalytic reactor should provide (i) homogeneous light distribution over catalyst surface, (ii) good mass transfer of oxygen and pollutants, and (iii) optimum efficiency in the light use at a reasonable cost [17, 371]. In areas with high solar potential, a flow-through photocatalytic system comprised of a raceway pond reactor (RPR), Table 2-9 and Fig. 9-1a, followed by a photovoltaic-powered membrane unit could offer a technical sound and environmentally friendly option. RPRs feature significant advantages over CPCs, including lower investment and maintenance cost, as well as ability to treat higher volumes of wastewater due to the adjustable liquid depth [252]. Fig. 9-2 illustrates the proposed integration of the photocatalytic system in the treatment train of a typical WWTP. Covered LED reactors, Fig. 9-1b, can be

used alternatively in areas with inadequate sunlight or complementary to solar systems during less sunny days or periods with increased influent loads (e.g. touristic periods). In the second scenario, photovoltaic-powered LEDs can be used to increase the sustainability of the process [372].

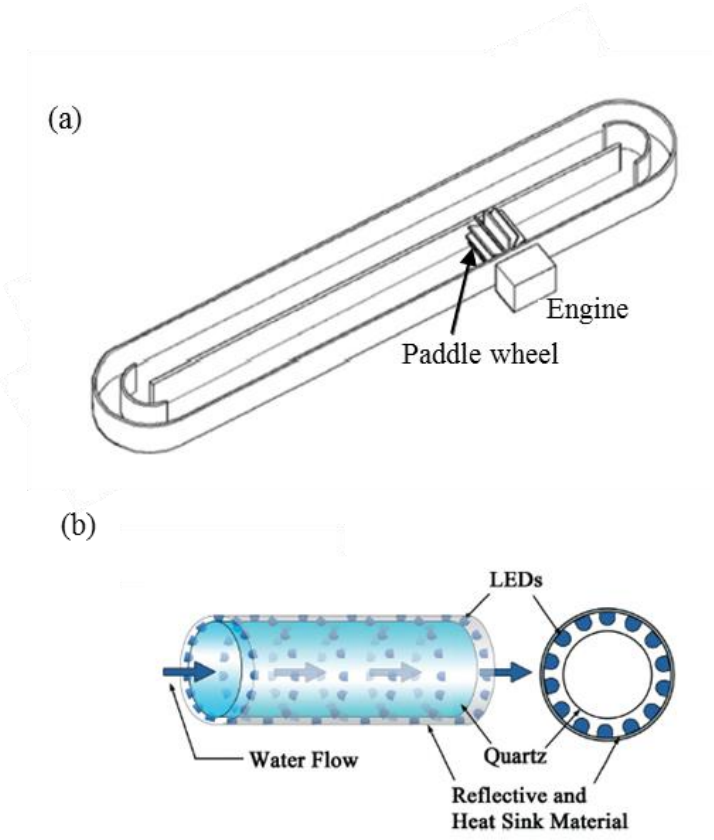

Fig. 9-1 Schematics of the (a) raceway pond reactor and (b) covered LED reactor, adopted from Rivas et al. (2015) [253] and Chen et al. (2017) [345], respectively.

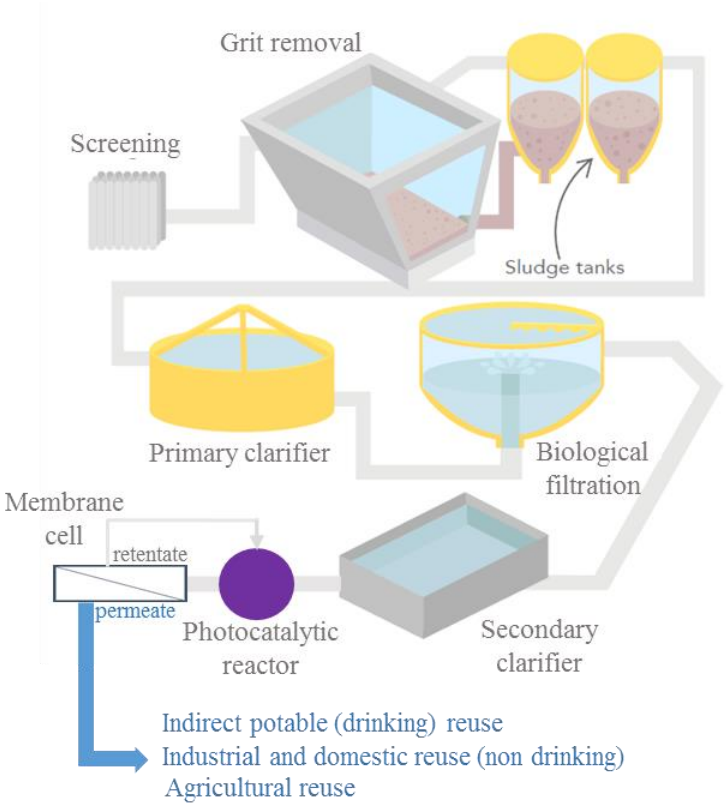

Fig. 9-2 Integration of TiO_2 photocatalytic system in WWTPs, adapted in part from Scottish Water [373].

Towards the up-scale and implementation of photocatalytic process in WWTPs for the elimination of EMs, it is recommended that future work considers:

- The evaluation of process efficiency in real secondary wastewater matrices with EMs present at environmentally relevant concentrations. Such a study should also cover the photocatalytic degradation of a wider list of EMs and EMs mixtures. This task includes the elucidation of reaction mechanisms, pathways, and process kinetics, as well as toxicity assessment. In LED-driven photocatalytic systems, the effect of controlled periodic illumination (CPI) on process efficiency should be thoroughly investigated. Studies have shown that CPI exhibits higher removal and photonic efficiencies than continuous

illumination during photocatalytic treatment [171]. Therefore, CPI can be applied to improve degradation rates while decreasing energy requirements. To this end, more research is required to optimise aspects of CPI, such as duty cycle (i.e. ratio of light time during one cycle) and cycle time (i.e. one cycle light/dark time length) [374].

- The assessment of process efficiency at pilot-scale, which sets the design and fabrication of engineering proper photoreactors as an a priori requirement. This task should include studies on process kinetics and optimisation of key operating parameters (e.g. catalyst: oxidant concentration, light intensity, treatment time) using appropriate tools, such as neural networks (NNs). NNs have attracted considerable attention for process modelling and optimisation, especially of nonlinear and complex systems such as the photocatalytic processes [304]. Due to the complex reactions involved in AOPs, the individual and joint effects of the operating parameters on process efficiency cannot be easily determined, creating uncertainties in the up-scale of photoreactors [304]. The complexity of homogeneous and heterogeneous photocatalytic processes, in particular, lies in the difficulty in solving equations that involve radiant energy balance, the spatial distribution of the absorbed photons, mass transfer, and the photocatalytic degradation mechanisms that involve radicals [304]. Obviously, simple linear multivariate models cannot address this problem. NNs have emerged as a promising modelling technique and are increasingly applied in water and wastewater studies allowing the knowledge and prediction of system's behaviour under various conditions, as well as the optimisation of

the operating variables [304]. Therefore, NNs turn out to be a very useful tool in the design and scale-up of photocatalytic processes.

- The comprehensive economic and environmental impact assessment of the process to establish its suitability as a tertiary treatment step in WWTPs before further scale-up. Life cycle assessment (LCA) methodology can be used to evaluate the environmental impact of the different technologies, compare them and identify the most sustainable [14]. LCA analyses three phases of the process's life cycle: construction, operation, and disposal/recycling after the end of the plant's life [375]. For this purpose, materials for plant's construction, land use, energy usage, chemical reagents (e.g. TiO_2, H_2O_2), equipment (e.g. pumps, sensors) and outputs (e.g. waterborne emissions) are usually considered [375]. Among these unit processes, energy and chemical consumption have been found to contribute mostly to the total environmental footprint of AOPs [14, 375], Ultimately, for the process selection and the final plant design, criteria, such as technical suitability, on-site available treatment options, system robustness, economic costings, environmental impacts, sustainability and space requirements should be considered [135, 368].

Stricter wastewater treatment regulations are expected to push up the carbon impact of WWTPs. To this end, the application of photocatalytic processes as a polishing step holds considerable promise. High efficiency, safe operation, potential use of renewable energy sources or, alternatively, low carbon solutions are among the key features of these processes. Extensive research is ongoing to overcome technical barriers and the full-scale application of photochemical oxidation technologies is a concept that is

likely to mature gradually into a sound treatment option for integrated wastewater management.

References

[1] C.G. Daughton, "Emerging" chemicals as pollutants in the environment: A 21st Century perspective, Renewable Resources Journal, 23 (2005) 6-23.

[2] V. Geissen, H. Mol, E. Klumpp, G. Umlauf, M. Nadal, M. van der Ploeg, S.E.A.T.M. van de Zee, C.J. Ritsema, Emerging pollutants in the environment: A challenge for water resource management, International Soil and Water Conservation Research, 3 (2015) 57-65.

[3] W. Brack, R. Altenburger, G. Schüürmann, M. Krauss, D. López Herráez, J. van Gils, J. Slobodnik, J. Munthe, B.M. Gawlik, A. van Wezel, M. Schriks, J. Hollender, K.E. Tollefsen, O. Mekenyan, S. Dimitrov, D. Bunke, I. Cousins, L. Posthuma, P.J. van den Brink, M. López de Alda, D. Barceló, M. Faust, A. Kortenkamp, M. Scrimshaw, S. Ignatova, G. Engelen, G. Massmann, G. Lemkine, I. Teodorovic, K.-H. Walz, V. Dulio, M.T.O. Jonker, F. Jäger, K. Chipman, F. Falciani, I. Liska, D. Rooke, X. Zhang, H. Hollert, B. Vrana, K. Hilscherova, K. Kramer, S. Neumann, R. Hammerbacher, T. Backhaus, J. Mack, H. Segner, B. Escher, G. de Aragão Umbuzeiro, The SOLUTIONS project: Challenges and responses for present and future emerging pollutants in land and water resources management, Science of The Total Environment, 503-504 (2015) 22-31.

[4] J.O. Tijani, O.O. Fatoba, L.F. Petrik, A Review of Pharmaceuticals and Endocrine-Disrupting Compounds: Sources, Effects, Removal, and Detections, Water, Air, & Soil Pollution, 224 (2013) 1770.

[5] A. Pruden, R. Pei, H. Storteboom, K. Carlson, Antibiotic Resistance Genes as Emerging Contaminants: Studies in Northern Colorado †, 2006.

[6] K. Fent, A.A. Weston, D. Caminada, Ecotoxicology of human pharmaceuticals, Aquatic Toxicology, 76 (2006) 122-159.

[7] S.D. Richardson, T.A. Ternes, Water Analysis: Emerging Contaminants and Current Issues, Anal. Chem., 90 (2018) 398-428.

[8] Y. Luo, W. Guo, H.H. Ngo, L.D. Nghiem, F.I. Hai, J. Zhang, S. Liang, X.C. Wang, A review on the occurrence of micropollutants in the aquatic environment and their fate and removal during wastewater treatment, Science of The Total Environment, 473-474 (2014) 619-641.

[9] V. Belgiorno, L. Rizzo, D. Fatta, C. Della Rocca, G. Lofrano, A. Nikolaou, V. Naddeo, S. Meric, Review on endocrine disrupting-emerging compounds in urban wastewater: occurrence and removal by photocatalysis and ultrasonic irradiation for wastewater reuse, Desalination, 215 (2007) 166-176.

[10] J.-Q. Jiang, Z. Zhou, V.K. Sharma, Occurrence, transportation, monitoring and treatment of emerging micro-pollutants in waste water — A review from global views, Microchemical Journal, 110 (2013) 292-300.

[11] M. Klavarioti, D. Mantzavinos, D. Kassinos, Removal of residual pharmaceuticals from aqueous systems by advanced oxidation processes, Environ. Int., 35 (2009) 402-417.

[12] O.K. Dalrymple, D.H. Yeh, M.A. Trotz, Removing pharmaceuticals and endocrine-disrupting compounds from wastewater by photocatalysis, Journal of Chemical Technology & Biotechnology, 82 (2007) 121-134.

[13] S. Esplugas, D.M. Bila, L.G.T. Krause, M. Dezotti, Ozonation and advanced oxidation technologies to remove endocrine disrupting chemicals (EDCs) and pharmaceuticals and personal care products (PPCPs) in water effluents, J. Hazard. Mater., 149 (2007) 631-642.

[14] E. Chatzisymeon, S. Foteinis, D. Mantzavinos, T. Tsoutsos, Life cycle assessment of advanced oxidation processes for olive mill wastewater treatment, Journal of Cleaner Production, 54 (2013) 229-234.

[15] I. Muñoz, J. Rieradevall, F. Torrades, J. Peral, X. Domènech, Environmental assessment of different advanced oxidation processes applied to a bleaching Kraft mill effluent, Chemosphere, 62 (2006) 9-16.

[16] M.N. Chong, A.K. Sharma, S. Burn, C.P. Saint, Feasibility study on the application of advanced oxidation technologies for decentralised wastewater treatment, Journal of Cleaner Production, 35 (2012) 230-238.

[17] S. Malato, P. Fernández-Ibáñez, M.I. Maldonado, J. Blanco, W. Gernjak, Decontamination and disinfection of water by solar photocatalysis: Recent overview and trends, Catal. Today, 147 (2009) 1-59.

[18] J.J. Pignatello, E. Oliveros, A. MacKay, Advanced Oxidation Processes for Organic Contaminant Destruction Based on the Fenton Reaction and Related Chemistry, Crit. Rev. Environ. Sci. Technol., 36 (2006) 1-84.
[19] O. Legrini, E. Oliveros, A.M. Braun, Photochemical processes for water treatment, Chemical Reviews, 93 (1993) 671-698.
[20] EPA, Aquatic life criteria for contaminants of emerging concern, (2008).
[21] I.A. Stefanakis, A.J. Becker, A Review of Emerging Contaminants in Water: Classification, Sources, and Potential Risks, in: A.E. McKeown, B. George (Eds.) Impact of Water Pollution on Human Health and Environmental Sustainability, IGI Global, Hershey, PA, USA, 2016, pp. 55-80.
[22] D.J. Lapworth, N. Baran, M.E. Stuart, R.S. Ward, Emerging organic contaminants in groundwater: A review of sources, fate and occurrence, Environmental Pollution, 163 (2012) 287-303.
[23] N.S. Thomaidis, A.G. Asimakopoulos, A. Bletsou, Emerging contaminants: a tutorial mini-review, Global NEST Journal 14 (2012) 72-79.
[24] A. Zygler, A. Wasik, J. Namieśnik, Analytical methodologies for determination of artificial sweeteners in foodstuffs, TrAC, Trends Anal. Chem., 28 (2009) 1082-1102.
[25] K.R. Tandel, Sugar substitutes: Health controversy over perceived benefits, Journal of Pharmacology & Pharmacotherapeutics, 2 (2011) 236-243.
[26] S. Chattopadhyay, U. Raychaudhuri, R. Chakraborty, Artificial sweeteners – a review, Journal of Food Science and Technology, 51 (2014) 611-621.
[27] Y. Zhu, Y. Guo, M. Ye, F.S. James, Separation and simultaneous determination of four artificial sweeteners in food and beverages by ion chromatography, Journal of Chromatography A, 1085 (2005) 143-146.
[28] F.T. Lange, M. Scheurer, H.-J. Brauch, Artificial sweeteners—a recently recognized class of emerging environmental contaminants: a review, Anal. Bioanal. Chem., 403 (2012) 2503-2518.
[29] S.D. Richardson, T.A. Ternes, Water Analysis: Emerging Contaminants and Current Issues, Analytical Chemistry, (2017).
[30] A.G. Renwick, The metabolism of intense sweeteners, Xenobiotica, 16 (1986) 1057-1071.
[31] D.R. Van Stempvoort, J.W. Roy, S.J. Brown, G. Bickerton, Artificial sweeteners as potential tracers in groundwater in urban environments, Journal of Hydrology, 401 (2011) 126-133.
[32] M. Scheurer, F.R. Storck, H.-J. Brauch, F.T. Lange, Performance of conventional multi-barrier drinking water treatment plants for the removal of four artificial sweeteners, Water Res., 44 (2010) 3573-3584.
[33] M. Scheurer, H.-J. Brauch, F.T. Lange, Analysis and occurrence of seven artificial sweeteners in German waste water and surface water and in soil aquifer treatment (SAT), Anal. Bioanal. Chem., 394 (2009) 1585-1594.
[34] I.J. Buerge, H.-R. Buser, M. Kahle, M.D. Müller, T. Poiger, Ubiquitous Occurrence of the Artificial Sweetener Acesulfame in the Aquatic Environment: An Ideal Chemical Marker of Domestic Wastewater in Groundwater, Environ. Sci. Technol., 43 (2009) 4381-4385.
[35] K. Saucedo-Vence, A. Elizalde-Velázquez, O. Dublán-García, M. Galar-Martínez, H. Islas-Flores, N. SanJuan-Reyes, S. García-Medina, M.D. Hernández-Navarro, L.M. Gómez-Oliván, Toxicological hazard induced by sucralose to environmentally relevant concentrations in common carp (Cyprinus carpio), Science of The Total Environment, 575 (2017) 347-357.
[36] Y. Ren, J. Geng, F. Li, H. Ren, L. Ding, K. Xu, The oxidative stress in the liver of Carassius auratus exposed to acesulfame and its UV irradiance products, Sci. Total Environ., 571 (2016) 755-762.
[37] A.J. Li, O.J. Schmitz, S. Stephan, C. Lenzen, P.Y.-K. Yue, K. Li, H. Li, K.S.-Y. Leung, Photocatalytic transformation of acesulfame: Transformation products identification and embryotoxicity study, Water Research, 89 (2016) 68-75.
[38] WHO, Evaluations of the Joint FAO/WHO Expert Committee on Food Additives (JECFA), in: W.H. Organization (Ed.) WHO technical reports seriesGeneva, 1993.
[39] L. Oniciu, L. Mureşan, Some fundamental aspects of levelling and brightening in metal electrodeposition, Journal of Applied Electrochemistry, 21 (1991) 565-574.
[40] I.J. Buerge, M. Keller, H.-R. Buser, M.D. Müller, T. Poiger, Saccharin and Other Artificial Sweeteners in Soils: Estimated Inputs from Agriculture and Households, Degradation, and Leaching to Groundwater, Environ. Sci. Technol., 45 (2011) 615-621.
[41] Z. Gan, H. Sun, B. Feng, R. Wang, Y. Zhang, Occurrence of seven artificial sweeteners in the aquatic environment and precipitation of Tianjin, China, Water Res., 47 (2013) 4928-4937.

[42] Z. Sang, Y. Jiang, Y.-K. Tsoi, K.S.-Y. Leung, Evaluating the environmental impact of artificial sweeteners: A study of their distributions, photodegradation and toxicities, Water Research, 52 (2014) 260-274.
[43] S. Stolte, S. Steudte, N.H. Schebb, I. Willenberg, P. Stepnowski, Ecotoxicity of artificial sweeteners and stevioside, Environ. Int., 60 (2013) 123-127.
[44] PubChem Compound Database, National Center for Biotechnology Information.
[45] USEPA, Endocrine Disruptor Screening and Testing Advisory Committee (EDSTAC) - Final Report, Washington, DC: US Environmental Protection Agency, 1998.
[46] European Commision, Communication from the Commission to the Council and the European Parliament on the implementation of the Community Strategy for Endocrine Disrupters - a range of substances suspected of interfering with the hormone systems of humans and wildlife (COM (1999) 706).
[47] Z.-h. Liu, Y. Kanjo, S. Mizutani, Removal mechanisms for endocrine disrupting compounds (EDCs) in wastewater treatment — physical means, biodegradation, and chemical advanced oxidation: A review, Sci. Total Environ., 407 (2009) 731-748.
[48] C. Zhang, Y. Li, C. Wang, L. Niu, W. Cai, Occurrence of endocrine disrupting compounds in aqueous environment and their bacterial degradation: A review, Crit. Rev. Environ. Sci. Technol., 46 (2016) 1-59.
[49] T.A. Ternes, M. Stumpf, J. Mueller, K. Haberer, R.D. Wilken, M. Servos, Behavior and occurrence of estrogens in municipal sewage treatment plants — I. Investigations in Germany, Canada and Brazil, Sci. Total Environ., 225 (1999) 81-90.
[50] E. Benfenati, D. Barcelò, I. Johnson, S. Galassi, K. Levsen, Emerging organic contaminants in leachates from industrial waste landfills and industrial effluent, TrAC, Trends Anal. Chem., 22 (2003) 757-765.
[51] M. Petrović, S. Gonzalez, D. Barceló, Analysis and removal of emerging contaminants in wastewater and drinking water, TrAC, Trends Anal. Chem., 22 (2003) 685-696.
[52] M.P. Fernandez, M.G. Ikonomou, I. Buchanan, An assessment of estrogenic organic contaminants in Canadian wastewaters, Sci. Total Environ., 373 (2007) 250-269.
[53] C. Zhang, Y. Li, C. Wang, L. Niu, W. Cai, Occurrence of endocrine disrupting compounds in aqueous environment and their bacterial degradation: A review, Critical Reviews in Environmental Science and Technology, (2015) 00-00.
[54] Y. Sun, H. Huang, Y. Sun, C. Wang, X. Shi, H. Hu, T. Kameya, K. Fujie, Occurrence of estrogenic endocrine disrupting chemicals concern in sewage plant effluent, Frontiers of Environmental Science & Engineering, 8 (2014) 18-26.
[55] M. Giulivo, M. Lopez de Alda, E. Capri, D. Barceló, Human exposure to endocrine disrupting compounds: Their role in reproductive systems, metabolic syndrome and breast cancer. A review, Environmental Research, 151 (2016) 251-264.
[56] F. Maqbool, S. Mostafalou, H. Bahadar, M. Abdollahi, Review of endocrine disorders associated with environmental toxicants and possible involved mechanisms, Life Sciences, 145 (2016) 265-273.
[57] M. Joffe, ARE PROBLEMS WITH MALE REPRODUCTIVE HEALTH CAUSED BY ENDOCRINE DISRUPTION?, Occupational and Environmental Medicine, 58 (2001) 281-281.
[58] E. Greiner, T. Kaelin, K. Nakamura, Bisphenol A. CEH Report by SRI Consulting., 2007.
[59] T. Deblonde, C. Cossu-Leguille, P. Hartemann, Emerging pollutants in wastewater: A review of the literature, Int. J. Hyg. Environ. Health, 214 (2011) 442-448.
[60] ReportLinker, Bisphenol-A – A Global Market Overview, 2016.
[61] B.S. Rubin, Bisphenol A: An endocrine disruptor with widespread exposure and multiple effects, The Journal of Steroid Biochemistry and Molecular Biology, 127 (2011) 27-34.
[62] J.R. Rochester, Bisphenol A and human health: A review of the literature, Reprod. Toxicol., 42 (2013) 132-155.
[63] B. Kasprzyk-Hordern, R.M. Dinsdale, A.J. Guwy, The removal of pharmaceuticals, personal care products, endocrine disruptors and illicit drugs during wastewater treatment and its impact on the quality of receiving waters, Water Res., 43 (2009) 363-380.
[64] S. Martin Ruel, M. Esperanza, J.M. Choubert, I. Valor, H. Budzinski, M. Coquery, On-site evaluation of the efficiency of conventional and advanced secondary processes for the removal of 60 organic micropollutants, Water science and technology : a journal of the International Association on Water Pollution Research, 62 (2010) 2970.

[65] Y. Nie, Z. Qiang, H. Zhang, W. Ben, Fate and seasonal variation of endocrine-disrupting chemicals in a sewage treatment plant with A/A/O process, Separation and Purification Technology, 84 (2012) 9-15.
[66] P. Pothitou, D. Voutsa, Endocrine disrupting compounds in municipal and industrial wastewater treatment plants in Northern Greece, Chemosphere, 73 (2008) 1716-1723.
[67] R. Rosal, A. Rodríguez, J.A. Perdigón-Melón, A. Petre, E. García-Calvo, M.J. Gómez, A. Agüera, A.R. Fernández-Alba, Occurrence of emerging pollutants in urban wastewater and their removal through biological treatment followed by ozonation, Water Res., 44 (2010) 578-588.
[68] S. Terzić, I. Senta, M. Ahel, M. Gros, M. Petrović, D. Barcelo, J. Müller, T. Knepper, I. Martí, F. Ventura, P. Jovančić, D. Jabučar, Occurrence and fate of emerging wastewater contaminants in Western Balkan Region, Science of The Total Environment, 399 (2008) 66-77.
[69] C.-P. Yu, K.-H. Chu, Occurrence of pharmaceuticals and personal care products along the West Prong Little Pigeon River in east Tennessee, USA, Chemosphere, 75 (2009) 1281-1286.
[70] S. Kleywegt, V. Pileggi, P. Yang, C. Hao, X. Zhao, C. Rocks, S. Thach, P. Cheung, B. Whitehead, Pharmaceuticals, hormones and bisphenol A in untreated source and finished drinking water in Ontario, Canada — Occurrence and treatment efficiency, Sci. Total Environ., 409 (2011) 1481-1488.
[71] X. Peng, Y. Yu, C. Tang, J. Tan, Q. Huang, Z. Wang, Occurrence of steroid estrogens, endocrine-disrupting phenols, and acid pharmaceutical residues in urban riverine water of the Pearl River Delta, South China, Science of The Total Environment, 397 (2008) 158-166.
[72] J. Regnery, W. Püttmann, Occurrence and fate of organophosphorus flame retardants and plasticizers in urban and remote surface waters in Germany, Water Research, 44 (2010) 4097-4104.
[73] A.S. Stasinakis, G. Gatidou, D. Mamais, N.S. Thomaidis, T.D. Lekkas, Occurrence and fate of endocrine disrupters in Greek sewage treatment plants, Water Research, 42 (2008) 1796-1804.
[74] J.-W. Kim, H.-S. Jang, J.-G. Kim, H. Ishibashi, M. Hirano, K. Nasu, N. Ichikawa, Y. Takao, R. Shinohara, K. Arizono, Occurrence of Pharmaceutical and Personal Care Products (PPCPs) in Surface Water from Mankyung River, South Korea, Journal of Health Science, 55 (2009) 249-258.
[75] R. Loos, G. Locoro, S. Comero, S. Contini, D. Schwesig, F. Werres, P. Balsaa, O. Gans, S. Weiss, L. Blaha, M. Bolchi, B.M. Gawlik, Pan-European survey on the occurrence of selected polar organic persistent pollutants in ground water, Water Res., 44 (2010) 4115-4126.
[76] K.K. Barnes, D.W. Kolpin, E.T. Furlong, S.D. Zaugg, M.T. Meyer, L.B. Barber, A national reconnaissance of pharmaceuticals and other organic wastewater contaminants in the United States — I) Groundwater, Science of The Total Environment, 402 (2008) 192-200.
[77] L.N. Vandenberg, T. Colborn, T.B. Hayes, J.J. Heindel, J.D.R. Jacobs, D.-H. Lee, T. Shioda, A.M. Soto, F.S. vom Saal, W.V. Welshons, R.T. Zoeller, J.P. Myers, Hormones and Endocrine-Disrupting Chemicals: Low-Dose Effects and Nonmonotonic Dose Responses, Endocr. Rev., 33 (2012) 378-455.
[78] S. Ehrlich, P.L. Williams, S.A. Missmer, J.A. Flaws, X. Ye, A.M. Calafat, J.C. Petrozza, D. Wright, R. Hauser, Urinary bisphenol A concentrations and early reproductive health outcomes among women undergoing IVF, Human Reproduction, 27 (2012) 3583-3592.
[79] M.L. E., E. S., W.P. L., P. J., W.D. L., C.A. M., Y. X., H. R., Urinary bisphenol A concentrations and ovarian response among women undergoing IVF, International Journal of Andrology, 33 (2010) 385-393.
[80] M.S. Bloom, D. Kim, F.S. vom Saal, J.A. Taylor, G. Cheng, J.D. Lamb, V.Y. Fujimoto, Bisphenol A exposure reduces the estradiol response to gonadotropin stimulation during in vitro fertilization, Fertility and Sterility, 96 (2011) 672-677.e672.
[81] V.Y. Fujimoto, D. Kim, F.S. vom Saal, J.D. Lamb, J.A. Taylor, M.S. Bloom, Serum unconjugated bisphenol A concentrations in women may adversely influence oocyte quality during in vitro fertilization, Fertility and Sterility, 95 (2011) 1816-1819.
[82] P.G. Signorile, E.P. Spugnini, L. Mita, P. Mellone, A. D'Avino, M. Bianco, N. Diano, L. Caputo, F. Rea, R. Viceconte, M. Portaccio, E. Viggiano, G. Citro, R. Pierantoni, V. Sica, B. Vincenzi, D.G. Mita, F. Baldi, A. Baldi, Pre-natal exposure of mice to bisphenol A elicits an endometriosis-like phenotype in female offspring, General and Comparative Endocrinology, 168 (2010) 318-325.
[83] E. Kandaraki, A. Chatzigeorgiou, S. Livadas, E. Palioura, F. Economou, M. Koutsilieris, S. Palimeri, D. Panidis, E. Diamanti-Kandarakis, Endocrine Disruptors and Polycystic Ovary Syndrome (PCOS): Elevated Serum Levels of Bisphenol A in Women with PCOS, The Journal of Clinical Endocrinology & Metabolism, 96 (2011) E480-E484.

[84] T. Takeuchi, O. Tsutsumi, Y. Ikezuki, Y. Takai, Y. Taketani, Positive Relationship between Androgen and the Endocrine Disruptor, Bisphenol A, in Normal Women and Women with Ovarian Dysfunction, Endocr. J., 51 (2004) 165-169.
[85] A. Shankar, S. Teppala, Relationship between Urinary Bisphenol A Levels and Diabetes Mellitus, The Journal of Clinical Endocrinology & Metabolism, 96 (2011) 3822-3826.
[86] M. Sugiura-Ogasawara, Y. Ozaki, S.-i. Sonta, T. Makino, K. Suzumori, Exposure to bisphenol A is associated with recurrent miscarriage, Human Reproduction, 20 (2005) 2325-2329.
[87] D. Cantonwine, J.D. Meeker, H. Hu, B.N. Sánchez, H. Lamadrid-Figueroa, A. Mercado-García, G.Z. Fortenberry, A.M. Calafat, M.M. Téllez-Rojo, Bisphenol a exposure in Mexico City and risk of prematurity: a pilot nested case control study, Environ. Health, 9 (2010) 62.
[88] D. Melzer, P. Gates, N.J. Osborn, W.E. Henley, R. Cipelli, A. Young, C. Money, P. McCormack, P. Schofield, D. Mosedale, D. Grainger, T.S. Galloway, Urinary Bisphenol A Concentration and Angiography-Defined Coronary Artery Stenosis, PLOS ONE, 7 (2012) e43378.
[89] S. Flint, T. Markle, S. Thompson, E. Wallace, Bisphenol A exposure, effects, and policy: A wildlife perspective, J. Environ. Manage., 104 (2012) 19-34.
[90] WHO, Pharmaceuticals in drinking-water, 2012.
[91] K. Kümmerer, The presence of pharmaceuticals in the environment due to human use – present knowledge and future challenges, J. Environ. Manage., 90 (2009) 2354-2366.
[92] PILLS, Pharmaceutical residues in the aquatic system-a challenge for the future, PILLS final conference Gelsenkirchen, Germany, 2012.
[93] M.L. Richardson, J.M. Bowron, The fate of pharmaceutical chemicals in the aquatic environment, Journal of Pharmacy and Pharmacology, 37 (1985) 1-12.
[94] J.L. Wilkinson, P.S. Hooda, J. Barker, S. Barton, J. Swinden, Ecotoxic pharmaceuticals, personal care products, and other emerging contaminants: A review of environmental, receptor-mediated, developmental, and epigenetic toxicity with discussion of proposed toxicity to humans, Crit. Rev. Environ. Sci. Technol., 46 (2016) 336-381.
[95] S.R. de Solla, È.A.M. Gilroy, J.S. Klinck, L.E. King, R. McInnis, J. Struger, S.M. Backus, P.L. Gillis, Bioaccumulation of pharmaceuticals and personal care products in the unionid mussel Lasmigona costata in a river receiving wastewater effluent, Chemosphere, 146 (2016) 486-496.
[96] H. Gong, W. Chu, M. Chen, Q. Wang, A systematic study on photocatalysis of antipyrine: Catalyst characterization, parameter optimization, reaction mechanism and toxicity evolution to plankton, Water Res., 112 (2017) 167-175.
[97] T.A. Ternes, Occurrence of drugs in German sewage treatment plants and rivers1Dedicated to Professor Dr. Klaus Haberer on the occasion of his 70th birthday.1, Water Research, 32 (1998) 3245-3260.
[98] S. Zühlke, U. Dünnbier, T. Heberer, Detection and identification of phenazone-type drugs and their microbial metabolites in ground and drinking water applying solid-phase extraction and gas chromatography with mass spectrometric detection, Journal of Chromatography A, 1050 (2004) 201-209.
[99] S. Wiegel, A. Aulinger, R. Brockmeyer, H. Harms, J. Löffler, H. Reincke, R. Schmidt, B. Stachel, W. von Tümpling, A. Wanke, Pharmaceuticals in the river Elbe and its tributaries, Chemosphere, 57 (2004) 107-126.
[100] K. Reddersen, T. Heberer, U. Dünnbier, Identification and significance of phenazone drugs and their metabolites in ground- and drinking water, Chemosphere, 49 (2002) 539-544.
[101] Y. Valcárcel, S.G. Alonso, J.L. Rodríguez-Gil, R.R. Maroto, A. Gil, M. Catalá, Analysis of the presence of cardiovascular and analgesic/anti-inflammatory/antipyretic pharmaceuticals in river- and drinking-water of the Madrid Region in Spain, Chemosphere, 82 (2011) 1062-1071.
[102] M. Cai, L. Zhang, F. Qi, L. Feng, Influencing factors and degradation products of antipyrine chlorination in water with free chlorine, Journal of Environmental Sciences, 25 (2013) 77-84.
[103] I. Michael, L. Rizzo, C.S. McArdell, C.M. Manaia, C. Merlin, T. Schwartz, C. Dagot, D. Fatta-Kassinos, Urban wastewater treatment plants as hotspots for the release of antibiotics in the environment: A review, Water Res., 47 (2013) 957-995.
[104] Metcalf, amp, I. Eddy, Wastewater engineering : collection, treatment, disposal, New York : McGraw-Hill, New York, 1972.
[105] P. Verlicchi, M. Al Aukidy, E. Zambello, Occurrence of pharmaceutical compounds in urban wastewater: Removal, mass load and environmental risk after a secondary treatment—A review, Science of The Total Environment, 429 (2012) 123-155.

[106] N.H. Tran, J. Gan, V.T. Nguyen, H. Chen, L. You, A. Duarah, L. Zhang, K.Y.-H. Gin, Sorption and biodegradation of artificial sweeteners in activated sludge processes, Bioresource Technology, 197 (2015) 329-338.
[107] A. Svenson, A.-S. Allard, M. Ek, Removal of estrogenicity in Swedish municipal sewage treatment plants, Water Res., 37 (2003) 4433-4443.
[108] H. Andersen, H. Siegrist, B. Halling-Sørensen, T.A. Ternes, Fate of Estrogens in a Municipal Sewage Treatment Plant, Environ. Sci. Technol., 37 (2003) 4021-4026.
[109] O. Braga, G.A. Smythe, A.I. Schäfer, A.J. Feitz, Fate of Steroid Estrogens in Australian Inland and Coastal Wastewater Treatment Plants, Environ. Sci. Technol., 39 (2005) 3351-3358.
[110] H.R. Rogers, Sources, behaviour and fate of organic contaminants during sewage treatment and in sewage sludges, Sci. Total Environ., 185 (1996) 3-26.
[111] E. Fernandez-Fontaina, F. Omil, J.M. Lema, M. Carballa, Influence of nitrifying conditions on the biodegradation and sorption of emerging micropollutants, Water Research, 46 (2012) 5434-5444.
[112] S. Suarez, J.M. Lema, F. Omil, Removal of Pharmaceutical and Personal Care Products (PPCPs) under nitrifying and denitrifying conditions, Water Research, 44 (2010) 3214-3224.
[113] A. Göbel, C.S. McArdell, A. Joss, H. Siegrist, W. Giger, Fate of sulfonamides, macrolides, and trimethoprim in different wastewater treatment technologies, Science of The Total Environment, 372 (2007) 361-371.
[114] M. Clara, B. Strenn, N. Kreuzinger, Carbamazepine as a possible anthropogenic marker in the aquatic environment: investigations on the behaviour of Carbamazepine in wastewater treatment and during groundwater infiltration, Water Research, 38 (2004) 947-954.
[115] M. Köck-Schulmeyer, M. Villagrasa, M. López de Alda, R. Céspedes-Sánchez, F. Ventura, D. Barceló, Occurrence and behavior of pesticides in wastewater treatment plants and their environmental impact, Science of The Total Environment, 458-460 (2013) 466-476.
[116] EC, Priority substances under the Water Framework Directive.
[117] I. Oller, S. Malato, J.A. Sánchez-Pérez, Combination of Advanced Oxidation Processes and biological treatments for wastewater decontamination—A review, Science of The Total Environment, 409 (2011) 4141-4166.
[118] R. Andreozzi, V. Caprio, A. Insola, R. Marotta, Advanced oxidation processes (AOP) for water purification and recovery, Catal. Today, 53 (1999) 51-59.
[119] C. Comninellis, A. Kapalka, S. Malato, S.A. Parsons, I. Poulios, D. Mantzavinos, Advanced oxidation processes for water treatment: advances and trends for R&D, Journal of Chemical Technology and Biotechnology, 83 (2008) 769-776.
[120] J.-M. Herrmann, Heterogeneous photocatalysis: fundamentals and applications to the removal of various types of aqueous pollutants, Catalysis Today, 53 (1999) 115-129.
[121] A. Fujishima, T.N. Rao, D.A. Tryk, Titanium dioxide photocatalysis, Journal of Photochemistry and Photobiology C: Photochemistry Reviews, 1 (2000) 1-21.
[122] B. Ohtani, Chapter 5 - Principle of Photocatalysis and Design of Active Photocatalysts A2 - Suib, Steven L, New and Future Developments in Catalysis, Elsevier, Amsterdam, 2013, pp. 121-144.
[123] H. Dong, G. Zeng, L. Tang, C. Fan, C. Zhang, X. He, Y. He, An overview on limitations of TiO2-based particles for photocatalytic degradation of organic pollutants and the corresponding countermeasures, Water Research, 79 (2015) 128-146.
[124] D. Dionysiou Dionysios, L. Puma Gianluca, J. Ye, J. Schneider, D. Bahnemann, Solar Photocatalysis: Fundamentals, Reactors and Applications, Royal Society of Chemistry2016.
[125] A. Fujishima, X. Zhang, D.A. Tryk, TiO2 photocatalysis and related surface phenomena, Surface Science Reports, 63 (2008) 515-582.
[126] M.N. Chong, B. Jin, C.W.K. Chow, C. Saint, Recent developments in photocatalytic water treatment technology: A review, Water Res., 44 (2010) 2997-3027.
[127] D. Dimitrakopoulou, I. Rethemiotaki, Z. Frontistis, N.P. Xekoukoulotakis, D. Venieri, D. Mantzavinos, Degradation, mineralization and antibiotic inactivation of amoxicillin by UV-A/TiO2 photocatalysis, Journal of Environmental Management, 98 (2012) 168-174.
[128] V.M. Daskalaki, Z. Frontistis, D. Mantzavinos, A. Katsaounis, Solar light-induced degradation of bisphenol-A with TiO2 immobilized on Ti, Catalysis Today, 161 (2011) 110-114.
[129] K. Sornalingam, A. McDonagh, J.L. Zhou, Photodegradation of estrogenic endocrine disrupting steroidal hormones in aqueous systems: Progress and future challenges, Sci. Total Environ., 550 (2016) 209-224.

[130] C. Berberidou, V. Kitsiou, E. Kazala, D.A. Lambropoulou, A. Kouras, C.I. Kosma, T.A. Albanis, I. Poulios, Study of the decomposition and detoxification of the herbicide bentazon by heterogeneous photocatalysis: Kinetics, intermediates and transformation pathways, Applied Catalysis B: Environmental, 200 (2017) 150-163.
[131] Y. He, N.B. Sutton, H.H.H. Rijnaarts, A.A.M. Langenhoff, Degradation of pharmaceuticals in wastewater using immobilized TiO2 photocatalysis under simulated solar irradiation, Applied Catalysis B: Environmental, 182 (2016) 132-141.
[132] A. Mirzaei, L. Yerushalmi, Z. Chen, F. Haghighat, J. Guo, Enhanced photocatalytic degradation of sulfamethoxazole by zinc oxide photocatalyst in the presence of fluoride ions: Optimization of parameters and toxicological evaluation, Water Res., 132 (2018) 241-251.
[133] K. Zaharieva, V. Rives, M. Tsvetkov, Z. Cherkezova-Zheleva, B. Kunev, R. Trujillano, I. Mitov, M. Milanova, Preparation, characterization and application of nanosized copper ferrite photocatalysts for dye degradation under UV irradiation, Mater. Chem. Phys., 160 (2015) 271-278.
[134] M.L. Yola, T. Eren, N. Atar, A novel efficient photocatalyst based on TiO2 nanoparticles involved boron enrichment waste for photocatalytic degradation of atrazine, Chem. Eng. J., 250 (2014) 288-294.
[135] S. Malato, P. Fernandez-Ibanez, I. Oller, I. Polo, M.I. Maldonado, S. Miralles-Cuevas, R. Sanchez, CHAPTER 6 Process Integration. Concepts of Integration and Coupling of Photocatalysis with Other Processes, Photocatalysis: Applications, The Royal Society of Chemistry2016, pp. 157-173.
[136] S. Kaneco, M.A. Rahman, T. Suzuki, H. Katsumata, K. Ohta, Optimization of solar photocatalytic degradation conditions of bisphenol A in water using titanium dioxide, Journal of Photochemistry and Photobiology A: Chemistry, 163 (2004) 419-424.
[137] E. Chatzisymeon, E. Stypas, S. Bousios, N.P. Xekoukoulotakis, D. Mantzavinos, Photocatalytic treatment of black table olive processing wastewater, J. Hazard. Mater., 154 (2008) 1090-1097.
[138] M.A. Henderson, A surface science perspective on TiO2 photocatalysis, Surface Science Reports, 66 (2011) 185-297.
[139] M. Pelaez, N.T. Nolan, S.C. Pillai, M.K. Seery, P. Falaras, A.G. Kontos, P.S.M. Dunlop, J.W.J. Hamilton, J.A. Byrne, K. O'Shea, M.H. Entezari, D.D. Dionysiou, A review on the visible light active titanium dioxide photocatalysts for environmental applications, Applied Catalysis B: Environmental, 125 (2012) 331-349.
[140] M.V. Dozzi, E. Selli, Doping TiO2 with p-block elements: Effects on photocatalytic activity, Journal of Photochemistry and Photobiology C: Photochemistry Reviews, 14 (2013) 13-28.
[141] S.G. Kumar, L.G. Devi, Review on Modified TiO2 Photocatalysis under UV/Visible Light: Selected Results and Related Mechanisms on Interfacial Charge Carrier Transfer Dynamics, The Journal of Physical Chemistry A, 115 (2011) 13211-13241.
[142] R. Daghrir, P. Drogui, D. Robert, Modified TiO2 For Environmental Photocatalytic Applications: A Review, Industrial & Engineering Chemistry Research, 52 (2013) 3581-3599.
[143] S. Rehman, R. Ullah, A.M. Butt, N.D. Gohar, Strategies of making TiO2 and ZnO visible light active, Journal of Hazardous Materials, 170 (2009) 560-569.
[144] H. Zhang, G. Chen, D.W. Bahnemann, Photoelectrocatalytic materials for environmental applications, J. Mater. Chem., 19 (2009) 5089-5121.
[145] A.H. Zyoud, N. Zaatar, I. Saadeddin, C. Ali, D. Park, G. Campet, H.S. Hilal, CdS-sensitized TiO2 in phenazopyridine photo-degradation: Catalyst efficiency, stability and feasibility assessment, J. Hazard. Mater., 173 (2010) 318-325.
[146] A.K. Jana, Solar cells based on dyes, Journal of Photochemistry and Photobiology A: Chemistry, 132 (2000) 1-17.
[147] D. Chatterjee, A. Mahata, Visible light induced photodegradation of organic pollutants on dye adsorbed TiO2 surface, Journal of Photochemistry and Photobiology A: Chemistry, 153 (2002) 199-204.
[148] K. Nakata, A. Fujishima, TiO2 photocatalysis: Design and applications, Journal of Photochemistry and Photobiology C: Photochemistry Reviews, 13 (2012) 169-189.
[149] A. Pichavant, E. Provost, M.-H. Berger, W. Fürst, J.-F. Hochepied, Interfaced titanium dioxide anatase–rutile nanocomposites by thermohydrolysis in presence of small amounts of Sn(IV) and their photocatalytic properties, Colloids Surf. Physicochem. Eng. Aspects, 462 (2014) 64-68.
[150] G. Li, K.A. Gray, The solid–solid interface: Explaining the high and unique photocatalytic reactivity of TiO2-based nanocomposite materials, Chemical Physics, 339 (2007) 173-187.

[151] A.G. Agrios, K.A. Gray, E. Weitz, Narrow-Band Irradiation of a Homologous Series of Chlorophenols on TiO2: Charge-Transfer Complex Formation and Reactivity, Langmuir, 20 (2004) 5911-5917.
[152] K. Komaguchi, T. Maruoka, H. Nakano, I. Imae, Y. Ooyama, Y. Harima, Electron-Transfer Reaction of Oxygen Species on TiO2 Nanoparticles Induced by Sub-band-gap Illumination, The Journal of Physical Chemistry C, 114 (2010) 1240-1245.
[153] M. Yan, F. Chen, J. Zhang, M. Anpo, Preparation of Controllable Crystalline Titania and Study on the Photocatalytic Properties, The Journal of Physical Chemistry B, 109 (2005) 8673-8678.
[154] T. Ohno, K. Tokieda, S. Higashida, M. Matsumura, Synergism between rutile and anatase TiO2 particles in photocatalytic oxidation of naphthalene, Applied Catalysis A: General, 244 (2003) 383-391.
[155] L. Zhao, M. Han, J. Lian, Photocatalytic activity of TiO2 films with mixed anatase and rutile structures prepared by pulsed laser deposition, Thin Solid Films, 516 (2008) 3394-3398.
[156] S.A. Tomás, A. Luna-Resendis, L.C. Cortés-Cuautli, D. Jacinto, Optical and morphological characterization of photocatalytic TiO2 thin films doped with silver, Thin Solid Films, 518 (2009) 1337-1340.
[157] L. Andronic, A. Duta, TiO2 thin films for dyes photodegradation, Thin Solid Films, 515 (2007) 6294-6297.
[158] R.L. Pozzo, M.A. Baltanás, A.E. Cassano, Supported titanium oxide as photocatalyst in water decontamination: State of the art, Catalysis Today, 39 (1997) 219-231.
[159] D. Chen, F. Li, A.K. Ray, Effect of mass transfer and catalyst layer thickness on photocatalytic reaction, AIChE Journal, 46 (2000) 1034-1045.
[160] S. Zhou, A.K. Ray, Kinetic Studies for Photocatalytic Degradation of Eosin B on a Thin Film of Titanium Dioxide, Industrial & Engineering Chemistry Research, 42 (2003) 6020-6033.
[161] S. Zhang, H. Jiang, Y. Liu, R. Chen, High catalytic efficiency of Pd nanoparticles immobilized on TiO2 nanorods-coated ceramic membranes, The Canadian Journal of Chemical Engineering, 95 (2017) 2374-2382.
[162] P. Wronski, J. Surmacki, H. Abramczyk, A. Adamus, M. Nowosielska, W. Maniukiewicz, M. Kozanecki, M. Szadkowska-Nicze, Surface, optical and photocatalytic properties of silica-supported TiO2 treated with electron beam, Radiation Physics and Chemistry, 109 (2015) 40-47.
[163] S. Bagheri, Z.A. Mohd Hir, A. Termeh Yousefi, S.B. Abd Hamid, Photocatalytic performance of activated carbon-supported mesoporous titanium dioxide, Desalination and Water Treatment, 57 (2016) 10859-10865.
[164] S. Nagarajan, N. Rajendran, Surface characterisation and electrochemical behaviour of porous titanium dioxide coated 316L stainless steel for orthopaedic applications, Applied Surface Science, 255 (2009) 3927-3932.
[165] H. Weinrib, A. Meiri, H. Duadi, D. Fixler, Uniformly Immobilizing Gold Nanorods on a Glass Substrate, Journal of Atomic, Molecular, and Optical Physics, 2012 (2012) 6.
[166] D.F. Ollis, E. Pelizzetti, N. Serpone, Photocatalyzed destruction of water contaminants, Environ. Sci. Technol., 25 (1991) 1522-1529.
[167] H. Zangeneh, A.A.L. Zinatizadeh, M. Habibi, M. Akia, M. Hasnain Isa, Photocatalytic oxidation of organic dyes and pollutants in wastewater using different modified titanium dioxides: A comparative review, Journal of Industrial and Engineering Chemistry, 26 (2015) 1-36.
[168] J. Engweiler, J. Harf, A. Baiker, WOx/TiO2Catalysts Prepared by Grafting of Tungsten Alkoxides: Morphological Properties and Catalytic Behavior in the Selective Reduction of NO by NH3, Journal of Catalysis, 159 (1996) 259-269.
[169] O. Tokode, R. Prabhu, L.A. Lawton, P.K.J. Robertson, UV LED Sources for Heterogeneous Photocatalysis, in: D.W. Bahnemann, P.K.J. Robertson (Eds.) Environmental Photochemistry Part III, Springer Berlin Heidelberg, Berlin, Heidelberg, 2015, pp. 159-179.
[170] W.-K. Jo, R.J. Tayade, New Generation Energy-Efficient Light Source for Photocatalysis: LEDs for Environmental Applications, Industrial & Engineering Chemistry Research, 53 (2014) 2073-2084.
[171] G. Matafonova, V. Batoev, Recent advances in application of UV light-emitting diodes for degrading organic pollutants in water through advanced oxidation processes: A review, Water Res., 132 (2018) 177-189.
[172] K. Natarajan, T.S. Natarajan, H.C. Bajaj, R.J. Tayade, Photocatalytic reactor based on UV-LED/TiO2 coated quartz tube for degradation of dyes, Chem. Eng. J., 178 (2011) 40-49.

[173] H. Hossaini, G. Moussavi, M. Farrokhi, The investigation of the LED-activated FeFNS-TiO2 nanocatalyst for photocatalytic degradation and mineralization of organophosphate pesticides in water, Water Res., 59 (2014) 130-144.
[174] USEPA, Air Quality Criteria for Ozone and Related Photochemical Oxidants. National Center for Environmental Assessment-RTP Office, Office of Research and Development, US Environmental Protection Agency, Research Triangle Park, North Carolina, USA., 2006.
[175] N.N. Mahamuni, Y.G. Adewuyi, Advanced oxidation processes (AOPs) involving ultrasound for waste water treatment: A review with emphasis on cost estimation, Ultrason. Sonochem., 17 (2010) 990-1003.
[176] E. Chatzisymeon, S. Foteinis, D. Mantzavinos, T. Tsoutsos, Life cycle assessment of advanced oxidation processes for olive mill wastewater treatment, Journal of Cleaner Production, 54 (2013) 229-234.
[177] E.M. Saggioro, A.S. Oliveira, T. Pavesi, M.J. Tototzintle, M.I. Maldonado, F.V. Correia, J.C. Moreira, Solar CPC pilot plant photocatalytic degradation of bisphenol A in waters and wastewaters using suspended and supported-TiO2. Influence of photogenerated species, Environmental Science and Pollution Research, 21 (2014) 12112-12121.
[178] E.F. Duffy, F. Al Touati, S.C. Kehoe, O.A. McLoughlin, L.W. Gill, W. Gernjak, I. Oller, M.I. Maldonado, S. Malato, J. Cassidy, R.H. Reed, K.G. McGuigan, A novel TiO2-assisted solar photocatalytic batch-process disinfection reactor for the treatment of biological and chemical contaminants in domestic drinking water in developing countries, Solar Energy, 77 (2004) 649-655.
[179] S. Malato, J. Blanco, J. Cáceres, A.R. Fernández-Alba, A. Agüera, A. Rodríguez, Photocatalytic treatment of water-soluble pesticides by photo-Fenton and TiO2 using solar energy, Catalysis Today, 76 (2002) 209-220.
[180] A. Bernabeu, R.F. Vercher, L. Santos-Juanes, P.J. Simón, C. Lardín, M.A. Martínez, J.A. Vicente, R. González, C. Llosá, A. Arques, A.M. Amat, Solar photocatalysis as a tertiary treatment to remove emerging pollutants from wastewater treatment plant effluents, Catal. Today, 161 (2011) 235-240.
[181] L. Prieto-Rodriguez, S. Miralles-Cuevas, I. Oller, A. Agüera, G.L. Puma, S. Malato, Treatment of emerging contaminants in wastewater treatment plants (WWTP) effluents by solar photocatalysis using low TiO2 concentrations, J. Hazard. Mater., 211-212 (2012) 131-137.
[182] P.S.M. Dunlop, M. Ciavola, L. Rizzo, J.A. Byrne, Inactivation and injury assessment of Escherichia coli during solar and photocatalytic disinfection in LDPE bags, Chemosphere, 85 (2011) 1160-1166.
[183] J.A. Byrne, P.A. Fernandez-Ibañez, P.S.M. Dunlop, D.M.A. Alrousan, J.W.J. Hamilton, Photocatalytic Enhancement for Solar Disinfection of Water: A Review, International Journal of Photoenergy, 2011 (2011) 12.
[184] I.K. Konstantinou, T.M. Sakellarides, V.A. Sakkas, T.A. Albanis, Photocatalytic Degradation of Selected s-Triazine Herbicides and Organophosphorus Insecticides over Aqueous TiO2 Suspensions, Environ. Sci. Technol., 35 (2001) 398-405.
[185] S. Malato, J. Blanco, C. Richter, B. Milow, M.I. Maldonado, Solar photocatalytic mineralization of commercial pesticides: Methamidophos, Chemosphere, 38 (1999) 1145-1156.
[186] W.-K. Jo, G.T. Park, R.J. Tayade, Synergetic effect of adsorption on degradation of malachite green dye under blue LED irradiation using spiral-shaped photocatalytic reactor, Journal of Chemical Technology & Biotechnology, 90 (2015) 2280-2289.
[187] Y. Ku, S.-J. Shiu, H.-C. Wu, Decomposition of dimethyl phthalate in aqueous solution by UV–LED/TiO2 process under periodic illumination, Journal of Photochemistry and Photobiology A: Chemistry, 332 (2017) 299-305.
[188] E. Korovin, D. Selishchev, A. Besov, D. Kozlov, UV-LED TiO2 photocatalytic oxidation of acetone vapor: Effect of high frequency controlled periodic illumination, Applied Catalysis B: Environmental, 163 (2015) 143-149.
[189] G.Y. Lui, D. Roser, R. Corkish, N. Ashbolt, P. Jagals, R. Stuetz, Photovoltaic powered ultraviolet and visible light-emitting diodes for sustainable point-of-use disinfection of drinking waters, Science of The Total Environment, 493 (2014) 185-196.
[190] L. Zhu, L. Cui, Q. Huang, Y. Wang, M. Vivar, Y. Jin, Y. Sun, Y. Cui, J. Fan, Performance study of SOL&PID system for the degradation of Acid Red 26 and 4-Chlorophenol, Energy Conversion and Management, 136 (2017) 361-371.

[191] D.H. Chen, X. Ye, K. Li, Oxidation of PCE with a UV LED Photocatalytic Reactor, Chemical Engineering & Technology, 28 (2005) 95-97.
[192] X. Wang, T.-T. Lim, Solvothermal synthesis of C–N codoped TiO2 and photocatalytic evaluation for bisphenol A degradation using a visible-light irradiated LED photoreactor, Applied Catalysis B: Environmental, 100 (2010) 355-364.
[193] D.P. Subagio, M. Srinivasan, M. Lim, T.-T. Lim, Photocatalytic degradation of bisphenol-A by nitrogen-doped TiO2 hollow sphere in a vis-LED photoreactor, Applied Catalysis B: Environmental, 95 (2010) 414-422.
[194] S.H. Kim, S.W. Lee, G.M. Lee, B.-T. Lee, S.-T. Yun, S.-O. Kim, Monitoring of TiO2-catalytic UV-LED photo-oxidation of cyanide contained in mine wastewater and leachate, Chemosphere, 143 (2016) 106-114.
[195] H. Hossaini, G. Moussavi, M. Farrokhi, The investigation of the LED-activated FeFNS-TiO2 nanocatalyst for photocatalytic degradation and mineralization of organophosphate pesticides in water, Water Research, 59 (2014) 130-144.
[196] S. Dominguez, M.J. Rivero, P. Gomez, R. Ibañez, I. Ortiz, Kinetic modeling and energy evaluation of sodium dodecylbenzenesulfonate photocatalytic degradation in a new LED reactor, Journal of Industrial and Engineering Chemistry, 37 (2016) 237-242.
[197] M.J. Arlos, R. Liang, M.M. Hatat-Fraile, L.M. Bragg, N.Y. Zhou, M.R. Servos, S.A. Andrews, Photocatalytic decomposition of selected estrogens and their estrogenic activity by UV-LED irradiated TiO2 immobilized on porous titanium sheets via thermal-chemical oxidation, J. Hazard. Mater., 318 (2016) 541-550.
[198] N. Jallouli, L.M. Pastrana-Martínez, A.R. Ribeiro, N.F.F. Moreira, J.L. Faria, O. Hentati, A.M.T. Silva, M. Ksibi, Heterogeneous photocatalytic degradation of ibuprofen in ultrapure water, municipal and pharmaceutical industry wastewaters using a TiO2/UV-LED system, Chemical Engineering Journal, 334 (2018) 976-984.
[199] P. Xiong, J. Hu, Decomposition of acetaminophen (Ace) using TiO2/UVA/LED system, Catalysis Today, 282 (2017) 48-56.
[200] R. Gorges, S. Meyer, G. Kreisel, Photocatalysis in microreactors, J. Photochem. Photobiol. A: Chem., 167 (2004) 95-99.
[201] Y. Matsushita, N. Ohba, S. Kumada, K. Sakeda, T. Suzuki, T. Ichimura, Photocatalytic reactions in microreactors, Chem. Eng. J., 135 (2008) S303-S308.
[202] A.-G. Rincón, C. Pulgarin, Effect of pH, inorganic ions, organic matter and H2O2 on E. coli K12 photocatalytic inactivation by TiO2: Implications in solar water disinfection, Applied Catalysis B: Environmental, 51 (2004) 283-302.
[203] M.A. Rauf, S.S. Ashraf, Fundamental principles and application of heterogeneous photocatalytic degradation of dyes in solution, Chemical Engineering Journal, 151 (2009) 10-18.
[204] D.M.A. Alrousan, P.S.M. Dunlop, T.A. McMurray, J.A. Byrne, Photocatalytic inactivation of E. coli in surface water using immobilised nanoparticle TiO2 films, Water Research, 43 (2009) 47-54.
[205] E.S. Tsimas, K. Tyrovola, N.P. Xekoukoulotakis, N.P. Nikolaidis, E. Diamadopoulos, D. Mantzavinos, Simultaneous photocatalytic oxidation of As(III) and humic acid in aqueous TiO2 suspensions, J. Hazard. Mater., 169 (2009) 376-385.
[206] M. Antonopoulou, C.G. Skoutelis, C. Daikopoulos, Y. Deligiannakis, I.K. Konstantinou, Probing the photolytic–photocatalytic degradation mechanism of DEET in the presence of natural or synthetic humic macromolecules using molecular-scavenging techniques and EPR spectroscopy, Journal of Environmental Chemical Engineering, 3 (2015) 3005-3014.
[207] C. Tang, V. Chen, The photocatalytic degradation of reactive black 5 using TiO2/UV in an annular photoreactor, Water Research, 38 (2004) 2775-2781.
[208] J. Tijani, O. Fatoba, L.F. Petrik, A Review of Pharmaceuticals and Endocrine-Disrupting Compounds: Sources, Effects, Removal, and Detections, Water, Air, Soil Pollut., 224 (2013) 1-29.
[209] J.-C. Sin, S.-M. Lam, A.R. Mohamed, K.-T. Lee, Degrading Endocrine Disrupting Chemicals from Wastewater by TiO2 Photocatalysis: A Review, International Journal of Photoenergy, 2012 (2012).
[210] A. Cesaro, V. Belgiorno, Removal of endocrine disruptors from urban wastewater by advanced oxidation processes (AOPs): A review, Open Biotechnology Journal, 10 (2016) 151-172.
[211] M. Gmurek, M. Olak-Kucharczyk, S. Ledakowicz, Photochemical decomposition of endocrine disrupting compounds – A review, Chem. Eng. J., 310 (2017) 437-456.

[212] C. Byrne, G. Subramanian, S.C. Pillai, Recent advances in photocatalysis for environmental applications, Journal of Environmental Chemical Engineering, (2017).
[213] V. Homem, L. Santos, Degradation and removal methods of antibiotics from aqueous matrices – A review, J. Environ. Manage., 92 (2011) 2304-2347.
[214] K. Ikehata, N. Jodeiri Naghashkar, M. Gamal El-Din, Degradation of Aqueous Pharmaceuticals by Ozonation and Advanced Oxidation Processes: A Review, Ozone: Science & Engineering, 28 (2006) 353-414.
[215] P. Calza, V.A. Sakkas, C. Medana, A.D. Vlachou, F. Dal Bello, T.A. Albanis, Chemometric assessment and investigation of mechanism involved in photo-Fenton and TiO2 photocatalytic degradation of the artificial sweetener sucralose in aqueous media, Applied Catalysis B: Environmental, 129 (2013) 71-79.
[216] P. Calza, C. Gionco, M. Giletta, M. Kalaboka, V.A. Sakkas, T. Albanis, M.C. Paganini, Assessment of the abatement of acelsulfame K using cerium doped ZnO as photocatalyst, Journal of Hazardous Materials, 323, Part A (2017) 471-477.
[217] M.J. López-Muñoz, A. Daniele, M. Zorzi, C. Medana, P. Calza, Investigation of the photocatalytic transformation of acesulfame K in the presence of different TiO2-based materials, Chemosphere, 193 (2018) 151-159.
[218] S.W. Chen, W.C. Li, Z.G. Sun, H.Y. Xie, Degradation of Artificial Sweetener Saccharin Sodium by Advanced Oxidation Technology, Applied Mechanics and Materials, 448-453 (2014) 7-10.
[219] W.-T. Tsai, M.-K. Lee, T.-Y. Su, Y.-M. Chang, Photodegradation of bisphenol-A in a batch TiO2 suspension reactor, Journal of Hazardous Materials, 168 (2009) 269-275.
[220] Y. Ohko, I. Ando, C. Niwa, T. Tatsuma, T. Yamamura, T. Nakashima, Y. Kubota, A. Fujishima, Degradation of Bisphenol A in Water by TiO2 Photocatalyst, Environ. Sci. Technol., 35 (2001) 2365-2368.
[221] N. Watanabe, S. Horikoshi, H. Kawabe, Y. Sugie, J. Zhao, H. Hidaka, Photodegradation mechanism for bisphenol A at the TiO2/H2O interfaces, Chemosphere, 52 (2003) 851-859.
[222] K. Chiang, T.M. Lim, L. Tsen, C.C. Lee, Photocatalytic degradation and mineralization of bisphenol A by TiO2 and platinized TiO2, Applied Catalysis A: General, 261 (2004) 225-237.
[223] E.M. Rodríguez, G. Fernández, N. Klamerth, M.I. Maldonado, P.M. Álvarez, S. Malato, Efficiency of different solar advanced oxidation processes on the oxidation of bisphenol A in water, Applied Catalysis B: Environmental, 95 (2010) 228-237.
[224] A. Zacharakis, E. Chatzisymeon, V. Binas, Z. Frontistis, D. Venieri, D. Mantzavinos, Solar Photocatalytic Degradation of Bisphenol A on Immobilized ZnO or TiO2, International Journal of Photoenergy, 2013 (2013) 9.
[225] C.-Y. Kuo, C.-H. Wu, J.-T. Wu, Y.-R. Chen, Synthesis and characterization of a phosphorus-doped TiO2 immobilized bed for the photodegradation of bisphenol A under UV and sunlight irradiation, Reaction Kinetics, Mechanisms and Catalysis, 114 (2015) 753-766.
[226] B. Erjavec, P. Hudoklin, K. Perc, T. Tišler, M.S. Dolenc, A. Pintar, Glass fiber-supported TiO2 photocatalyst: Efficient mineralization and removal of toxicity/estrogenicity of bisphenol A and its analogs, Applied Catalysis B: Environmental, 183 (2016) 149-158.
[227] R. Wang, D. Ren, S. Xia, Y. Zhang, J. Zhao, Photocatalytic degradation of Bisphenol A (BPA) using immobilized TiO2 and UV illumination in a horizontal circulating bed photocatalytic reactor (HCBPR), J. Hazard. Mater., 169 (2009) 926-932.
[228] T. Nakashima, Y. Ohko, D.A. Tryk, A. Fujishima, Decomposition of endocrine-disrupting chemicals in water by use of TiO2 photocatalysts immobilized on polytetrafluoroethylene mesh sheets, J. Photochem. Photobiol. A: Chem., 151 (2002) 207-212.
[229] V. Repousi, A. Petala, Z. Frontistis, M. Antonopoulou, I. Konstantinou, D.I. Kondarides, D. Mantzavinos, Photocatalytic degradation of bisphenol A over Rh/TiO2 suspensions in different water matrices, Catal. Today, 284 (2017) 59-66.
[230] Y. Kanigaridou, A. Petala, Z. Frontistis, M. Antonopoulou, M. Solakidou, I. Konstantinou, Y. Deligiannakis, D. Mantzavinos, D.I. Kondarides, Solar photocatalytic degradation of bisphenol A with CuOx/BiVO4: Insights into the unexpectedly favorable effect of bicarbonates, Chemical Engineering Journal, 318 (2017) 39-49.
[231] E. Bilgin Simsek, Solvothermal synthesized boron doped TiO2 catalysts: Photocatalytic degradation of endocrine disrupting compounds and pharmaceuticals under visible light irradiation, Applied Catalysis B: Environmental, 200 (2017) 309-322.

[232] W.-D. Oh, L.-W. Lok, A. Veksha, A. Giannis, T.-T. Lim, Enhanced photocatalytic degradation of bisphenol A with Ag-decorated S-doped g-C3N4 under solar irradiation: Performance and mechanistic studies, Chem. Eng. J., 333 (2018) 739-749.
[233] M.P. Blanco-Vega, J.L. Guzmán-Mar, M. Villanueva-Rodríguez, L. Maya-Treviño, L.L. Garza-Tovar, A. Hernández-Ramírez, L. Hinojosa-Reyes, Photocatalytic elimination of bisphenol A under visible light using Ni-doped TiO2 synthesized by microwave assisted sol-gel method, Mater. Sci. Semicond. Process., 71 (2017) 275-282.
[234] R.-a. Doong, C.-Y. Liao, Enhanced visible-light-responsive photodegradation of bisphenol A by Cu, N-codoped titanate nanotubes prepared by microwave-assisted hydrothermal method, J. Hazard. Mater., 322 (2017) 254-262.
[235] L.-F. Chiang, R.-a. Doong, Cu–TiO2 nanorods with enhanced ultraviolet- and visible-light photoactivity for bisphenol A degradation, J. Hazard. Mater., 277 (2014) 84-92.
[236] S. Wen Chen, W. Chao Li, Z. Guo Sun, H. Yong Xie, Degradation of Artificial Sweetener Saccharin Sodium by Advanced Oxidation Technology, 2013.
[237] M.M. Khan, Nanocomposites for Visible Light-induced Photocatalysis, Springer International Publishing2017.
[238] S. Papoutsakis, C. Pulgarin, I. Oller, R. Sánchez-Moreno, S. Malato, Enhancement of the Fenton and photo-Fenton processes by components found in wastewater from the industrial processing of natural products: The possibilities of cork boiling wastewater reuse, Chemical Engineering Journal, 304 (2016) 890-896.
[239] L. Clarizia, D. Russo, I. Di Somma, R. Marotta, R. Andreozzi, Homogeneous photo-Fenton processes at near neutral pH: A review, Applied Catalysis B: Environmental, 209 (2017) 358-371.
[240] W. Gernjak, M. Fuerhacker, P. Fernández-Ibañez, J. Blanco, S. Malato, Solar photo-Fenton treatment—Process parameters and process control, Applied Catalysis B: Environmental, 64 (2006) 121-130.
[241] T. Krutzler, H. Fallmann, P. Maletzky, R. Bauer, S. Malato, J. Blanco, Solar driven degradation of 4-chlorophenol, Catal. Today, 54 (1999) 321-327.
[242] W. Feng, D. Nansheng, Photochemistry of hydrolytic iron (III) species and photoinduced degradation of organic compounds. A minireview, Chemosphere, 41 (2000) 1137-1147.
[243] A. Bozzi, T. Yuranova, P. Lais, J. Kiwi, Degradation of industrial waste waters on Fe/C-fabrics. Optimization of the solution parameters during reactor operation, Water Res., 39 (2005) 1441-1450.
[244] F. Martínez, G. Calleja, J.A. Melero, R. Molina, Heterogeneous photo-Fenton degradation of phenolic aqueous solutions over iron-containing SBA-15 catalyst, Applied Catalysis B: Environmental, 60 (2005) 181-190.
[245] E.G. Garrido-Ramírez, B.K.G. Theng, M.L. Mora, Clays and oxide minerals as catalysts and nanocatalysts in Fenton-like reactions — A review, Applied Clay Science, 47 (2010) 182-192.
[246] E. Oliveros, O. Legrini, M. Hohl, T. Müller, A.M. Braun, Industrial waste water treatment: large scale development of a light-enhanced Fenton reaction, Chemical Engineering and Processing: Process Intensification, 36 (1997) 397-405.
[247] W. Gernjak, T. Krutzler, A. Glaser, S. Malato, J. Caceres, R. Bauer, A.R. Fernández-Alba, Photo-Fenton treatment of water containing natural phenolic pollutants, Chemosphere, 50 (2003) 71-78.
[248] M. Pérez, F. Torrades, J.A. García-Hortal, X. Domènech, J. Peral, Removal of organic contaminants in paper pulp treatment effluents under Fenton and photo-Fenton conditions, Applied Catalysis B: Environmental, 36 (2002) 63-74.
[249] W. Sabaikai, M. Sekine, M. Tokumura, Y. Kawase, UV light photo-Fenton degradation of polyphenols in oolong tea manufacturing wastewater, Journal of Environmental Science and Health, Part A, 49 (2014) 193-202.
[250] D. Bahnemann, Photocatalytic water treatment: solar energy applications, Solar Energy, 77 (2004) 445-459.
[251] N. Klamerth, S. Malato, A. Agüera, A. Fernández-Alba, Photo-Fenton and modified photo-Fenton at neutral pH for the treatment of emerging contaminants in wastewater treatment plant effluents: A comparison, Water Res., 47 (2013) 833-840.
[252] S. Arzate, J.L. García Sánchez, P. Soriano-Molina, J.L. Casas López, M.C. Campos-Mañas, A. Agüera, J.A. Sánchez Pérez, Effect of residence time on micropollutant removal in WWTP

secondary effluents by continuous solar photo-Fenton process in raceway pond reactors, Chem. Eng. J., 316 (2017) 1114-1121.
[253] G. Rivas, I. Carra, J.L. García Sánchez, J.L. Casas López, S. Malato, J.A. Sánchez Pérez, Modelling of the operation of raceway pond reactors for micropollutant removal by solar photo-Fenton as a function of photon absorption, Applied Catalysis B: Environmental, 178 (2015) 210-217.
[254] I. De la Obra, L. Ponce-Robles, S. Miralles-Cuevas, I. Oller, S. Malato, J.A. Sánchez Pérez, Microcontaminant removal in secondary effluents by solar photo-Fenton at circumneutral pH in raceway pond reactors, Catal. Today, 287 (2017) 10-14.
[255] L. Prieto-Rodríguez, D. Spasiano, I. Oller, I. Fernández-Calderero, A. Agüera, S. Malato, Solar photo-Fenton optimization for the treatment of MWTP effluents containing emerging contaminants, Catal. Today, 209 (2013) 188-194.
[256] I. Carra, J.A. Sánchez Pérez, S. Malato, O. Autin, B. Jefferson, P. Jarvis, Application of high intensity UVC-LED for the removal of acetamiprid with the photo-Fenton process, Chem. Eng. J., 264 (2015) 690-696.
[257] I. de la Obra, B. Esteban Garcia, J.L. Garcia Sanchez, J.L. Casas Lopez, J.A. Sanchez Perez, Low cost UVA-LED as a radiation source for the photo-Fenton process: a new approach for micropollutant removal from urban wastewater, Photochemical & Photobiological Sciences, 16 (2017) 72-78.
[258] G. Pliego, P. Garcia-Muñoz, J.A. Zazo, J.A. Casas, J.J. Rodriguez, Improving the Fenton process by visible LED irradiation, Environmental Science and Pollution Research, 23 (2016) 23449-23455.
[259] Y. Gao, Y. Wang, H. Zhang, Removal of Rhodamine B with Fe-supported bentonite as heterogeneous photo-Fenton catalyst under visible irradiation, Applied Catalysis B: Environmental, 178 (2015) 29-36.
[260] M.I. Polo-López, P. Fernández-Ibáñez, E. Ubomba-Jaswa, C. Navntoft, I. García-Fernández, P.S.M. Dunlop, M. Schmid, J.A. Byrne, K.G. McGuigan, Elimination of water pathogens with solar radiation using an automated sequential batch CPC reactor, J. Hazard. Mater., 196 (2011) 16-21.
[261] J.A. Sánchez Pérez, P. Soriano-Molina, G. Rivas, J.L. García Sánchez, J.L. Casas López, J.M. Fernández Sevilla, Effect of temperature and photon absorption on the kinetics of micropollutant removal by solar photo-Fenton in raceway pond reactors, Chem. Eng. J., 310 (2017) 464-472.
[262] I. Carra, L. Santos-Juanes, F.G. Acién Fernández, S. Malato, J.A. Sánchez Pérez, New approach to solar photo-Fenton operation. Raceway ponds as tertiary treatment technology, J. Hazard. Mater., 279 (2014) 322-329.
[263] J. De Laat, G. Truong Le, B. Legube, A comparative study of the effects of chloride, sulfate and nitrate ions on the rates of decomposition of H2O2 and organic compounds by Fe(II)/H2O2 and Fe(III)/H2O2, Chemosphere, 55 (2004) 715-723.
[264] E. Lipczynska-Kochany, G. Sprah, S. Harms, Influence of some groundwater and surface waters constituents on the degradation of 4-chlorophenol by the Fenton reaction, Chemosphere, 30 (1995) 9-20.
[265] J. Bacardit, J. Stötzner, E. Chamarro, S. Esplugas, Effect of Salinity on the Photo-Fenton Process, Industrial & Engineering Chemistry Research, 46 (2007) 7615-7619.
[266] I. Oller, S. Malato, J.A. Sánchez-Pérez, M.I. Maldonado, W. Gernjak, L.A. Pérez-Estrada, Advanced oxidation process–biological system for wastewater containing a recalcitrant pollutant, Water Sci. Technol., 55 (2007) 229-235.
[267] J. Farias, E.D. Albizzati, O.M. Alfano, Kinetic study of the photo-Fenton degradation of formic acid: Combined effects of temperature and iron concentration, Catal. Today, 144 (2009) 117-123.
[268] A. Safarzadeh-Amiri, J.R. Bolton, S.R. Cater, Ferrioxalate-mediated solar degradation of organic contaminants in water, Solar Energy, 56 (1996) 439-443.
[269] A. Durán, J.M. Monteagudo, A. Carnicer, I. San Martín, P. Serna, Solar photodegradation of synthetic apple juice wastewater: Process optimization and operational cost study, Solar Energy Materials and Solar Cells, 107 (2012) 307-315.
[270] J.M. Monteagudo, A. Durán, R. González, A.J. Expósito, In situ chemical oxidation of carbamazepine solutions using persulfate simultaneously activated by heat energy, UV light, Fe2+ ions, and H2O2, Applied Catalysis B: Environmental, 176-177 (2015) 120-129.
[271] M.M. Ahmed, S. Chiron, Solar photo-Fenton like using persulphate for carbamazepine removal from domestic wastewater, Water Res., 48 (2014) 229-236.

[272] L.W. Matzek, K.E. Carter, Activated persulfate for organic chemical degradation: A review, Chemosphere, 151 (2016) 178-188.
[273] I.M. Kolthoff, A.I. Medalia, H.P. Raaen, The Reaction between Ferrous Iron and Peroxides. IV. Reaction with Potassium Persulfate1a, Journal of the American Chemical Society, 73 (1951) 1733-1739.
[274] A. Mirzaei, Z. Chen, F. Haghighat, L. Yerushalmi, Removal of pharmaceuticals from water by homo/heterogonous Fenton-type processes – A review, Chemosphere, 174 (2017) 665-688.
[275] S. Rahim Pouran, A.R. Abdul Aziz, W.M.A. Wan Daud, Review on the main advances in photo-Fenton oxidation system for recalcitrant wastewaters, Journal of Industrial and Engineering Chemistry, 21 (2015) 53-69.
[276] N. De la Cruz, L. Esquius, D. Grandjean, A. Magnet, A. Tungler, L.F. de Alencastro, C. Pulgarín, Degradation of emergent contaminants by UV, UV/H2O2 and neutral photo-Fenton at pilot scale in a domestic wastewater treatment plant, Water Res., 47 (2013) 5836-5845.
[277] N. Klamerth, L. Rizzo, S. Malato, M.I. Maldonado, A. Agüera, A.R. Fernández-Alba, Degradation of fifteen emerging contaminants at μgL−1 initial concentrations by mild solar photo-Fenton in MWTP effluents, Water Research, 44 (2010) 545-554.
[278] P. Calza, V.A. Sakkas, C. Medana, A.D. Vlachou, F. Dal Bello, T.A. Albanis, Chemometric assessment and investigation of mechanism involved in photo-Fenton and TiO2 photocatalytic degradation of the artificial sweetener sucralose in aqueous media, Applied Catalysis B: Environmental, 129 (2013) 71-79.
[279] E. Kattel, M. Trapido, N. Dulova, Oxidative degradation of emerging micropollutant acesulfame in aqueous matrices by UVA-induced H2O2/Fe2+ and S2O82−/Fe2+ processes, Chemosphere, 171 (2017) 528-536.
[280] M.E. Balmer, B. Sulzberger, Atrazine Degradation in Irradiated Iron/Oxalate Systems: Effects of pH and Oxalate, Environmental Science & Technology, 33 (1999) 2418-2424.
[281] L.O. Conte, A.V. Schenone, O.M. Alfano, Ferrioxalate-assisted solar photo-Fenton degradation of a herbicide at pH conditions close to neutrality, Environmental Science and Pollution Research, 24 (2017) 6205-6212.
[282] I.N. Dias, B.S. Souza, J.H.O.S. Pereira, F.C. Moreira, M. Dezotti, R.A.R. Boaventura, V.J.P. Vilar, Enhancement of the photo-Fenton reaction at near neutral pH through the use of ferrioxalate complexes: A case study on trimethoprim and sulfamethoxazole antibiotics removal from aqueous solutions, Chemical Engineering Journal, 247 (2014) 302-313.
[283] A. Durán, J.M. Monteagudo, I. Sanmartín, A. Carrasco, Solar photo-Fenton mineralization of antipyrine in aqueous solution, Journal of Environmental Management, 130 (2013) 64-71.
[284] A. Durán, J.M. Monteagudo, I. Sanmartín, A. Valverde, Solar photodegradation of antipyrine in a synthetic WWTP effluent in a semi-industrial installation, Solar Energy Materials and Solar Cells, 125 (2014) 215-222.
[285] A.J. Expósito, J.M. Monteagudo, A. Durán, I. San Martín, L. González, Study of the intensification of solar photo-Fenton degradation of carbamazepine with ferrioxalate complexes and ultrasound, Journal of Hazardous Materials, 342 (2018) 597-605.
[286] A.A. Nogueira, B.M. Souza, M.W.C. Dezotti, R.A.R. Boaventura, V.J.P. Vilar, Ferrioxalate complexes as strategy to drive a photo-FENTON reaction at mild pH conditions: A case study on levofloxacin oxidation, Journal of Photochemistry and Photobiology A: Chemistry, 345 (2017) 109-123.
[287] J.H.O.S. Pereira, D.B. Queirós, A.C. Reis, O.C. Nunes, M.T. Borges, R.A.R. Boaventura, V.J.P. Vilar, Process enhancement at near neutral pH of a homogeneous photo-Fenton reaction using ferricarboxylate complexes: Application to oxytetracycline degradation, Chemical Engineering Journal, 253 (2014) 217-228.
[288] B.M. Souza, M.W.C. Dezotti, R.A.R. Boaventura, V.J.P. Vilar, Intensification of a solar photo-Fenton reaction at near neutral pH with ferrioxalate complexes: A case study on diclofenac removal from aqueous solutions, Chem. Eng. J., 256 (2014) 448-457.
[289] C. Comninellis, A. Kapalka, S. Malato, S.A. Parsons, I. Poulios, D. Mantzavinos, Advanced oxidation processes for water treatment: advances and trends for R&D, Journal of Chemical Technology & Biotechnology, 83 (2008) 769-776.
[290] L. Rizzo, C.D. Rocca, V. Belgiorno, M. Bekbolet, Application of photocatalysis as a post treatment method of a heterotrophic–autotrophic denitrification reactor effluent, Chemosphere, 72 (2008) 1706-1711.

[291] R.J.A. L'Amour, E.B. Azevedo, S.G.F. Leite, M. Dezotti, Removal of phenol in high salinity media by a hybrid process (activated sludge+photocatalysis), Separation and Purification Technology, 60 (2008) 142-146.
[292] M. Barreto-Rodrigues, J.V.B. Souza, É.S. Silva, F.T. Silva, T.C.B. Paiva, Combined photocatalytic and fungal processes for the treatment of nitrocellulose industry wastewater, Journal of Hazardous Materials, 161 (2009) 1569-1573.
[293] J. Rajesh Banu, S. Anandan, S. Kaliappan, I.-T. Yeom, Treatment of dairy wastewater using anaerobic and solar photocatalytic methods, Solar Energy, 82 (2008) 812-819.
[294] R. Ahmad, Z. Ahmad, A.U. Khan, N.R. Mastoi, M. Aslam, J. Kim, Photocatalytic systems as an advanced environmental remediation: Recent developments, limitations and new avenues for applications, Journal of Environmental Chemical Engineering, 4 (2016) 4143-4164.
[295] P. Fernandez-Ibanez, J.A. Byrne, M.I. Polo-Lopez, P.S.M. Dunlop, P. Karaolia, D. Fatta-Kassinos, CHAPTER 3 Solar Photocatalytic Disinfection of Water, Photocatalysis: Applications, The Royal Society of Chemistry2016, pp. 72-91.
[296] S. Papoutsakis, C. Pulgarin, I. Oller, R. Sánchez-Moreno, S. Malato, Enhancement of the Fenton and photo-Fenton processes by components found in wastewater from the industrial processing of natural products: The possibilities of cork boiling wastewater reuse, Chem. Eng. J., 304 (2016) 890-896.
[297] F. Khodadadian, M. Nasalevich, F. Kapteijn, A.I. Stankiewicz, R. Lakerveld, J. Gascon, CHAPTER 8 Photocatalysis: Past Achievements and Future Trends, Alternative Energy Sources for Green Chemistry, The Royal Society of Chemistry2016, pp. 227-269.
[298] G.E.P. Box, Statistics for experimenters : design, innovation and discovery, Second edition.. ed., Hoboken, N.J. : Wiley, Hoboken, N.J., 2005.
[299] A. Carabin, P. Drogui, D. Robert, Photocatalytic Oxidation of Carbamazepine: Application of an Experimental Design Methodology, Water, Air, & Soil Pollution, 227 (2016) 122.
[300] S. Papoutsakis, S. Miralles-Cuevas, I. Oller, J.L. Garcia Sanchez, C. Pulgarin, S. Malato, Microcontaminant degradation in municipal wastewater treatment plant secondary effluent by EDDS assisted photo-Fenton at near-neutral pH: An experimental design approach, Catalysis Today, 252 (2015) 61-69.
[301] E. Chatzisymeon, E. Diamadopoulos, D. Mantzavinos, Effect of key operating parameters on the non-catalytic wet oxidation of olive mill wastewaters, Water Sci. Technol., 59 (2009) 2509-2518.
[302] R.L. Mason, R.F. Gunst, J.L. Hess, Statistical Principles in Experimental Design, Statistical Design and Analysis of Experiments, John Wiley & Sons, Inc.2003, pp. 107-139.
[303] M.M. Nelson, A practical guide to neural nets, Reading, Mass.; Wokingham : Addison-Wesley, Reading, Mass.; Wokingham, 1991.
[304] A.R. Khataee, M.B. Kasiri, Artificial neural networks modeling of contaminated water treatment processes by homogeneous and heterogeneous nanocatalysis, J. Mol. Catal. A: Chem., 331 (2010) 86-100.
[305] R. Nath, B. Rajagopalan, R. Ryker, Determining the saliency of input variables in neural network classifiers, Computers & Operations Research, 24 (1997) 767-773.
[306] Evonik, Aeroxide-Fumed Metal Oxides, Technical Overview.
[307] Kronos, KRONOClean 7050 TiO2-photocatalyst, Product Data Sheet.
[308] Cristal, Cristal ACTiV PC105, Product Data Sheet.
[309] H. de Lasa, B. Serrano, M. Salaices, Novel Photocatalytic Reactors for Water and Air Treatment, Photocatalytic Reaction Engineering, Springer US, Boston, MA, 2005, pp. 17-47.
[310] S.L. Murov, I. Carmichael, G.L. Hug, Handbook of Photochemistry, 2nd ed., Marcel Dekker, New York, 1993.
[311] I. Trandafir, V. Nour, M.E. Ionică, Development and validation of an HPLC methods for simulatneous quantification of acesulfame-K, saccharin, aspartame, caffeine and benzoic acid in cola soft drinks, Scientific Study & Research X(2009) 185-194.
[312] Z. Frontistis, V.M. Daskalaki, A. Katsaounis, I. Poulios, D. Mantzavinos, Electrochemical enhancement of solar photocatalysis: Degradation of endocrine disruptor bisphenol-A on Ti/TiO2 films, Water Res., 45 (2011) 2996-3004.
[313] A.G. Trovó, R.F.P. Nogueira, A. Agüera, A.R. Fernandez-Alba, C. Sirtori, S. Malato, Degradation of sulfamethoxazole in water by solar photo-Fenton. Chemical and toxicological evaluation, Water Res., 43 (2009) 3922-3931.

[314] A.J. Expósito, D.A. Patterson, W.S.W. Mansor, J.M. Monteagudo, E. Emanuelsson, I. Sanmartín, A. Durán, Antipyrine removal by TiO2 photocatalysis based on spinning disc reactor technology, J. Environ. Manage., 187 (2017) 504-512.
[315] J.G. Calvert, J.N. Pitts Jr, Photochemistry, John Wiley & Sons Inc, New York, 1996.
[316] C.S. Turchi, D.F. Ollis, Mixed reactant photocatalysis: Intermediates and mutual rate inhibition, J. Catal., 119 (1989) 483-496.
[317] D. Tsonev, S. Videv, H. Haas, Towards a 100 Gb/s visible light wireless access network, Opt. Express, 23 (2015) 1627-1637.
[318] A.A. Gribb, J.F. Banfield, Particle size effects on transformation kinetics and phase stability in nanocrystalline TiO2, Am. Mineral., 82 (1997) 717-728.
[319] D.P. Morgan, C.L. Scofield, Neural Networks and Speech Processing, Kluwer Academic Publishers, London, 1991.
[320] G.D. Garson, Interpreting neural-network connection weights, AI Expert, 6 (1991) 46-51.
[321] A. Durán, J.M. Monteagudo, M. Mohedano, Neural networks simulation of photo-Fenton degradation of Reactive Blue 4, Applied Catalysis B: Environmental, 65 (2006) 127-134.
[322] N. Serpone, A. Salinaro, Terminology, relative photonic efficiencies and quantum yields in heterogeneous photocatalysis. Part I: Suggested protocol, 1999.
[323] James R. Bolton, Keith G. Bircher, William Tumas, and Chadwick A. Tolman Figures-of-merit for the technical development and application of advanced oxidation technologies for both electric- and solar-driven systems, Pure Appl. Chem., 73 (2001) 627-637.
[324] S. Cassaignon, M. Koelsch, J.-P. Jolivet, Selective synthesis of brookite, anatase and rutile nanoparticles: thermolysis of TiCl4 in aqueous nitric acid, Journal of Materials Science, 42 (2007) 6689-6695.
[325] A. Di Paola, M. Bellardita, R. Ceccato, L. Palmisano, F. Parrino, Highly Active Photocatalytic TiO2 Powders Obtained by Thermohydrolysis of TiCl4 in Water, The Journal of Physical Chemistry C, 113 (2009) 15166-15174.
[326] F. Fresno, D. Tudela, J.M. Coronado, J. Soria, Synthesis of Ti1−xSnxO2 nanosized photocatalysts in reverse microemulsions, Catal. Today, 143 (2009) 230-236.
[327] A.O. Kondrakov, A.N. Ignatev, F.H. Frimmel, S. Bräse, H. Horn, A.I. Revelsky, Formation of genotoxic quinones during bisphenol A degradation by TiO2 photocatalysis and UV photolysis: A comparative study, Applied Catalysis B: Environmental, 160–161 (2014) 106-114.
[328] N. Miranda-García, S. Suárez, M.I. Maldonado, S. Malato, B. Sánchez, Regeneration approaches for TiO2 immobilized photocatalyst used in the elimination of emerging contaminants in water, Catalysis Today, 230 (2014) 27-34.
[329] M. Argyle, C. Bartholomew, Heterogeneous Catalyst Deactivation and Regeneration: A Review, Catalysts, 5 (2015) 145.
[330] S. Salaeh, M. Kovacic, D. Kosir, H. Kusic, U. Lavrencic Stangar, D.D. Dionysiou, A. Loncaric Bozic, Reuse of TiO2-based catalyst for solar driven water treatment; thermal and chemical reactivation, Journal of Photochemistry and Photobiology A: Chemistry, 333 (2017) 117-129.
[331] J. Araña, E. Tello Rendón, J.M. Doña Rodríguez, J.A. Herrera Melián, O. González Díaz, J. Pérez Peña, High concentrated phenol and 1,2-propylene glycol water solutions treatment by photocatalysis: Catalyst recovery and re-use, Applied Catalysis B: Environmental, 30 (2001) 1-10.
[332] P. Fernández-Ibáñez, J. Blanco, S. Malato, F.J.d.l. Nieves, Application of the colloidal stability of TiO2 particles for recovery and reuse in solar photocatalysis, Water Res., 37 (2003) 3180-3188.
[333] D. Ensminger, Ultrasonics: Fundamentals, Technology, Applications, Second Edition, Revised and Expanded, 1988.
[334] S. Malato, M.I. Maldonado, P. Fernández-Ibáñez, I. Oller, I. Polo, R. Sánchez-Moreno, Decontamination and disinfection of water by solar photocatalysis: The pilot plants of the Plataforma Solar de Almeria, Materials Science in Semiconductor Processing, 42 (2016) 15-23.
[335] Z. Wang, J. Liu, Y. Dai, W. Dong, S. Zhang, J. Chen, CFD modeling of a UV-LED photocatalytic odor abatement process in a continuous reactor, J. Hazard. Mater., 215–216 (2012) 25-31.
[336] S. Dominguez, M.J. Rivero, P. Gomez, R. Ibañez, I. Ortiz, Kinetic modeling and energy evaluation of sodium dodecylbenzenesulfonate photocatalytic degradation in a new LED reactor, Journal of Industrial and Engineering Chemistry, 37 (2016) 237-242.

[337] J.-L. Shie, C.-H. Lee, C.-S. Chiou, C.-T. Chang, C.-C. Chang, C.-Y. Chang, Photodegradation kinetics of formaldehyde using light sources of UVA, UVC and UVLED in the presence of composed silver titanium oxide photocatalyst, J. Hazard. Mater., 155 (2008) 164-172.
[338] L.H. Levine, J.T. Richards, J.L. Coutts, R. Soler, F. Maxik, R.M. Wheeler, Feasibility of Ultraviolet-Light-Emitting Diodes as an Alternative Light Source for Photocatalysis, J. Air Waste Manage. Assoc., 61 (2011) 932-940.
[339] E. Selli, D. Baglio, L. Montanarella, G. Bidoglio, Role of humic acids in the TiO2-photocatalyzed degradation of tetrachloroethene in water, Water Res., 33 (1999) 1827-1836.
[340] J.E. Toth, K.A. Rickman, A.R. Venter, J.J. Kiddle, S.P. Mezyk, Reaction Kinetics and Efficiencies for the Hydroxyl and Sulfate Radical Based Oxidation of Artificial Sweeteners in Water, The Journal of Physical Chemistry A, 116 (2012) 9819-9824.
[341] H. Lin, J. Wu, N. Oturan, H. Zhang, M.A. Oturan, Degradation of artificial sweetener saccharin in aqueous medium by electrochemically generated hydroxyl radicals, Environmental Science and Pollution Research, 23 (2016) 4442-4453.
[342] J.L. Coutts, L.H. Levine, J.T. Richards, D.W. Mazyck, The effect of photon source on heterogeneous photocatalytic oxidation of ethanol by a silica–titania composite, J. Photochem. Photobiol. A: Chem., 225 (2011) 58-64.
[343] H.-W. Chen, Y. Ku, C.-Y. Wu, Effect of LED optical characteristics on temporal behavior of o-cresol decomposition by UV/TiO2 process, Journal of Chemical Technology & Biotechnology, 82 (2007) 626-635.
[344] D. Haranaka-Funai, F. Didier, J. Giménez, P. Marco, S. Esplugas, A. Machulek-Junior, Photocatalytic treatment of valproic acid sodium salt with TiO2 in different experimental devices: An economic and energetic comparison, Chem. Eng. J., 327 (2017) 656-665.
[345] J. Chen, S. Loeb, J.-H. Kim, LED revolution: fundamentals and prospects for UV disinfection applications, Environmental Science: Water Research & Technology, 3 (2017) 188-202.
[346] N. Klamerth, S. Malato, A. Agüera, A. Fernández-Alba, G. Mailhot, Treatment of Municipal Wastewater Treatment Plant Effluents with Modified Photo-Fenton As a Tertiary Treatment for the Degradation of Micro Pollutants and Disinfection, Environ. Sci. Technol., 46 (2012) 2885-2892.
[347] Y. Sun, J.J. Pignatello, Chemical treatment of pesticide wastes. Evaluation of iron(III) chelates for catalytic hydrogen peroxide oxidation of 2,4-D at circumneutral pH, Journal of Agricultural and Food Chemistry, 40 (1992) 322-327.
[348] Y. Sun, J.J. Pignatello, Activation of hydrogen peroxide by iron(III) chelates for abiotic degradation of herbicides and insecticides in water, J. Agric. Food. Chem., 41 (1993) 308-312.
[349] J. Ndounla, C. Pulgarin, Evaluation of the efficiency of the photo Fenton disinfection of natural drinking water source during the rainy season in the Sahelian region, Science of The Total Environment, 493 (2014) 229-238.
[350] S. Khokhar, R.K. Owusu Apenten, Iron binding characteristics of phenolic compounds: some tentative structure–activity relations, Food Chem., 81 (2003) 133-140.
[351] M.S. Masoud, A.E. Ali, S.S. Haggag, N.M. Nasr, Spectroscopic studies on gallic acid and its azo derivatives and their iron(III) complexes, Spectrochimica Acta Part A: Molecular and Biomolecular Spectroscopy, 120 (2014) 505-511.
[352] L. Bertin, F. Ferri, A. Scoma, L. Marchetti, F. Fava, Recovery of high added value natural polyphenols from actual olive mill wastewater through solid phase extraction, Chem. Eng. J., 171 (2011) 1287-1293.
[353] M. Andjelković, J. Van Camp, B. De Meulenaer, G. Depaemelaere, C. Socaciu, M. Verloo, R. Verhe, Iron-chelation properties of phenolic acids bearing catechol and galloyl groups, Food Chem., 98 (2006) 23-31.
[354] N. Kalogerakis, M. Politi, S. Foteinis, E. Chatzisymeon, D. Mantzavinos, Recovery of antioxidants from olive mill wastewaters: A viable solution that promotes their overall sustainable management, Journal of Environmental Management, 128 (2013) 749-758.
[355] W. Huang, M. Brigante, F. Wu, K. Hanna, G. Mailhot, Development of a new homogenous photo-Fenton process using Fe(III)-EDDS complexes, Journal of Photochemistry and Photobiology A: Chemistry, 239 (2012) 17-23.
[356] S. Papoutsakis, F.F. Brites-Nóbrega, C. Pulgarin, S. Malato, Benefits and limitations of using Fe(III)-EDDS for the treatment of highly contaminated water at near-neutral pH, J. Photochem. Photobiol. A: Chem., 303 (2015) 1-7.

[357] A. De Luca, R.F. Dantas, S. Esplugas, Assessment of iron chelates efficiency for photo-Fenton at neutral pH, Water Res., 61 (2014) 232-242.
[358] E. Chatzisymeon, N.P. Xekoukoulotakis, E. Diamadopoulos, A. Katsaounis, D. Mantzavinos, Boron-doped diamond anodic treatment of olive mill wastewaters: Statistical analysis, kinetic modeling and biodegradability, Water Res., 43 (2009) 3999-4009.
[359] D. Mantzavinos, N. Kalogerakis, Treatment of olive mill effluents, Environ. Int., 31 (2005) 289-295.
[360] W. Gernjak, M.I. Maldonado, S. Malato, J. Cáceres, T. Krutzler, A. Glaser, R. Bauer, Pilot-plant treatment of olive mill wastewater (OMW) by solar TiO2 photocatalysis and solar photo-Fenton, Solar Energy, 77 (2004) 567-572.
[361] J.M. Monteagudo, A. Durán, R. Culebradas, I. San Martín, A. Carnicer, Optimization of pharmaceutical wastewater treatment by solar/ferrioxalate photo-catalysis, J. Environ. Manage., 128 (2013) 210-219.
[362] G.V. Buxton, C.L. Greenstock, W.P. Helman, A.B. Ross, Critical Review of rate constants for reactions of hydrated electrons, hydrogen atoms and hydroxyl radicals (·OH/·O− in Aqueous Solution, J. Phys. Chem. Ref. Data, 17 (1988) 513-886.
[363] J.M. Monteagudo, A. Durán, A. Fernandez, A. Carnicer, M.A. Alonso, J.M. Frades, Treatment of synthetic municipal wastewater containing antipyrine by sonophotocatalysis, 13th Mediterranean Congress in Chemical EngineeringBarcelona, Spain, 2014.
[364] H.-P. Cheng, Y.-H. Huang, C. Lee, Decolorization of reactive dye using a photo-ferrioxalate systemwith brick grain-supported iron oxide, J. Hazard. Mater., 188 (2011) 357-362.
[365] S. Miralles-Cuevas, L. Prieto-Rodríguez, E. De Torres Socías, M. Polo-López, P. Fernandez-Ibanez, I. Oller, S. Malato, Strategies for hydrogen peroxide dosing based on dissolved oxygen concentration for solar foto-Fenton treatment of complex wastewater, 16 (2014).
[366] R. Matta, S. Tlili, S. Chiron, S. Barbati, Removal of carbamazepine from urban wastewater by sulfate radical oxidation, Environmental Chemistry Letters, 9 (2011) 347-353.
[367] G.P. Anipsitakis, D.D. Dionysiou, Radical Generation by the Interaction of Transition Metals with Common Oxidants, Environ. Sci. Technol., 38 (2004) 3705-3712.
[368] M.N. Chong, A.K. Sharma, S. Burn, C.P. Saint, Feasibility study on the application of advanced oxidation technologies for decentralised wastewater treatment, Journal of Cleaner Production, 35 (2012) 230-238.
[369] R. Molinari, F. Pirillo, V. Loddo, L. Palmisano, Heterogeneous photocatalytic degradation of pharmaceuticals in water by using polycrystalline TiO2 and a nanofiltration membrane reactor, Catal. Today, 118 (2006) 205-213.
[370] V. Augugliaro, E. García-López, V. Loddo, S. Malato-Rodríguez, I. Maldonado, G. Marcì, R. Molinari, L. Palmisano, Degradation of lincomycin in aqueous medium: Coupling of solar photocatalysis and membrane separation, Solar Energy, 79 (2005) 402-408.
[371] C. Casado, R. Timmers, A. Sergejevs, C.T. Clarke, D.W.E. Allsopp, C.R. Bowen, R. van Grieken, J. Marugán, Design and validation of a LED-based high intensity photocatalytic reactor for quantifying activity measurements, Chem. Eng. J., 327 (2017) 1043-1055.
[372] L. Zhu, L. Cui, Q. Huang, Y. Wang, M. Vivar, Y. Jin, Y. Sun, Y. Cui, J. Fan, Performance study of SOL&PID system for the degradation of Acid Red 26 and 4-Chlorophenol, Energy Convers. Manage., 136 (2017) 361-371.
[373] Scottish Water, How is water treated?
[374] P. Xiong, J. Hu, Decomposition of acetaminophen (Ace) using TiO2/UVA/LED system, Catal. Today, 282 (2017) 48-56.
[375] S. Foteinis, J.M. Monteagudo, A. Durán, E. Chatzisymeon, Environmental sustainability of the solar photo-Fenton process for wastewater treatment and pharmaceuticals mineralization at semi-industrial scale, Sci. Total Environ., 612 (2018) 605-612.

Appendix A – Data sheets

1- UVA-LED emitter

LED ENGIN
BRIGHT LIGHT. TINY PACKAGE.

High Efficacy
365nm UV LED Emitter

LZ4-00U600

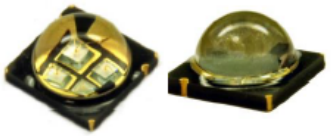

Key Features

- High Efficacy 365nm 11W UV LED
- Ultra-small foot print – 7.0mm x 7.0mm
- Surface mount ceramic package with integrated glass lens
- Very low Thermal Resistance (1.1°C/W)
- Individually addressable die
- Electrically neutral thermal path
- Highest Radiant Flux density
- JEDEC Level 1 for Moisture Sensitivity Level
- Lead (Pb) free and RoHS compliant
- Reflow solderable (up to 6 cycles)
- Emitter available on Standard and Serially connected MCPCB (optional)

Typical Applications

- Curing
- Sterilization
- Medical
- Currency Verification
- Fluorescence Microscopy
- Inspection of dyes, rodent and animal contamination,
- Leak detection
- Forensics

Description

The LZ4-00U600 UV LED emitter provides superior radiometric power in the wavelength range specifically required for applications like curing, sterilization, currency verification, and various medical applications. With a 7.0mm x 7.0mm ultra-small footprint, this package provides exceptional optical power density. The patented design has unparalleled thermal and optical performance. The high quality materials used in the package are chosen to optimize light output, have excellent UV resistance, and minimize stresses which results in monumental reliability and radiant flux maintenance.

LED Engin | 651 River Oaks Parkway | San Jose, CA 95134 USA | ph +1 408 922 7200 | fax +1 408 922 0158 | em sales@ledengin.com | www.ledengin.com

Part number options

Base part number

Part number	Description
LZ4-00U600-xxxx	LZ4 emitter
LZ4-40U600-xxxx	LZ4 emitter on Standard Star 1 channel MCPCB

Bin kit option codes

U6, Ultra-Violet (365nm)			
Kit number suffix	Min flux Bin	Color Bin Range	Description
0000	L	U0 - U1	full distribution flux; full distribution wavelength
00U0	L	U0 - U0	full distribution flux; wavelength U0 bin only
00U1	L	U1 - U1	full distribution flux; wavelength U1bin only

Notes:
1. Default bin kit option is -0000

LED Engin | 651 River Oaks Parkway | San Jose, CA 95134 USA | ph +1 408 922 7200 | fax +1 408 922 0158 | em sales@ledengin.com | www.ledengin.com

Radiant Flux Bins

Table 1:

Bin Code	Minimum Radiant Flux (Φ) @ I_F = 700mA[1,2] (w)	Maximum Radiant Flux (Φ) @ I_F = 700mA[1,2] (W)
L	0.80	1.00
M	1.00	1.25
N	1.25	1.60
P	1.60	2.00
Q	2.00	2.40
R	2.40	3.00

Notes for Table 1:
1. Radiant flux performance guaranteed within published operating conditions. LED Engin maintains a tolerance of ± 10% on flux measurements.
2. Future products will have even higher levels of radiant flux performance. Contact LED Engin Sales for updated information.

Peak Wavelength Bins

Table 2:

Bin Code	Minimum Peak Wavelength (λ_P) @ I_F = 700mA[1] (nm)	Maximum Peak Wavelength (λ_P) @ I_F = 700mA[1] (nm)
U0	365	370
U1	370	375

Notes for Table 2:
1. LED Engin maintains a tolerance of ± 2.0nm on peak wavelength measurements.

Forward Voltage Bins

Table 3:

Bin Code	Minimum Forward Voltage (V_F) @ I_F = 700mA[1,2] (V)	Maximum Forward Voltage (V_F) @ I_F = 700mA[1,2] (V)
0	14.72	19.52

Notes for Table 3:
1. Forward Voltage is binned with all four LED dice connected in series.
2. LED Engin maintains a tolerance of ± 0.16V for forward voltage measurements for the four LEDs.

LED Engin | 651 River Oaks Parkway | San Jose, CA 95134 USA | ph +1 408 922 7200 | fax +1 408 922 0158 | em sales@ledengin.com | www.ledengin.com

Absolute Maximum Ratings

Table 4:

Parameter	Symbol	Value	Unit
DC Forward Current at Tjmax=100°C[1]	I_F	700	mA
Peak Pulsed Forward Current[2]	I_{FP}	850	mA
Reverse Voltage	V_R	See Note 3	V
Storage Temperature	T_{stg}	-40 ~ +150	°C
Junction Temperature	T_J	100	°C
Soldering Temperature[4]	T_{sol}	180	°C
Allowable Reflow Cycles		6	
ESD Sensitivity[5]		> 2,000 V HBM Class 2 JESD22-A114-D	

Notes for Table 4:
1. Maximum DC forward current is determined by the overall thermal resistance and ambient temperature. Follow the curves in Figure 10 for current derating.
2: Pulse forward current conditions: Pulse Width ≤ 10msec and Duty Cycle ≤ 10%.
3. LEDs are not designed to be reverse biased.
4. Use low temperature solders. LED Engin recommends 58Bi-42Sn (wt.%) Solder. See Reflow Soldering Profile Figure 3.
5. LED Engin recommends taking reasonable precautions towards possible ESD damages and handling the LZ4-00U600 in an electrostatic protected area (EPA). An EPA may be adequately protected by ESD controls as outlined in ANSI/ESD S6.1.

Optical Characteristics @ T_C = 25°C

Table 5:

Parameter	Symbol	Typical	Unit
Radiant Flux (@ I_F = 700mA)	Φ	1.80	W
Peak Wavelength[1]	λ_P	365	nm
Viewing Angle[2]	$2\Theta_{½}$	115	Degrees
Total Included Angle[3]	$\Theta_{0.9}$	175	Degrees

Notes for Table 5:
1. When operating the UV LED, observe IEC 60825-1 class 3B rating. Avoid exposure to the beam.
2. Viewing Angle is the off axis angle from emitter centerline where the radiant power is ½ of the peak value.
3. Total Included Angle is the total angle that includes 90% of the total radiant flux.

Electrical Characteristics @ T_C = 25°C

Table 6:

Parameter	Symbol	Typical		Unit
		1 Die	4 Dice	
Forward Voltage (@ I_F = 700mA)	V_F	4.1	16.4	V
Temperature Coefficient of Forward Voltage	$\Delta V_F/\Delta T_J$	-14.8		mV/°C
Thermal Resistance (Junction to Case)	$R\Theta_{J-C}$	1.1		°C/W

IPC IPC/JEDEC Moisture Sensitivity Level

Table 7 - IPC/JEDEC J-STD-20D.1 MSL Classification:

			Soak Requirements			
	Floor Life		Standard		Accelerated	
Level	Time	Conditions	Time (hrs)	Conditions	Time (hrs)	Conditions
1	Unlimited	≤ 30°C/ 85% RH	168 +5/-0	85°C/ 85% RH	n/a	n/a

Notes for Table 7:
1. The standard soak time includes a default value of 24 hours for semiconductor manufacturer's exposure time (MET) between bake and bag and includes the maximum time allowed out of the bag at the distributor's facility.

Mechanical Dimensions (mm)

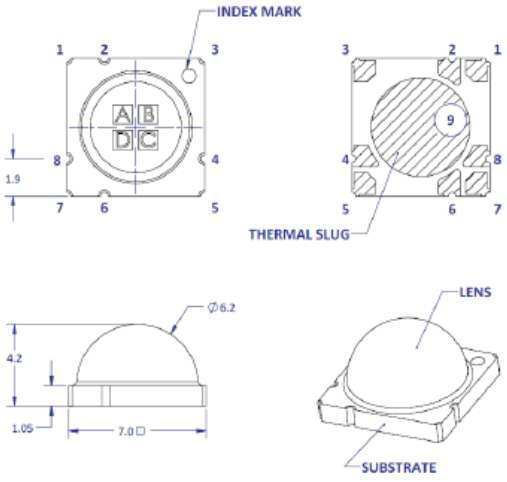

Pin Out		
Pad	Die	Function
1	A	Anode
2	A	Cathode
3	B	Anode
4	B	Cathode
5	C	Anode
6	C	Cathode
7	D	Anode
8	D	Cathode
9[2]	n/a	Thermal

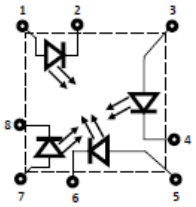

Figure 1: Package outline drawing.

Notes for Figure 1:
1. Unless otherwise noted, the tolerance = ± 0.20 mm.
2. Thermal contact, Pad 9, is electrically neutral.

Recommended Solder Pad Layout (mm)

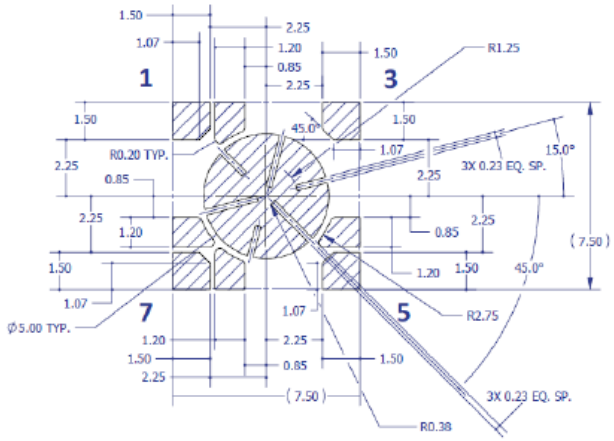

Figure 2a: Recommended solder pad layout for anode, cathode, and thermal pad.

Note for Figure 2a:
1. Unless otherwise noted, the tolerance = ± 0.20 mm.
2. This pad layout is "patent pending".

Recommended Solder Mask Layout (mm)

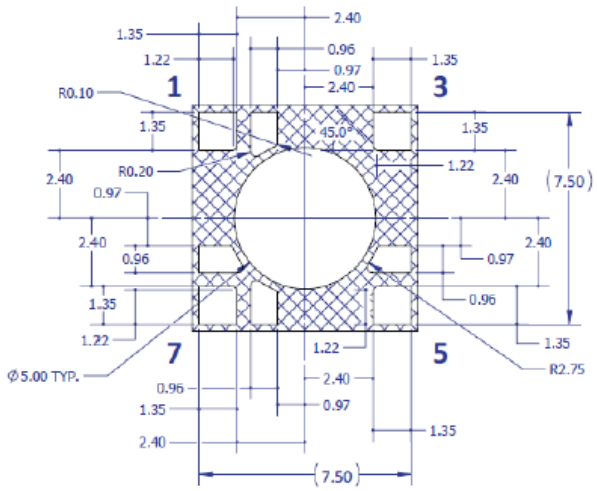

Figure 2b: Recommended solder mask opening (hatched area) for anode, cathode, and thermal pad.

Note for Figure 2b:
1. Unless otherwise noted, the tolerance = ± 0.20 mm.

Reflow Soldering Profile

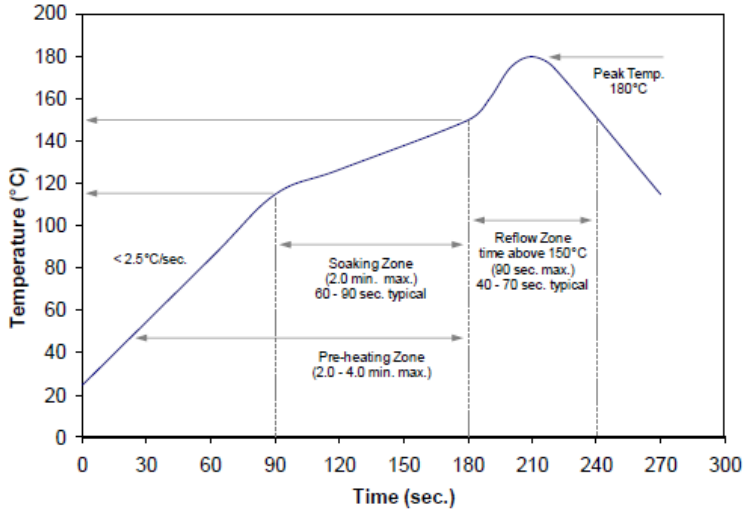

Figure 3: Reflow soldering profile for low temperature lead free soldering.

Typical Radiation Pattern

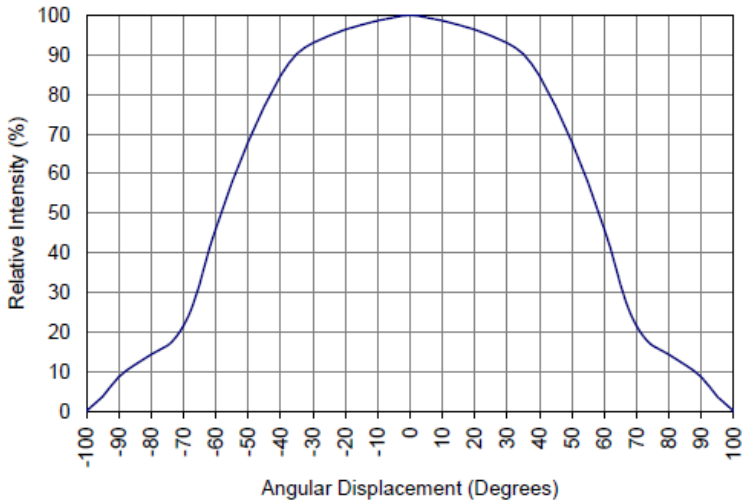

Figure 4: Typical representative spatial radiation pattern.

Typical Relative Spectral Power Distribution

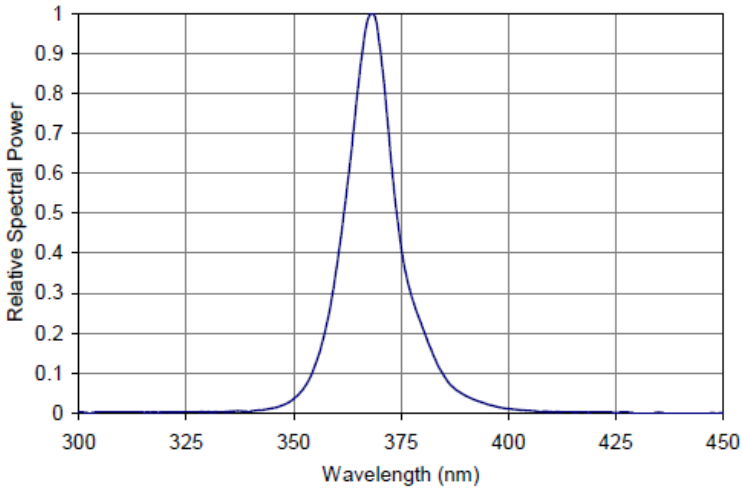

Figure 5: Typical relative spectral power vs. wavelength @ T_C = 25°C.

2- Heat sink

S Series

LED Heatsinks

Ohmite S Series LED Heatsinks are low cost and easy assembly heat sinks for "Star" LED packages supplied by Cree, Lumileds, Osram and others. This simple heat sink can hold LED modules and can be mounted simply with some thread forming screws. The heat sink has two types of surface finish and can be used in either natural (free) or forced convection cooling applications.

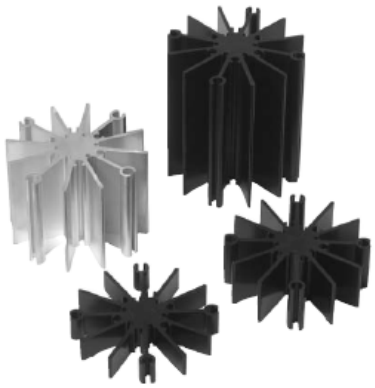

SERIES SPECIFICATIONS

Heatsink Part Number	Height (in/mm)	Surface area (in^2/mm^2)	Weight (oz/g)	Thermal resistance (°C/W) Free conv.	Forced conv.
SV-LED-113E SA-LED-113E	0.50 / 12.7	18 / 11,739	0.077 / 35	6.67 5.33	4.33
SV-LED-125E SA-LED-125E	1.00 / 25.4	36 / 23,478	0.154 / 70	5.33 4.27	2.88
SV-LED-151E SA-LED-151E	2.00 / 50.8	72 / 46,956	0.308 / 140	4.00 3.20	1.89
SV-LED-176E SA-LED-176E	3.00 / 76.2	108 / 70,434	0.462 / 210	3.11 2.49	1.55

CHARACTERISTICS

Heat Sink	Aluminum Alloy 6063-T5 or Equivalent with either degreased or black anodized finish.
Mounting Hardware	1/4, #10, and #4 thread forming SS screws are preferred
Compliance	Either degreased or black anodized finished parts are RoHS compliant.

Heat Dissipation

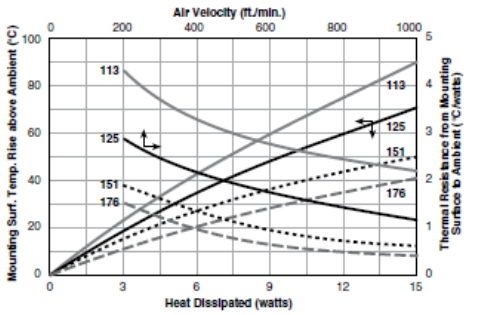

(continued)

S Series

LED Heatsinks

DIMENSIONS

(in./mm)

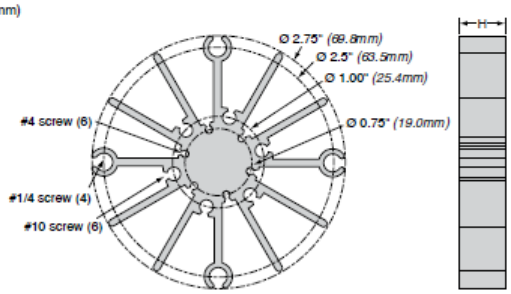

Part Number	Height H (in/mm)	Surface area (in^2/mm^2)	Weight (oz/g)
SV-LED-113E SA-LED-113E	0.50 / 12.7	18 / 11,739	0.077 / 35
SV-LED-125E SA-LED-125E	1.00 / 25.4	36 / 23,478	0.154 / 70
SV-LED-151E SA-LED-151E	2.00 / 50.8	72 / 46,956	0.308 / 140
SV-LED-176E SA-LED-176E	3.00 / 76.2	108 / 70,434	0.462 / 210

ORDERING INFORMATION

RoHS Compliant

S V - L E D - 1 1 3 E

Series: S
Coating: V = degreased; A = black anodized
Height: 113E

Standard part numbers

Part Number	Description	Packaging
SV-LED-113E	12.7mm, no finish (degreased)	Bulk
SA-LED-113E	Black Anodized, 12.7mm	Bulk
SV-LED-125E	25.4mm, no finish (degreased)	Bulk
SA-LED-125E	Black Anodized, 25.4mm	Bulk
SV-LED-151E	50.8mm, no finish (degreased)	Bulk
SA-LED-151E	Black Anodized, 50.8mm	Bulk
SV-LED-176E	76.2mm, no finish (degreased)	Bulk
SA-LED-176E	Black Anodized, 76.2mm	Bulk

Appendix B – List of publications

Peer-reviewed scientific journals

1. **K. Davididou**, E. Chatzisymeon, L. Perez-Estrada, I. Oller, S. Malato, Photo-Fenton treatment of saccharin in a solar pilot compound parabolic collector: Use of olive mill wastewater as iron chelating agent, preliminary results, J. Hazard. Mater., (2018) (*In Press*).
2. **K. Davididou**, R. Nelson, J.M. Monteagudo, A. Durán, A.J. Expósito, E. Chatzisymeon, Photocatalytic degradation of bisphenol-A under UV-LED, blacklight and solar irradiation, J. Clean. Prod., (2018) (*Under review*).
3. **K. Davididou**, E. Hale, N. Lane, E. Chatzisymeon, A. Pichavant, J.F. Hochepied, Photocatalytic treatment of saccharin and bisphenol-A in the presence of TiO_2 nanocomposites tuned by Sn(IV), Catal. Today, 287 (2017), 3-9.
4. **K. Davididou**, C. McRitchie, M. Antonopoulou, I. Konstantinou, E. Chatzisymeon, Photocatalytic degradation of saccharin under UV-LED and blacklight irradiation, J. Chem. Technol. Biotechnol., 93 (2018), 269-276.
5. **K. Davididou**, J.M. Monteagudo, E. Chatzisymeon, A. Durán, A.J. Expósito, Degradation and mineralization of antipyrine by UV-A LED photo-Fenton reaction intensified by ferrioxalate with addition of persulfate, Sep. Purif. Technol., 172 (2017), 227-235.

Proceedings of international scientific conferences

1. **K. Davididou**, C. McRitchie, M. Antonopoulou, I. Konstantinou, E. Chatzisymeon, UV-A LED vs blacklight irradiation for the photocatalytic treatment of saccharin, 5th European Conference on Environmental Applications of Advanced Oxidation Processes (EAAOP5), 25-29 June 2017, Prague, Czech Republic.
2. **K. Davididou**, A. J. Expósito, J.M. Monteagudo, E. Chatzisymeon, A. Durán, Solar/UV-A-LED ferrioxalate photochemistry-based degradation of antipyrine. A comparative study, 9th European Meeting on Solar Chemistry and Photocatalysis: Environmental Applications (SPEA9), 13-17 June 2016, Strasbourg, France.
3. **K. Davididou**, E. Hale, N. Lane, E. Chatzisymeon, A. Pichavant, J.-F. Hochepied, Photocatalytic Treatment of Micropollutants in the Presence of TiO_2 Nanocomposites, 9th European Meeting on Solar Chemistry and Photocatalysis: Environmental Applications (SPEA9), 13-17 June 2016, Strasbourg, France.
4. **K. Davididou**, R. Nelson, E. Chatzisymeon, UV-LED TiO_2 photocatalysis for the degradation of bisphenol-A: LED vs. black light fluorescent lamp & investigation of key parameters, 4th European Conference on Environmental Applications of Advanced Oxidation Processes (EAAOP4), 21-24 October 2015, Athens, Greece.

Appendix C – Conference participation

1. School of Engineering, Research Conference, 21 April 2015, Edinburgh, UK. Poster Presentation.
2. 4th European Conference on Environmental Applications of Advanced Oxidation Processes (EAAOP4), 21-24 October 2015, Athens, Greece. Oral presentation.
3. Infrastructure and Environment Scotland 3rd Postgraduate Conference, 9 December 2015, Edinburgh, UK. Oral presentation. (*Award for the best presentation*).
4. 9th European Meeting on Solar Chemistry and Photocatalysis: Environmental Applications (SPEA9), 13-17 June 2016, Strasbourg, France. Poster presentation.
5. STEM for Britain, 13 March 2017, London, UK. Poster presentation.
6. 5th European Conference on Environmental Applications of Advanced Oxidation Processes (EAAOP5), 25-29 June 2017, Prague, Czech Republic. Poster presentation.

LIGHT EMITTING DIODES (LEDs) FOR CLEAN WATER

Energy efficient UV-LEDs Vs mercury lamps for the photocatalytic removal of Endocrine Disrupting Compounds (EDCs)

THE UNIVERSITY of EDINBURGH
School of Engineering
Konstantina DAVIDIDOU
K.Davididou@ed.ac.uk
Supervised by
Dr Thalia CHATZISYMEON

INTRODUCTION

EDCs are substances that pose a threat to human health and wildlife by affecting reproduction, growth and development. Their widespread detection in water reflects the inefficiency of current wastewater treatment processes and thus necessitates the **identification of new green-methods able to deal with EDCs pollution.**

EDCs sources

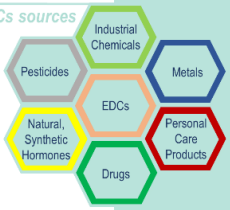

Heterogeneous photocatalysis, an advanced oxidation process known for its efficiency in EDC removal, makes use of a **catalyst** and **UV-A light** to degrade the pollutants. **Major drawback** of this method though is the **mercury lamps** being used to provide the UV-A.

(-) Increased operational cost
High environmental impact
Toxic mercury

OUR NOVELTY

We used a **UV-LED** as an **eco-friendly** alternative to mercury lamps and quantified the benefits arising from its use. For this reason, we tested the UV-LED and a mercury lamp in parallel experiments under identical conditions.

(+) Increased light intensity
Directional light output
Narrow emission spectra
Extended lifetime
Small environmental impact
Free of mercury

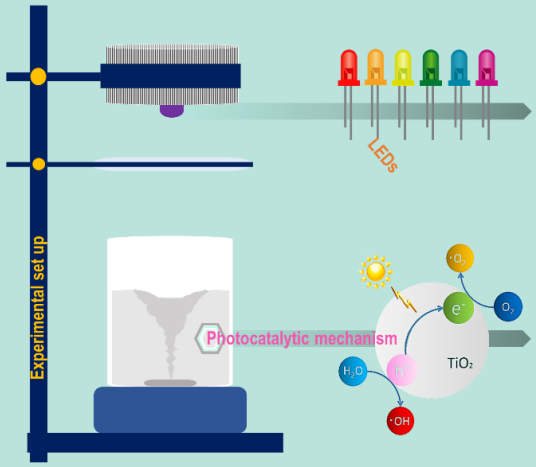

CHEMICALS

Bisphenol-A (BPA) was used as the **model compound**

The **catalyst** was TiO_2 nanoparticles (**Aeroxide P25**) in suspension

Bisphenol-A
- Flame-retardant
- Plastic monomer
- EDC

RESULTS

1-Removal efficiency

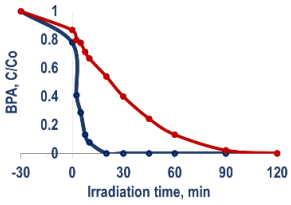

250 mg/L TiO_2
2.5 mg/L BPA
UV-LED
Mercury lamp

The **pure emission spectra** and **high photon flux** produced by LED lead to **higher degradation rates** and thus **shorter treatment time**

2- Cost efficiency

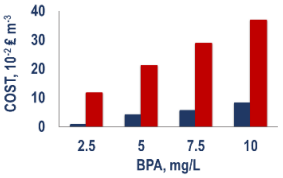

250 mg/L TiO_2
2.5-10 mg/L BPA
UV-LED
Mercury lamp

LED-driven photocatalysis delivered the **best cost efficiency**

CONCLUSIONS

Since **cost** and **efficiency** are key considerations for every process, the present work proved that **LED-driven photocatalysis** is a **viable** technology with great potential in real water applications for **EDC abatement.**

BENEFITS FOR ALL

Delivery of an **efficient** and **low cost technology** for the **control of water pollution by EDCs** that is **environmentally friendly** and **easily applicable** in both developed and developing countries.

School of Engineering, Research Conference, 21 April 2015, Edinburgh, UK.

Photocatalytic treatment of micropollutants in the presence of TiO_2 nanocomposites

by K. Dadididou,[1] E. Hale,[1] N. Lane,[1] E. Chatzisymeon,[1] A. Pichavant,[2,3] J.-F. Hochepied [2,3]

[1] Institute for Infrastructure and Environment, School of Engineering, The University of Edinburgh, Edinburgh EH9 3JL, United Kingdom (K.Dadididou@ed.ac.uk). [2] MINES ParisTech, PSL Research University, Centre des Matériaux, BP87 91003 Evry, France. [3] ENSTA ParisTech, Unité Chimie et Procédés, 828 Bd des Maréchaux, 91762 Palaiseau Cedex, France.

Aims & Objectives

This study deals with the **photocatalytic treatment** of **saccharin** (SAC) and **bisphenol-A** (BPA) under UV irradiation. SAC, the forerunner of artificial sweeteners, and BPA, a listed endocrine disrupting compound (EDC), are contaminants of increased environmental and health concern.

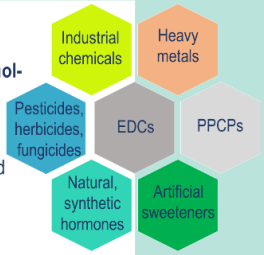

Novelty

Submicronic **anatase–rutile nanocomposite particles** with tuned phase ratio were produced by developing a simple and robust process based on **thermohydrolysis** of acidic Ti(IV) solutions in the presence of controlled amount of Sn(IV).

Materials & Methods

Experimental summary

- Organic substrates: SAC or BPA at $[C]_0$: 0-10 mg/L
- TiO_2 catalysts*: ANA (pure anatase), R15 (anatase/rutile-85/15) and R30 (anatase/rutile-70/30) at [C]: 0-600 mg/L

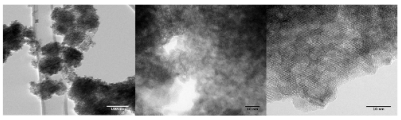

TEM observations for nanocomposites anatase-rutile

*Catalyst materials, preparation and characterisation techniques are described by Pichavant *et al* 2014 [1]

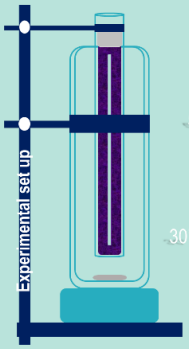

Experimental conditions

immersion well, batch mode

500 mL working volume

11W low pressure blacklight fluorescent lamp

30' adsorption/ 90' UV irradiation

pH ~ 4.6 (SAC), 6.4 (BPA)

Results

1- catalyst screening

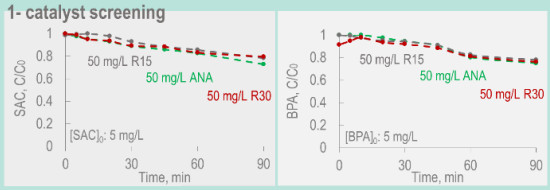

2- effect of initial substrate concentration

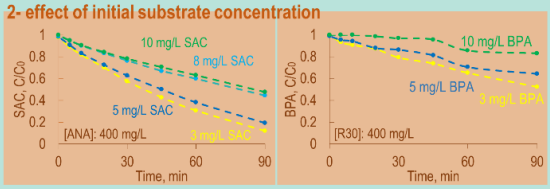

3- effect of catalyst loading

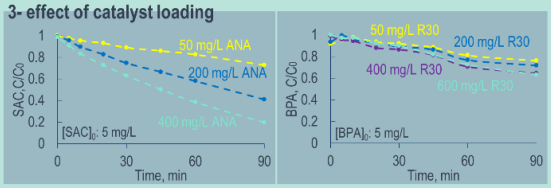

4- catalyst recovery & reuse

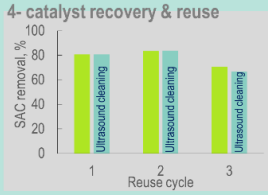

Photocatalytic conditions: $[SAC]_0$: 5 mg/L, [ANA]: 400 mg/L (at 1st cycle)

Recovery: the reactant mixture was centrifuged for catalyst particles recovery, at the end of each reuse cycle.

Ultrasound cleaning: the reactant mixture was placed into an ultrasound bath for 10 min, prior to treatment.

Conclusions

All the novel TiO_2 nanocomposites yielded similar SAC or BPA removal efficiencies. Catalyst loading and initial organics concentration were the factors affecting mostly the process performance. Furthermore, results obtained by catalyst recovery and reuse are promising; catalyst maintained its activity and led to 70% SAC removal, at the end of the 3rd cycle. Nonetheless, ultrasound cleaning of the reaction mixture, prior to treatment, did not improve the photocatalytic removal of SAC.

References

[1] A. Pichavant, E. Provost, M.-H. Berger, W. Fürst, J.-F. Hochepied, Interfaced titanium dioxide anatase–rutile nanocomposites by thermohydrolysis in presence of small amounts of Sn(IV) and their photocatalytic properties, Colloids and Surfaces A: Physicochemical and Engineering Aspects, 462 (2014) 64-68.

THE UNIVERSITY of EDINBURGH School of Engineering

ENSTA ParisTech

MINES ParisTech

9th European Meeting on Solar Chemistry and Photocatalysis: Environmental Applications (SPEA9), 13-17 June 2016, Strasbourg, France.

LED-photocatalysis for the removal of artificial sweeteners from water: eco-friendly & cost-efficient

by K. Davididou, C. McRitchie and E. Chatzisymeon

THE UNIVERSITY *of* EDINBURGH

The motivation

'Artificial sweeteners (ASs) are low-calorie or calorie-free chemical substances that are used instead of sugar to sweeten foods and drinks.'-NHS

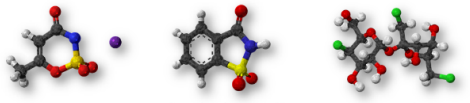

Acesulfame-K Saccharin (SAC) Sucralose

ASs have been recently recognised as emerging environmental contaminants due to their widespread occurrence in waterways.

Contamination

Formation of toxic by-products during natural attenuation

Unawareness of long-term ecological effects

Environmental persistence

Aim

The development of an efficient and eco-friendly water purification method for ASs treatment.

Our Approach

Heterogeneous photocatalysis is a chemical-free and simple process that makes use of a catalyst and UV light to oxidise the pollutants.

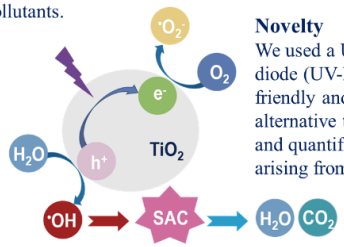

Photocatalytic mechanism

Novelty

We used a UV-light emitting diode (UV-LED) as an eco-friendly and inexpensive alternative to mercury lamps and quantified the benefits arising from its use.

Performance

A UV-LED and a mercury lamp (UV-BL) were tested in parallel experiments, under identical conditions, for SAC photocatalytic degradation.

Removal efficiency

UV-LED ≥ 86% UV-BL ≥ 35%

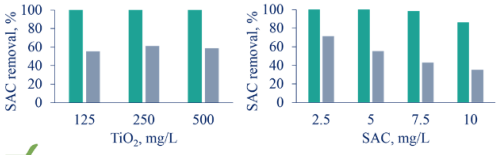

Treatment time

UV-LED ≥ 20 min UV-BL ≥ 45 min

Energy-efficiency

UV-LED 4-16 times more energy-efficient than UV-BL

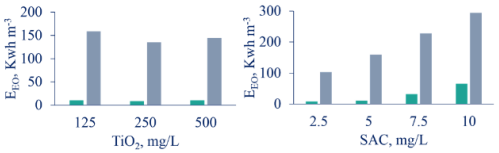

E_{EO}-energy required for 90% degradation of a pollutant per cubic meter of contaminated water.

Cost-efficiency

UV-LED 4-16 times cheaper than UV-BL

Why UV-LED performs better than UV-BL?

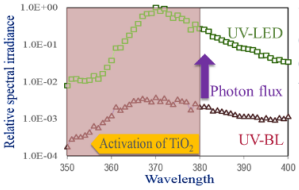

UV-LED is more energy-efficient in the conversion of electricity to light than UV-BL.

Benefits for all

An efficient and low cost technology for the control of water pollution by persistent microcontaminants that is eco-efficient and easily applicable in both developed and developing countries.

STEM for BRITAIN 2017 London

K.Davididou@ed.ac.uk

STEM for Britain, 13 March 2017, London, UK.

UV-LED vs blacklight irradiation for the photocatalytic treatment of saccharin

by K. Davididou[a], C. McRitchie[a], M. Antonopoulou[b], I. Konstantinou[c] and E. Chatzisymeon[a]

[a] Institute for Infrastructure and Environment, School of Engineering, The University of Edinburgh, Edinburgh EH9 3JL, United Kingdom [b] Department of Environmental & Natural Resources Management, University of Patras, 2 Seferi St., GR-30100 Agrinio, Greece [c] Department of Chemistry, University of Ioannina, GR-45110 Ioannina, Greece

The motivation

'Artificial sweeteners (ASs) are low-calorie or calorie-free chemical substances that are used instead of sugar to sweeten foods and drinks.'-NHS

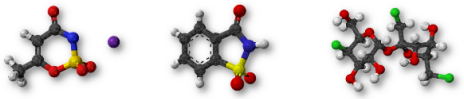

Acesulfame-K Saccharin (SAC) Sucralose

ASs have been recently recognised as emerging environmental contaminants due to their widespread occurrence in waterways.

Contamination

Formation of toxic by-products during natural attenuation

Unawareness of long-term ecological effects

Environmental persistence

Aim

The development of an efficient and eco-friendly water purification method for ASs treatment.

Our Approach

Heterogeneous photocatalysis makes use of a catalyst and UV light to oxidise the pollutants.

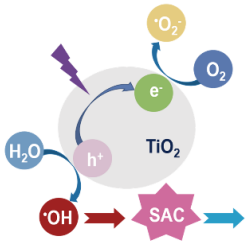

Photocatalytic mechanism

Novelty

We used a UV-light emitting diode (UV-LED) as an eco-friendly and inexpensive alternative to mercury lamps and quantified the benefits arising from its use.

Performance

A UV-LED and a mercury lamp (UV-BL) were tested in parallel experiments, under identical conditions, for SAC photocatalytic degradation.

Removal efficiency

UV-LED ≥ 86% UV-BL ≥ 35%

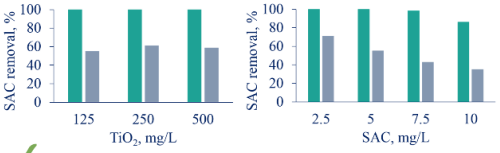

Treatment time

UV-LED ≥ 20 min UV-BL ≥ 45 min

Energy-efficiency

UV-LED 4-16 times more energy-efficient than UV-BL

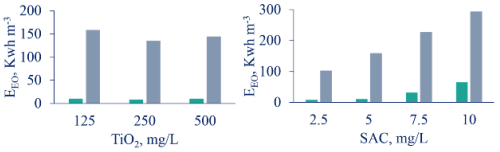

E_{EO}-energy required for 90% degradation of a pollutant per cubic meter of contaminated water.

Cost-efficiency

UV-LED 4-16 times cheaper than UV-BL

Why UV-LED performs better than UV-BL?

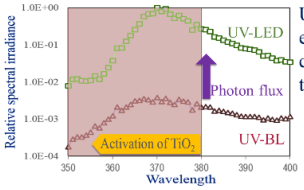

UV-LED is more energy-efficient in the conversion of electricity to light than UV-BL.

Benefits for all

An efficient and low cost technology for the control of water pollution by persistent microcontaminants that is eco-efficient and easily applicable in both developed and developing countries.

THE UNIVERSITY of EDINBURGH ΠΑΝΕΠΙΣΤΗΜΙΟ ΠΑΤΡΩΝ UNIVERSITY OF PATRAS University of Ioannina

K.Davididou@ed.ac.uk

EAAOP5 Prague, Czech Republic

5th European Conference on Environmental Applications of Advanced Oxidation Processes (EAAOP5), 25-29 June 2017, Prague, Czech Republic.